eman ta zabal zazu

Universidad del País Vasco
Euskal Herriko Unibertsitatea

Departamento de Bioquímica y Biología Molecular
Facultad de Ciencia y Tecnología

Targeting metabolism in emerging liver diseases

Tesis Doctoral presentada por

MARIA MERCADO GÓMEZ

Leioa

2024

Targeting metabolism in emerging liver diseases

Tesis Doctoral presentada por

Maria Mercado Gómez

Para la obtención del título de doctora en

Biología Molecular y Biomedicina **por la**

Universidad del País Vasco /Euskal Herriko Unibersitatea

Tesis dirigida por

Dra. Malu Martínez Chantar

Dra. Teresa de Jesus Cardoso Delgado

The project exposed in this thesis was performed at Center for Cooperative Research in Biosciences (CIC bioGUNE) under the supervision of Dra. Malu Martínez Chantar and Dra. Teresa de Jesus Cardoso Delgado.

Acknowledgments

Hace casi cinco años llegué a Bilbao con solo dos maletas, mucha incertidumbre y muchas ganas de empezar lo que se convertiría en la mejor etapa de mi vida. Después de dos años en el laboratorio de investigación biomédica del Hospital de Reus, sabía con certeza que mi vocación era la ciencia y que mi lugar estaba en el laboratorio, donde las horas volaban. Un día, vi la oferta de Malu en el que buscaba a un estudiante de doctorado en enfermedades de hígado, ¡justamente lo que me apasionaba! Aún me siento muy agradecida por haber sido seleccionada para este puesto en un laboratorio tan increíble.

Gracias, **Malu,** por confiar en mí desde el primer día. Admiro profundamente tu dedicación, tu capacidad de esfuerzo, tu habilidad para resolver problemas y tu determinación. Siempre he pensado que eres una genio. Gracias por guiarme en el mundo de la ciencia y enseñarme que no hay límites, que podemos lograr todo lo que nos propongamos. Ya sea estudiar un virus en medio de una pandemia o iniciar una línea de investigación sobre una enfermedad nueva en el laboratorio, siempre me has demostrado que la perseverancia y la curiosidad científica son esenciales para avanzar.

Al llegar el primer día de laboratorio, me recibieron dos personas que se convertirían en grandes modelos para mí: **Teresa** y **David**. Gracias, Teresa, por tu apoyo constante. Haber tenido la oportunidad de que fueras mi directora de tesis ha sido un regalo, porque eres una científica excepcional y mejor persona. Tu dedicación y pasión por la ciencia han sido una fuente de inspiración para mí y para todos. Gracias por enseñarme que la verdadera esencia de la ciencia no es solo la búsqueda de conocimiento, sino también la perseverancia, la humildad y el compromiso con los demás.

Como no, también quiero agradecer a mis compis de labo todos los momentos compartidos. A **Clàudia**, la meva companya de grans moments dins i fora del labo: llargues tardes a l'animalari, congressos que acaben de matinada a la part superior d'un bus a Londres o llargues xerrades sobre drames romàntics. Gràcies per la teva alegria i la teva amistat. A **Estefanía**, que, aunque hayas llegado hace relativamente "poco" al laboratorio, te has convertido en una parte esencial. Gracias por tus mil detalles y por ser mi mano derecha en los momentos más difíciles, eres una fantástica persona. A **Naroa** e **Irene**, por vuestra paciencia y por vuestro amor a la ciencia. Hacéis un trabajo increíble. A **Rubén**, por estar siempre dispuesto a ayudar y, de paso, sacarme una sonrisa. Nunca olvidaré todas las perfusiones juntos a las 8 de la mañana o los sábados en el labo. A **Claudia** y **Patri**, por crear un ambiente de equipo y de buen rollo en el labo. A **Álvaro**, por echarme una mano en el proyecto y por todos sus valiosos consejos. A **Marina**, por enseñarme todo lo que sé de animalario y por ser un ejemplo de esfuerzo y trabajo. A **Petar**, por tus ganas de compartir conocimiento y tu

buen humor. A **Alfonso**, por ayudarme siempre que lo he necesitado y por tus sabios consejos. A **Fer**, por ser mi primer profesor en el laboratorio en el mundo de las inmunoprecipitaciones y por tu alegría que nos animaba cada día. A **Rosario**, **Agustina**, **Miren**, **Sofía**, **Jorge**, **Carmen**, **Jon Ander**… por hacer del labo un lugar mejor. A todas las visitas inspiradoras: **Carol**, **Martina**, **Pietro**, **Laura**, **Mason**, **Duaa**, **Lolia**… A **Gotxi** y **Arantza**, por su trabajo diario y todos sus consejos.

También agradecer a nuestros vecinos de laboratorio. A **Ale**, por tu ayuda y por todas las tardes de roco y roca. A **Endika**, por tu paciencia y las horas delante de FACS viendo pasar aquellos desconocidos hepatos. A **Ana**, por tu alegría y tus consejos. A **Leire**, por ayudarnos cuando lo hemos necesitado. A **Asier**, por ser un gran compañero. A **Borja**, por transmitirme alegría constante. A **Laura**, por tus ganas de enseñarme el mundo de las HEK293 y tu capacidad de compartir. En general, quiero agradecer a toda la gente de bioGUNE por su disposición y por haber hecho que esta experiencia sea única.

Four months before finishing my PhD contract, I embarked on an exciting adventure to travel to another laboratory in Portugal, led by Cecília Rodrigues, to further investigate a relatively new type of cell death: ferroptosis. The best thing about Portugal is certainly the people (apart from pastéis de nata!). From the beginning, everyone welcomed me with open arms, especially **Marta**. You are an outstanding scientist and your ability to create such an amazing, friendly and motivated atmosphere is invaluable. You inspire me greatly. I would also like to thank **Cecília** for your constant smile and willingness to help. Your support and encouragement have been invaluable to my research and personal growth. Additionally, I extend my gratitude to the fantastic Portuguese team formed by **Mariana**, **Jan**, **Andre** and all the people. Thank you for making my stay in Lisbon easier. Muito obrigada a todos pela vossa ajuda!

Durante los años de doctorado me crucé con personas maravillosas que se convirtieron en lo mejor de mi etapa en Bilbao. Gracias a **Anna** por ser una compañera de piso, una amiga, una hermana… Gracias por compartir confidencias y momentos juntas. Luego vino **Andrea**, quien se convirtió en mi alma gemela. Gracias por las mil locuras juntas y por hacerme sentir siempre como en casa ¡Que te quiero! Gracias **Yuri**, por ser mi mejor amigo, por compartir tantos momentos de montaña juntos y, más importante, por escucharme y querer lo mejor para mí. Gracias **Silvia**, por todas esas conversaciones y por tener esa energía vibrante que hace que estar a tu lado sea un regalo. Eskerrik asko **Jon**, per fer sentir tant a gust les persones que estem al teu costat. Cada dia aprenc una mica més de tu, ets molt gran! Gràcies **Clara,** per ser una font d'inspiració: els teus valors, la teva tranquilitat, la teva empatía… Ets fantàstica. Eskerrik asko **Aitor**, tu presencia ha hecho que esta etapa

sea inolvidable, eres una persona maravillosa. 谢谢 **Simon**, por tu positividad contagiosa y por la habilidad de sacarnos sonrisas en los momentos más difíciles. Eskerrik asko **Kike**, por todas esas charlas tan interesantes y por ser un gran amigo. També donar les gràcies a persones que han estat sempre, **Marta**, '¡ya son más de 27 años!' i tots els que ens queden per viure juntes. Gràcies **Pau**, pel teu suport i per ajudar-me a crèixer.

Vull agrair també a les amigues "de la uni", que més que "de la uni" sou amigues "de la vida". M'heu demostrat que puc comptar amb vosaltres sempre i del valor de l'amistat. **Nú**, gràcies pel teu suport incondicional en els bons i en els mals moments. La teva amistat significa molt per a mi. **Meri**, estic molt agraida de tenir-te com a amiga, gràcies per ser un gran pilar sobretot aquests últims mesos. **Silvia**, qui ens hauria dit fa uns anys que acabariem tan unides per la feina! El destí m'ha donat aquesta sort de tenir-te com amiga. **Berta**, en res presentaràs la teva tesi. Vals moltíssim i estic segura que tothom ho sabrà apreciar. **Ingrid**, admiro moltíssim la teva empatía i com has evolucionat fins a convertirte en una persona i una mestra excepcional durant aquests darrers anys. **Sònia**, gràcies per acompañar-me en les aventures arreu del món. Em fa molt feliç veure't tan radiant com estàs ara. **Raül**, sempre has estat un amic molt important per mi i espero que compartim molts més moments junts.

En especial, m'agradaria agrair aquesta tesis a la meva familia que han estat el suport més important per mi durant aquests 4 anys. Especialment a la meva mare, l'Ana, la meva àvia i la meva tieta. **Mama**, gràcies per ser un gran exemple de superació i de treball; i per confirar en mi més del que jo ho faig. **Ana**, gracias por ser mi mejor amiga y por poder contar contigo siempre que lo necesito. **Iaia**, gràcies per rebre'm sempre amb les mans obertes i per ser un gran pilar en la meva vida. **Tieta**, gràcies pel teu suport i pels teus savis consells. **Glòria** i **Toni**, gràcies pel vostre recolzament. També agrair-li a **Carlos** la seva ajuda en tot moment. Finalment un especial agraiment a les petites de la casa: **Neula** i **Avellana**. Sense tots vosaltres aquesta tesis no hagués estat posible.

Finalmente, quiero dedicarle esta tesis a mi abuelo **Manolito**. Gracias por enseñarme el verdadero valor de la familia y por siempre creer en mí.

Eskerrik asko!

Abbreviations

2-DG	2-deoxy-D-glucose
3D	Three-dimensional
4-HNE	4-hydroxynonenal
α-KG	Alpha-ketoglutarate
ABC	ATP-binding cassette
ACE2	Angiotensin-converting enzyme 2
ACD	Accidental cell death
ACDP	Ancient conserved domain protein
AFP	Alpha-fetoprotein
AKI	Acute kidney injury
AKT	Protein kinase B
ALOX	Arachidonate lipoxygenases
ALP	Alkaline phosphatase
ALT	Alanine aminotransferase
AMPK	AMP-activated protein kinase
Ang 1-7	Angiotensin 1-7
Ang II	Angiotensin II
ANOVA	Analysis of variance
ARDS	Acute respiratory distress syndrome
ASGPR	Asialoglycoprotein receptor
AST	Aspartate transamine
ATP	Adenosine triphosphate
ATR	Angiotensin II receptor
BLCA	Bladder Urothelial Carcinoma
BMI	Body mass index
BRCA	Breast invasive carcinoma
BTC	Biliary tract cancer
CA19-9	Carbohydrate antigen 19-9
Ca^{2+}	Calcium ion
CAM	Chick chorioallantoic membrane
CCA	Cholangiocarcinoma
cDNA	Complementary DNA
CEA	Carcinoembryonic antigen
CESC	Cervical squamous cell carcinoma and endocervical adenocarcinoma
CHOL	Cholangiocarcinoma
CisGem	Cisplatin and gemcitabine
CK19	Cytokeratin 19
CNNM	CBS-pair domain divalent cation transport mediator
CNNM4	Cyclin M4
COAD	Colon adenocarcinoma
COVID-19	Coronavirus disease 2019
CSC	Cancer stem cell
CRP	C-reactive protein
DAVID	Database for annotation, visualization and integrated discovery
dCCA	Distal cholangiocarcinoma
DCT	Distal convoluted tubule
DFS	Disease free survival
DILI	Drug-induced liver injury
DMEM	Dulbecco's Modified Eagle Medium

E protein	Envelope protein
ECAR	Extracellular acidification rate
EGF	Epidermal growth factor
EGFR	Epidermal growth factor receptor
ELISA	Enzyme-linked immunosorbent assay
EMT	Epithelial-mesenchymal transition
EpCAM	Epithelial cell adhesion molecule
ER	Endoplasmic reticulum
ERK	Extracellular signal-regulated kinase
ESCA	Esophageal carcinoma
Fe^{2+}	Ferrous ion
Fe^{3+}	Ferric ion
FBXW7	F-box and wd repeat domain containing 7
FGFR	Fibroblast growth factor receptor
FOLFOX	5-fluorouracil and oxaliplatin
FT	Flow through
FXR	Farnesoid X activated receptor
GalNAc	*N*-acetylgalactosamine
GBM	Glioblastoma multiforme
GEMOX	Gemcitabine and oxaliplatin
GGT	Gamma-glutamyltransferase
GLI	Glioma-associated oncogene
GLS	Glutaminase
GLS2	Glutamine synthase 2
GPX4	Glutathione peroxidase 4
GS	Glutamine synthetase
GSH	Reduced glutathione
H&E	Hematoxylin and eosin
hACE2	Humanized angiotensin-converting enzyme 2
HCC	Hepatocellular carcinoma
HDL	High-density lipoprotein
HER2	Human epidermal growth factor receptor-2
HH	Hedgehog
HIF-1α	Hypoxia-inducible factor-1 alpha
HNSC	Head and Neck squamous cell carcinoma
HO-1	Heme oxygenase-1
HOMA	Homeostasis model assessment
HSC	Hepatic stellate cells
iCCA	Intrahepatic cholangiocarcinoma
ICU	Intensive care unit
IDH1	Isocitrate dehydrogenase 1
IDH2	Isocitrate dehydrogenase 2
IG-iCCA	Intraductal-growing intrahepatic cholangiocarcinoma
IHC	Immunohistochemistry
IL-1β	Interleukin 1 betac
IL-6	Interleukin 6
IL6R	Interleukin 6 receptor
IL-12	Interleukin 12
IL-17	Interleukin 17

IP	Immunoprecipitation
IQR	Interquartile
JAK	Janus kinase
KICH	Kidney Chromophobe
KIRC	Kidney renal clear cell carcinoma
JNK	c-Jun N-terminal kinase
LC-MS/MS	Liquid chromatography with tandem mass spectrometry
LDH	Lactate dehydrogenase
LDL	Low-density lipoprotein
LIHC	Liver hepatocellular carcinoma
LNP	Lipid nanoparticle
LSEC	Liver sinusoidal endothelial cell
LUAD	Lung adenocarcinoma
LUSC	Lung squamous cell carcinoma
M	Presence of metastasis
M protein	Membrane glycoprotein
MagT1	Magnesium transporter 1
MASLD	Metabolic dysfrunction-associated steatotic liver disease
MAPK	Mitogen-activated protein kinases
MCD	Methionine-choline deficient
MCSCs	Metastatic cancer stem cells
MDA	Malondialdehyde
MEM	Minimum Essential Medium
MASH	Metabolic dysfunction-associated steatohepatitis
Met	Metformin
MF-iCCA	Mass-forming intrahepatic cholangiocarcinoma
Mg^{2+}	Magnesium ion
miRNA	microRNA
MMgT	Membrane magnesium transporter
MOC	Mechanisms of chemoresistance
MRS2	Mitochondrial RNA splicing 2
mTOR	Mechanistic target of rapamycin
N	Extend of spread to the lymph nodes
N protein	Nucleocapsid protein
Na^{+}	Sodium ion
NAAT	Nucleic acid amplification test
NADPH	Nicotinamide adenine dinucleotide phosphate
NAFLD	Non-alcoholic fatty liver disease
NASH	Non-alcoholic steatohepatitis
NETosis	neutrophil extracellular trap-associated cell death
NG	Normoglycemia
NGAL	Neutrophil gelatinase-associated lipocalin
NF-κB	Nuclear factor kappa B
NICD	Notch intracellular domain
NOX	NADPH oxidase
NRP-1	Neuropilin-1
NUPR-1	Nuclear protein 1
OAT	Organic anion-transporter

OATP	Organic anion-transporting polypeptide
OCR	Oxygen consumption rate
OCT	Organic cation transporters
OS	Overall survival
PAAD	Pancreatic adenocarcinoma
PARK16	Parkinson disease 16
PCA	Principal component analysis
pCCA	Perihilar cholangiocarcinoma
PCD	Programmed cell death
PCNA	Proliferating cell nuclear antigen
PCPG	Pheochromocytoma and Paraganglioma
PD-1	Programmed cell death 1
PDX	Patient-derived xenograft
PI3K	Phosphoinositide 3-kinase
PI-iCCA	Periductal-infiltrating intrahepatic cholangiocarcinoma
PL	Phospholipid
POR	Cytochrome P450 oxidoreductase
PPAR	Peroxisome proliferator-activated receptor
PPP	Pentose phosphate pathway
PRAD	Prostate adenocarcinoma
PRR	Pattern-recognition receptor
PT	Proximal tube
PTEN	Phosphatase and tensing homolog
PUFA	Polyunsaturated fatty acids
PUFA-PL-OOH	Polyunsaturated fatty acids phospholipid hydroperoxides
PUFA-PL-OH	PUFA phospholipid alcohols
q-PCR	Quantitative polymerase chain reaction
RAS	Renin-angiotensin system
RBD	Receptor-binding protein
RCD	Regulated cell death
READ	Rectum adenocarcinoma
RIPA	Radio-immunoprecipitation assay
ROS	Reactive oxygen species
RPS6K	Ribosomal protein S6 kinase
RT	Room temperature
S protein	Spike protein
SARC	Sarcoma
SAV-PE	Streptavidin-phycoerythrin
SARS-CoV-2	Severe acute respiratory syndrome coronavirus 2
SEM	Standard error of the mean
shRNA	Short hairpin RNA
siRNA	Small interfering RNA
SKCM	Skin Cutaneous Melanoma
SL	Surrounding tissue
SLC	Solute carriers
SLC41	Solute carrier family 41
SLC7A11	Solute carrier family 7 member 11 or system x_c^- antiporter
SMO	Smoothened
SOCS-3	Suppression of cytokine 3
STAD	Stomach adenocarcinoma

STAT	Signal transducers and activators of transcription
T	Extent of the tumor
T2DM	Type 2 diabetes mellitus
TAL	Thick ascending limb
TCA	Tricarboxylic acid
TCGA	The cancer genome atlas
TGF-β	Transforming growth factor betta
TGF-βR	Transforming growth factor betta receptor
THCA	Thyroid carcinoma
THR	Thyroid hormone receptor
THYM	Thymoma
TIC	Tumor initiating cells
TIGER	The Thailand Initiative in Genomics and Expression Research
TLR	Toll-like receptor
TMPRSS2	Transmembrane protease serine 2
TMPS6	Transmembrane protease serine 6
TNF	Tumor necrosis factor
TRPM6-7	Transient receptor potential melastatin 6-7
UCEC	Uterine Corpus Endometrial Carcinoma
VOC	Variants of concern
vWF	Von willebrand factor
WHO	World Health Organization
WT	Wild-type
XMEN	X-linked *MAGT1* deficiency with increased susceptibility to EBV-infection and N-linked glycosylation defect
YAP1	Yes1 associated transcriptional regulator
ZnPP	Zinc protoporphyrin

Table of content

Summary

This PhD thesis is structured into two distinct studies, each focusing on a different disease: cholangiocarcinoma and COVID-19, with the inclusion of COVID-19 due to the emergence of the pandemic during this research. Despite the apparent disparity between cholangiocarcinoma and COVID-19 approaches, these studies reveal shared molecular pathways that will be discussed throughout this work.

S.1. Study 1

Magnesium (Mg^{2+}) is an essential micronutrient predominantly located intracellularly, crucial for metabolism, cellular proliferation and structural integrity. Mg^{2+} homeostasis in mammals is regulated by Mg^{2+}-binding molecules, organelle storage and six families of Mg^{2+} channels and exchangers, including the lesser-studied CNNM family. The CNNM family, consisting of four proteins (CNNM1-4), regulates Mg^{2+} homeostasis across various cellular membranes. Mg^{2+} deficiency has been linked to a variety of diseases, such as an increased metastatic potential, as demonstrated in inducible mouse models of colon tumors. However, its role in cholangiocarcinoma (CCA) remains unexplored. CCA, a heterogeneous neoplasm of biliary tree cells, is highly aggressive with poor prognosis and limited treatment options, representing the most common biliary tract malignancy and the second most prevalent primary liver tumor.

Our group, the Liver Disease Laboratory, has previously identified the Mg^{2+} transporter CNNM4 as a critical factor in liver conditions such as metabolic dysfunction-associated steatohepatitis (MASH) and drug-induced liver injury (DILI). However, the role of magnesium homeostasis in the pathobiology of CCA and its potential as a therapeutic target in this condition remains unknown.

Herein, we demonstrate that CNNM4 is the only CNNM transporter consistently upregulated in hepatic biopsies from CCA patients, in livers from *in vivo* transposon-based CCA mouse models and in CCA cell lines. Notably, CNNM4 expression is higher in CCA compared to various other tumor types. Moreover, depletion of *CNNM4* in CCA cell lines results in elevated cytoplasmic and mitochondrial Mg^{2+} levels, thus identifying CNNM4 as an efflux transporter of Mg^{2+} in cholangiocytes. Our findings elucidate the implication of CNNM4 in the pathophysiology of CCA, as *CNNM4* silencing in CCA cell lines promotes excessive ROS production leading to iron-dependent cell death, known as ferroptosis. This effect is also observed following liver-specific *Cnnm4* silencing *in vivo*. Consequently, this process reduces tumoral proliferation, diminishes cancer stem cell renewal and proliferation, decreases chemotherapy resistance, limits metastatic capacity and mitigates the metabolic rewiring characteristic of cancer, the Warburg effect.

In conclusion, our results indicate that increased CNNM4 expression drives CCA progression and malignancy and that its liver-specific inhibition may be an effective therapeutic strategy to limit proliferation and metastasis in CCA patients.

S.2. Study 2

Coronavirus disease 19 (COVID-19) caused by severe acute respiratory syndrome coronavirus 2 (SARS-CoV-2), is a highly contagious disease leading to severe respiratory infections and significant mortality globally. This pandemic virus expresses four key structural proteins: nucleocapsid (N), spike (S), membrane (M), and envelope (E), with the spike protein facilitating viral entry into host cells via binding to ACE2 receptors. Besides ACE2, other factors such as TMPRSS2 and NRP-1 facilitate SARS-CoV-2 binding to the cell membrane.

Upon entry, SARS-CoV-2 triggers innate immune responses and cytokine release, leading to hyperinflammation and potential multiorgan failure in severe cases. The virus also disrupts the renin-angiotensin system, potentially exacerbating inflammatory responses through altered ACE2 function. Notably, COVID-19 impacts liver function, evidenced by elevated liver enzymes, steatosis in autopsies and worsened outcomes in patients with pre-existing liver diseases like MASH. Various hypotheses have emerged to explain the underlying mechanisms of liver effects in COVID-19. Besides direct viral-induced liver damage, potential mechanisms include immune-mediated injury, ischemia-reperfusion injury, and drug-related hepatotoxicity.

In our research, we found that hepatocytes could bind to the SARS-CoV-2 spike protein through interactions involving ACE2, TMPRSS2 and NRP1. This interaction triggers alterations in iron metabolism-related signaling pathways, leading to increased mitochondrial ROS production, disruption of cellular oxidative balance and enhanced mitochondrial activity. Additionally, dysregulation of the renin-angiotensin system contributes to these effects. Steatotic hepatocytes show increased infection by spike particles correlating with ACE2 levels, which are reduced upon treatment with metformin, a conventional therapy for hyperglycemic patients with metabolic dysfunction-associated steatotic liver disease (MASLD).

In conclusion our findings provide evidence that hepatocytes are susceptible to SARS-CoV-2 pseudovirus infection and we propose that metformin could be a therapeutic option to attenuate SARS-CoV-2 infection in patients with MASLD.

Introduction

This thesis is structured around two different research lines, each presented in separate sections (Study 1 and 2). The first study, titled '*Silencing CNNM4 halts progression and metastasis in cholangiocarcinoma sensitizing cells to ferroptosis***'** presents unpublished research. The second study '*Obese patients with MASH have increased hepatic expression of SARS-CoV-2 critical entry points. The spike of SARS-CoV-2 promotes metabolic rewiring in hepatocytes'* is based on two published papers.

1. Study 1

I.1.1. Magnesium (Mg2+)

I.1.1.1. Mg^{2+} in evolution

The significance of Mg^{2+} traces its origin to the inception of life on Earth, when magnesium silicate, abundant in both the crust and the primordial ocean, served as a fundamental metabolic substrate for the earliest cellular organisms. Following this era, Mg^{2+} fulfilled a vital function in the process of photosynthesis as an integral component of chlorophyll, thereby facilitating the oxygenation of the atmosphere, distinguishing Earth from other planets. Furthermore, Mg^{2+} played a critical role in the development of animal cells, particularly in the biosynthesis of adenosine triphosphate (ATP), where it functions as an indispensable cofactor[1].

I.1.1.2. Mg^{2+} physiology

Taking the above into consideration, Mg^{2+} stands as a crucial micronutrient, accounting for the primary divalent intracellular cation and the fourth most abundant ion in the body[2,3]. This element has been detected within the nucleus, cytoplasm, mitochondria and endoplasmic reticulum (ER)[4]. While Mg^{2+} typically exists in concentrations of approximately 10–30mM, most of the intracellular Mg^{2+} is bound to ribosomes, polynucleotides and ATP, resulting in a freely available Mg^{2+} concentration within the low millimolar range (0.5–1.2mM)[2].

Mg^{2+} is a versatile ion involved in practically every major metabolic and biochemical process within the cell. The extensive number of enzymes reliant on Mg^{2+} is an example of its magnitude (600 acting as cofactor and 200 as activator) including nucleotide polymerases, DNA repair enzymes, maintenance of genomic and genetic stability and, notably, as an essential part of ATP, which is indispensable for glycolysis and various other metabolic pathways[5]. Additionally, despite similar free Mg^{2+} concentrations in the cell and in the extracellular fluid, thereby lacking a considerable transmembrane gradient, Mg^{2+} plays a key role in signal transduction. Notably, the Mg^{2+}/calcium (Ca^{2+}) ratio holds significant importance in many organs considering Mg^{2+} role as a Ca^{2+} antagonist within cells[3]. Furthermore, it participates in energy metabolism regulation, T-cell activation,

growth factor stimulation and regulates N-methyl-D-aspartate or glutamate receptors through mechanisms that involve Mg^{2+} availability within the cell[6–8]. For instance, Mg^{2+} can be released from the ER upon stimulation by ligands such as L-lactate, translocating into the mitochondria and altering cellular metabolism[9]. The broad spectrum of functions accomplished by Mg^{2+} includes being part of some biological structures, such as in DNA and RNA tertiary structures as it binds with the electronegatively elements O and N molecules within the polynucleotide chains[10]. Moreover, cellular proliferation is directly correlated to Mg^{2+} content, as it promotes nucleotide and protein synthesis in healthy cells. In tumoral cells, severe Mg^{2+} deprivation induces growth arrest while chronic Mg^{2+} deprivation results in adaptation of tumor cells to both growth rates and Mg^{2+} content[11].

I.1.1.3. Mg^{2+} homeostasis

Given its extensive physiological roles, maintaining a stable intracellular concentration of Mg^{2+} within a narrow range is essential. This balance is tightly regulated through dynamic processes involving Mg^{2+} intake, intestinal absorption, renal excretion, bone storage and tissue-specific demands (**Figure I.1**)[5,12].

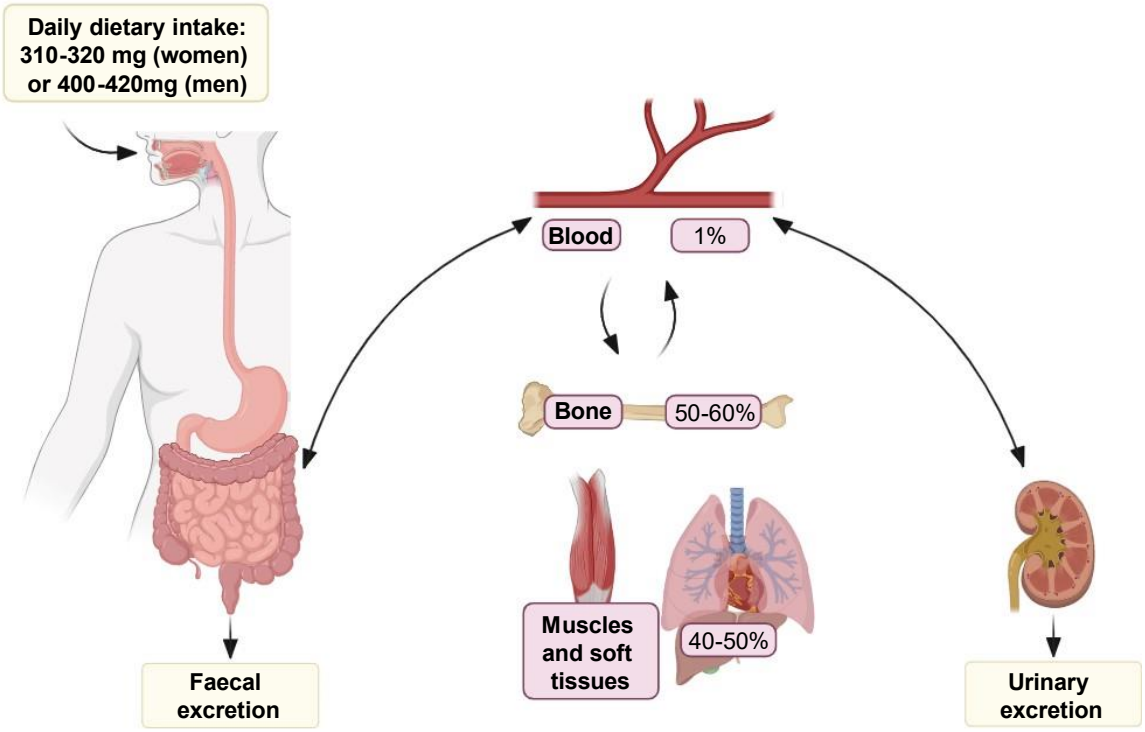

Figure I.1. Magnesium homeostasis across the body. The recommended dietary allowance is 310-320 mg for women and 400-420 mg form men. Magnesium is absorbed in the intestine, mainly stored in the bone, muscle and soft tissues and eliminated via fecal and urinary excretion.

As an essential micronutrient, Mg^{2+} cannot be synthetized in the body and must therefore be obtained through dietary intake. The recommended dietary allowance for adults is 400-420 mg daily for men and 310-320 mg for women[13].

Mg^{2+} is mainly located in the intracellular space, predominantly stored in bone (50-60%) and distributed among muscles and soft tissues (40-50%), whereas less than 1% is circulating in serum[14]. Consequently, due to the expulsion of magnesium by cells into the extracellular fluid to stabilize serum levels, serum magnesium is a poor indicator of intracellular magnesium content. In cases of magnesium deficiency, serum magnesium concentrations are specific but not sensitive[15]. Magnesium is excreted by both the intestine and the kidneys, detailed in section '*I.1.1.3.2. Mg^{2+} (re)absorption in intestine and kidney*'.

I.1.1.3.1. Mg2+ transporting proteins

The precise regulation of Mg^{2+} homeostasis in mammals relies on the involvement of Mg^{2+}-binding molecules, Mg^{2+} storage in organelles and the function of six families of Mg^{2+} channels and exchangers[16] (**Table I.1**). Some molecular mechanisms related to Mg^{2+} transport remain still being questioned and thus, a comprehensive understanding of cellular magnesium homeostasis has yet to be achieved.

I.1.1.3.1.1. Transient receptor potential melastatin (TRPM) family

TRPM6 and its homologue TRPM7, members of transient receptor potential channel melastatin family, are commonly known as "channel kinases" due to their unusual bifunctional nature as kinase-coupled divalent cation-selective channels[17,18]. Both channels are modulated by intracellular magnesium and are permeable to divalent cations such as Mg^{2+}, Ca^{2+} or Zn^{2+} [17,19]. TRPM7 presents ubiquitous expression across all mammal cells, with elevated levels in the heart and kidney, whereas TRPM6 is primarily expressed in epithelial cells of the kidney, placenta and intestine[20]. Beyond their physiological functions, these channels have been implicated in several pathological processes such as hypomagnesemia with secondary hypocalcemia and neurodegenerative, renal and cardiac diseases[21–25].

I.1.1.3.1.2. Solute carrier family 41 (SLC41)

The 41st solute carrier family comprises three isoforms: SLC41A1, SLC41A2 and SLC41A3, all of which play roles in the flux of divalent cations across the plasma membrane or organellar membranes[26]. Specifically, SLC41A1 and SLC41A3 function as Na^{+}-dependent Mg^{2+} exchangers responsible for Mg^{2+} efflux in the plasma membrane and the inner mitochondrial membrane, respectively[27,28]. The role of SLC41A2 remains

controversial, although it is presumed to be associated with Mg^{2+} flux across cellular membranes[29]. The presence of SLC41A1 gene in the PARK16 (Parkinson Disease 16) locus implicates single nucleotide polymorphisms or genetic variants in altering the risk of Parkinson disease[30–33]. Moreover, specific genetic variants of SLC41A1 have been linked to nephronophthisis-related ciliopathies and alterations in its expression have been associated with preeclampsia[34,35]. SLC41A2 is implicated in modulating cellular responses to chemotherapeutic agents and in protecting against cellular instability, particularly in conditions such as drug-induced cytotoxicity and Parkinson disease models[36,37]. Furthermore, SLC41A3 has been linked to severe hydronephrosis, abnormal locomotor function and serves as a potential biomarker for hepatocellular carcinoma[26,38].

I.1.1.3.1.3. Mitochondrial RNA splicing 2 (MRS2)

MRS2, a member of the evolutionarily conserved CorA superfamily of Mg^{2+} transporters, resides within the inner mitochondrial membrane of mammalian cells. It acts as the primary Mg^{2+} entry protein channel into the mitochondrial matrix, regulating mitochondrial metabolism and facilitating inter-organ communication[9,39]. The disfunction of MRS2 has been linked to severe pathologies, including neurodegeneration, impaired oxidative-phosphorylation, reduced cell viability and aggravated cancer progression[40–43].

I.1.1.3.1.4. Magnesium transporter 1 (MagT1)

MagT1 has been identified as a channel facilitating Mg^{2+} movement across the plasma membrane and is essential for maintaining Mg^{2+} levels in the absence of TRPM7[44]. Additionally, MagT1 functions as a subunit of the oligosaccharyltransferase complex, playing a crucial role in glycan transfer onto proteins[45]. In humans, loss-of-function mutations in the *MAGT1* gene lead to "X-linked *MAGT1* deficiency with increased susceptibility to EBV-infection and N-linked glycosylation defect" (XMEN) syndrome, a multisystem disorder that compromises the immunology system[45,46].

Table I.1. Magnesium transporting proteins. Abbreviations: TRPM, Transient receptor potential melastatin; SLC41, solute carrier family 41; HCC, hepatocellular carcinoma; MRS2, mitochondrial RNA splicing 2; MagT1, magnesium transporter 1; ER; endoplasmic reticulum; XMEN, X-linked MAGT1 deficiency with increased susceptibility to EBV-infection and N-linked glycosylation defect; MmgT1, membrane magnesium transporter 1; CNNM, CBS-pair domain divalent cation transport mediator; MASH, Metabolic dysfunction-associated steatohepatitis.

Transporting protein	Subcellular localization	Tissue distribution	Function	Mechanism	Diseases	Ref
TRPM family						
TRPM6	Apical plasma membrane	Intestine, placenta, kidney	Mg^{2+} influx	Channel	Hypomagnesaemia with secondary hypocalcemia	17,18,20,21
TRPM7	Plasma membrane	Ubiquitous	Mg^{2+} influx	Channel	Neurodegenerative diseases, cancer, renal ischemia, cardiac atrial fibrillation…	17–20,22–25
SLC41A family						
SLC41A1	Plasma membrane	Ubiquitous	Na^{+}-dependent Mg^{2+} efflux	Exchanger	Parkinson disease, nephronophthisis-related ciliopathies, preclampsia	26,27,30–35
SLC41A2	Plasma and organellar membrane	Ubiquitous	Mg^{2+} flux (unknown)	Unknown	Chemotherapeutic cytotoxicity, Parkinson disease	26,29,36,37
SLC41A3	Inner mitochondrial membrane	Ubiquitous	Na^{+}-dependent Mg^{2+} efflux	Exchanger	Hydronephrosis, abnormal locomotor coordination, HCC	26,28,38
MRS2	Inner mitochondrial membrane	Ubiquitous	Mg^{2+} influx	Channel	Neurodegeneration, cancer	9,39–43
MagT1	Plasma membrane/ER	Ubiquitous	Mg^{2+} influx	Channel	XMEN syndrome	44–46
MMgT family						
MMgT1	Golgi and post-Golgi vesicles /ER	Ubiquitous	Mg^{2+} influx	Channel	Tuberculosis	47,48
MMgT2	Golgi and post-Golgi vesicles /ER	Ubiquitous	Mg^{2+} influx	Channel		47
CNNM family						
CNNM1	Cytosol and nucleus	Brain, testis	Mg^{2+} efflux	Transporter	Gonadogenesis defect, cancer	16,49–55
CNNM2	Plasma membrane	Ubiquitous	Mg^{2+} influx and efflux	Transporter	Familial hypomagnesemia, schizophrenia, sleep apnea, cancer…	16,56–64
CNNM3	Plasma membrane/ Golgi /ER	Ubiquitous	Mg^{2+} influx	Transporter	Cervical cancer, lung adenocarcinoma, Rosette-forming glioneuronal rumor, HCC	16,65–69
CNNM4	Plasma membrane/ER	Brain, testis, intestine	Mg^{2+} efflux	Transporter	Jalili syndrome, MASH, acetaminophen toxicity	16,70–76

I.1.3.1.5. Membrane magnesium transporter (MMgT) family

MMgT1 and MMgT2 constitute the MMgT family, two proteins that facilitate Mg^{2+} transport across membranes of Golgi and post-Golgi organelles in epithelium-derived cells, thereby regulating the metabolism, protein assembly and glycosylation within those organelles. The expression of both proteins is modulated by Mg^{2+} availability and they colocalize in the Golgi complex. However, there is only a partial colocalization within the post-Golgi vesicles, suggesting that they might traffic to separate compartments[47]. Recently, MMgT1 has been associated with Mycobacterium tuberculosis, as a defect in *MMGT1* gene promotes the persistence of infection[48].

I.1.1.3.1.6. CBS-pair domain divalent cation transport mediator (CNNM) family

The genetic deficiency of *CNNM2* resulting in familial hypomagnesemia highlights the critical role of the CNNMs in the regulation of magnesium regulation[56]. The CNNM family consists of four proteins (CNNM1-4) that have been evolutionarily conserved, therefore they were originally named as ancient conserved domain protein (ACDP)[77]. CNNM is a complex protein with four independent domains that together have the capability to transport Mg^{2+} ions across cellular membranes, such as the plasma membrane but also in the ER and the Golgi organelle in the case of CNNM3 and regulate Mg^{2+} homeostasis within the cell[16,69]. The tissue distribution of CNNM isoforms varies across different tissues in the body (**Figure I.2**). CNNM2 and CNNM3 are ubiquitous, with CNNM2 exhibiting high expression levels in the brain, endocrine tissues, bone marrow, and kidney, specifically in the distal convoluted tubule and the tick ascending limb of Henle's loop[57,78]. In contrast, CNNM1 shows higher expression in the testis and seminal vesicle, with notable expression also observed in the brain, the adrenal gland and the kidney. Finally, CNNM4 exhibits high expression in various brain regions, the testis and the digestive tract, where dietary Mg^{2+} absorption occurs. Under physiological conditions, CNNM4 expression is minimal in the liver[16,78].

Despite the evident association with Mg^{2+} transport, several hypotheses have emerged over time regarding the biological function of mammalian CNNM proteins. Initially, it was suggested that CNNM proteins may indirectly modulate the influx of Mg^{2+} into the cytosol[56,79]. Alternative theories suggest that CNNMs might function as Na^+/Mg^{2+} exchangers responsible for extruding cytosolic Mg^{2+} from the cell. The first evidence of their role in Mg^{2+} transport came from studies involving CNNM4. Overexpression of CNNM4 in human cultured HEK293 cells led to a decrease in $Mg^{2+}$and increase Na^+ levels within the cell whereas depletion of CNNM4 resulted in an increase in intracellular Mg^{2+} levels[80]. Moreover, recent studies suggest that CNNMs may act as bifunctional proteins, employing TRPM7 channel to facilitate the

influx of divalent cation while also possessing a separate TRPM7-independentfunction for Mg^{2+} efflux[81,82]. Further investigations are needed to elucidate these mechanisms.

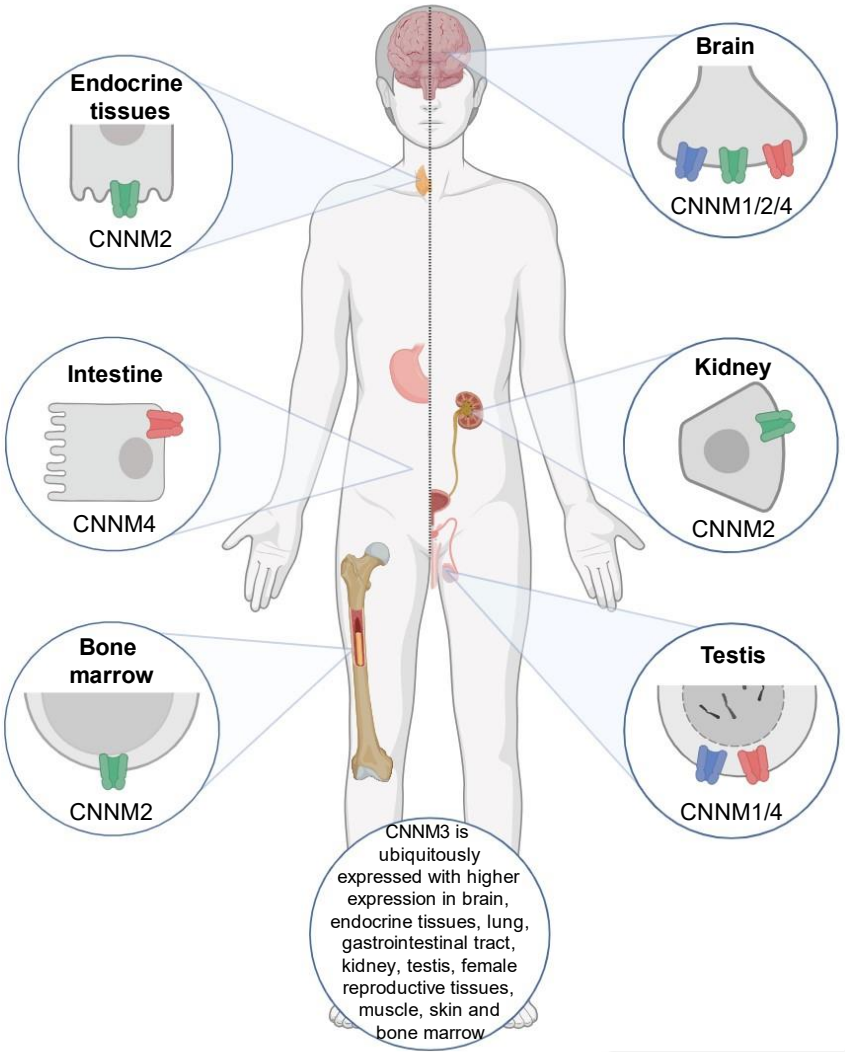

Figure I.2. CNNMs distribution pattern across the body. CNNM1 is primary expressed in the brain and testis, CNNM2 is mainly present in the brain, endocrine tissues, kidney and bone marrow, CNNM3 is ubiquitously expressed whereas CNNM4 exhibits higher expression in the bran, large intestine and testis.

CNNMs have been linked with a large number of diseases since their discovery. CNNM1, primarily expressed in the testis, is implicated in gonadogenesis defect as well as various cancers (prostate cancer, hepatocellular carcinoma, pulmonary carcinoid tumors, breast cancer, B lymphoma…)[49–54]. This fact could be explained by the association of CNNM1 in processes related to stemness, cell cycle and differentiation[55]. Point mutation in *CNNM2* are responsible for familiar hypomagnesemia, showing

symptoms of mental retardation and seizures[56,58]. Apart from that, dysregulated expression of CNNM2 is associated with multiple diseases such as psychiatric disorders (schizophrenia and epilepsy), sleep apnea and different types of cancer (non-Hodgkin B-cell lymphoma, ovarian cancer and osteosarcoma)[59–64]. CNNM3, although the least studied among the CNNM family members, has been associated with cervical cancer, lung adenocarcinoma, rosette-forming glioneuronal tumor and hepatocellular carcinoma[65–68]. Finally, Jalili syndrome is a rare multisystem autosomal recessive disorder caused by mutations in the *CNNM4* gene. This condition is characterized by early-onset visual dysfunction known as cone-rod dysfunction, as well as amelogenesis imperfecta, which manifests as small, discolored teeth prone to breakage due to enamel formation defects[70,71]. Initially identified by Jalili between 1985 and 1987, more than 24 mutations in the *CNNM4* gene have been documented so far[70,72]. Furthermore, elevated expression of CNNM4 has been observed in patients with metabolic dysfunction-associated steatohepatitis (MASH), a condition characterized by hepatic fat accumulation and inflammation. These symptoms were alleviated through liver-specific silencing of *CNNM4*, resulting in increased microsomal triglyceride transfer activity, which in turn promotes hepatic lipid clearance by enhancing the secretion of very-low-density lipoprotein[73]. Similar liver protective effects were observed in acetaminophen-induced liver injury, wherein CNNM4 overexpression modulates ATP production and reactive oxygen species generation, thereby inducing ER stress[74]. Finally, CNNM4 has been suggested to act as a tumor suppressor in colon cancer, exerting an evident impact on metastasis[75,76].

I.1.1.3.2. Mg^{2+} (re)absorption in intestine and kidney

I.1.1.3.2.1. Intestinal absorption

Mg^{2+} absorption in the intestine primarily occurs in the small intestine through a paracellular pathway, specifically in the jejunum and ileum, where it is transported via simple diffusion through small gaps between epithelial cells (**Figure I.3.A**)[2]. This process is facilitated by the relatively low expression of some 'tightening' proteins known as claudins (claudin 1, 3, 4, 5 and 8) and the absence of others (claudin 16 and 19), which regulate tight junction movement.[83–85]. Additionally, this transport mechanism is non-saturable and passive, indicating that the movement of Mg^{2+} across the cells is driven by the high luminal Mg^{2+} concentration although the transepithelial potential of the small intestine is lumen negative[86,87]. Smaller Mg^{2+} quantities are absorbed in the cecum and colon, predominantly via a transcellular pathway mediated by transmembrane TRPM6/7 channels, the expression of which is tightly regulated by intracellular Mg^{2+} levels[88,89]. At the basolateral membrane, CNNM4 facilitates Mg^{2+} extrusion from the

enterocyte. According to the hypothesis proposing CNNM4 as a Na^+/Mg^{2+} exchanger, it is believed to exert its function by secondary active transport[80].

Intestinal absorption of Mg^{2+} is believed to occur as an ion and it is influenced by various endogenous factors such as the intestinal integrity or the age of the person and exogenous factors among which there are Mg^{2+} dose, food matrix, enhancing and inhibiting factors or the type of Mg^{2+} salt[90].

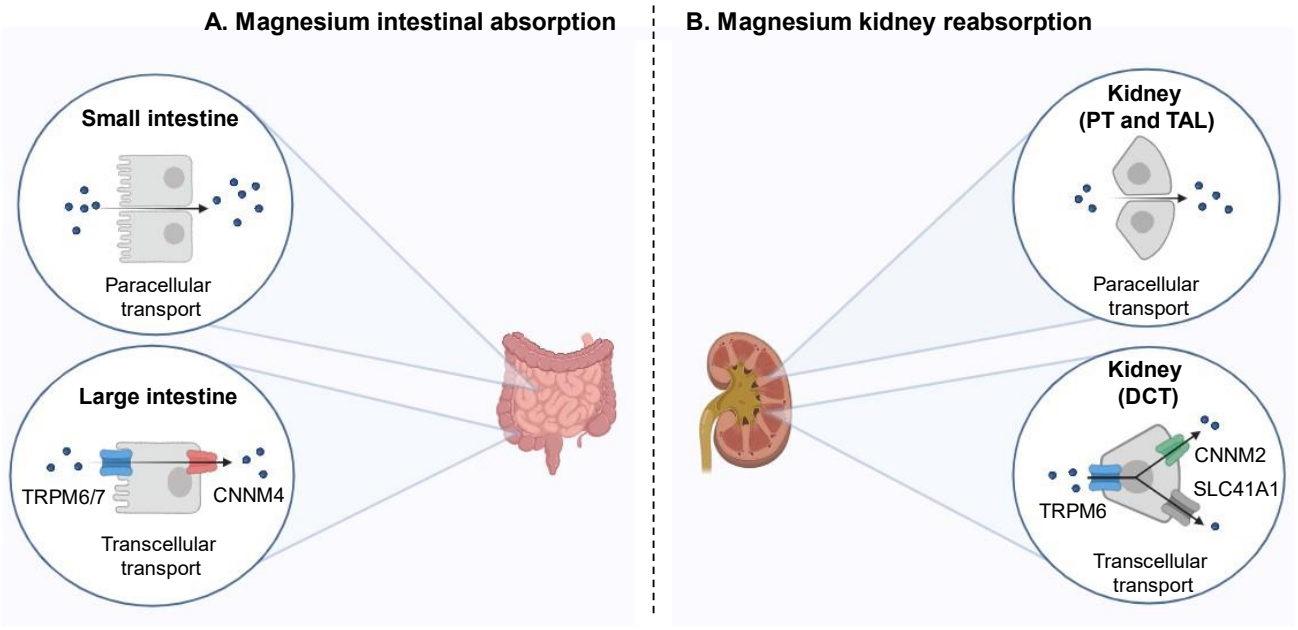

Figure I.3. Molecular mechanisms of intestinal and renal magnesium (re)absorption. (A) Magnesium is absorbed in the intestine through the action of TRPM6/7 and CNNM4 transporters. (B) SLC41A1 and CNNM2 are implicated in magnesium reabsorption in the kidney. Abbreviations: PT, proximal tube; TAL, thick ascending limb; DCT, distal convoluted tubule.

I.1.1.3.2.2. Renal reabsorption

The kidney, in collaboration with the intestine, plays a crucial role in maintaining magnesium homeostasis. Although the precise mechanisms governing magnesium absorption in the intestine remain incompletely understood, the kidney rapidly adapts to changes in serum magnesium levels within minutes (**Figure I.3.B)**[87,91].

In the proximal tubule, only 10-20% of filtered Mg^{2+} is reabsorbed, a process believed to occur through a passive paracellular mechanism. This mechanism is thought to be unregulated, as it remains linear and unsaturable across a wide range of luminal Mg^{2+} concentration[92]. Two claudins members (claudin 2 and 10a) are candidates to mediate Mg^{2+} transport due to their high expression in the proximal tubule[93,94]. However, the specific molecular pathways of Mg^{2+} reabsorption in the proximal tubule remain unknown.

In the thick ascending limb, approximately 60% of filtered magnesium is reabsorbed, being the predominant site of magnesium reabsorption in the kidney[95]. A complex system of ion transport proteins generates a lumen-positive transepithelial voltage, facilitating the passive translocation of Mg^{2+} to the basolateral side. The coordinated action of claudins 14, 16, and 19 forms a cation-selective pore responsible for paracellular Mg^{2+} reabsorption[87,91]. This process is regulated by the Ca^{2+}-sensing receptor, parathyroid hormone and mechanistic target of rapamycin (mTOR) signaling[91].

Finally, the transcellular reabsorption of Mg^{2+} occurs in the distal convoluted tubule[95]. On the luminal side, Mg^{2+} interacts to TRPM6/7, whose activity is dependent on intracellular Mg^{2+} levels, hormonal regulation, metabolic activity, and interaction with other proteins[87,91]. Basolateral Mg^{2+} extrusion is still poorly understood but it is dependent on the Na^{+} gradient though a mechanism that involves CNNM2 and SLC41A3[91].

I.1.1.4. Low Mg^{2+} in cancer

As previously mentioned, magnesium is related to various diseases, including cancer. Epidemiological data suggest that approximately 50% of cancers cases are preventable, with diet being identified as one of the contributing risk factors[96]. The habitual intake of fruits, cereals, and vegetables, which are abundant in beneficial micronutrients, vitamins, and minerals is linked to a decreased risk of cancer[97–99]. Conversely, magnesium intake, predominantly found in unprocessed grains and green leafy vegetables, exhibits an association with decreased risk of various cancer types such as breast, lung, colorectal and liver cancer, including cholangiocarcinoma[100–104].

The etiology of hypomagnesemia can be classified based on the underlying pathophysiological mechanisms: dietary deficiency, transcellular shift, gastrointestinal losses and kidney losses. Cancer and magnesium deficiency are connected in a bidirectional way. Primarily, magnesium is essential for DNA synthesis, repair and maintenance of genomic stability. Consequently, magnesium deficiency may induce DNA mutations, thereby promoting cancer initiation[105,106]. For instance, mice with tumor cell implatation fed a magnesium-deficient diet exhibited larger colon tumors compared to those fed a normal diet.[107] Similarly, mice fed a low-magnesium diet demonstrated higher metastatic potential than control mice[108]. Furthermore, magnesium deficiency has been implicated in cancer development through the induction of chronic inflammation, primarily involving the activation of nuclear factor-κB (NF-κB), Nmethyl-D-aspartate receptor and phagocytic cells along with the opening of calcium channels[109]. The elevated cancer risk observed in individuals with

hypomagnesemia may be attributed to the presence of chronic inflammation, given the established association between inflammation and cancer[110].

Conversely, cancer-specific treatments, such as platinum-based chemotherapy, monoclonal antibodies targeting the epidermal growth factor receptor (EGFR), human EGF receptor-2 (HER2) inhibitors and calcineurin inhibitors, have been demonstrated to induce hypomagnesemia[111]. Also, patients with cancer are susceptible to opportunistic infections and frequently experience cardiovascular complications. For that reason, they often receive medications that trigger or exacerbate hypomagnesemia[112].

I.1.2. Interplay between the liver and the biliary tract

I.1.2.1. Anatomy

The liver, located in the right upper quadrant of the abdomen, constitutes approximately 2% of an adult's total body weight, making it the largest solid organ in the body[113,114]. From a macroscopic perspective, the liver can be divided based on its appearance or function. According to the external one, the liver exhibits two big lobes, known as right and left lobes, and two accessory lobes called caudate and quadrate lobes. Functionally, the liver is sectioned into eight different segments[113].

Adjacent to the liver lies the biliary tract. The biliary tract compromises the gallbladder and a complex network of ducts intricately involved in regulating the production, composition, and transport of bile from the liver to the duodenum[115]. The ductules, the smaller biliary ducts with luminal diameters of less than 15µm, converge to form more external ducts characterized by progressive increases in size: interlobular ducts (15-100µm), septal ducts (100-300µm), area ducts (300-400µm), segmental ducts (400-800 µm), and the right and left hepatic ducts (>800µm), which represent the initial segment of the extrahepatic biliary tree. The extrahepatic biliary tree encompasses structures such as the common hepatic duct, cystic duct, gallbladder, and common bile duct, with its distal portion draining into the duodenum (**Figure I.4**)[116,117].

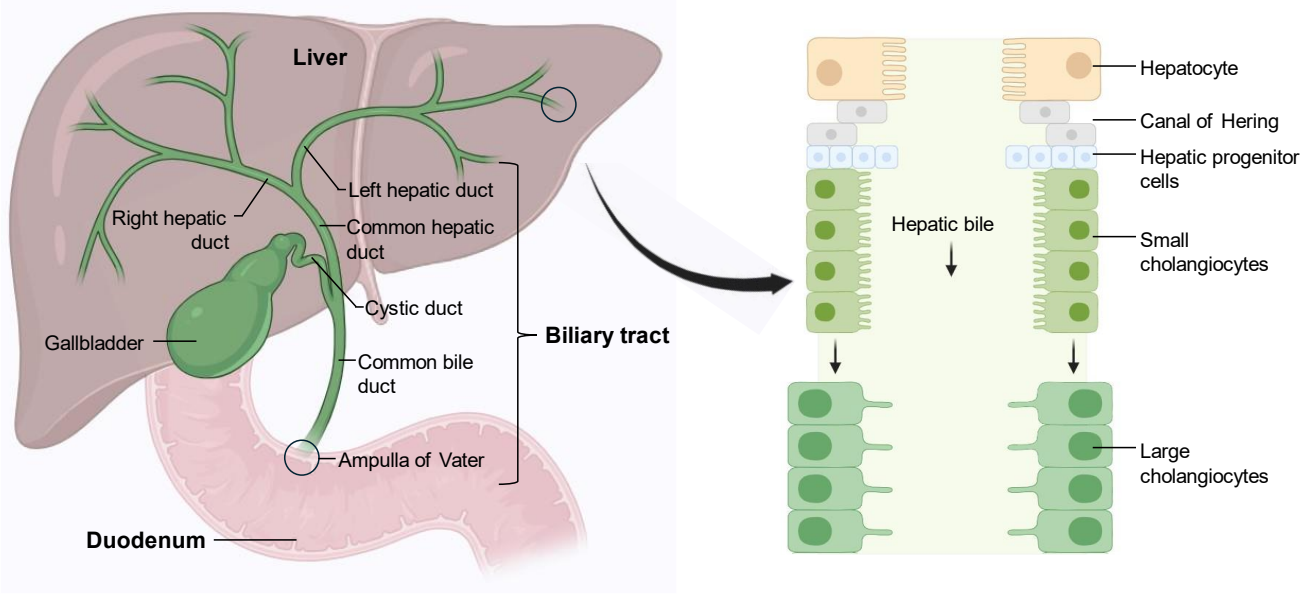

Figure I.4. Macroscopic anatomy of the biliary tree and transition of hepatic bile flow. The biliary tree encompasses a complex network of intrahepatic and extrahepatic tubular ducts responsible for modifying and transporting hepatocyte-secreted bile to the duodenum. Hepatic bile transitions from hepatocytes to cholangiocytes take place in the canal of Hering, situated adjacent to hepatic progenitor cells.

At the cellular level, the liver is composed of two primary types of cells. Parenchymal cells, consisting of hepatocytes and cholangiocytes (the epithelial cells lining the biliary tree), constitute approximately 60% of the total cell population. Non-parenchymal cells make up the remaining 40% and include resident macrophages known as Kupffer cells, sinusoidal endothelial cells, hepatic stellate cells and liver-associated lymphocytes[118]. The functional unit of the liver is the lobule, characterized by hepatocytes arranged in a hexagonal structure with a portal triad, comprising the portal vein, hepatic artery, and bile duct, located at each corner, and a central vein at its center (**Figure I.5**)[114,119]. Oxygenated and nutrient-rich blood flows from the periphery of the lobule, via the hepatic arteries and portal veins, through sinusoids where it is filtered before reaching the central vein. From there, blood is directed through progressively larger hepatic veins to the inferior vena cava. Within the lobules, hepatocytes synthesize bile, which moves in the opposite direction of blood flow, towards the biliary ducts within the portal triad[114].

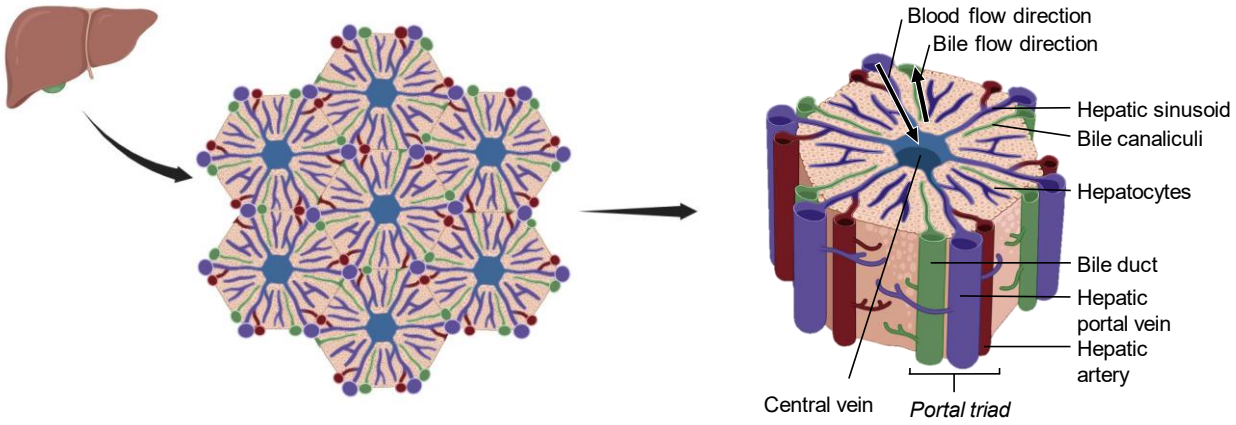

Figure I.5. Hepatic lobule architecture. The hepatic lobule, the functional unit of the liver, comprises hepatocytes arranged in a hexagonal pattern around a central vein. At each corner of the hexagon lies a portal triad consisting of branches from the bile duct, hepatic portal vein, and hepatic artery.

Hepatocytes and cholangiocytes are connected by canals of Hering, specialized channels composed of both cell types. These channels serve as the anatomical and physiological transition zones from canaliculi lined solely by hepatocytes to ductules lined solely by cholangiocytes (**Figure I.4**)[120]. Notably, hepatic stem/progenitor cells, located next to canal of Hering, possess the capability to differentiate into both hepatocytes and cholangiocytes[121]. Conversely, cholangiocytes within the intrahepatic biliary tree share a close embryological origin with hepatocytes, originating from hepatoblasts[122].

I.1.2.2. Physiology

The liver plays a pivotal role in various physiological processes such as metabolism, immune response, digestion, detoxification and storge of iron, copper and fat-soluble vitamins[123]. As a central metabolic organ, the liver possesses the capacity to store glucose in the form of glycogen and release it during fasting periods through the gluconeogenic pathway. The liver is involved in lipid oxidation, as well as packaging of excessive lipid for secretion to and storage in other tissues, such as adipose tissue. Finally, the liver is a crucial regulator of protein and amino acid metabolism, orchestrating the secretion of most of the proteins secreted into the bloodstream (including albumin, transferrin, fibrinogen and apolipoproteins), the conversion of amino acids for energy, and the elimination of nitrogenous waste resulting from protein breakdown through urea metabolism[123,124]. The liver's strategic anatomical location, receiving blood supply from both the portal vein (about 75%) and the hepatic artery (about 25%) establishes it as the primary site for initial detoxification of ingested drugs, harmful substances, and pathogens. This detoxification process is facilitated by specialized

immune cells within the liver, including Kupffer cells and pit cells, which are liver-specific macrophages and natural killer cells, respectively[123]. Moreover, the liver functions as both an endocrine and exocrine organ. The hepatic endocrine system includes several crucial hormones or hormone precursors: insulin-like growth factor (somatomedin), angiotensinogen, thrombopoietin, and hepcidin[125]. The exocrine role of the liver mainly involved the synthesis of the primary bile, which consists of bile salts, lipids, cholesterol, conjugated bilirubin, electrolytes and water[126]. Bile is secreted into the common hepatic duct of the biliary system and undergoes extensively modifications through a series of resorptive and secretory processes executed by cholangiocytes[127]. It is then stored in the gallbladder, and upon stimulation by food-induced hormones, the gallbladder contracts, leading to the release of bile acids into the duodenum, where they promote fat absorption and digestion. Bile also functions to remove waste products from the body, including hemoglobin in the form of conjugated bilirubin derived from degraded erythrocytes, as well as excess cholesterol[126,128].

I.1.2.3. Clinical significance

Liver disease contributes to approximately two million deaths annually and is responsible for 4% of all deaths. Common liver conditions include viral hepatitis infections (such as hepatitis A, B or C), fatty liver disease resulting from alcohol consumption or other factors, autoimmune disorders and potentially consequent conditions like liver cancer[129].

I.1.3. Cholangiocarcinoma

I.1.3.1. Definition and outcome

The malignancies occurring at any location of the biliary tract referred to as biliary tract cancers (BTCs) encompass gallbladder cancer and cholangiocarcinoma (CCA). CCA represents a spectrum of heterogeneous neoplasms, located along the biliary tree[130]. This disease probably originated from the malignant transformation of cholangiocytes, although it may also develop from hepatocytes through transdiferentiation or hepatic stem/progenitor cells located adjacent to the canal of Hering or within the peribiliary glands[131,132].

CCA represents the most common biliary tract malignancy and the second most prevalent primary liver tumor following HCC, comprising approximately 15% of all primary liver cancers and 3% of gastrointestinal malignancies. This cancer is very aggressive and has a high risk of recurrence, with a five-year survival rate of

only 5% among patients, representing the 2% of all cancer-related mortalities[133,134]. The elevated lethality of this disease can be attributed to its clinically asymptomatic onset, highly aggressive nature and chemotherapy resistance.

I.1.3.2. Classification

According to their primary anatomical location, these tumors are classified as intrahepatic (iCCA), which occurs above the hepatic ducts within the liver; perihilar (pCCA), also called *Klatskin tumor*, situated outside the liver at the level of large bile ducts located posterior to the hepatic duct and above the insertion of the cystic duct; and distal (dCCA) originating outside the liver below the insertion of the cystic duct (**Figure I.6**). Both pCCA and dCCA are encompassed under the term of extrahepatic CCA (eCCA). Each of the anatomic subtypes is characterized by unique genetic aberrations, clinical presentations and management options[130,133]. pCCA represents approximately 50 - 60% of all CCA, while dCCA accounts for 20 - 30% and iCCA approximately 10 - 20%[135]. However, some misclassifications of pCCA as iCCA may have occurred[136]. iCCAs present three different growth patterns: mass-forming (MF-iCCA), periductal-infiltrating (PI-iCCA), intraductal-growing (IG-iCCA), and MF+PI[137,138]. iCCA also encompasses two different subtypes: the large duct type and the small duct type, each characterized by distinct clinicopathological features and mutation profiles[139]. pCCA and dCCA, typically grouped as extrahepatic CCA (eCCA) exhibit a different growth pattern, usually as poorly defined nodular sclerosing tumors and less frequently as intraductal papillary tumors, sharing comparable growth patterns to PI- and IG-type of iCCAs[130]. Although the anatomical classification is the most widely used, alternative parameters such as tumor growth pattern or the cell of origin may be better predictors of CCA behavior[140].

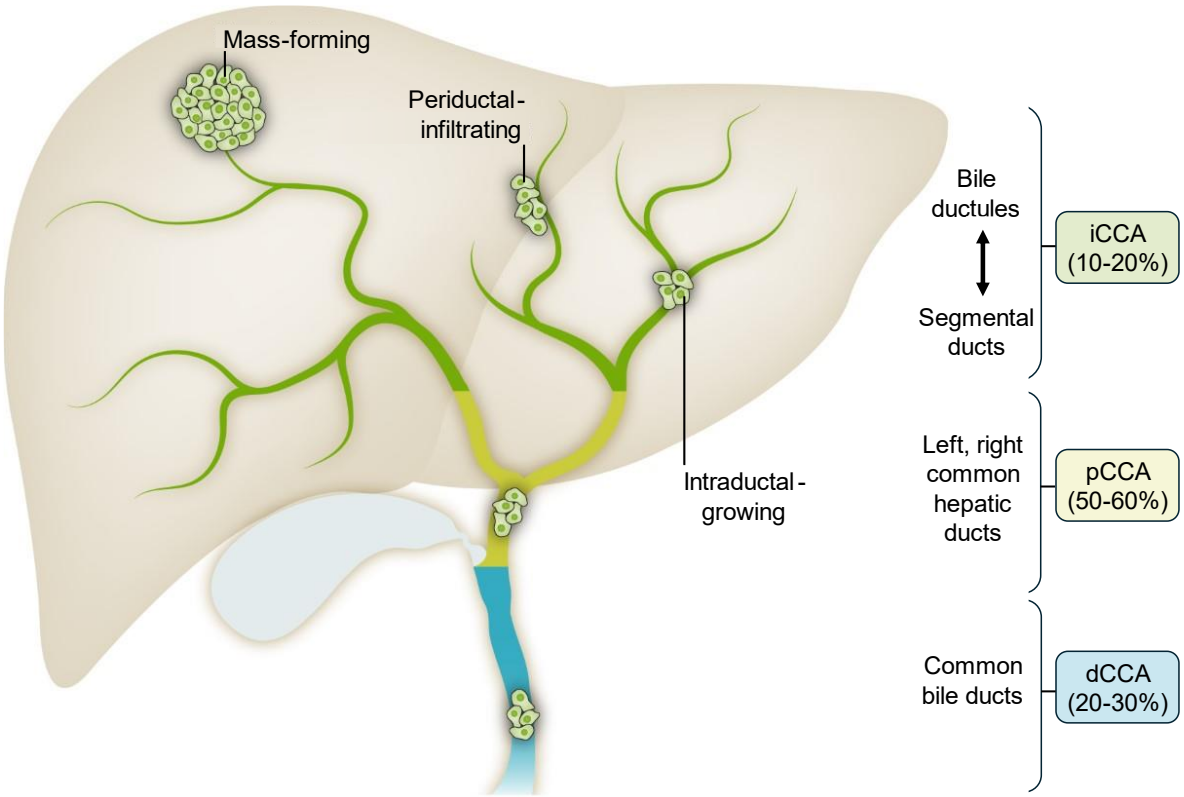

Figure I.6. Anatomical classification of cholangiocarcinoma. Cholangiocarcinoma (CCA) is categorized into as intrahepatic (iCCA), perihilar (pCCA), or distal (dCCA), according to its anatomical location. iCCAs are further subdivided based on their growth pattern into mass-forming, periductal infiltrating or intraductal growing[133].

I.1.3.3. Epidemiology

Globally, CCA exhibits an incidence rate of 0.3-6/100,000 inhabitants per year, with a mortality rate of 1-6/100,000 inhabitants per year. Specific geographical areas within Southeast Asia, including South Korea, China, Thailand and Japan show a particularly high incidence rate, with more than 6 cases/100,000 habitants per year[141]. The observed differences are probably attributed to exposure to specific risk factors, such as endemic liver fluke parasites, and because of potential genetic predispositions as exposed in section 'I.3.4.1. Risk factors'[133]. The three subtypes of CCA can have different epidemiological trends. For instance, the incidence and the mortality of iCCA has risen, while those of eCCA remained stable or increased more slowly in Western regions[142]. The incidence is heterogeneous within populations, showing variations based on age, gender, and race. In the United States, individuals aged 45 years or older exhibit a higher incidence rate of iCCA compared to those under 45, with a slight predominance among males and a higher incidence observed

among Hispanic individuals compared to non-Hispanic counterparts. Moreover, mortality rates are notably higher among Black and American Indian/Alaska Natives groups in the United States[143].

I.1.3.4. Etiology

I.1.3.4.1. Risk factors

The high degree of heterogeneity observed in CCA, varying in incidence across different regions worldwide, suggests unique risk factors in various geographical areas, probably due to differences in the environment and the genetic load. Consequently, researchers have suggested distinct risk factors specific to different regions[144]. Nonetheless, conventional risk factors common to all subtypes of CCA converge on chronic biliary inflammation and bile stasis as the underlying pathobiological mechanisms[134].

In East Asian countries, where CCA exhibits higher prevalence rates compared to other regions, infection with endemic parasitic liver fluke *Opisthorchis viverrini* and *Clonorchis sinensis,* represents the primary risk factor for CCA development[145,146]. It is believed that these parasites induce cholangiocarcinoma by infecting humans through the consumption of raw or undercooked fish, residing in the bile ducts for extended periods, often exceeding 10 years[147,148]. These parasites may induce CCA by causing physical damage to biliary epithelia, triggering an immune and oxidative response and releasing mitogenic and anti-apoptotic molecules[148,149]. Ultimately, this results in chronic infection and inflammation, concomitant with DNA damage, contributing to the development of an extremely invasive and highly metastatic form of CCA [148].

In Western countries, a minority of CCA cases are associated with the limited accepted risk factors and in most cases, the disease is sporadic, occurring without any accepted or known risk factors. CCA is linked to certain biliary diseases such as sclerosing cholangitis, cholelithiasis, choledocholithiasis, Caroli Disease and importantly choledochal cysts, the most associated with CCA[134]. Chronic viral infections with hepatitis B virus and hepatitis C virus together with cirrhosis may also represent a risk factor for CCA development, with a stronger predilection for iCCA[150,151]. Other risk factors include metabolic dysfunction-associated steatotic liver disease (MASLD), type 2 diabetes mellitus (T2DM), inflammatory bowel disease, alcohol consumption, and tobacco smoking, while the roles of obesity and hypertension remain controversial[144,152].

Several environmental toxins potentially induce CCA, including thorium dioxide, a radiographic contrast agent now prohibited in clinical use; asbestos specifically linked to iCCA; aristolochic acid, a toxic compound commonly used in alternative medicines; and 1,2-dichloropropane and dichloromethane, utilized in painting manufacturing processes[140,150].

I.1.3.4.2. Genetic and epigenetic mutations

Changes in cholangiocarcinogenesis include those caused by gene mutation resulting in loss or gain of function, which regulate apoptosis and cell cycle, as well as histone modifications, dysregulation of methylation and aberrant expression of non-coding RNA.

I.1.3.4.2.1. Genetic alterations

Several mutations across different genes can contribute to cholangiocarcinogenesis, which can be categorized based on its biological function: glucose metabolism, kinase signaling, cell cycle regulation, DNA damage and genomic stability, immune dysregulation, and chromatin remodeling[133]. Below are some examples of genes altered in CCA.

Isocitrate dehydrogenase 1 and 2 (*IHD1* and *IDH2*) are crucial enzymes for glucose metabolism, converting isocitrate to alpha-ketoglutarate. However, mutations in these IDH genes, present in 9-13% of iCCA patients, result in the production of 2-hydroxyglutarate, an oncometabolite associated with increased levels of DNA methylation, cellular growth and angiogenesis[153]. Genetic alterations affecting the fibroblast growth factor receptor (*FGFR*) genes are prevalent in a significant proportion of CCAs, being more frequently in iCCA than eCCA. Among these alterations, fusion events are more prevalent than mutations[154]. Another set of genes that significantly contribute to CCA development and associated with worse overall survival are phosphorylation-activated PAS proteins[155,156]. Particularly, *NRAS* and more predominantly *KRAS* activate the RAF/MEK/ERK signaling pathway, which subsequently triggers cancer cell proliferation, differentiation, and metastasis. The *KRAS* and *NRAS* genes, along with the *BRAF* gene, are implicated in various cancer types, with mutations in the BRAF gene being predominantly observed in iCCA. The ErbB tyrosine kinase also plays a role in CCA pathogenesis, through heterodimerization of its members, such as *HER2*, following stimulation by epidermal growth factor (EGF) or transforming growth factor (TGF). This process triggers the activation of various signal transduction pathways involved in cell proliferation, differentiation, and adhesion. Mutations in *HER2* have been identified in 5% of iCCA and 20% of eCCA[157]. Phosphoinositide 3-kinase (PI3K)/protein kinase B (AKT)/mTOR signaling pathway plays a critical role in cell cycle regulation as well as CCA pathogenesis. Mutations in *PI3K*, and to a lesser extent, its inhibitor, the tumor suppressor phosphatase and tensing homolog (*PTEN*), are frequently observed in CCA, resulting in mTOR pathway activation and increased cancer cells proliferation[158]. Another tumor suppressor implicated in CCA is *TP53*, with loss of function mutations associated with poorer prognosis[159].

Finally, ARID1, PBRM1 and BAP are genes related to histone modifying and chromatin remodeling that have been detected to be mutated in iCCA and eCCA[160].

I.1.3.4.2.2. Epigenetic alterations

In addition to being useful biomarkers for CCA, microRNAs (miRNAs) can act as oncogenes or tumor suppressors, depending on their target genes. Examples of oncogenic miRNAs encompass miR-221 and miR-21, whereas examples of tumor suppressors comprise miR-34a and miR-200b[161,162]. For instance, increased miR-21 expression in CCA induce proliferation, migration and tumor metastasis by modulating the expression of *PTEN* gene[163].

Methylation patterns are also dysregulated in CCA compared to those in healthy individuals, often characterized by hypermethylation of multiple CpG sites[164]. This hypermethylation impact cell cycle inhibitors by inactivating them, as demonstrated in the case of SOX17 or P16INK4a[164–166]. Furthermore, some miRNAs have been observed to be modulated by methylation, such as miR-370, influenced by interleukin-6 (IL-6) overexpression[167]. IL-6, in turn, is upregulated due to epigenetic suppression of cytokine 3 (SOCS-3), significantly contributing to cholangiocarcinogenesis[168]. Additionally, comprehensive that involving 489 CCA cases from 10 countries presents a novel etiological classification based on integrative genetic and DNA methylation analyses[169].

Histone acetylation or deacetylation plays an important role in regulating the proliferation, metastasis and migration of cancerous cells, including CCA, as they can induce the relaxation or compression of histone tails, respectively, influencing the loading of transcription factors onto DNA. In contrast, the effects of histone methylation/demethylation are opposed to those of histone acetylation/deacetylation [170]. Regarding CCA, a typical example is the methylation of histone 3 at lysine 27 by the enhancer of zeste homolog 2, a methylation associated with gene repression. Overexpression of zeste homolog 2 in CCA patients is associated with a poor prognosis[171].

I.1.3.5. Molecular pathogenesis

Cholangiocarcinogenesis occurs in the context of cholestasis, characterized by a reduction or interruption of bile flow, and chronic inflammation. This condition is marked by overproduction of pro-inflammatory cytokines, growth factors and toxic bile acids, which are believed to initiate and sustain the multistep process of malignacy[172]. The subsequent progressive epithelial damage and accumulation of chromosomal, genetic

and epigenetic alterations result in significant changes in cell physiology. These changes include dysregulated growth, increased invasiveness, enhanced metastatic potential, and epithelial-to-mesenchymal transition (EMT)[173]. A summary of the main signaling pathways is depicted in **Figure I.7**.

In the inflammatory environment that contributes to CCA, the IL-6/IL6R signal transducers and activators of transcription 3 (STAT3) pathway is critical. IL-6 drives a cycle of cellular stress, damage, inflammation, and compensatory proliferation, significantly impacting CCA progression. It activates several molecular cascades, including Janus kinases (JAK) activation, PI3K/AKT, mitogen-activated protein kinases (MAPK) and signal transducers and activators of transcription (STAT), which expression is upregulated in iCCA and is associated with a worse prognosis[173–175]. Additionally, TGF-β is another cytokine implicated in CCA, promoting tumor activity by enhancing cell proliferation and EMT[176,177].

Five key regulators influence cell survival pathways in the development of CCA: the ERGF pathway, FGF2 fusions, BRAF/KRAS/TP53 mutations, secretin and histamine pathways and cell death pathways[173]. The EGFR pathway, comprising HER1-4 proteins, is induced in both iCCA and eCCA and is associated with poor prognosis. Specifically, HER1 and HER2 promote proliferation, migration and invasion through the JAK/STAT, RAS/MEK/ERK and PI3K/AKT cascades[178]. Mutations in BRAF, KRAS, and TP53 also contribute to CCA via the MEK/ERK and PI3K/AKT pathways[173]. FGF2 fusions exert oncogenic effects through the RAS pathway[179]. Furthermore, the secretin is downregulated, and the histamine pathways is upregulated in CCA, affecting cancer hallmarks such as cell proliferation, inflammation and cell death[180,181]. The final altered survival-related pathway is cell death, which impacts various signaling pathways depending on the type of cell death[182].

Considering the developmental pathways, the Notch pathway, consisting of four isoforms (NOTCH1-4), plays a significant role in CCA development. ɣ-secretase cleaves Notch, releasing the Notch intracellular domain (NICD), which then translocates to the nucleus to activate target genes[183]. In CCA, elevated expression of these isoforms correlates with various aspects of tumor progression: NOTCH1 with increased proliferation and invasiveness; NOTCH2 hepatocyte-derived CCA formation in murine models; NOTCH3 with CCA onset and advancement via the PI3K/AKT pathway; and NOTCH4 with poor prognosis in iCCA[173]. The Hedgehog (HH) signaling pathway is also crucial in CCA. Ligand binding (SHH, IDD, or DHH) to the Patched receptor relieves inhibition of the SMO transmembrane protein, promoting nuclear localization of GLI proteins. Aberrant HH signaling in CCA is driven by genetic alterations, particularly in GLI and DHH proteins, and overexpression of proteins such as GLI, Patched, and SHH. Activation of the HH pathway has been significantly correlated with

tumor progression and prognosis in CCA[184]. Moreover, the Wnt/β-catenin pathway is involved in cell proliferation, differentiation, migration and apoptosis in CCA through nuclear translocation of β-catenin, typically bound to E-cadherin[173]. Overexpression of SOX17 in CCA cells reduces tumorigenic capacity by increasing oxidative stress and apoptosis, and inhibiting cell migration and Wnt/β-catenin-dependent proliferation[165].

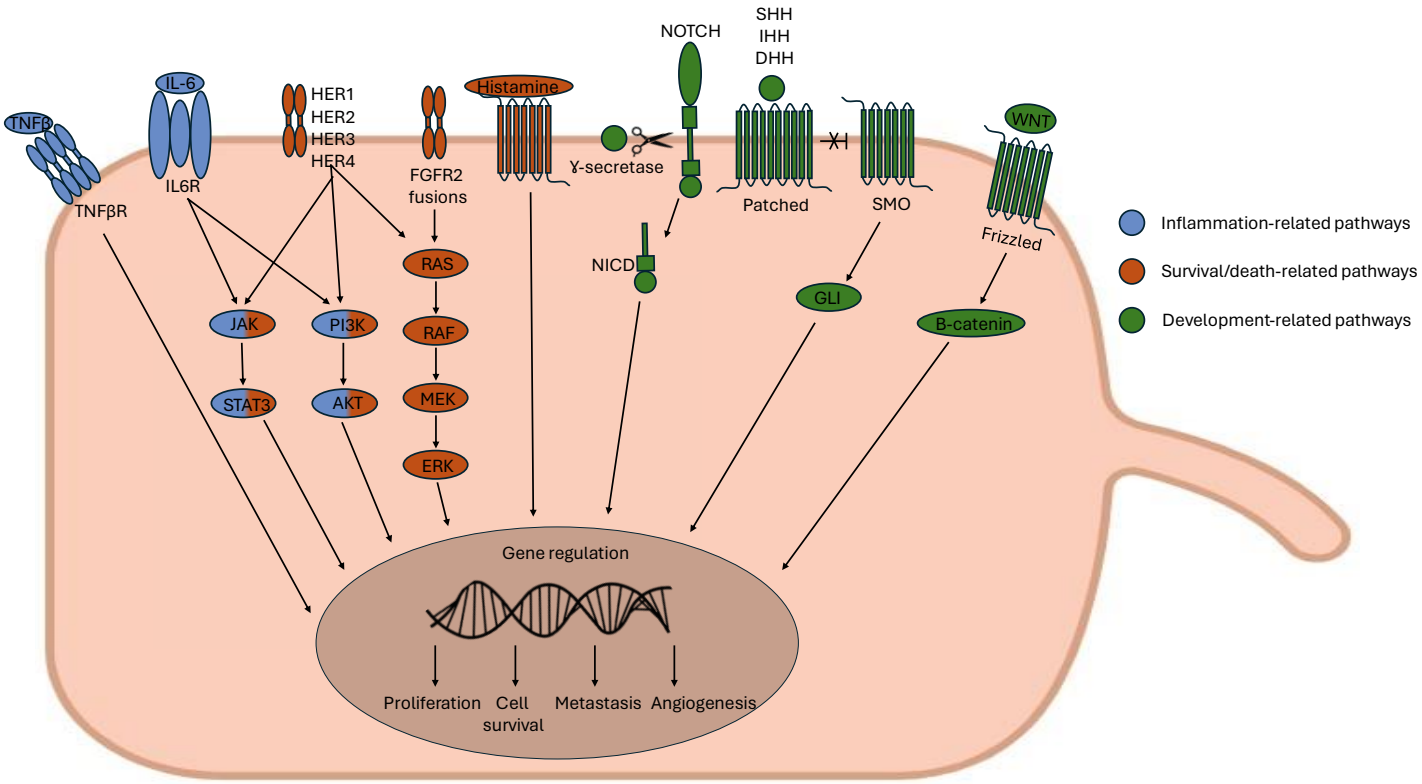

Figure I.7. Main signaling pathways involved in CCA progression. The signaling pathways can be classified into three main types: (i) inflammation-related pathways, including IL-6 and TGFβ pathways; (II) survival-related pathways including HER receptors, FGFR2 fusions or histamine and secretin pathways; and (iii) development-related pathways, including Notch, Hedgehog and WNT/β-catenin. Abbreviations: CCA, cholangiocarcinoma; FGFR2, fibroblast growth factor receptor 2; GLI, glioma-associated oncogene; HER, human epidermal growth factor receptor; IL-6 interleukin 6; IL6R IL-6 receptor; JAK, janus kinase; NICD, NOTCH intracellular domain; PI3K, phosphatidylinositol 3-kinase; SMO, smoothened; STAT3, signal transducer and activator of transcription 3; TGF-β, transforming growth factor-β; TGF-βR, TGF-β receptor. Adapted from Fouassier *et al*[173].

I.1.3.6. Diagnosis

In the early stages of the disease, CCA typically presents asymptomatic, often going unnoticed until symptoms associated with metastasis emerge or jaundice develops in pCCA and dCCA cases. Additionally, around 20-25% of iCCA cases are incidentally identified during cross-sectional imaging procedures conducted for other

clinical purposes[185]. Furthermore, diagnosing CCA can be challenging due to its location, which is often inaccessible, missing accurate diagnostic imaging criteria and imprecise non-invasive biomarkers[186]. This results in approximately 70% of CCA cases being diagnosed in advanced stages[133]. While there are no specific symptoms indicative of CCA, manifestations such as nausea, bloating, abdominal pain, night sweats, asthenia or unexplained weight loss may appear as the tumor progresses[185,187].

Initial approaches to diagnose CCA involve the use of multiple laboratory tests. In eCCA, tumor-induced biliary obstruction results in elevated total and direct bilirubin and alkaline phosphatase (ALP), while transaminases levels remain unaltered. Patients with iCCA present normal bilirubin levels but abnormal ALP levels, a finding commonly corroborated by gamma-glutamyltransferase (GGT) levels[185]. Carcinoembryonic antigen (CEA) and carbohydrate antigen 19-9 (CA19-9) are frequently employed biomarkers in CCA, although their diagnostic effectiveness is limited due to significant overlap with benign conditions and other cancers, and limited sensitivity in detecting early-stage CCA. Moreover, alpha-fetoprotein (AFP) allows to differentiate iCCA from HCC. To improve current challenges in diagnosing CCA, artificial intelligence is under development through integration with medical data[188].

Confirmation of CCA diagnosis involves the utilization of imaging techniques. For jaundiced patients, transabdominal ultrasonography is typically the initial imaging modality employed. In cases where ultrasonography fails to provide confirmation of a benign etiology, further imaging with computed tomography or magnetic resonance imaging is recommended[130]. Since imaging may not reveal findings in up to one third of patients, biopsy becomes essential for confirming the presence of tumor. Upon biopsy confirmation, clinicians should conduct an esophagogastroduodenoscopy and colonoscopy to exclude the possibility of a metastatic liver lesion[189]. Common sites of metastasis include lymph nodes, peritoneum, and liver, with occasional occurrences in the lungs and bones[190]. Moreover, patients with unresectable or metastatic disease who are candidates for systemic therapy should undergo comprehensive molecular profiling[191].

I.1.3.7. Therapeutic options

I.1.3.7.1. Resectable cases

Surgical resection stands as the primary curative approach in CCA. However, successful resection is possible for less than 30% of patients, due to metastatic or locally aggressive disease, extensive tumor growth or compromised clinical status. Besides, the overall survival following surgical resection for CCA presents

suboptimal outcomes, with high risk of disease recurrence (around 60–70% of patients) and short survival (5-year survival of 23% for iCCA, 32.5% for pCCA and 20-40% for dCCA)[192–195]. This has promoted interest in conducting prospective trials to assess adjuvant therapies. For instance, capecitabine has shown promise in enhancing both overall survival (OS) and disease-free survival (DFS) and should therefore be regarded as standard of care for patients with resected CCA[196,197]. An ongoing phase III trial is currently investigating the efficacy of combination chemotherapy with cisplatin and gemcitabine (CisGem) compared to capecitabine monotherapy[198]. In addition, adjuvant chemoradiotherapy is being proposed to improve OS and DFS in patients with resected BTC, while adjuvant radiotherapy alone has been shown to only improve OS, although further validation is needed[199].

I.1.3.7.2. Unresectable cases

Unfortunately, the silent clinical progression of most cases of CCA until advanced stages, together with the lack of effective screening methods, results in many CCAs being diagnosed as unresectable tumors. Those cases are managed with palliative chemotherapy, primarily based on first-line CisGem[200]. Chemoimmunotherapy, involving durvalumab as a first agent followed by pembrolizumab, is recommended for all unresectable cases receiving CisGem treatment due its efficacy in improving OS without exacerbating toxicity[201,202]. Additional alternative options for initial therapy in advanced CCA include gemcitabine plus oxaliplatin (GEMOX), gemcitabine plus capecitabine, gemcitabine plus nanoparticle albumin-bound paclitaxel, gemcitabine plus S-1, among others[203–206].

For patients exhibiting resistance to first-line therapy, secondary treatment options may include regimens such as folinic acid, 5-fluorouracil and oxaliplatin (FOLFOX), gemcitabine plus capecitabine, etc[206,207]. However, there is currently no consensus regarding the optimal regimen for each candidate[208]. Consequently, targeted testing of advanced CCAs for specific molecular alterations, for which a specific inhibitor might be available, is recommended. Some of the most responsive alterations are *IDH1/2*, *BRAF* and *KRAS* mutations; *FGFR*, *NTRK*, *RET* fusions; and *HER2* overexpression or amplification[209]. Tumors from patients presenting mismatch repair deficiency exhibit more mutations and higher immunogenicity compared to tumors lacking such mismatch repair defects. In these instances, inhibition of the immune checkpoint programmed cell death 1 (PD-1) has demonstrated therapeutic benefit. Immunotherapeutic approaches targeting PD-1 are also employed in patients with PD-1 ligand overexpression or with elevated tumor mutational burden[210].

I.1.3.7.3. Cell death in cancer treatment

Cell death is a physiological mechanism regulating cell proliferation, exerting crucial roles in growth and development throughout life. Dysregulation of cell death and division is a hallmark of cancer, leading to uncontrolled tumor growth and replicative immortality. Consequently, many current treatment approaches focus on selectively inducing cell death in cancer cells without harming non-malignant cells[211,212]. For instance, certain chemotherapeutic agents employed in CCA treatment, such as cisplatin and gemcitabine, induce apoptotic cell death in cancer cells. Additionally, ferroptosis has been shown to contribute to the tumor suppressive effects of several chemotherapies, targeted therapies and immunotherapies[213–216]. Cancer cells may also acquire mutations that disrupt the cell death pathways, making them resistant to conventional anticancer therapies[217]. Introducing novel forms of cell death could potentially reverse these effects. Some cell deaths are implicated in cancer progression. For instance, metastasis-prone or metastatic cancer cells show higher susceptibility to ferroptosis[218]. Hence, the growing emergence of novel forms of cell death could represent promising new opportunities for tumor therapeutics.

I.1.2.7.3.1. Definition and classification of cell death

Cell death refers to the irreversible demise of vital cellular functions through a group of biochemical events and meets at least one of the following molecular and morphological criteria: (1) loss of plasma membrane integrity; (2) fragmentation of cell and its components, including the nucleus; and/or (3) engulfment of these fragments by adjacent cells *in vivo*[219,220].

Accidental cell death (ACD) occurs instantaneously and uncontrolled in cells exposed to severe physical (such as high pressures, temperatures, osmotic forces), chemical (such as extreme pH variation) or mechanical (like shear forces) stressors. In contrast, regulated cell death (RCD) depends on a sophisticated molecular machinery, indicating that it can be modulated (either delayed or accelerated) by pharmacological or genetic interventions[221]. In turn, RCD can manifest independently of external triggers, originating from physiological processes that regulate development or tissue maintenance, also known as programmed cell death (PCD)[222]. On the contrary, RCD can arise in response to intense or prolonged intracellular or extracellular perturbations that exceed the capacity of adaptive cellular responses to restore homeostasis. This phenomenon confers an evolutionary advantage to the organism by enabling the elimination of useless or hazardous cells[220].

Historically, three main types of cell death have been proposed: type I or apoptosis, characterized by cell shrinkage, caspases activation and apoptotic bodies formation; type II or autophagy exhibiting autophagosomes formation and ATG proteins participation; and type III or necrosis, displaying dilatation and cellular swelling, However, research has unveiled numerous additional forms of cell death, including anoikis, pyroptosis, neutrophil extracellular trap-associated cell death (NETosis), ferroptosis, entosis, methuosis, paraptosis, mitoptosis, parthanatos and necroptosis (**Figure I.8**)[223].

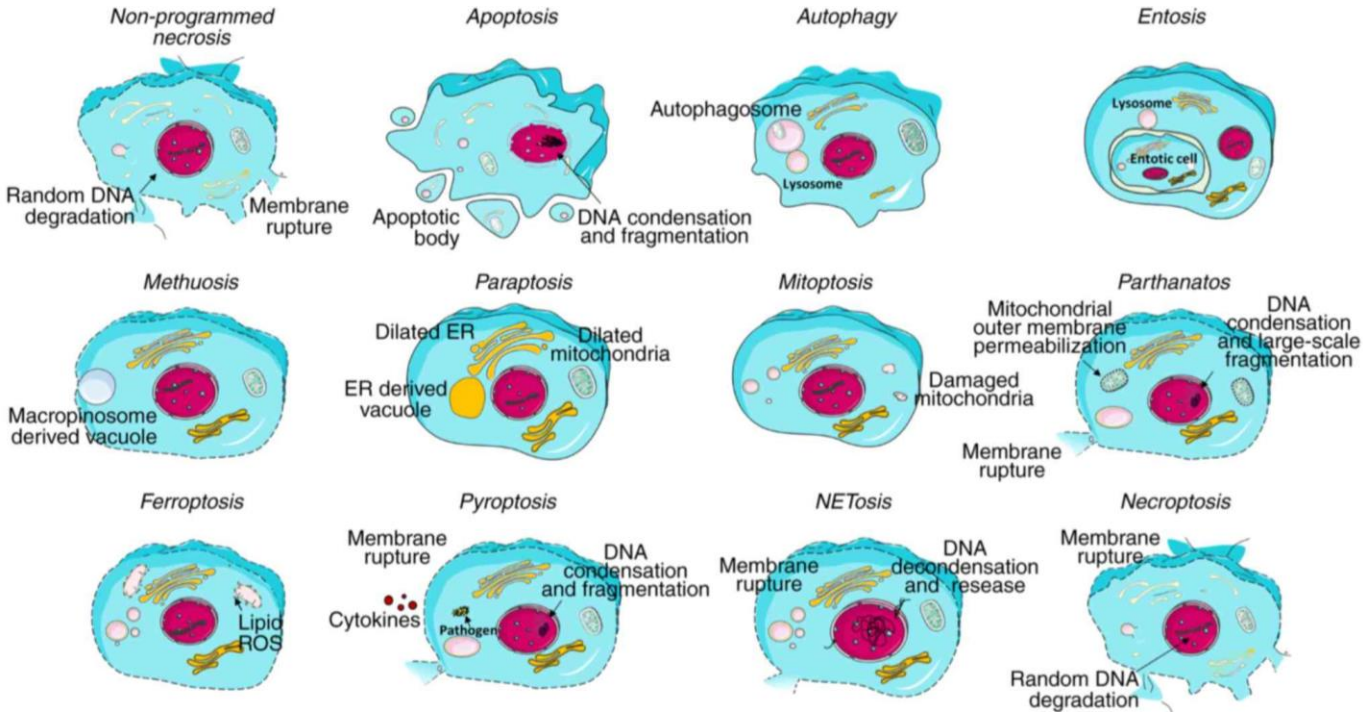

Figure I.8. Typical morphology associated with different types of cell death. The morphological alteration in cell size, membrane integrity, chromatin density, organelle arrangement and the presence of vacuoles. Extracted from Yan *et al.*[224].

I.1.2.7.3.2. Ferroptosis

Ferroptosis, introduced twelve years ago, is a programmed cell death characterized by oxidative stress and iron dependency, ultimately resulting in lipid peroxidation[225]. Ferroptosis distinguishes form other modes of cell death at morphological, biochemical and genetic levels. Morphologically, ferroptosis is represented by a peculiar rounded shape and marked mitochondria shrinkage with increased membrane density and diminished or absent of mitochondrial cristae[226,227]. Biochemically, ferroptosis involves three main metabolisms: thiol, iron and lipid. The selenoprotein glutathione peroxidase 4 (GPX4) acts as a central repressor of ferroptosis, although other inhibitory pathways are FSP1-CoQ10,

GCH1-BH4, DHODH-CoQH2 and sex hormones[218]. GPX4 gathers its reducing power from reduced glutathione (GSH) coming from the system x_c^- antiporter (SLC7A11) and utilizes it to transform reactive polyunsaturated fatty acids (PUFA) phospholipid hydroperoxides (PUFA-PL-OOH) into non-reactive and non-lethal PUFA phospholipid alcohols (PUFA-PL-OH). PUFA-PLs are oxidized by labile Fe^{2+} and Fe^{2+}-dependent enzymes, such as arachidonate lipoxygenases (ALOX), nicotinamide adenine dinucleotide phosphate (NADPH) oxidases (NOX), and cytochrome P450 oxidoreductase (POR). This, together with increased reactive oxygen species (ROS) levels, leads to compromised plasma membrane integrity while lipid hydroperoxides degrade into several toxic aldehydes like 4-hydroxynonenal (4-HNE) and malondialdehyde (MDA)[227,228]. Importantly, the regulation of ferroptosis is significantly influenced by the various processes of iron metabolism, including its absorption, storage, export, and utilization.[229]. Ultimately, biochemical traits of ferroptosis include greater lipid peroxidation, iron accumulation and decreased endogenous antioxidant activity of molecules. Finally, ferroptosis is controlled by multiple genes, including several tumor suppressors and oncogenes[230].

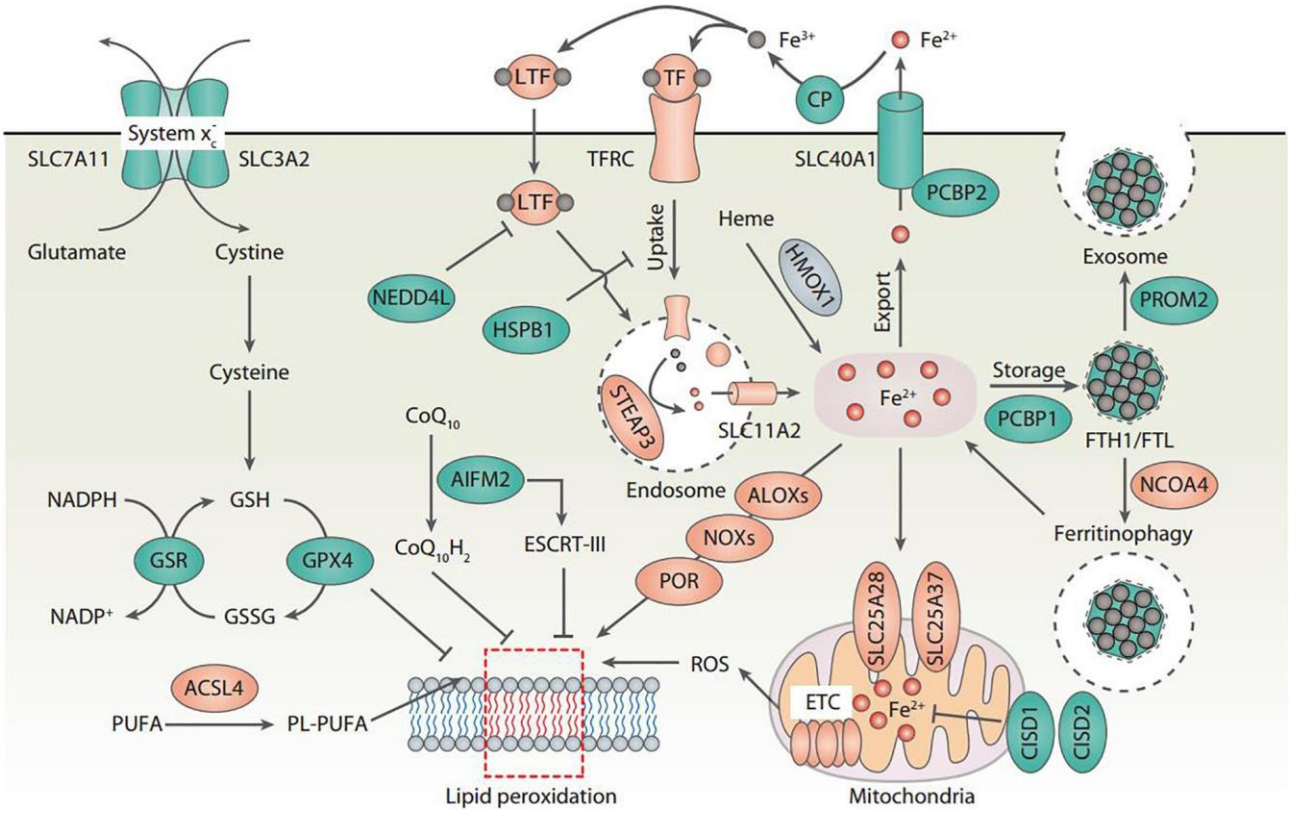

Figure I.9. Main molecular mechanisms driving ferroptosis. Ferroptosis is a form of regulated cell death characterized by decreased endogenous antioxidant activity and iron accumulation, culminating in lipid peroxidation and membrane damage. In particular, the uptake of cystine via x_c^- system and subsequent cysteine production are required for glutathione (GSH)

biosynthesis, which further enhances the anti-lipid peroxidation activity of glutathione peroxidase 4 (GPX4). Inhibition of solute carrier family 7 member 11 (SLC7A11) and GPX4 results in increased iron-dependent lipid peroxidation, thereby triggering ferroptotic cell death. Activation of ALOX, NOX, or POR promotes lipid peroxidation. Importantly, iron metabolism intermediates systems, including absorption, storage, export, and utilization, have an important regulatory effect on ferroptosis. Extracted from Chen *et al.*[229].

I.1.2.7.3.3. Nuclear protein 1 (NUPR-1)

Recently, nuclear protein 1 (NUPR-1) has emerged as a crucial inhibitor of ferroptosis[231]. Inactivation of NUPR-1 modulates mitochondrial function and energy metabolism in cancer cells and triggers ferroptosis via iron metabolism, ROS homeostasis and the GSH/GPX4 pathway[232]. In the context of iron metabolism, the inhibition of NUPR-1 results in elevated levels of heme oxygenase 1 (HO-1), a critical enzyme involved in heme degradation, producing carbon monoxide, ferrous iron and biliverdin. HO-1 exerts a cytoprotective effect by scavenging ROS during moderate activation. However, upon pronounced activation of HO-1, a substantial release of iron occurs, resulting in increased ROS levels and ultimately, a promotion of ferroptosis (**Figure I.10**)[233]. Considering the implication of ferroptosis in pathology, preliminary studies indicate that genetic and pharmacological inactivation of NUPR1 suppresses different types of tumor growth, including HCC and CCA[234–236].

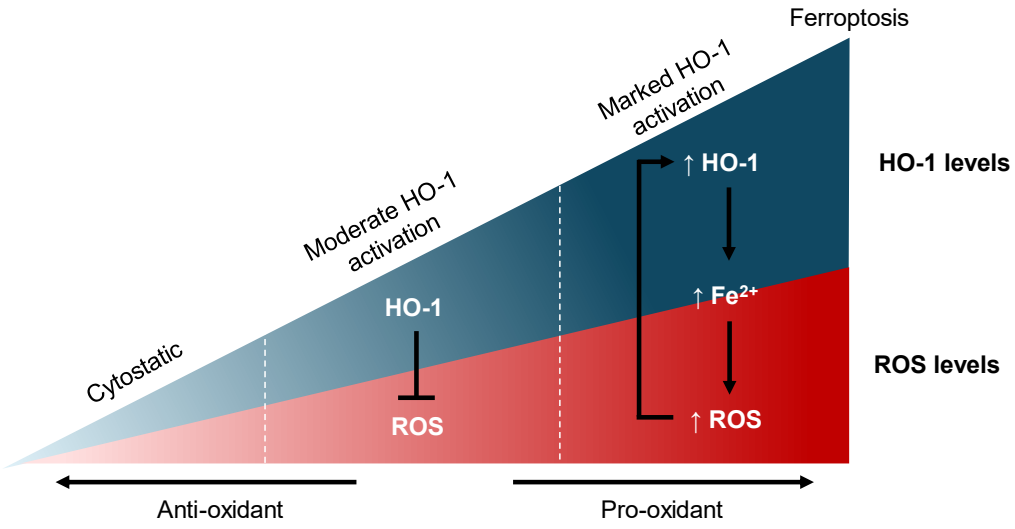

Figure I.10. Role of heme oxygenase (HO-1) in the promotion of ferroptosis. HO-1 exerts a cytoprotective function by scavenging ROS during moderate activation. Conversely, pronounced activation of HO-1 leads to an increase in labile Fe^{2+}, resulting in ROS overload and subsequent cancer cell death. Adapted from Chiang et al.[233]

I.1.3.7.4. Liver targeted siRNA delivery as promising therapy in CCA

Liver diseases resulting from critical gene-product overexpression can be effectively targeted using liver-targeted small interfering RNA (siRNA), a promising therapeutic strategy. Liver-targeted siRNA is typically administered systemically, allowing it to enter the bloodstream, undergo organ distribution, and avoid degradation by nucleases and elimination through the kidneys. This method offers several advantages over non-targeted systems, including improved pharmaceutical activity, reduced side effects, lower required doses and preservation of siRNA integrity without modifications[237,238].

Currently, lipid nanoparticle (LNP) and *N*-acetylgalactosamine (GalNAc) conjugation represent the only clinically validated methodologies for delivering siRNA to the liver[237]. In 2018, LNP became the first approach approved for liver delivery, which relies on the interaction between apolipoprotein E and the low-density lipoprotein receptor. However, GalNAc technology has now replaced LNP delivery for targeting liver disease[239].

I.1.3.7.4.1. N-acetylgalactosamine drug delivery system

The asialoglycoprotein receptor (ASGPR) is membrane protein mainly expressed on the surface of mammalian hepatocytes and hepatic cancer cells[238]. In physiological conditions, ASGPR functions to eliminate desialylated glycoproteins from the serum that present terminal galactose or GalNAc residues. In a therapeutic context, GalNAc-siRNA selectively targets and binds to ASGPR on the sinusoidal surface of hepatocytes. Upon binding, ASGPR internalizes these complexes into endosomes, where the GalNAc-siRNA conjugate is released from the receptor due to a decrease in pH. Subsequently, the GalNAc molecule is rapidly cleaved from the oligonucleotide before the siRNA slowly translocates to the cytoplasm over an extended period, and the GalNAc molecule undergoes degradation. ASGPR is then recycled to the cell surface (**Figure I.11**)[240]. To date, the FDA has approved four GalNAc-conjugated siRNA drugs: givosiran, inclisiran, lumasiran and vutrisiran[241].

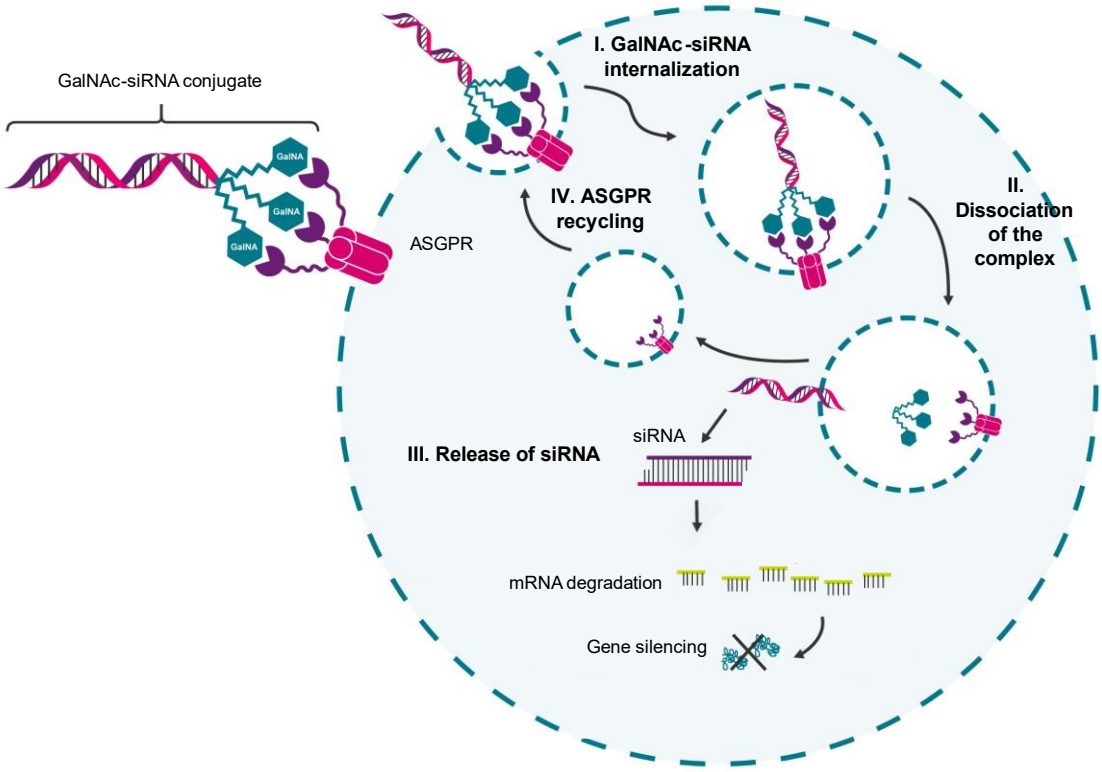

Figure I.11. Cellular uptake of GalNAc-siRNA conjugates. I) GalNAc-siRNA conjugates bind specifically to ASGPR on the cell membrane and are subsequently internalized via endocytosis. II) Within the endosomal compartment, a decrease in pH triggers the dissociation of the conjugate from the receptor. III) The siRNA is released into the cytoplasm, where it exerts its biological activity. IV) Following cargo release, ASGPR undergoes recycling back to the cell surface for further uptake. Abbreviations: GalNAc, *N*-acetylgalactosamine; ASGPR, asialoglycoprotein receptor; siRNA, small-interfering RNA. Adapted from Biosearch Technologies.

2. Study 2

I.2.1. Coronavirus disease 2019 (COVID-19)

I.2.1.1. General features

Coronavirus disease 2019 (COVID-19), caused by the severe acute respiratory syndrome coronavirus 2 (SARS-CoV-2), is a highly contagious and pathogenic disease in humans, often resulting in severe lower respiratory tract infections and high potentiality of fatal respiratory illnesses[242,243]. This disease primarily spreads through person-to-person transmission via the respiratory route, wherein infectious virions are suspended and transported via short-range small aerosol particles[244].

After the first cases reported in Wuhan (China) in late December 2019, SARS-CoV-2 rapidly spread across the globe, prompting the World Health Organization (WHO) to declare it a global pandemic on March 11, 2020. Over the course of five years, COVID-19 has had a devastating impact worldwide, resulting in over 7 million deaths. This pandemic has stood as one of the most consequential global health crises since the influenza pandemic of 1918[245,246]. SARS-CoV-2 has shown a uniform global distribution, with COVID-19 cases reported across all continents. However, a distinct seasonal pattern is observed worldwide, with the highest incidence of coronavirus infections typically occurring during the winter season[247–249]. During the pandemic, outbreaks were primarily attributed to genetic evolution and the emergence of mutation, facilitating the virus's adaptation. While several variants of SARS-CoV-2 have been described, only a few are considered as variants of concern (VOCs) due to their impact on diagnostics, treatments, or vaccines, exhibiting elevated transmissibility and disease severity. To date, five SARS-CoV-2 VOCs have been identified since the beginning of the pandemic: alpha (B.1.1.7), beta (B.1.351), gamma (P.1), delta (B.1.617.2) and omicron (B.1.1.529)[250].

I.2.1.2. Pathophysiology

I.2.1.2.1. SARS-CoV-2 structure

SARS-CoV-2 belongs to the subfamily Coronaviruses, which includes two other viruses responsible for devastating outbreaks: the 2003 SARS-CoV pandemic and the 2012 MERS pandemic. Coronaviruses are a family of enveloped, single-stranded, positive-sense RNA and polyadenylated viruses that infect mammals, including humans, and cause a wide variety of diseases[251]. The genome size of SARS-CoV-2 ranges between

29.8 kb and 29.9 bk and expresses four structural genes crucial for viral infection encoding the nucleocapsid protein (N), the spike protein (S), and the membrane glycoprotein (M) and envelope protein (E). Additionally, the genome encodes non-structural proteins and accessory proteins that contribute to various aspects of viral replication and pathogenesis (**Figure I.12**)[252].

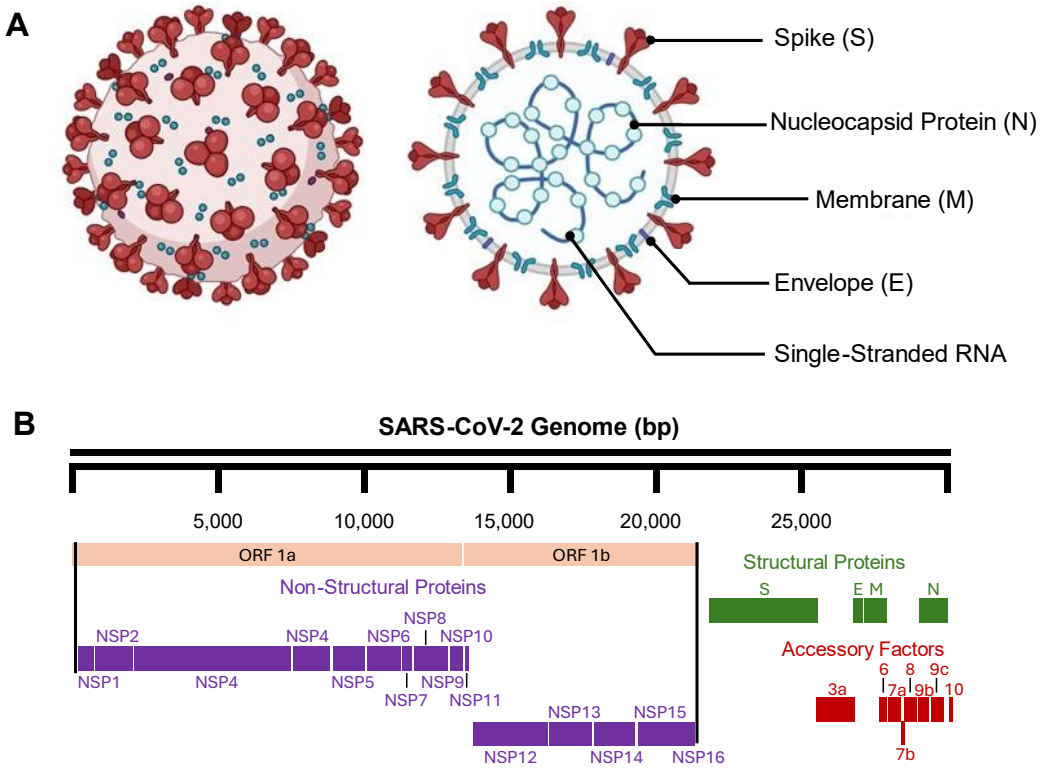

Figure I.12. Structure of human SARS-CoV-2. (**A**) SARS-CoV-2 comprises structural components such as the spike, envelope and membrane proteins and internal elements, including single-stranded RNA and nucleocapsid protein. (**B**) Components of the SARS-CoV-2 genome. Adapted from Jamison Jr *et al.*[253]

I.2.1.2.2. SARS-CoV-2 entry process via ACE2 receptor and spike protein binding

To understand the peculiar impact of SARS-CoV-2, we should consider the mechanisms of SARS-CoV-2 entry into host cell. The S glycoprotein, located on the surface of the viral particle, holds significant importance as it mediates viral attachment and internalization into host cells[254]. The S protein is composed of two subunits: a receptor-binding subunit (S1), housing the receptor-binding domain (RBD) responsible for binding to angiotensin-converting enzyme 2 (ACE2) receptors on host cell surfaces, thereby influencing viral host range, tropism, and infectivity; and a membrane-fusion subunit (S2) which enables fusion of the host and viral

membranes, allowing viral entry into host cells. Following SARS-CoV-2 and host interaction, the virus may use two potential entry routes, each characterized by distinct cleavage events of the S protein (**Figure I.13**) [255].

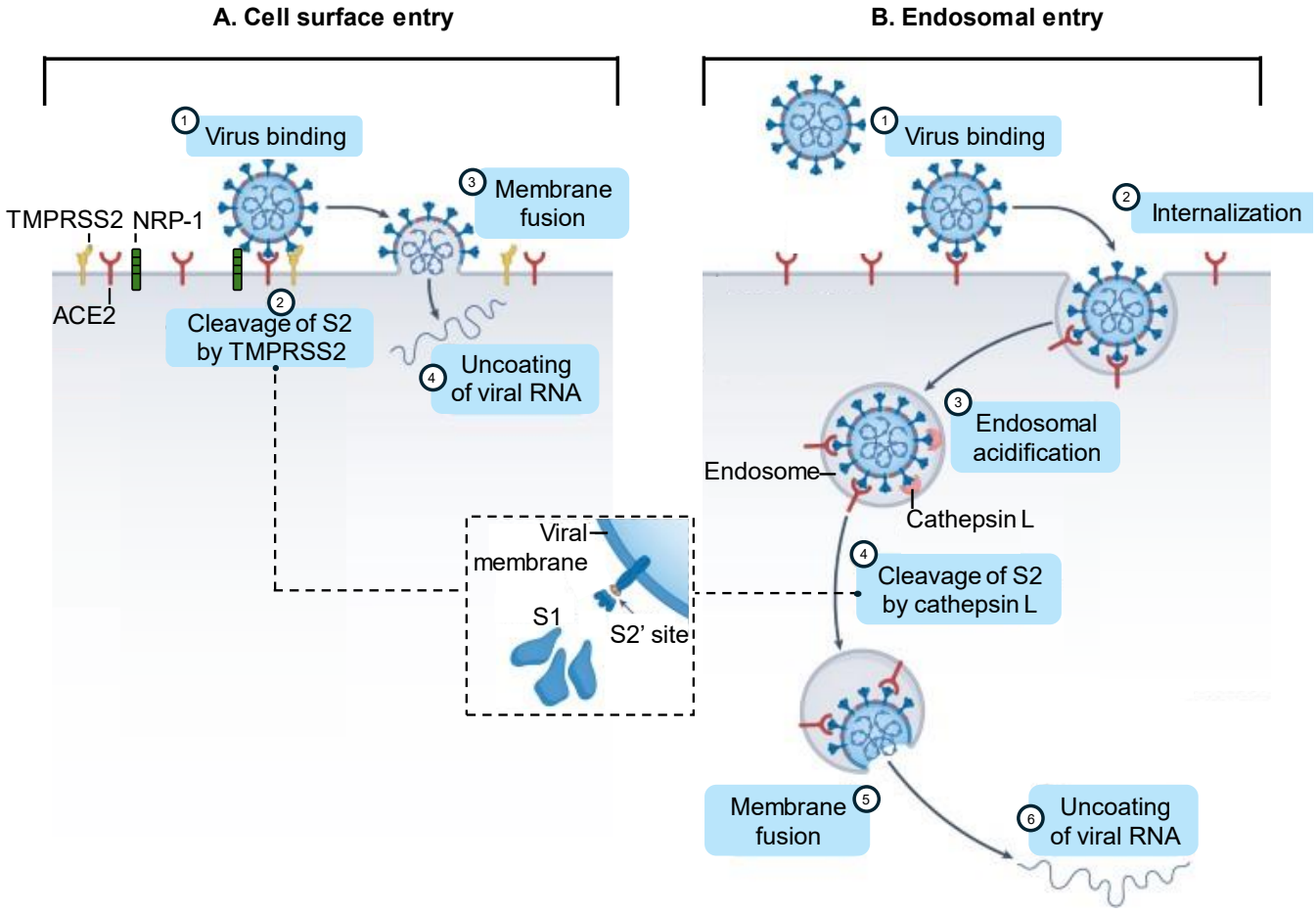

Figure I.13. SARS-CoV-2 entry mechanisms in the host cell. Critical features essential for virus internalization include ACE2-dependent binding and spike protein cleavage. (**A**) Preferential SARS-CoV-2 entry involves the cleavage of S2 by TMPRSS2, followed by membrane fusion. (**B**) Secondary SARS-CoV-2 entry occurs via internalization into an endosome and cleavage of S2 by cathepsin. Adapted from Jackson *et al.*[254]

In the primary and preferred route, the host transmembrane protease, serine 2 (TMPRSS2) cleaves at two sites at the cell surface: the S1-S2 boundary and an internal site in the S2 subunit, termed the 'S2' site', facilitating subsequent membrane fusion and cellular entry (**Figure I.13.A**) [256,257]. In the secondary route, if the target cell expresses insufficient TMPRSS2 or when the virus-ACE2 complex fails to interact with TMPRSS2, internalization occurs through clathrin-mediated endocytosis. Subsequently, within the endolysosomes, cleavage of S2' is facilitated by cathepsins, enzymes that require an acidic environment for their activity (**Figure I.13.B**)[254]. Apart from ACE2 and TMPRSS2, additional host factors facilitate SARS-CoV-2 binding to the cell surface, thereby

influencing the tissue/organ tropism of the virus. Among these factors is neuropilin-1 (NRP-1), which also interacts with the S1 protein[258] .

I.2.1.2.3. Immune response and cytokine storm

Upon entry into the cell, SARS-CoV-2 triggers the rapid activation of the host's innate immune response, followed by the engagement of the adaptive immune system[259]. In the innate immune phase, various immune cells including natural killer cells, macrophages, monocytes, dendritic cells, and neutrophils are quickly recruited and activated to produce both type I interferons (IFNs) and pro-inflammatory cytokines, such as tumor necrosis factor (TNF), IL-6, interleukin 1 beta (IL-1β), interleukin 12 (IL-12) and interleukin 17 (IL-17), which exert antiviral effects. Subsequently, B and T lymphocytes are activated to initiate immunological memory[260].

In severe cases of COVID-19, cytokines play a dual role, acting as both defenders against viral infections and, due to excessive production and unregulated release, contributing to a life-threatening condition known as cytokine storm, which leads to hyperinflammation and multiorgan failure[261]. Innate immune cells, particularly neutrophils, macrophages and natural killer cells are the most often implicated in the pathogenesis of cytokine due to their expression of pattern-recognition receptors (PRRs). These receptors enable these cells to detect and respond to a diverse range of microbial pathogens, leading to the production of cytokines that activate cells of the adaptive immune system[262].

In the lungs, cytokine storms can cause a serious clinical complication known as acute respiratory distress syndrome (ARDS) leading to difficulty breathing and low oxygen saturation in the bloodstream. While the prognosis for ARDS associated with COVID-19 is generally more severe compared to non-COVID-19-related ARDS, certain immunosuppressive agents have demonstrated therapeutic benefits, as explained in section '<u>I.2.1.6. Therapeutic strategies</u>'[263].

I.2.1.2.4. Host signaling during SARS-CoV-2 infection

SARS-CoV-2 exerts physiological effects through direct cell infection and intercellular signaling. Upon viral infection and cell-surface receptors modulation, multiple intracellular pathways are activated. Subsequently, the progression of SARS-CoV-2 infection alters host cell metabolism and signaling, facilitating the viral

replication cycle, through signaling pathways that regulate processes of DNA repair and replication, immune response, transcription, metabolism, cell cycle and apoptosis[264].

Proteomic studies revealed significant changes in response to SARS-CoV-2 infection, which involves diverse kinases known to control many key cellular functions. Some of the multiple examples are ribosomal protein S6 kinase (RPS6K), implicated in cell activation and survival; Akt, which regulates cell growth, survival and motility; p38, c-Jun N-terminal kinase (JNK) and extracellular signal-regulated kinase (ERK), associated with the stress response[265,266]. During the initial phases of infection, the PI3K/AKT/(mTOR pathway is notably activated. Specific inhibitors targeting this pathway may potentially improve the course of COVID-19 by downregulating excessive inflammatory responses, promoting cellular protection, and exerting antiviral effects[267]. Additionally, the transcription factors most prominently activated include NF-κB, which is downstream of the MAPK pathway, known for its role in stimulating proinflammatory cytokines[268]. Moreover, pathways involving type I and III interferon, TGFβ and Toll-like receptors (TLR) are also observed to be modulated following SARS-CoV-2 infection[264].

Ultimately, pathways dysregulated in the context of SARS-CoV-2 infection antagonize host antiviral responses and play essential roles in viral replication, entry, propagation, and/or apoptosis/viral release.

I.2.1.2.5. The renin-angiotensin system

The renin-angiotensin system (RAS) plays a crucial role in regulating blood pressure and electrolyte balance and fluid homeostasis by controlling hormonal feedback. However, its dysregulation is implicated in various pathologies affecting multiple organs, including the liver. RAS is compromised by two main pathways (**Figure I.14.A**): (i) the classic RAS, which culminates in the generation of angiotensin II (AngII) via the ACE/AngII/AT1 axis. AngII exerts pro-inflammatory, pro-oxidant, and pro-apoptotic effects by binding to AT_1R receptors, contributing to organ damage. (ii) Conversely, an alternative RAS pathway involves the production of angiotensin 1-7 (Ang1-7) through the ACE2/Ang1-7/MAS axis, which counters the effects of the classical route[269]. *In vitro* studies of SARS-CoV-2 infection reveal that the virus binding to its receptor induces downregulation of ACE2 at both transcriptional and protein expression levels. This downregulation may subsequently elevate ACE activity, potentially contributing to the cytokine storm characteristic of patients experiencing lung injury (**Figure I.14.B**). However, the clinical implications of RAS dysregulation in the context of SARS-CoV-2 infection remain controversial in clinical studies, partly due to confounding factors such as the use of ACE inhibitors or angiotensin-receptor blockers by participants[270]. Understanding the impact of comorbidities on RAS regulation involves considering the release of ACE2 from the cell membrane into the

bloodstream following tissue damage. Given that SARS-CoV-2 uses ACE2 as a cellular entry point, it may change the catalytic activity of ACE2 at the tissue level. This altered activity could prevent the huge release of ACE2 into the bloodstream, as seen in conditions like cardiovascular disease, hypertension, and chronic kidney disease, where circulating ACE2 serves as a prognostic marker[270].

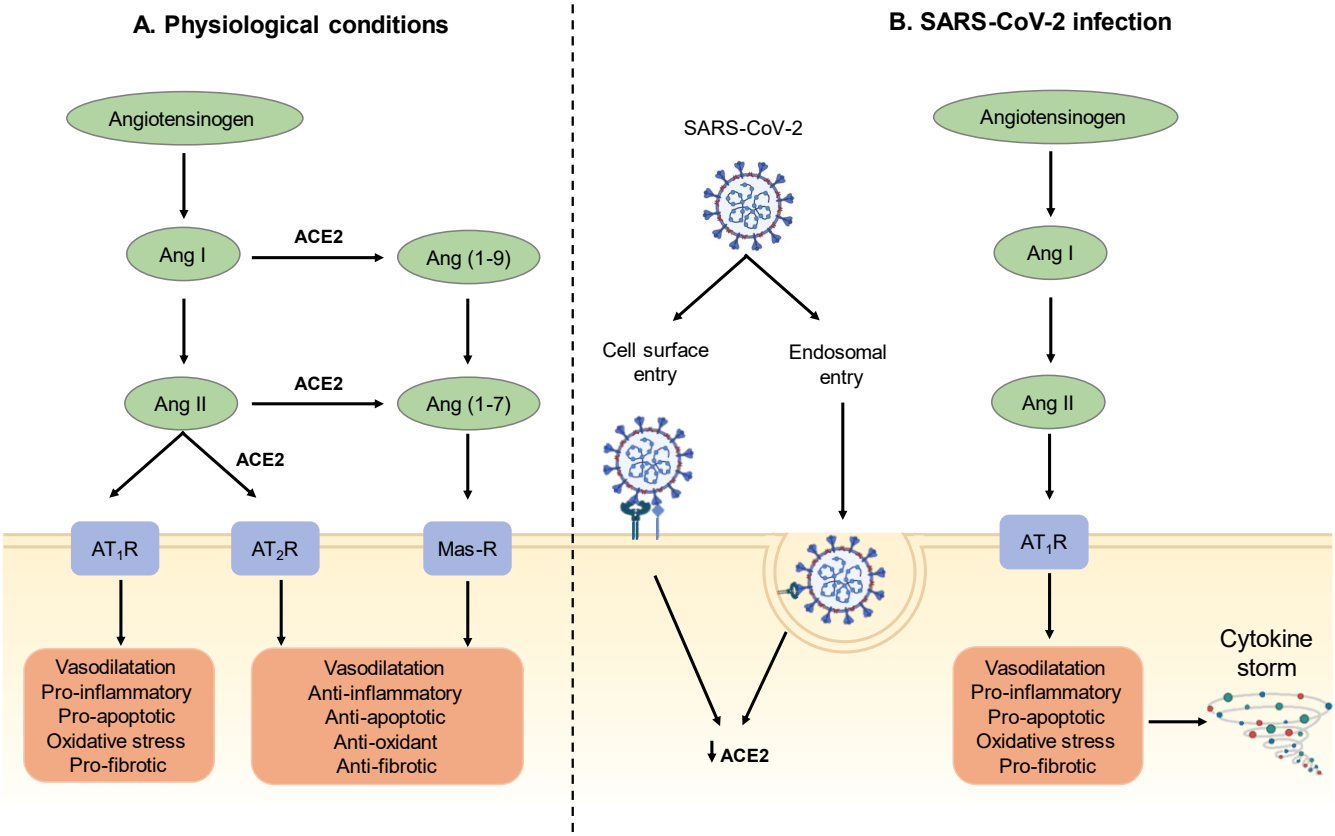

Figure I.14. Potential interplay between the Renin-Angiotensin System (RAS) and SARS-CoV-2 infection. (**A**) Under physiological conditions, RAS balance is orchestrated by two pathways: ACE/AngII/AT1 and ACE2/Ang1-7/MAS axis which regulates blood pressure and electrolyte balance and fluid homeostasis. (**B**) Under SARS-CoV-2 infection, dowregulation of ACE2 leads to dysregulated RAS pathway with pro-inflammatory effects that can make the sytokine storm worse. Abbreviations: Ang, angiotensin; AT_1R, Ang II type I receptor; AT_2R, Ang II type II receptor; ACE2, angiotensin-converting enzyme 2; Mas-R, Mas receptor.

1.2.1.3. Risk factors for severe illness

The disease spectrum of COVID-19 ranges from asymptomatic cases, typically observed in the youngest and healthiest individuals, whose incidence has been augmented by vaccination; to mild illness, featuring symptoms like fever or cough without evidence of lower respiratory tract involvement; to moderate illness,

characterized by lower respiratory tract infection with oxygen saturation levels of 94 percent or higher; and finally, severe disease, characterized by oxygen saturation levels below 94 percent, tachypnea, and/or lung infiltrates affecting more than 50 percent of lung parenchyma on imaging[271]. The last group may manifest in any healthy individuals but is more commonly observed in adults with specific risk factors (**Table I.2**). The primary risk factor is vaccination against COVID-19, which significantly reduces the risk of severe illness and is correlated with a reduction in mortality rates[272]. Age is another crucial factor, with individuals aged 50 or older being most affected, particularly those over 65, who face a higher risk of severe disease and mortality[273,274]. Additionally, certain comorbidities and underlying conditions increase the risk of COVID-19, with patients having these conditions experiencing mortality rates up to 12 times greater than those without any reported comorbidities[275]. Studies also suggest that patients who die from COVID-19 have an average of 2.7 pre-existing comorbidities[276]. Two additional important risk factors are gender and socioeconomic status. The male gender exhibits increased susceptibility to severe illness or mortality across diverse cohorts worldwide[277–280]. Likewise, Black, Hispanic, or Southern Asian individuals also present elevated rates of COVID-19 infections and mortality[277–279]. Another susceptible group are socioeconomically vulnerable populations, as demonstrated in a study involving prison populations[281]. Moreover, biochemical findings correlate with poorer prognoses (**Table I.2**)[280,282]. Host genetic factors also play a role in severe COVID-19 outcomes. For instance, polymorphisms in genes related to the ABO blood group system have been linked to respiratory failure from COVID-19, with type A associated with a higher risk and type O with a lower risk[283,284].

Table I.2. Factors contributing to severe COVID-19 risk. Abbreviations: BMI, body mass index; MASLD, metabolic dysfrunction-associated liver disease; IL-6, interleukin 6; TNF-α, tumor necrosis factor-alpha; and AKI, acute kidney injury.

Risk factors	Specifications	Ref
Vaccination		272
Age	≥65 years	273,274,277–280,282,285
Comorbidities		
Asthma		279
Cancer		277,279,285,286
Cerebrovascular disease		277
Chronic kidney disease		277,279,280
Chronic lung disease	Interstitial lung disease, pulmonary embolism, pulmonary hypertension, bronchiectasis, chronic obstructive pulmonary disease	277,279,285,287
Chronic liver disease	Cirrhosis, MASLD, alcoholic liver disease, autoimmune hepatitis	277,279
Cystic fibrosis		288
Type 1 and 2 diabetes mellitus		277–279,282,285,287
Disabilities	Attention deficit hyperactivity disorder, cerebral palsy, congenital malformations, limitations with self-care or activities of daily living, intellectual and developmental disabilities, learning disabilities, spinal cord injuries	289
Heart conditions	Eg, heart failure, coronary artery disease, or cardiomyopathies	277–280,282,285,287
HIV		290
Mental health disorders	Mood disorders including depression, schizophrenia spectrum disorders	279
Neurologic conditions	Dementia	277,279
Obesity and overweight	Obesity (BMI ≥30 kg/m2) and overweight (BMI 25 to 29 kg/m2), or ≥95th percentile in children	278,280,291,292
Physical inactivity		293
Pregnancy		294
Primary immunodeficiencies		279
Smoking	Current or former	295
Sickle cell disease or thalassemia		296
Solid organ or blood stem cell transplantation		297,298
Substance use disorders		299
Tuberculosis		300
Prolonged use of corticosteroids or other immunosuppressive medications		279,301
Socioeconomic background	Socioeconomically vulnerable populations	277–279
Gender and ethnicity	Male gender and Black, Hispanic or Southern Asian individuals	277–280
Laboratory abnormalities	Lymphopenia, thrombocytopenia, elevated liver enzymes, elevated lactate dehydrogenase, elevated inflammatory markers (eg, C-reactive protein, ferritin) and inflammatory cytokines (eg, IL-6 and TNF-α), elevated D-dimer, elevated prothrombin time, elevated troponin, elevated creatine phosphokinase, AKI	280,282
Genetic factors	ABO blood group	283,284

I.2.1.4. Disease prevention

The primary preventive strategy for COVID-19 consists of pre-exposure prophylaxis with vaccination, effectively preventing infection. The principal antigenic target for COVID-19 vaccines is the RBD of the spike protein, so thereby impeding viral attachment to host cells and neutralizing its virulence. The advent of COVID-19 vaccination has unveiled new platforms such as mRNA and DNA, although some approaches include traditional platforms such as inactivated virus or recombinant proteins[302]. In regions where community transmission is widespread, additional measures are essential, including optimizing indoor ventilation; adhering to rigorous hand washing and respiratory hygiene; practicing social distancing with potentially infected individuals; and wearing masks[303].

I.2.1.5. Diagnosis

The incubation period for COVID-19 is generally within 14 days post-exposure, with most cases occurring approximately four to five days after exposure[304]. Although some individuals infected may remain asymptomatic, COVID-19 symptoms are typically non-specific, including nasal congestion, sneezing, cough, myalgias, headache, diarrhea, sore throat and/or alterations in smell or taste. In cases of severe COVID-19, pneumonia may also develop. Among these symptoms, changes in smell or taste are more strongly associated with COVID-19 compared to other viral respiratory infections during the pandemic period[305].

Diagnostic assays for COVID-19 include nucleic acid amplification tests (NAATs), antigen tests and serology tests. Among these, NAATs, with reverse-transcription polymerase chain reaction (q-PCR) being the most used, are recommended for their superior sensitivity. However, they necessitate a turnaround time of 24-48 hours and are typically conducted in a laboratory setting[306]. In contrast, antigen tests offer greater accessibility, convenience and cost-effectiveness, with shorter turnaround times. Nonetheless, their sensitivity is inferior to that of NAATs, and negative results from antigen tests conducted on symptomatic individuals or those recently exposed generally require confirmation with additional testing[307]. Consequently, antigen testing is advised for use in home settings and point-of-care sites. Additionally, it is recommended for individuals who previously tested positive for SARS-CoV-2 within the preceding three months and necessitate repeat testing, as a positive result from NAATs may more likely indicate prolonged viral RNA shedding rather than a new infection. Ultimately, serologic tests identify antibodies specific to SARS-CoV-2 in the bloodstream can help identify individuals with prior SARS-CoV-2 infection, as well as those currently infected who have had symptoms for three to four weeks[306,308].

I.2.1.6. Therapeutic strategies

Despite extensive research to develop an effective COVID-19 vaccine, there remains a need to identify potential drug candidates for treating immunocompromised patients and those with severe clinical symptoms.

In cases of moderate COVID-19, symptomatic patients are advised to intensify hygiene practices and maintain adequate hydration. Additionally, antithrombotic prophylaxis may be administered if needed, along with nonsteroidal anti-inflammatory drugs. For moderate patients at high risk of disease progression, such as transplant recipients or those with immunodeficiency, antiviral medications and monoclonal antibodies are recommended therapeutic options. While remdesivir, an RNA polymerase inhibitor, and the nirmatrelvir/ritonavir combination, a protease inhibitor, have gained FDA approval since the onset of the pandemic, alternative therapies are also available[309]. Among these alternative therapies are neutralizing antibody therapies, derived from convalescent plasma or specific monoclonal or polyclonal antibodies. These therapies function similarly to those naturally produced by the body when exposed to SARS-CoV-2, blocking the virus's ability to infect host cells[310].

Severe COVID-19 commonly manifests with an oxygen saturation level below 94%, attributed to various factors impeding the diffusion of oxygen from alveoli to arterial blood[311]. For that reason, 10-15% of COVID-19 patients require intensive care unit (ICU) admission to receive advanced respiratory support[312]. In the management of severe COVID-19 cases requiring hospitalization, corticosteroids like dexamethasone or IL-6 blockers are administered. These medications function by mitigating the overstimulation of the immune system commonly observed in severe cases of COVID-19[309].

I.2.1.7. COVID-19 in the liver

I.2.1.7.1. Evidence of COVID-19 implication in the liver

Aside from its impact on the respiratory tract and lungs, which are the primary organs affected, SARS-CoV-2 can also infect various organs and systems, resulting in multi-organ dysfunction and diverse symptom manifestations. These affected organs include the lymph nodes, brain, kidneys, gastrointestinal tract, testes, and notably, the liver[313]. Liver function abnormalities have been frequently observed in COVID-19 patients[314]. Severe patients of COVID-19 exhibit a notable elevation in liver enzymes ranging from 14.8% to 58% of cases[315–326]. Indeed, elevated transaminase levels have been correlated with disease severity, with severe patients, especially those hospitalized in the internal cure unit, exhibiting greater increase in these enzymes

compared to patients with mild to moderate severity[320,324]. Additionally, postmortem biopsies performed in COVID-19 patients have revealed mixed microvesicular and macrovesicular steatosis with mild lobular and portal activity, together with focal necrosis[327,328]. In turn, pre-existing liver disease is associated with worse outcomes and higher mortality rated in patients with COVID-19[279,329–337]. In those studies, the predominant etiologies among patients with chronic liver disease were MASLD and MASH, although cirrhosis, alcohol-related liver disease and autoimmune hepatitis were also associated to this condition[338]. Moreover, patients with chronic liver disease had lower immunologic response to SARS-CoV-2 vaccines than healthy population, making them more susceptible to infection and necessitating the administration of booster doses of the SARS-CoV-2 vaccine to enhance their immune response[339].

I.2.1.7.2. Mechanisms of COVID-19 associated liver injury

Multiple hypotheses have emerged to elucidate the mechanisms underlying the hepatic effects of COVID-19. In addition to direct viral-induced liver injury, potential mechanisms include immune-mediated damage, ischemia and hypoxia reperfusion injury and drug-related hepatotoxicity, all contributing to liver injury in COVID-19 patients (**Figure I.15**).

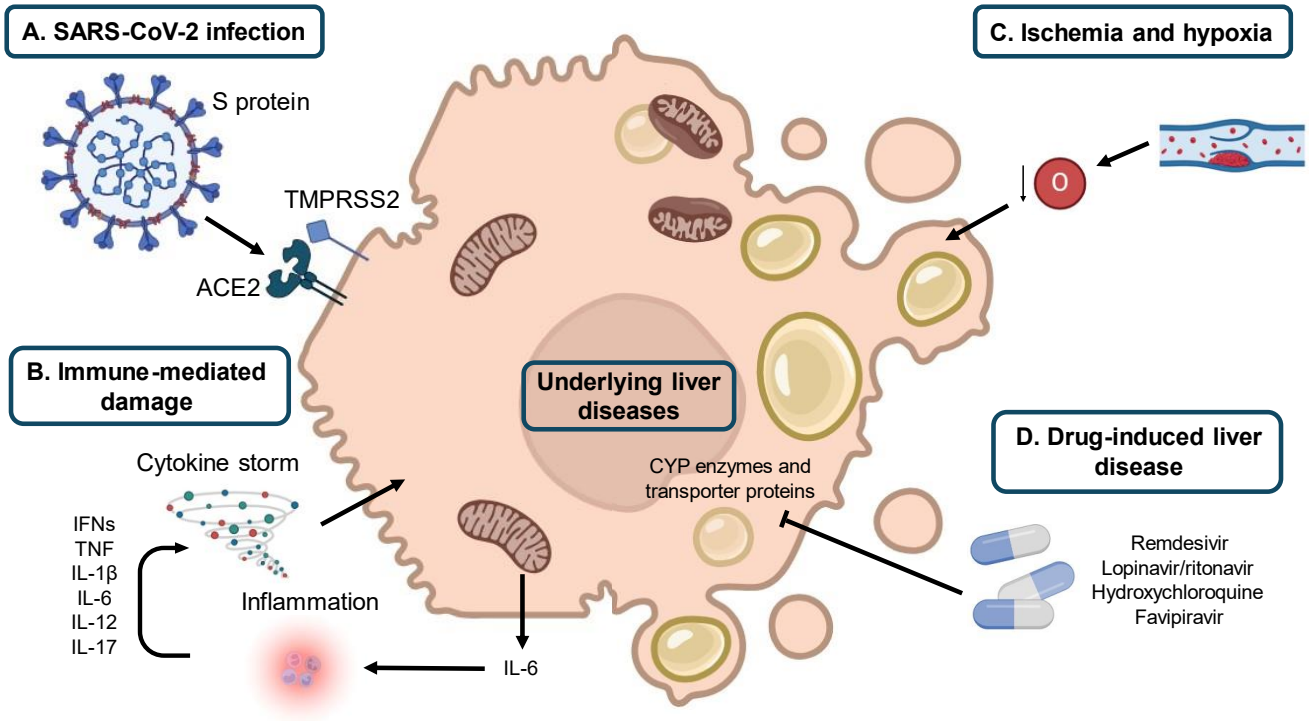

Figure I.15. Mechanisms of liver injury associated with COVID-19 infection. SARS-CoV-2 may induce liver damage through various pathways, including direct viral-induced injury (**A**), immune-mediated mechanisms (**B**), ischemia and hypoxia reperfusion

injury (**C**) and drug-related hepatotoxicity (**D**). Abbreviations; SARS-CoV-2: severe acute respiratory syndrome coronavirus 2; S protein: spike protein; ACE2: angiotensin-converting enzyme 2; TMPRSS2: transmembrane protease, serine 2; IFN: interferon; TNF: tumor necrosis factor; IL: interleukin; CYP: cytochrome.

I.2.1.7.2.1. Cytopathic damage

One hypothesis suggests that, similar to other viruses, SARS-CoV-2 may induce a direct cytopathic effect on liver cells. SARS-CoV-2 employs ACE2 receptors to invade host cells and utilizes other molecules to facilitate infection, including TMPRSS2 and NRP-1. Despite ACE2 expression is more prevalent in cholangiocytes than in hepatocytes, reaching levels comparable to alveolar type 2 cells in the lung, alanine aminotransferase (ALT), aspartate transaminase (AST) and lactate dehydrogenase (LDH) are more commonly elevated than bilirubin, alkaline phosphatase (ALP) or GGT, which describe bile duct injury[340]. In contrast, Kupffer cells as well as T and B lymphocytes did not express ACE2, even though COVID-19-infected patients' livers frequently showed Kupffer cell activation and proliferation induced by systemic immune response[318,341]. NRP-1 is expressed in the liver, particularly in a diverse range of liver-related conditions including cancer, liver fibrosis, MASLD, and inflammatory disorders, potentially contributing to the predisposition of patients to be infected. While NRP-1 is found in some liver-resident cells, it is notably upregulated in nonparenchymal cells, such as liver sinusoidal endothelial cells (LSECs) and hepatic stellate cells (HSCs)[342]. Histologic analyses confirm the current hypothesis as some authors have uncovered the presence of intact SARS-CoV-2 viral particles in the cytoplasm of hepatocyte samples[318]. Additionally, investigations utilizing in situ hybridization and electron microscopy have revealed that SARS-CoV-2 directly infiltrates liver cells, inducing histological alterations such as apoptosis and mixed inflammatory infiltrates in portal tracts. [343]. Clinical evidence of the cytopathic effect of SARS-CoV-2 has shown rapid progression from acute hepatitis to fulminant liver failure, accompanied by a mild increase in transaminase levels, without the development of respiratory symptoms[344].

I.2.1.7.2.2. Immune dysfunction and cytokine storm

The liver plays a crucial role in immune function, harboring a significant population of immune-related cells[345]. Patients exhibiting abnormal liver function demonstrate elevated levels of procalcitonin and C-reactive protein (CRP)[322]. However, how does the systemic cytokine release impact on hepatic function? Cytokines exert systemic effects that can detrimentally affect the liver. Cytokines play a crucial role in immune cell recruitment by inducing vasodilation and increasing vascular permeability. Consequently, immune cells infiltrate the site of infection, leading to endothelial dysfunction and hypoxia[346]. This

dysfunction manifests as alveolar edema in the lungs and edema in other organs, such as the liver, where microcirculatory flow is significantly reduced by 50% during a cytokine storm[347]. Likewise, cytokines trigger cellular injury and death by a ROS-dependent pathways[348]. The inflammatory and cytopathic effects of COVID-19 may be linked through the RAS, as downregulation of ACE2 has been demonstrated to alter the RAS axis, shifting it away from anti-inflammatory pathway Ang 1-7/angiotensin 1–9 towards the pro-inflammatory and pro-oxidant Ang II–AT1 pathway, thereby promoting tissue injury[349,350].

Locally, several cells within the liver mediate hepatic response to cytokine release, including Kupffer cells, neutrophils, hepatocytes and LSEC. Kupffer cells, as resident macrophages in the liver, are key players in initiating the inflammatory response by releasing cytokines upon activation, generating ROS and nitric oxide (NO), thereby inducing LSEC to generate hepatocyte injury. Additionally, hepatocytes can also produce cytokines in response to various stimuli, notably IL-6 which increases caspase-3 levels, indicative of hepatocellular apoptosis. Neutrophils, which are recruited to the liver during inflammation, also contribute to cytokine and ROS release, which may cause mitochondrial damage. LSECs can also produce cytokines and participate in the inflammatory cascade[351].

Autopsies confirm this hypothesis, as they have revealed that patients with COVID-19 exhibit hepatomegaly accompanied by lobular focal necrosis and infiltration of neutrophils, lymphocytes, and monocytes within the portal area[352]. Furthermore, the severity of the disease and levels of inflammatory markers correlate with increasing elevations in liver transaminase levels in adult patients with COVID-19[353]. As a result, pro-inflammatory cytokine release appears to be a driver of disease progression in COVID-19.

I.2.1.7.2.3. Ischemia and hypoxia reperfusion injury

Two potential outcomes derived from severe cases of COVID-19 are hepatic hypoxia and ischemia, as evidenced by studies indicating elevated prevalence of these conditions among ICU patients, often resulting in a high mortality rate[354]. Hypoxia refers to the insufficient supply of oxygen to tissues, either in localized regions or throughout the body. Conversely, ischemia is characterized by reduced blood flow to specific areas of the body, resulting in oxygen deprivation and subsequent hypoxia[355]. Systemic and localized inflammation induced by SARS-CoV-2 infection, together with ARDS, may contribute to diminished or obstructed hepatic blood flow. Consequently, this condition triggers lipid buildup, glycogen depletion, decreased ATP production and an inadequate oxygen supply, culminating in hepatocyte death and the development of a hypoxic state. Ultimately, this cascade of events culminates in shock liver, a

critical medical condition characterized by ongoing hepatocyte destruction until liver function is severely compromised [356].

I.2.1.7.2.4. Drug-related hepatotoxicity

Drug-induced liver injury (DILI) is an important consideration in patients with COVID-19 due to the utilization of several medications in its treatment regimen, including over-the-counter drugs like paracetamol, as well as antivirals like remdesivir, lopinavir/ritonavir, hydroxychloroquine and favipiravir. Significantly, these drugs have exhibited higher incidence of abnormal liver function during the antiviral treatment of COVID-19 patients[357]. The cumulative prevalence of acute liver injury among COVID-19 patients was 23.7% (16.1%–33.1%)[358].

Hepatic drug metabolism encompasses a complex process involving uptake, metabolism and excretion mechanisms. Drug uptake can occur either passively or through active transport mediated by various proteins located on the basolateral membrane. These proteins include members of the solute carriers (SLCs), organic anion-transporting polypeptides (OATPs), organic anion-transporter (OAT) family, and organic cation transporters (OCTs). Drugs are metabolized by cytochrome P450 (CYP450) or conjugated to endogenous molecules. Subsequently, metabolized drugs are excreted into either the bile or blood sinusoids by ATP-binding cassette (ABC) transporters. Throughout this metabolic process, drugs induce cellular stress, marked by mitochondrial impairment, oxidative stress and ER stress[359]. In this context, antiviral drug entry into the liver inhibits the function of CYP enzymes and transporter proteins, disrupting the redox balance and drug excretion processes governed by these pathways. This may lead to a homeostasis imbalance, thereby causing DILI[357].

I.2.2. Metabolic dysfunction-associated steatotic liver disease (MASLD)

I.2.2.1. Definition

Metabolic dysfunction-associated steatotic liver disease (MASLD), formerly known as non-alcoholic fatty liver disease (NAFLD), has emerged as a significant risk factor for severe COVID-19[360]. MASLD has become one of the most relevant forms of chronic liver disease worldwide, affecting more than a third of the world's adult population, and therefore has been a major health and economic burden to all societies. However, the prevalence of MASLD is particularly high in regions with a high incidence of obesity and T2DM, such as North America, Western Europe, and parts of Asia[361].

MASLD histological classification comprises hepatic steatosis, involving greater than 5% of parenchyma, with or without mild non-specific inflammation; and metabolic dysfunction-associated steatohepatitis (MASH), previously known as non-alcoholic steatohepatitis (NASH), characterized by hepatocellular injury in an environment of steatosis with varying degrees of liver fibrosis (**Figure I.16**)[362]. MASLD may progress to liver fibrosis considered as the most important histological predictor of hepatic-related death and as a pre-state of cirrhosis to HCC[363].

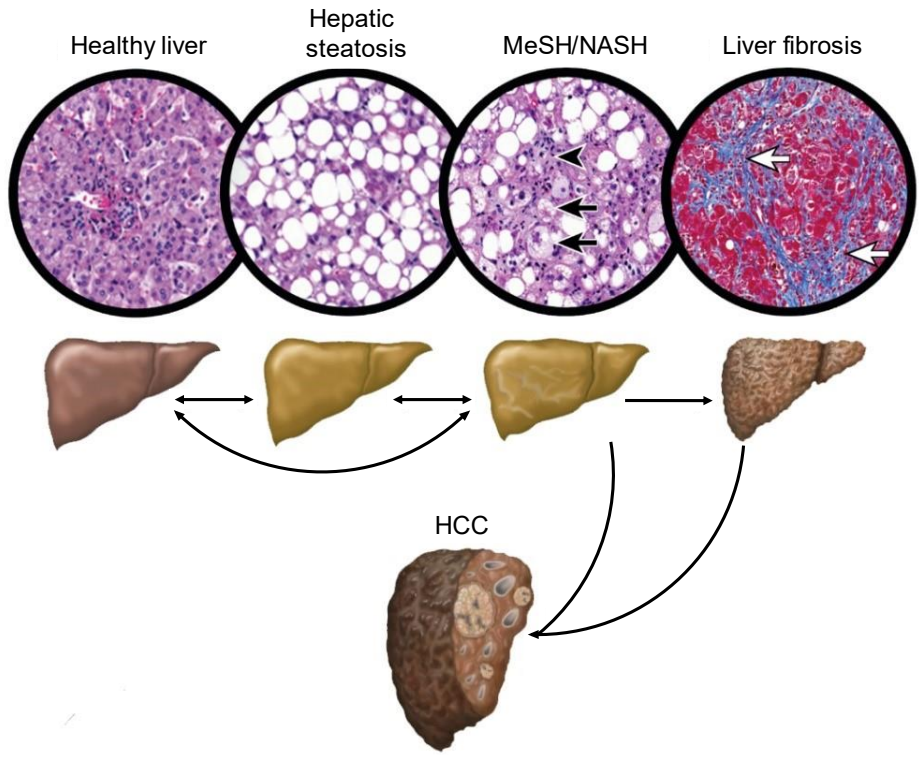

Figure I.16. Histological progression of metabolic dysfunction-associated steatotic liver disease (MASLD), previously known as non-alcoholic fatty liver disease (NAFLD). The development of MASLD is divided into four stages: hepatic steatosis (accumulation of fat in >5% of parenchyma); metabolic dysfunction-associated steatohepatitis (MASH)/non-alcoholic steatohepatitis (NASH) (accumulation of fat with liver inflammation and cell damage) to liver cirrhosis (excess of fibrous tissue and permanently hepatocellular injury) and eventually hepatocellular carcinoma (HCC). Adapted from Arab *et al*[364].

Clinically, MASLD is defined as a condition characterized by the presence of hepatic steatosis, confirmed through imaging techniques, blood biomarkers/scores, or liver histology in association with T2DM and overweight/obesity, regardless of alcohol consumption or exclusion of other chronic liver disease etiologies. Diagnosis of MASLD in lean/normal weight individuals requires the presence of hepatic steatosis and at least two metabolic risk abnormalities, including high waist circumference, arterial hypertension, dyslipidemia, prediabetes, elevated homeostasis model assessment (HOMA) score and increased CRP serum levels[365].

I.2.2.2. Pathophysiology

Insulin resistance, obesity with adipocyte proliferation and dysfunction and altered gut microbiome, consequences of dietary habits, environmental and genetic factors, are characteristic of MASLD[366]. Other involved endocrine organs are the pancreas, the muscle or the stomach[367]. Considering this, the pathogenesis of MASLD is multifactorial and complex.

I.2.2.3. Treatment

The primary approach to treating MASLD involves nutritional intervention and lifestyle modification. This includes abstaining from alcohol, addressing cardiovascular disease risk factors (such as optimizing blood glucose control and implementing lipid-lowering therapy) and achieving weight loss through dietary therapy and exercise[368]. Several drugs are currently undergoing phase 1 and 2 clinical trials. These investigational therapies target various aspects of MASLD's complex pathophysiology, which involves both genetic and environmental factors. The drugs under investigation include glucose-lowering agents, antioxidants, bile and non-bile acid farnesoid X activated receptor (FXR) agonists, peroxisome proliferator-activated receptor (PPAR) agonists, and thyroid hormone receptor (THR) agonists[369]. Resmetirom, a liver-targeted thyroid hormone receptor-β selective agonist, has demonstrated efficacy in phase 3 clinical trials for the treatment of non-cirrhotic MASH with moderate to advanced fibrosis, being a promising therapy for MASH[370]. Additionally, tirzepatide, an agonist of the glucagon-like peptide-1 receptor, has shown positive results in phase 2 clinical studies[370]. Notably, metformin, the first-line drug to treat T2DM, is the preferred treatment for MASLD patients with concurrent T2DM. Metformin’s benefits include inhibiting hepatic gluconeogenesis, improving hepatic fatty acid metabolism (such as inhibition of adipose tissue lipolysis), increasing fatty acid oxidation, inhibiting lipogenesis and enhancing insulin sensitivity[371]. Although its ability to improve liver histology is controversial, metformin has been shown to reduce MASLD-related mortality, fibrosis, and the risk of HCC[372–374]. In the context of COVID-19, metformin has been shown to reduce mortality, disease severity and long-term symptoms in T2D patients infected with SARS-CoV-2[375,376].

Hypothesis and Objectives

H.1. Study 1

Maintaining Mg^{2+} homeostasis is crucial for various physiological processes, including metabolism, cellular proliferation and structural integrity. The Mg^{2+} transporter CNNM4 has emerged as a key player in liver diseases such as MASLD and DILI. Upregulation of CNNM4 in CCA suggests its involvement in cholangiocarcinogenesis. Therefore, this dissertation investigates the potential role of CNNM4 in CCA pathogenesis and the efficacy of its silencing by using the GalNAc molecule to halt CCA progression.
Hence, the following objectives were proposed to be assessed:

I. Characterize the contribution of CNNM4 to the pathogenesis of CCA by examining its expression in human CCA tissue and its impact on key CCA features.

II. Determine the impact of genetic *CNNM4* silencing on cellular proliferation, drug resistance, energy metabolism and spheroid formation in CCA cell lines.

III. Evaluate the impact of genetic silencing of *CNNM4* on metastasis potential in chick chorioallantoic membrane (CAM) *ex ovo* and *in ovo* models.

IV. Identify the underlying mechanisms through which CNNM4 exerts its functions in CCA pathogenesis.

V. Assess the effects of genetic *CNNM4* silencing on the progression of CCA in *in vivo* models.

H.2. Study 2

SARS-CoV-2, the causative agent of the COVID-19 pandemic, causes multi-organ impairment, including hepatic dysfunction, observed in 14.8% to 58% of cases. Liver injury in COVID-19 patients may result from various factors, including direct cytopathic effects induced by viral interaction with hepatic cells, exacerbated immune responses, ischemia and hypoxia reperfusion injury or adverse effects of therapeutic drugs. In this study, we propose that SARS-CoV-2 binding to hepatic cells may induce liver damage, mitochondrial dysfunction and metabolic rewiring.

Moreover, in 2020, limited knowledge existed regarding the susceptibility of certain conditions to severe COVID-19 outcomes. Patients with obesity exhibited poorer prognoses and elevated mortality rates. Therefore, we hypothesized that individuals with MASLD might be at increased risk for COVID-19, and that metformin, a widely prescribed therapy for hyperglycemia in patients with MASH, could potentially mitigate SARS-CoV-2 infection.

Hence, the following objectives were proposed to be assessed:

I. Evaluate the potential binding and infectivity of hepatocytes, both in primary hepatocytes and cell lines, using viral particles expressing the spike protein of SARS-CoV-2.

II. Identify the cellular changes in primary hepatocytes post-infection with pseudotyped viral particles expressing the spike of SARS-CoV-2 at the proteomic and metabolic levels.

III. Characterize the regulation of the renin-angiotensin system in primary hepatocytes following infection with SARS-CoV-2.

IV. Analyze the susceptibility of obese patients with MASH to SARS-CoV-2 and assess the beneficial effects of metformin on the prognosis of SARS-CoV-2-infected patients.

Materials and methods

M.1. Human and organoid samples

The research protocol was approved by their respective ethics committee and all patients signed written consents to allow the use of their samples for biomedical research.

M.1.1. Transcriptomic studies

M.1.1.1. Study 1

CCA and control resected human tissues (either normal bile ducts or adjacent healthy liver tissues) from 8 independent cohort of patients (Montal, The Thailand Initiative in Genomics and Expression Research [TIGER-LC], Job, Ahn, The Cancer Genome Atlas [TCGA], Andersen, Regensburg and Salamanca cohorts) were studied at the transcriptomic level[377–382]. A cohort of patient-derived organoids (Bradshaw) was employed for the investigation of gene expression. Cohort information is depicted in **Table M.1**.

Table M.1. Description of cholangiocarcinoma cohorts. Abbreviations: CCA, cholangiocarcinoma; eCCA, extrahepatic CCA; iCCA, intrahepatic CCA; dCCA, distal CCA; q-PCR, quantitative polymerase chain reaction.

Cohort identification	Samples	Methodology
Montal (GSE132305)	182 eCCA and 38 adjacent healthy samples	Microarray (Affymetrix Human Genome U219 Array)
The Thailand Initiative in Genomics and Expression Research (TIGER; GSE76311)	92 iCCA and 93 adjacent healthy samples	Microarray (Affymetrix Human Transcriptome Array 2.0)
Job (E-MTAB-6389)	78 iCCA and 31 adjacent healthy samples	Microarray (Affymetrix GeneChip HTA-2_0)
Ahn (GSE107943)	30 CCA and 27 adjacent healthy samples	RNA-Seq (Illumina NextSeq 500)
The Cancer Genome Atlas (TCGA) – Cholangiocarcinoma (CHOL)	30 iCCA, 6 eCCA and 9 adjacent healthy samples	RNA-Seq (IlluminaHiSeq_RNASeqV2)
Andersen (GSE26566)	104 CCA, 59 adjacent healthy and 6 normal bile duct samples	Microarray (Illumina human Ref-8 v2.0 expression beadchip)
Regensburg (Germany; #17-1015-101)	32 iCCA and 32 adjacent healthy samples	q-PCR
Salamanca (PI2020-02-422)	12 iCCA, 6 dCCA, 12 adjacent healthy and 2 normal bile duct samples	q-PCR
Bradshaw (GSE84073)	7 tumoral CCA and 6 healthy organoids	Illumina HiSeq 1500

M.1.1.2. Study 2

Liver samples were obtained from patients with obesity undergoing bariatric surgery (n=94) at the Clínica Universidad de Navarra and at the Marqués de Valdecilla University Hospital (Santander, Spain) and q-PCR was used to determinate ACE2 and TMPRSS2. The clinical characteristics of these patients are indicated in **Table M.2**

Table M.2. Anthropometric, biochemical and clinical characteristics of obese patients. Abbreviations: BMI, body mass index; LDL, low-density lipoprotein; HDL, high-density lipoprotein; AST, aspartate transaminase; ALT, alanine transaminase; HOMA, homeostasis model assessment.

	Without MASLD	**Steatosis**	**MASH**
n	17	57	20
Age (years, mean ± SD)	43.1 ± 8.7	46 ± 10.9	49.2 ± 10.4
Gender (F / M)	12 / 5	29 / 28	11 / 9
Weight (kg ± SD)	116.3 ± 27.8	123.1 ± 22.9	137 ± 23.7
BMI	40.2 ± 7.7	43.8 ± 6.3	48.3 ± 6.8
LDL (mg/dl ± SD)	107.8 ± 33.8	112.5 ± 33.5	105.9 ± 32.2
HDL (mg/dl ± SD)	48.3 ± 12.6	45.8 ± 15.4	42.5 ± 11.6
Triglycerides (mg/dl ± SD)	102.6 ± 67.5	140.8 ± 65.9	161.4 ± 74
Cholesterol (mg/dl ± SD)	176.8 ± 41.2	188.9 ± 38.7	185.5 ± 36.1
AST (U/L ± SD)	17.6 ± 4.9	21.1 ± 6.2	36.3 ± 20.9
ALT (U/L ± SD)	21 ± 8.5	27.6 ± 13.3	44.6 ± 25.3
Glucose (mg/dl ± SD)	109.9 ± 55.4	110.8 ± 42.3	121.3 ± 38.5
Insulin (mg/dl ± SD)	12 ± 8.3	26.7 ± 41.5	17.8 ± 12.6
HOMA	3.7 ± 4.3	5.7 ± 3.7	5.5 ± 5
Type 2 diabetes	29.4%	47.4%	55%
NAS score > 5	0%	15.8%	45%
Metabolic syndrome	35.3%	54.5%	78.9%

Inclusion criteria were based on alcohol intake lesser than 20g/day for woman and lesser than 30g/day for men, no evidence of hepatitis B and/or C virus infection as well as human immunodeficiency virus (HIV) and, no evidence of concomitant liver disease such as autoimmune liver diseases, haemochromatosis, Wilson's disease or α-1 antitrypsin deficiency. Comorbidities, anthropometric measures, laboratory data (ALT, AST, GGT, triglycerides, cholesterol, HDL, LDL) and histology data were collected. Hepatic histopathological analysis was performed according to the scoring system of Kleiner et al.[383] Simple steatosis was defined as the presence of at least 5% of steatotic hepatocytes with or without mild lobular or portal inflammation but in the absence of features of hepatocellular injury (ballooning, apoptosis or necrosis) and fibrosis. On the other hand, minimal criteria for the histological diagnosis of definite metabolic dysfunction-associated steatohepatitis included the combined presence of grade 1 steatosis, hepatocellular injury and lobular inflammation with or without fibrosis.

M.1.2. Histological studies

M.1.2.1. Study 1

Immunohistochemistry (IHC) was performed in paraffin-embedded liver tissue from the whole ENS-CCA cohort (12 iCCA, 11 eCCA and 9 adjacent healthy samples) and a representative part of Regensburg cohort (5 iCCA and 1 adjacent healthy samples).

M.1.2.1. ENS-CCA cohort

For the ENS-CCA cohort, CCA specimens were collected from n=23 patients undergoing liver resection with curative intent. According to the anatomical location, tumors were classified as intrahepatic CCA (iCCA; n=12) and extrahepatic CCA (eCCA; n=11). Age, gender and tumor staging are reported in **Table M.3**. Three µm-thick formalin-fixed paraffin-embedded sections of resected CCA samples were collected from the Pathology Department of each participating institution. These samples were then sent to Sapienza University of Rome for inclusion in the ENS-CCA Histology Registry. In n=9 cases, non-tumoral surrounding liver was present in the provided sections and was used as control for normal cholangiocytes. Individual patient data were obtained from medical records by the participating hospitals and retrieved from International Cholangiocarcinoma Registry, as described elsewhere[190]. Anatomical classification followed the International Classification of Diseases 11th revision criteria[139]. TNM stage was obtained by either histology or imaging techniques, according to the American Join Committee on Cancer / International Union Against Cancer staging system, 8th edition.

Table M.3. Clinical and tumoral characteristics of CCA patients from the ENS-CCA cohort. Abbreviations: IQR, interquartile range; T, extent of the tumor; N, extend of spread to the lymph nodes; M, presence of metastasis.

	All	iCCA	eCCA	p-value
n	23	12	11	
Age (years, mean [IQR])	72 [8]	70 [8]	75 [7]	ns
Gender (F / M)	8 / 15	5 / 7	3 / 8	ns
TNM Staging System (#)				
T (#)	T1: 5 T2: 12 T3: 5 T4: 1	T1: 4 T2: 7 T3: 1 T4: 0	T1: 1 T2: 5 T3: 4 T4: 1	ns
N (#)	N0: 19 N1: 4	N0: 10 N1: 2	N0: 9 N1: 2	ns
M (#)	M0: 20 M1: 3	M0: 10 M1: 2	M0: 10 M1: 1	ns
Stage (#)	I: 5 II: 14 III: 1 IV: 3	I: 4 II: 5 III: 1 IV: 2	I: 1 II: 9 III: 0 IV: 1	ns

M.1.3. Correlation studies in TCGA

Clinical information from cholangiocarcinoma patients in the TCGA database was obtained from the Broad GDAC Firehose (BROAD Institute of MIT & Harvard, https://gdac.broadinstitute.org/).

M.2. Cell lines and culture conditions

M.2.1. Study 1

M.2.1.1. Cell lines

H69 cells, an SV40-transformed normal human cholangiocyte cell line (Lonza Cat#: 712) and TFK-1 cells (DSMZ Cat#: ACC344) were cultured in RPMI (Thermo Fisher Cat#: 11875093); EGI-1 cells (DSMZ Cat#: ACC385) were cultured in Dulbecco's Modified Eagle Medium (DMEM)/F12 (Gibco Cat#: 11320033); and HEK293T cells (Takara Bio Inc. Cat#: 632180) were cultured in DMEM (Gibco Cat#: 41966-029). Human liver epithelial THLE-2 cells (ATCC

Cat#: CRL-2706) were cultured in Bronchial Epithelial Cell Growth medium (Lonza Cat#: CC3170) supplemented all items included in the BulletKit (Lonza Cat#: CC4175), except for Gentamycin/Amphotericin and Epinephrine, and supplemented with 5ng/mL EGF (Thermo Fisher Cat#: PHG0315) and 70 ng/mL Phosphorylethanolamine (Sigma Aldrich Cat#: P0503). All cell lines were cultured under standard conditions (37°C and 5% CO_2) and supplemented with 10% (v/v) FBS (Gibco Cat#: 10270106), 1% (v/v) PSA (Thermo Fisher Cat#: 15240062) and 1% (v/v) glutamine (Thermo Fisher Cat#: 25030024).

M.2.2. Study 2

M.2.2.1. Mice and human primary hepatocytes

Preparation of the experimental animals and isolation of primary hepatocytes was performed as follows: briefly, after anesthesia of humanized ACE2 (hACE2) and wild-type (WT) mice with isoflurane (1.5% (v/v) isoflurane in O_2) and insertion of a catheter into the vena cava, liver was perfused with buffer A (1X PBS, 5mM EGTA) (37ºC, oxygenated) while portal vein was cut. Buffer B (1XPBS, 1mM $CaCl_2$, collagenase type I (Worthington)) (37ºC, oxygenated) was subsequently used to perfuse and disaggregate the liver. Then, disaggregated liver was placed in a Petri plate containing 10% (v/v)-FBS MEM medium supplemented with PSG and cells were disassembled with the help of forceps and filtered through sterile gauze. Perfused livers were first centrifuged at 400 rpm during 4 minutes at 4ºC and pellet was resuspended in 10% (v/v)-FBS Minimum Essential Medium (MEM) (Gibco Cat#: 31095-029) containing penicillin (100U/mL), streptomycin (100U/mL) and glutamine (2mM) (PSG) (Thermo Fisher Cat#: 10378-016). Subsequently, cells were washed in MEM twice (500rpm during 5 minutes at 4ºC) and plated on collagen-coated plate. Primary hepatocytes were cultured under standard conditions (37°C and 5% CO_2).
Second-generation human upcyte hepatocytes, culture medium, high-performance medium, and thawing medium were all obtained from Upcyte Technologies (Heidelberg, Germany) and cultured as previously described[384].

M.2.2. Cell lines

HEK293T cells (Takara Bio Inc. Cat#: 632180) were cultured in DMEM (Gibco Cat#: 41966-029) and Vero E6 cells (ATCC Cat#: CRL-1586) were cultured in MEM (Gibco Cat#: 31095-029). Human liver epithelial THLE-2 cells (ATCC Cat#: CRL-2706) were cultured in Bronchial Epithelial Cell Growth medium (Lonza Cat#: CC3170) supplemented all items included in the BulletKit (Lonza Cat#: CC4175), except for Gentamycin/Amphotericin and Epinephrine, 5ng/mL EGF (Thermo Fisher Cat#: PHG0315) and 70ng/mL Phosphorylethanolamine (Sigma Aldrich Cat#: P0503). All cell lines were cultured under standard conditions (37°C and 5% CO_2) and supplemented with 10% (v/v) FBS

(Gibco Cat#: 10270106), 1% (v/v) PSA (Thermo Fisher Cat#: 15240062) and 1% (v/v) glutamine (Thermo Fisher Cat#: 25030024).

M.2.3. Generation of viral particles and titration

M.2.3.1. Study 1

For short hairpin RNA (shRNA) stable cell lines generation, $5x10^6$ HEK293 cells, kindly provided by Arkaitz Caracedo lab, were seeded in $10mm^2$ plated. After 24h, 2µg pCMV, 0.5µg pCMV-VSV-G and 1.5µg control or CNNM4 shRNA were transfected into HEK293 cells using JetPEI protocol (Polyplus, Cat#: 101000053). Control and 5 different pLKO.1 CNNM4 (TRCN0000045213, TRCN0000045214, TRCN0000045215, TRCN0000045216 and TRCN0000045217) shRNA were supplied by Serge Hardy lab. After 48h, the supernatant was collected, filtered through a 0.45µm syringe and mixed with Lenti-X concentrator (Takarabio, Cat#:631232) in a ratio of 1:3. After incubation for 30 minutes at 4ºC, centrifuge at 1500G for 45 minutes at 4ºC. Aspirate the supernatant and resuspend the pellet with PBS, which will be added to EGI-1 and TFK-1 cells. All these procedures were performed in a class II biosafety cabinet.

M.2.3.2. Study 2

In order to generate pseudotyped viral particles expressing the spike protein of SARS-CoV-2, HEK293T cells were transfected using a 3rd generation five-plasmid system kindly provided by Drs. Jean-Philippe Julien (University of Toronto) and Jesse D. Bloom (Fred Hutchinson Cancer Research Center), as previously described[26]. Briefly, plasmids encoding for HDM-Hgpm2 (NR-52517), pRC-CMV-Rev1b (NR-52519), HDM-tat1b (NR-52518), the SARS-CoV-2 spike protein (NR-52514) and the lentiviral backbone that express ZsGreen (NR-52520) were administered to HEK293T cells (50-70% of confluence) using JetPEI kit (Polyplus-transfection #101-10N). Pseudotyped lentiviral particles were collected from supernatants 48 hours after transfection and filtered using a 0.45µm filter (VWR Cat#: 514-0063). After concentrating the viral particles using Lenti-X Concentrator (Takara Bio Inc. Cat#: 631231) they were stored in PBS at -80°C until use. Control pseudotyped viral particles were generated using HEK293T cells. $5x10^6$ cells were seeded in T175 flasks in DMEM media supplemented with 10% (v/v) FBS, glutamine and NEAA. For transfection, a mixture of plasmids encoding for luciferase IRES ZsGreen, HDM-Hgpm2, pRC-CMV-Rev1b and HDM-tat1b were diluted in 2.5mL of DMEM and then mixed with additional 2.5mL of DMEM containing lipofectamine. After 24 hours, the media was replaced with complete media supplemented with 5mM of sodium butyrate. After 60 hours, viral particles were collected and stored at -80ºC. Viral titration was performed in THLE-2 and upcyte second-generation human hepatocytes cells as described in Crawford *et al* [385]. Cells were

incubated with pseudotyped lentiviral particles for 48 hours. The infected cells expressed ZsGreen, allowing their detection by flow cytometry.

M.2.4. Cell treatments

M.2.4.1. Study 1

Stable cell lines were seeded onto 24-well plates (50.000 cells/well) and after 12 hours cells were exposed to different treatments. The specificity of CNNM4 in cell viability was assessed by adding magnesium (Merk Cat#: M2670-100G) to the medium, reaching a final concentration of 5mM. The role of energy production in TFK-1 cells was studied by exposing the cells to 10mM 1-deoxy-D-glucose (Merck Cat#: D8375-25G) for 24 hours. To asses CNNM4 role in chemoresistance, cells were treated with 1µM cisplatin (Merck Cat#: C2210000, dissolved in water), 200nM Doxorubicin (Thermo Scientific Cat#: J64000.MA, dissolved in DMSO), 2.5µM Gemcitabine (Merck Cat#: G6423, dissolved in water) and 5µM 5-Fluorouracil (Merck Cat#: F6627, dissolved in DMSO). Finally, cells were treated with 50µM Deferiprone (Merk Cat#: Y0001976) for 24 hours and with 25µM Zinc Protoporphyrin (Zn(II)-protoporphyrin IX) (MedChemExpress Cat#: HY-101193) for 48 hours. H69 and THLE-2 were transfected with 100nM of *CNNM4* siRNA (Life technologies, Cat#: S25465) using DharmaFECT1 transfection reagent (Cat#: T-2001-03).

M.2.4.2. Study 2

Rates of infection on THLE-2 and primary hACE2 or WT hepatocytes were calculated after incubation with pseudotyped viral particles (MOI: 0.8). Cells were incubated for 48 hours to allow expression of ZsGreen, which allows detection of infected cells by flow cytometry, as previously described[385] . Steatotic conditions were induced in primary hepatocytes as follows: incubation overnight on 0% (v/v)-FBS MEM medium containing PSG followed by incubation in methionine-choline deficient (MCD) medium (Gibco Cat#: ME120128L1) supplemented with PSG. Metformin (Sigma Aldrich Cat#: PHR1084) was administered at 1mM (final concentration) to primary hepatocytes after overnight incubation with 10%(v/v)-FBS MEM containing PSG. After 6 or 24 hours, plates were washed thrice with PBS, frozen (-80ºC) and processed for western blot analysis. Hepatocytes were cultured overnight with 0%(v/v)- FBS MEM (containing PSG) prior to incubation in MCD medium containing metformin (1mM) for 10 hours. Hereafter, plates were washed thrice with PBS, frozen (-80ºC) and processed for western blot analysis or incubated with pseudotyped viral particles for 48 hours. For pharmacological inhibition of the ACE2/Ang 1-7/Mas axis, cells were treated with A779 (Tocris Bioscience Cat#: 5937) for 1 hour followed by lentiviral infection.

M.3. Mouse models

All mouse experiments were carried out following the ethical guidelines established by the Biosafety and Welfare Committee at CIC bioGUNE (P-CBG-CBBA-0518). They were maintained on a 12/12 hour light/dark cycle at temperature of 21±1ºC, humidity of 45±10% and *ad libitum* access to water and standard chow diet (Teklad Global 14% Protein Rodent Maintenance diet; Envigo RMS Spain Cat#: 2014C). All animal experiments were performed according to the ARRIVE guidelines and carried out in accordance with the National Institutes of Health guide for the care and use of Laboratory animals (NIH Publications N0.8023, revised 1978) and the guidelines of European Research Council for animal care and use.

M.3.1. Study 1

C57BL/6 mice (male) were provided by Charles River Laboratories International, Inc.

M.3.1.1. Sleeping Beauty model of CCA and GalNAc siRNAs treatment

when mice reached a body weight of 20g, they were hydrodynamically injected via the tail vein with 30µg pT3-EF1α-HA-myr-AKT (Adgene Cat#: 31789), 30µg pT3-EF1α-YapS127A, and 2µg SB-13 plasmids, following established protocols[386]. Two weeks post-injection, liver evaluations were performed using echography (Vevo770, VisualSonics), and the animals were evenly divided into two groups depending on the subcutaneous treatment: GalNAc si*Cnnm4* or GalNAc siControl. The GalNAc#1 and #2 molecules consist of double-stranded 19mer RNAs with 2′-O-methyl, 2′-fluoro-2′deoxy modifications and phosphorothioate bonds targeting Cnnm4, conjugated to a triantennary GalNAc unit. A non-targeting control siRNA conjugate was used as a comparison, targeting Luciferase (Photinus pyralis) and also linked to the same GalNAc unit. The *Cnnm4* molecules were synthesized, purified, and provided by Silence Therapeutics GmbH[387].

M.3.1.2. Basal glucose measurement

Basal glucose was measured using Accu-Chek Aviva test strip (Accu-Check Cat #: 06453953) in fresh blood collected from the mice's tails after nicking the tip using a pair of sterile scissors.

M.3.1.3. Iron content determination

Ferric, ferrous and total iron levels were determined using a commercial kit (Sigma Aldrich Cat#: MAK025) following the manufacturer's recommendations.

M.3.1.4. Lipid peroxidation measurement

MDA, a well-stablished lipid peroxidation biomarker, was analyzed using a commercial kit (Sigma Aldrich Cat#: MAK085) following the manufacturer's recommendations.

M.3.2. Study 2

hACE2 and WT mice (male) were kindly provided by Development & Plasticity of the Neuroendocrine Brain laboratory (Institut National de la Santé et de la Recherché Médicale, INSERM).

M.4. Chick chorioallantoic membrane (CAM) assay

CAM assays have been widely used to study various aspects of cancerogenesis including tumor cell invasion and metastasis[388]. In this study, the *ex ovo* CAM model was developed as described previously[389]. Briefly, fertilized chicken eggs purchased from a local provider (Vykrm Trebic) were incubated lying horizontally with intermittent rotation at 37.5°C and 65% humidity for 3 days. Then, the eggshells were cracked, and embryos were transferred into small, sterile plastic bowls (VWR, Radnor, PA, USA). Then, the bowls were covered using Petri dishes and incubated for additional 7 days after which embryos were xenografted with EGI-1 cells. Before xenografting, EGI-1 cells (transfected with shRNA ctrl, shRNA 2 and shRNA 5 as described above) were pre-labeled with CellTracker Green (Invitrogen) and implanted on the CAM at an initial seeding density of ~500.000 in each ring (two rings in different sites that were always near to small vessels) to form macrotumors and 50.000 of cells to form microtumors. Then, *ex ovo* cultures were further incubated at 37.5°C for 3 days. After that, the embryos were sacrificed by cutting the vitelline arteries. The CAM sites that developed tumors were extracted and fixed using 3.7% (v/v) paraformaldehyde in PBS. *In ovo* CAM model was produced as described by Crespo *et al*.[390]. Briefly, ~1.500.000 EGI-1 cells were injected onto CAM of embryos to induce tumor formation. Tumor growth was continually monitored. Harvesting of tissues was performed on day 7 and the number of EGI-1 cells in the distal CAM and lungs was analyzed by Alu q-PCR. A standard curve was generated using serial dilutions of human DNA corresponding to originally engrafted tumor cells. Ct values were measured in triplicates and the number of cells able to intravasate into the CAM or metastasize to the lungs was determined by extrapolation of Ct values versus the standard curve[391]. The tumor growth in the CAM was confirmed by hematoxylin and eosin staining. To examine EGI-1 cells intravasation and extravasation, we carried out other independent experiments. In these cases, for the purpose of fluorescence angiography, vascular endothelium was labeled with rhodamine-labeled *Lens culinaris* agglutinin (50µL of 10 µg/mL) (Vector Laboratories) administered in peripheral vein with 30-gauge

hypodermic needle at day 7 after xenografting. Upon this procedure, the embryos were further incubated (3 min) to enable LCA to circulate and stain vascular endothelium. CAM sites that produced primary tumors were extracted with a 3cm margin around tumors as well as distal CAM and the tissues were fixed using 3.7% (v/v) paraformaldehyde in PBS. Finally, excised lungs were sliced, fixed and counterstained using Hoechst 33342 (Invitrogen) and observed for presence of metastasizing EGI-1 cells. All analyses were performed using the fluorescent microscope EVOS FL Auto Imaging System (Thermo Fisher). EGI-1-labeled cells signal was collected at 517nm using 492nm excitation source. LCA signal was collected at 575nm using 550nm excitation source.

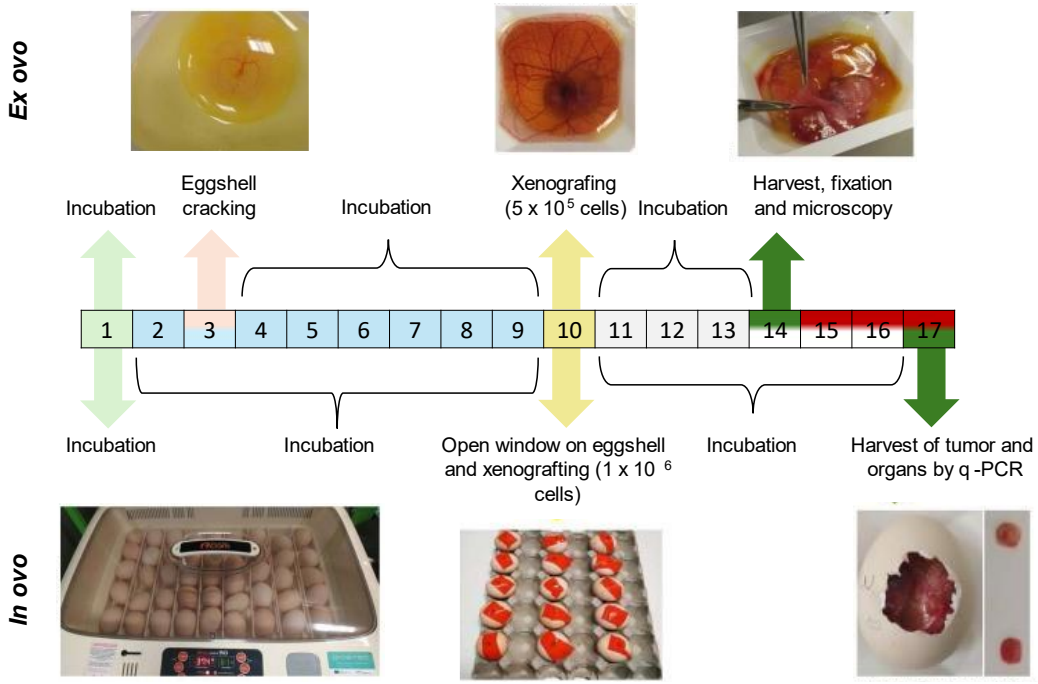

Figure M.1. Protocol for *ex ovo* and *in ovo* chick chorioallantoic membrane (CAM) assays in the development of cholangiocarcinoma (CCA) xenografts using EGI-1 cells. In the *ex ovo* CAM assay, fertilized eggs were incubated for 3 days before cracking the eggshell and transferring the content into sterile dishes for further incubation (an additional 6 days). EGI-1 cells were then grafted onto the CAM, specifically targeting vascular branches, and embryos were further incubated for 3 days. CAM areas containing microtumors were extracted, leaving a 1-cm margin of healthy tissue, and subsequently fixed. In the *in ovo* CAM assay, fertilized eggs were incubated for 10 days vefore creating a window in the eggshell for xenografting EGI-1 cells. The eggs were then incubated for an additional 6 days. Adapted from Merlos Rodrigo MA *et al.* [389].

M.5. Gene expression analysis

M.5.1. RNA isolation and quantification

Total RNA was extracted from cultured cell lines or from liver tissue using TRIzol reagent (Invitrogen Cat#: 15596026) according to manufacturer's instruction. Briefly, cells were lysed with 1mL of TRIzol, 200µL of chloroform (Merck Millipore Cat#: 107024) was added to each tube. The mixture was vigorously inverted for 5 seconds to ensure thorough mixing of the phases, followed by centrifugation at 12,000 rpm, 4ºC, for 10 minutes. The aqueous phase containing RNA was transferred to a new sterile tube, and 0.5 mL of 2-propanol (Sigma Aldrich Cat#: I9516-500ML) and 5 µL of glycogen (Invitrogen Cat#: AM9510) was added. The solutions were mixed by inversion and stored overnight at -80ºC. The following day, tubes were centrifuged at 12,000 rpm, 4ºC, for 10 minutes, and the supernatant was discarded. The RNA pellet was washed with 1 mL of 70% (v/v) ethanol (PanReac AppliChem Cat#: A3678) by slight vortexing and centrifuged at 12,000 rpm for 10 minutes at 4ºC. After removing the supernatant, the RNA pellet was air-dried at room temperature. RNA pellets were resuspended in 20µL of sterile DNase/RNase-free distilled water (Sigma-Aldrich Cat#: W4502). RNA concentration and purity were determined using ultraviolet spectrophotometry with the NanoDrop ND-1000 apparatus (Thermo Fisher Scientific).

M.5.2. Reverse transcription (RT)

Total RNA (1-2µg in 8µL) was reverse transcribed to synthesize complementary DNA (cDNA). To remove any contaminating genomic DNA, a mixture of DNAse I and its buffer (Invitrogen Cat#: 18068015) was added to each tube and incubated for 14 minutes. Subsequently, EDTA was added to stop the reaction, followed by incubation at 65ºC for 10 minutes. A mix containing buffer, DTT, random primers (diluted 1/10), dNTPs (diluted 1/10), M-MLV, and RNAseOUT (all from Invitrogen Cat#: 28025013, 48190011, 10297018, and 10777019, respectively) was prepared and added to the reaction tubes. The cDNA synthesis protocol was carried out in a Veriti 384-Well thermal cycler (Applied Biosystems Cat#: 4452301), including the following steps: I) 10 minutes at 25ºC, II) 90 minutes at 37ºC, III) 15 minutes at 70ºC, and IV) storage at 4ºC until collection. The resulting cDNA was diluted 1/10 or 1/20 in RNAse-free water (Sigma-Aldrich Cat#: W4502), depending on the initial amount of RNA used (1 or 2 µg, respectively).

M.5.3. Real time quantitative polymerase chain reaction (q-PCR)

The mRNA expression levels of various genes were assessed using q-PCRs performed on either the ViiA 7 or the QS6 Real time PCR System. A master mix was prepared, consisting of 0.15µL of 100µM primer solution, 3µL of SYBR Select Master Mix (Applied Biosystems, Cat#: 4472908), and DNase/RNase-free water added to achieve a final volume of 5µL per sample. This master mix was dispensed into a 384-well PCR plate (Applied Biosystems, Cat#: 4343370). Subsequently, 2µL of cDNA template was added to each well. All reactions were performed in triplicate. PCR conditions were optimized for each primer set, and amplification was conducted over 40 cycles with a melting temperature of 60ºC and a duration of 30 seconds per step. Primer sequences are provided in **Table M.4 and M.5.** Following q-PCR amplification, the specificity of the products was confirmed by analyzing the melting curves and data were normalized to the expression levels of housekeeping genes (ARP, HPRT1).

Table M.4. Human and mouse primers sequences employed for q-PCR analysis in Study 1 (all from Merck Life Technologies)

Gene	Sequence	
	Forward (5'-3')	**Reverse (5'-3')**
Human		
CNNM1	GGCTGGAGTAGGAGGTCTGA	CAACATGGCTGAGTCCCACT
CNNM2	ACCCTATGATTGGCTGTGGC	CCATCTTCCAAGTGGGCAGT
CNNM3	TGGGAGGAAGGGATCGTCAT	TGCAACAGGCAGCTACTCTC
CNNM4	ACCCGGATGGCATCATCTTC	AGATGTTGCCCAGGCTGTAG
TRPM6	GTTGGAATCCCTCCTTGGGG	TGGTACAGGCACACCACATC
TRPM7	TACAGAACAGAGCCCAACGG	AGCTCTGTAGGAATGAGAACCC
SLC1A1	GAAACCGGCGAGGAAAGGAT	GGTAATGCCTAGCACCACCG
AKT1	TCCCCCAGTTCTCCTACTCG	TCCCTCCAAGCTATCGTCCA
C-MYC	CCCTCCACTCGGAAGGACTA	GCTGGTGCATTTTCGGTTGT
TP53	TTGCTTGCAATAGGTGTGCG	GTGCAGGCCAACTTGTTCAG
OATP1A2	AAGACCAACGCAGGATCCAT	GAGTTTCACCCATTCCACGTACA
OATP1B3	AGATTGTGTAAAGGAATCTGGGTCACA	AGTGCAAAGCCAATGACTGGAC
CNT3	GGTTCTGGCTGAAGTGGGTGAT	ACATTATGAGCCCACCGAAGGACA
OATP4A1	CCCAAGGGCATCCTGTTCTT	TCCAGGGAGGTGATGACTGT
MRP3	CCAAGTTCTGGGACTCCAACCTG	ATGATGTAGCCACGACAATGGTGC
UGT1	CTTTGGGCAAAATCCCTCAGACAGT	GTCATCGGGTGACCAAGCAGAT
DHFR	GGCAGTTCTGTTTATAAGGAAGCCATGAA	TGCATCAGAGAGAACACCTGGGTA
TCEA	TCGACTCCGAGGATCACCACATTT	CACGTGGTCATGGTCCGTCT

BAX	ATGGAGCTGCAGAGGATGATTGC	GTTCTGATCAGTTCCGGCACCTT
PTEN	GGCGGAACTTGCAATCCTCAGTTT	AGGTAACGGCTGAGGGAACTCAAA
XIAP	CTGGTTGCAGATCTAGTGAATGCTCAG	GCCTTAGCTGCTCTTCAGTACTAATCTCT
CD44	GCCTGGCGCAGATCGATTTGAATA	CCTCCGTCCGAGAGATGCTGTA
SOX9	TGGGCAAGCTCTGGAGACTTCT	CGGGTGGTCCTTCTTGTGCT
TGFB1	TTGACTTCCGCAAGGACCTC	CTCCAAATGTAGGGGCAGGG
ALDH1A1	TGCTGCTGGCGACAATGGA	ACCTGCACAGTAGCGCAATGTTT
SOX2	GGCAATAGCATGGCGAGC	TTCATGTGCGCGTAACTGTC
SOX9	GAAGGACCACCCGGATTACA	GAGATGTGCGTCTGCTCCG
OCT4	AACCGAGTGAGAGGCAACC	TGGCTGATCTGCTGCAGTGT
NOTCH2	GCACCCTCACCTTGTGTCAA	CTCACAGGTGCTCCCTTCAA
AIFM2	CACTGACGTTCCTCCTGTCC	CTTGGTCAGCCGAACCATGA
NRF2	CGTGCATGATGCCCAATGTG	TGGGGTTTTCCGATGACCAG
VDAC2	GCAGTCCTGCAGTCACCTAT	TCATTATTGGTGGGTAGCGCA
VDAC3	TGGCTTTGGCATGGTCAAGA	TCAGTGTAAGCATGACCAGAAGT
ACSL4	GGAATGACAGGCCAGTGTGA	TAGCACATGAGCCAAAGGCA
LPCAT3	GGGCTCCCGGAGTTAAGATG	CTGGAAACCCGACTGCAGAA
ALOX5	ATTGCCATCCAGCTCAACCA	TGGCCAAAAGCCAGTCGTAT
ALOX12	GAGAAGGTTCGCCAGTGCT	ATGGGGTTGGCACCATTGAG
ALOX15	TGTGAAAGACGACCCAGAGC	AGAGACAGGAAACCCTCGGT
ALOXE3	CAGCTGTAACAACCTCCTCCT	TGTGAAGTGCTCATCTGGGT
POR	GGCACCCTTCATAGGCTTCA	CGTAGTACAGCAGCGTCTCC
IREB2	TGCTGCAGGTCTTTTGGCTA	TGTGTAACCATCCCACTGCC
TFRC1	TGAAGGTCTGACACGTCTGC	TGATGGTTCACTCACGGAGC
TFRC2	CCTACCCATGGACAGCAGTG	AAAGGAGAACTCGACGGCAG
FTL	AACCAACCATGAGCTCCCAG	TAGGAGGCCTGCAGGTACAA
FTH	ACTACCACCAGGACTCAGAGG	ACAGGTAAACGTAGGAGGCG
SLC40A1	GGATTTTTACTCCTTTCCGCTGC	TGCCACATCCGATCTCCCTA
HFE	CTTTGGACCCTACGCAAGGA	GGAGGACACCGTGTGTGAAG
NUPR1	GACTCAACAGATGTCGGGGG	TCTGCAGTGTGGGGCTTATG
HPRT1	GCTTTCCTTGGTCAGGCAGT	CAACACTTCGTGGGGTCCTT
ARP	CGACCTGGAAGTCCAACTAC	ATCTGCTGCATCTGCTTG
Mouse		
Cnnm1	CCTACAACAGCAGCTTCGGA	CCGTCTGCGGACTTCTTTCT

Cnnm2	CCCTGTCTCGCACCTTTGTT	GGGGCGAGGAGGTGACTTAT
Cnnm3	GGCTCCTTGGTGACAAGTCC	TCCAAGTGTGCCAAAGAGGG
Cnnm4	GCTCGCAAGATAGAGCCCAT	GTTGACTAGCACGTTCCCCA
Trpm6	AAACTTGCTTGGCCTCCACT	CCAGTCCGGATCTACCTCCA
Trpm7	CCAAGCTCCAAAGACCCTCA	GCATGCATGTTGCTTGACCA
Slc41a1	TGGGATCAACCCAGACAACG	CTGAGAGGAGTGCCAAGGTG
Hprt1	GTTGGGCTTACCTCACTGCT	TAATCACGACGCTGGGACTG
Arp	CGACCTGGAAGTCCAACTAC	ATCTGCTGCATCTGCTTG

Table M.5. Human and mouse primers sequences employed for q-PCR analysis in Study 2 (all from Merck Life Technologies)

Gene	**Sequence**	
	Forward (5'-3')	**Reverse (5'-3')**
Human		
ACE2	GTGCACAAAGGTGACAATGG	GGCTGCAGAAAGTGACATGA
NRP-1	TGTGCCAAAGATGTCAGAGA	ACCTGGTGTTTTCTGTCCAC
TMPRSS2	CTCTCCCTAACCCCTTGTCC	AGAGGTGACAGCTCCATGCT
GLUT1	GGCTTCTCCAACTGGACCTC	CCGGAAGCGATCTCATCGAA
GLUT2	TGGGACTTGTGCTGCTGAAT	GGCCTGGCCCAATTTCAAAG
HK2	TAGGGCTTGAGAGCACCTGT	CCACACCCACTGTCACTTTG
G6PD	GTCCTGCATGAGCCAGATAGG	GGTCGATGCGGTAGATCTGG
PKLR	CTGGTGATTGTGGTGACAGG	TGGGCTGGAGAACGTAGACT
PKM2	AGTACCATGCGGAGACCATC	GCGTTATCCAGCGTGATTTT
PFKL	GGAGCTTCGAGAACAACTGG	CTGTGTGTCCATGGGAGATG
LDHA	GACGTCAGCATAGCTGTTCC	GAATCGGGAATGCACGTCG
LDHB	CTTTGTCTTCTCCGCACGAC	CTTCCGCAACTGGTGCAATG
GLS1	GGAAGCCTGCAAAGTAAACCC	CCAAAGTGCAGTGCTTCATCC
GLS2	TTCTCCTTCATCCCCAACGC	AAAGCTGGCTCCAGGGTTAG
GLUL	AGGCCAGCTGTGGTTTTCTT	GCTGCTTTGGGCAGTTACAC
FTH	AGAACTACCACCAGGACTCAGA	GACAGGTAAACGTAGGAGGCG
FTL	AAGGCTCACTCTCAAGCACG	AAAGCTGCCTATTGGCTGGA
TRFC1	TGAAGGTCTGACACGTCTGC	TGATGGTTCACTCACGGAGC
TRFC2	CCTACCCATGGACAGCAGTG	AAAGGAGAACTCGACGGCAG
TNF	ATCCTGGGGGACCCAATGTA	AAAAGAAGGCACAGAGGCCA
IL-6	AGGAGACTTGCCTGGTGAAA	CAGGGGTGGTTATTGCATCT

ARP	CGACCTGGAAGTCCAACTAC	ATCTGCTGCATCTGCTTG
Mouse		
Nrp-1	CGCTACCAGAAGCCAGAGGA	CATCCACAGCAATCCCACCAA
Tmprss2	CCTGCGTTTAGGGGTGTCA	CGACCTACTCCAGTTCTCGC
Glut1	CGGGGTCTTAAGTGCGTCAG	CTCCCACAGCCAACATGAGG
Glut2	TCGGGGACAAACTTGGAAGG	GAGTGTGGTTGGAGCGATCT
Hk2	TAGCTCCTAGCCCCTTCTCC	TCAACCAAAACCAAGTGCAG
G6pd	CCCAGCCCTTCCCCTATGTA	GGGCTCAGTGCTTGTGAGTA
Pklr	CATATATGTGGGGGCCAAG	GACACACAGGTTGGTGATGC
Pkm2	CGCAGCTGTGATAACCTTGA	TGTGTTCCAGGAAGGTGTCA
Pfkl	GAGGGATGTGGGGGTCTAC	GCAATGTGGGTCTGACTGGA
Ldha	CAAGGAGCAGTGGAAGGAGG	CCAAGTCTGCCACAGAGAGG
Ldhb	TGGTGGACAGTGCCTATGAA	CCTCATCGTCCTTCAGCTTC
Gls1	ACAGGGGTGTCAGAACCAAG	TGTGAATGAGCCGCTAACTG
Gls2	CTCGCACGTCTGGAGCG	GTTCTGCAGAGCCCTCATGG
Glul	GCGGAGAATGGGAGTAGAGC	GGATGGGTGAACAGGTCAGG
Fth	GGAGCATGCCGAGAAACTGA	TCTCCCAGTCATCACGGTCT
Ftl	TTGCCCGGGACTTAGAGCA	TGGAGAGACTTGTAAAGGCGG
Trfc1	GCACCACTCGCCCAAGTTAT	TGGAATCCCATTATGCACGGT
Trfc2	CTCTCCCCGCTTAGGCAAAC	GAATGTCCTGAGTCAGAGCGG
Tnf	AGCCCACGTCGTAGCAAACCAC	ATCGGCTGGCACCACTAGTTGGT
Il-6	TTCTCATTTCCACGATTTCCCAG	ACCACGGCCTTCCCTACTTCAC
Arp	CGACCTGGAAGTCCAACTAC	ATCTGCTGCATCTGCTTG

M.6. Determination of protein expression by Western Blotting

M.6.1. Protein extraction and quantification

Cell lysis was performed by incubating approximately 2-3 x 10^6 cells in 80µL of cold radio-immunoprecipitation assay (RIPA) lysis buffer. For liver tissue, approximately 50mg was lysed with 1mL of RIPA lysis buffer using the Precellys-24 apparatus (Bertin Technologies). The composition of the RIPA buffer contains 100mM NaCl, 1.6mM Na2HPO4, 8.4mM NaH2PO4, 0.5% (w/v) sodium deoxycholate, 0.1% (w/v) SDS and 0.005% (w/v) sodium azide, 1µM sodium orthovanadate, 50mM sodium fluoride, Triton X-100 0.1% (v/v) and distilled H_2O supplemented with a protease and phosphatase inhibitor cocktail (Roche). Following lysis, homogenates were centrifuged at

14,000 rpm for 20 minutes at 4ºC, and the resulting supernatant was collected. The total protein content in the supernatant was quantified using either the Bradford protein assay (Pierce, Cat#: 23200) or the BCA protein assay (Pierce, Cat#: 23225), depending on the type of lysis buffer used. Protein concentration was determined using a Spectramax M3 spectrophotometer.

M.6.2. Western Blotting

To assess changes in protein expression, an appropriate amount of protein (ranging from 10 to 50µg) was extracted from whole-cell lysates or S1 and RBD-immunoprecipitation (IP) cell lysates, depending on the protein of interest. The protein samples were denatured by adding SDS-PAGE sample buffer (250mM Tris-HCl pH 6.8, 500mM β-mercaptoethanol, 50% (v/v) glycerol, 10% (v/v) SDS, bromophenol blue) and heating at 95ºC for 5 minutes. Subsequently, the denatured proteins were separated by sodium dodecyl sulfate-polyacrylamide gel electrophoresis (SDS-PAGE) using 7% to 15% acrylamide gels in a Mini-PROTEAN Electrophoresis System (Bio Rad). The separated proteins were then transferred onto nitrocellulose or PVDF blotting membranes (GE Healthcare Life Science). Blotting membranes were blocked with 5% non-fat milk in TBS pH 8 containing 0.1% Tween-20 (TBST-0.1% [v/v]) for 60 minutes at room temperature, followed by three washes with TBST-0.1% (v/v) for 10 minutes each. Membranes were then incubated overnight at 4ºC with commercially available primary antibodies (dilution: 1:1000). Details of the primary antibodies and their optimal incubation conditions are provided in **Table M.6 and M.7**. After incubation with primary antibodies, membranes were washed again three times for 10 minutes with TBST-0.1% (v/v) and then incubated for 1 hour at room temperature with a secondary antibody conjugated with horseradish-peroxidase (HRP) in blocking solution. Immunoreactive proteins were detected using Western Lightning Enhanced Chemiluminescence reagent (ECL, PerkinElmer, USA) and exposed to an iBright CL 1500 Imaging System (Invitrogen, Cat#: A44240CFR).

Table M.6. Antibodies used for WB assays in Study 1.

Antibody	Company	Reference	Secondary antibody
CNNM4	Abcam	ab191207	Rabbit
NUPR-1	Proteintech	15056-1-AP	Rabbit
GPX4	Cell Signaling	52455	Rabbit
ALOX5	Santa Cruz Biotechnology	sc-136195	Mouse
4-HNE	Abcam	ab46545	Rabbit
β-actin	Sigma Aldrich	A5441	Mouse

Table M.7. Antibodies used for WB and IP assays in Study 2.

Antibody	Company	Reference	Secondary antibody
ACE2	Bioss Inc	BS-1004R	Rabbit
NRP-1	Bio-Techne Corporation	NBP2-67539	Rabbit
TMPRSS2	Bio-Techne Corporation	NBP3-00492	Rabbit
Phospho-AMPKα (Thr172)	Cell Signaling	2531	Rabbit
β-actin	Sigma Aldrich	A5441	Mouse

M.7. Immunoprecipitation

Cells were resuspended in RIPA lysis buffer, sonicated and centrifuged at 14,000 rpm for 30 minutes at 4°C. The pellet was discarded. Of total supernatant, 50µL were kept for use as the control in the western blot assay. After quantification, 1,180µg of protein were incubated with 2µg of biotinylated S1 (Acrobiosystems Cat#: S1N-C82E8) or RBD (Acrobiosystems Cat#: SPD-C82E9) recombinant proteins for 2 hours at 4ºC with constant inversion. Then, 50µL of prewashed High Capacity Neutravidin beads (Thermo Fisher Cat#: 11805845) were added to the mix and incubated for additional 30 minutes at 4ºC with constant inversion. After centrifugation of beads, supernatants were kept as flow through inputs for the western blot. Proteins bound to the beads were washed with RIPA buffer for 5 minutes at room temperature with constant inversion and eluted in 20µL of 4X Laemmli buffer. Outputs from the pulldown assay were boiled for 10 minutes at 95ºC prior to western blot assay (**Figure M.2**).

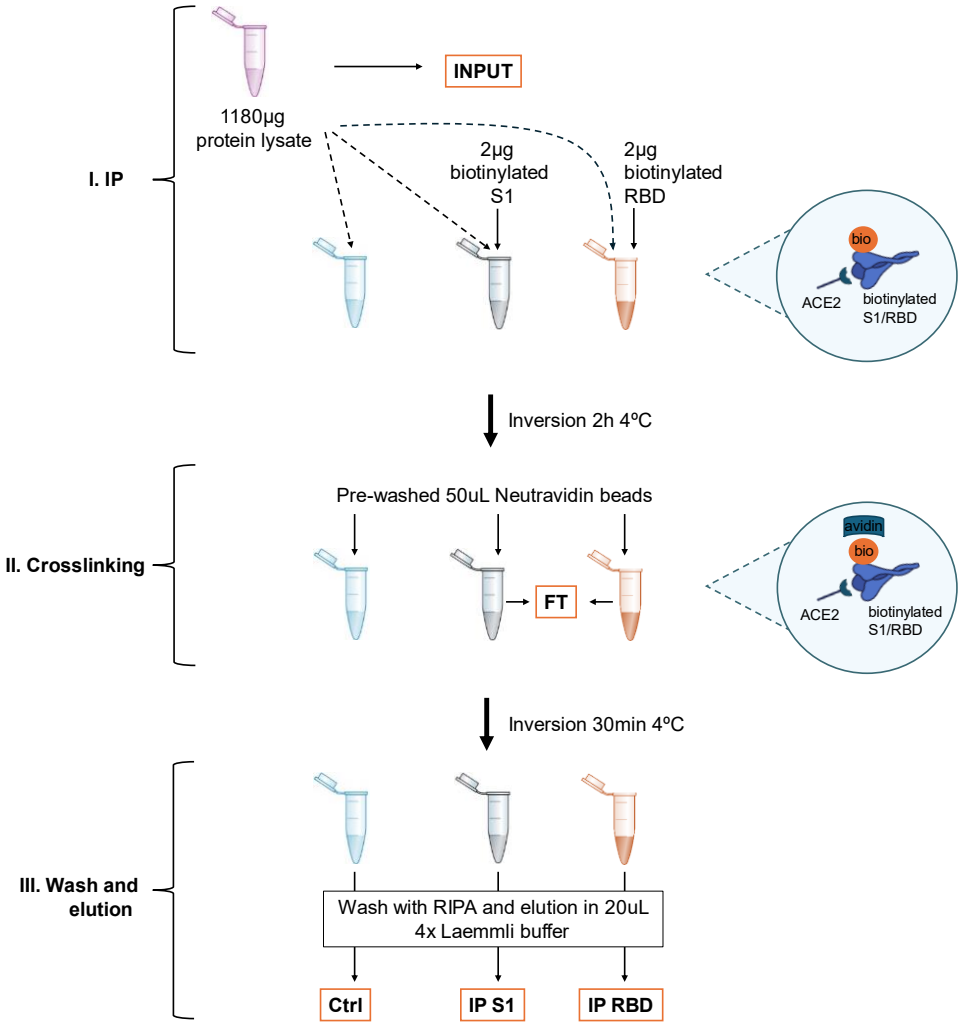

Figure M.2. Immunoprecipitation protocol scheme. Schematic protocol showing the precipitation of S1 and RBD-conjugated proteins. I) Incubation of protein extracts with the crosslinked biotinylated S1 or RBS proteins, II) Crosslinking pre-washed neutravidin beads to the biotinylated S1 and RBD-ACE2 complexes, III) Wash with TIPA buffer and elution in 20µL 4x Laemmli buffer. Abbreviations: RBD, receptor binding domain; FT, flow through, IP, immunoprecipitation.

M.8. Assessment of binding of recombinant RBD of the cell surface

Binding of recombinant RBD (Acrobiosystems Cat#: SPD-C82E9) to THLE-2 and Vero E6 cells, as well as to primary hepatocytes was measured as described [392]. Briefly, cells were harvested from culture plates using cell dissociation buffer (Thermo Fisher Cat#: 13151-014), counted and 100.000 cells were distributed in 96-well polystyrene conical bottom plates (Thermo Fisher Cat#: 249570). After washing cells with blocking buffer (PBS containing 0.5% (w/v) BSA; Sigma Aldrich Cat#: A9647) they were incubated with biotinylated RBD (20µg/mL) for 40 minutes on ice. After incubation, cells were washed again with blocking buffer and incubated for additional 15 minutes with streptavidin-PE (1:200, Thermo Fisher Cat#: 12-4317-87) on ice in a total volume of

100µL of blocking buffer. Finally, cells were washed twice and resuspended in blocking buffer containing DAPI (Invitrogen Cat#: D1306) to discriminate alive cells. All centrifugation steps were performed at 300G for 5 min at 4°C. Cells were acquired on a FACSymphony cytometer (BD Biosciences) and results were analyzed using FlowJo version 10 (BD Biosciences).

M.9. Mass spectrometry and proteomic analyses

M.9.1. In solution digestion

Different protein samples were analyzed; in the first study, EGI-1 and TFK-1 cells; and in the second study, hACE2-derived primary hepatocytes. Cells were treated with cell lysis buffer (7M urea, 2M thiourea, 4% (w/v) CHAPS), vortexed and spined down to remove debris. Extracted protein was digested following the SP3 protocol described by Hughes et al.[393], with minor modifications. Trypsin was added to a trypsin:protein ratio of 1:10, and the mixture was incubated 2 hours at 37ºC. Resulting peptides were dried out and resuspended in 0.1% (v/v) formic acid.

M.9.2. Mass spectrometry analysis

Samples were analyzed in a novel hybrid trapped ion mobility spectrometry-quadrupole time of flight mass spectrometer (timsTOF Pro with PASEF, Bruker Daltonics) coupled online to a EVOSEP ONE (EVOSEP). This mass spectrometer takes advantage of a novel scan mode termed parallel accumulation-serial fragmentation , which multiplies the sequencing speed without any loss in sensitivity[394]. Samples (200 ng) were directly loaded in a 15 cm analytical column (EVOSEP) and resolved at 300 nl/min with a 44 min gradient. Protein identification and quantification was carried out using PEAKS software using default settings. Searches were carried out against a database consisting of mice protein entries (Uniprot/SwissProt), with precursor and fragment tolerances of 20 ppm and 0.05 Da. Only proteins identified with at least two peptides at FDR<1% were considered for further analysis. Data was loaded onto Perseus platform[395] and further processed (log2 transformation, imputation).

M.9.3. Functional enrichment proteomic analysis

Statistical analyses between groups were performed with a student's t-test. Principal Component Analysis and heatmaps showing the differentially expressed proteins between Ctrl vs sh2 and Ctrl vs sh5 (study 1) and the 25-top upregulated and downregulated proteins (study 2) were represented using GraphPad PRISM v8. Enriched Gene Ontology were inferred using DAVID (https://david.ncifcrf.gov/home.jsp). Ingenuity Pathway Analysis (IPA) software was used to analyze upstream regulators (QIAGEN).

M.10. Histological analyses

Tissue samples were initially preserved in 4% (v/v) paraformaldehyde. Subsequently, the tissues were embedded in paraffin and sectioned at a thickness of 5µm. These sections were then deparaffinized using either xylene or a xylene substitute (Histoclear I solution, Electron Microscopy Sciences), followed by rehydration through a series of graded alcohol solutions. Upon hydration, sections were subjected to the following stainings:

M.10.1. Hematoxylin and eosin (H&E) staining

Histological analysis of tissue morphology was conducted using hematoxylin and eosin (H&E) staining on sections of mouse and human liver tissue. Slides were then incubated in Harris hematoxylin (Merck Millipore Cat#: 105175) for 5 minutes. Following this, the samples were washed with tap water and subsequently incubated in eosin (Merck Millipore Cat#: 109844) for another 5 minutes at room temperature. After a washing step with tap water, samples were dehydrated u sing a series of increasing concentration alcohol solutions (50%, 70%, and 100% (v/v) ethanol). Finally, slides were incubated in xylene for two 5 minutes intervals at room temperature and mounted with DPX (Sigma Cat#: 06522-500ML). Images were taken with an upright light microscope (Zeiss).

M.10.1.1. Tumoral score

An independent pathologist evaluated hematoxylin and eosin-stained tissue sections by scoring them according to the quantity of tumor clusters visible within each $9mm^2$ field of view. A score of 1 indicated fewer than 10 foci, a score of 2 indicated between 10 and 20 foci and a score of 3 indicated more than 20 foci, with or without isolated cells.

M.10.2. Immunohistochemistry (IHC)

IHC was conducted in formalin-fixed and paraffin-embedded sections of mouse and human liver tissue. Paraffin-embebed sections underwent antigen retrieval based on the primary antibody requirements and were then subjected to peroxide hydrogen (3% (v/v) H_2O_2 in PBS) for 10 minutes at room temperature to block endogenous peroxidases. For staining with mouse-hosted antibodies in mouse tissues, samples underwent blocking with goat anti-mouse Fab fragment (Jackson Immunoresearch Cat#: 115-007-003) at a dilution of 1:10 for 1 hour at room temperature, followed by additional blocking with 2.5% (v/v) normal goat serum (Vector Cat#: S-1000-20) for 30 minutes at room temperature. Primary antibodies (**Table M.8**) in antibody diluent with

0.02g/ml BSA were incubated in a humid chamber overnight at 4ºC. After washing the antibodies with PBS 1x , slides were incubated with Envision anti-rabbit or anti-mouse (DAKO) or ImmPRESS anti-rat (Vector Cat#: MP-7404-50) HRP-conjugated secondary antibody incubation for 30 minutes at room temperature. Vector VIP chromogen (Vector Cat#:SK-4600) or DAB (Vector Cat#: 30215 and 30216) were used for antigen visualization. Slides were counterstained with Mayer's hematoxylin, dehydrated in increasing concentrations of ethanol solutions until 100%, cleared in Histoclear I solution and mounted using DPX mounting medium. Images were taken with an upright microscope (Zeiss) and analysis was performed with ImageJ software v1.53t.

Table M.8. Antibodies used for IHC assays in Study 1.

Antibody	Dilution	Unmasking	Company	Reference
CNNM4	1:100	Citrate	Proteintech	14066-1-AP
CK19	1:800	Citrate	Abcam	ab52625
SOX9	1:100	Citrate	Abcam	ab185966
GS	1:1000	Citrate	Abcam	ab73593
EpCAM	1:100	Citrate	Abcam	ab71916
4-HNE	1:100	None	Abcam	ab46545

M.11. *In vitro* experiments

M.11.1. Intracellular magnesium measurement

CCA cells were cultured on glass coverslips in 24-well plates. They were then exposed to 2µM Mag-S-AM41 and Mg-S-TTP-AM to assess intracellular Mg^{2+} levels. This was done in a medium containing 0% (v/v) FBS MEM, and the cells were kept at 37 °C with 5% CO2 for 30 minutes. Afterward, the medium was replaced with fresh 0% (v/v) FBS MEM and incubated for an additional hour. The coverslips were subsequently rinsed in a buffer solution with a composition of 20mM Tris-HCl, 2.4mM $CaCl_2$, 10mM glucose, and a pH of 7.4. They were mounted in a controlled-temperature perfusion chamber on a microspectrofluorometer based on an Eclipse TE 300 system from Nikon, and the samples were viewed using a 40x oil-immersion fluorescence objective. To determine intracellular Mg^{2+} levels, the relative fluorescence ratio was calculated by comparing the light emitted by the Mg^{2+}-labeled probe when excited at 340nm to that of the non-labeled probe when excited at 380nm. This ratio was measured using a Delta system (Photon Technologies International).

M.11.2. Extracellular L-lactate concentration

L-lactate concentrations were determined in medium of EGI-1 and TFK-1 stable cell lines (Study 1) and in infected or control primary hepatocytes (Study 2) using a commercial kit (Sigma Aldrich Cat#: MAK064; Trinity Biotech Cat#: 735-10) following the manufacturer's recommendations.

M.11.3. Determination of mitochondrial reactive oxygen species (ROS)

Mitochondrial ROS production in CCA stable cell lines was assessed using MitoSOX Red mitochondrial superoxide indicator (Invitrogen Cat #: M36008). Cells were labelled with 2mM MitoSOX for 10 min at 37ºC in a CO_2 incubator. After that, cells were washed thrice with PBS. Five to ten random images per sample were taken using an upright fluorescent microscope (Axioimager D1). Percentage of stained areas were calculated using FIJI (ImageJ) and normalized by cell number.

M.11.4. Iron content determination

Total iron levels were determined using a commercial kit (Sigma Aldrich Cat#: MAK025) following the manufacturer's recommendations.

M.11.5. Lipid peroxidation measurement

MDA, a well-stablished lipid peroxidation biomarker, was analyzed using a commercial kit (Sigma Aldrich Cat#: MAK085) following the manufacturer's recommendations.

M.11.6. Caspase-3 activity assay

Cells were washed with PBS twice and lysed in 30µL of caspase-3 reaction buffer (250mM PIPES pH 7.4, 100mM EDTA, 2.5% (w/v) CHAPS and 125mM DTT). Total protein was extracted, and protein concentration was determined by Bradford assay. 40µg of total protein were added to a mix containing 25µM Ac-DEVD-AFC caspase-3 fluorogenic substrate (ALX-260-032, Enzo Life Sciences) in reaction buffer, to a final volume of 500µL. Each sample was measured in duplicate by adding 200µL of the reaction mixture to each well of a 96-well black flat bottom assay plate (Corning Cat#: 3915). The reaction plate was incubated at 37ºC with gentle shaking for 4 hours and fluorescence (λ_{ex}= 390nm, λ_{em}= 510nm) was measured every hour in a SpectraMax M2/M2e microplate reader (Molecular Devices). Caspase-3 activity was determined by calculating the increase in fluorescence from 0 to 4 hours after background correction and normalized against total protein.

M.11.7. Extracellular and intracellular ATP concentration

Extracellular and intracellular ATP concentrations were measured using the ATPlite luminescence assay system (PerkinElmer Cat#: 6016943), following the manufacturer's recommendations and normalizing by total protein content.

M.11.8. Assessment of extracellular angiotensin 1-7 (Ang1-7) levels

Assessment of extracellular Ang 1-7 levels was performed by enzyme-linked immunosorbent assay (ELISA) (Cloud-Clone Corp. Cat#: CES085Mi), following the manufacturer's recommendations.

M.12. Proliferation and viability assays

Proliferation differences were determined in the first study using crystal violet staining. H69, EGI-1, and TFK-1 cells underwent different treatments as described in the cell culture section. The cells were rinsed with PBS, fixed using formalin, and rinsed once more with PBS. Afterward, these cells were gently rinsed with PBS and then exposed to a 0.5% (w/v) crystal violet solution at room temperature for 20–30 minutes. Then, cells were washed thrice before being left to air-dry for macroscopic imaging. To quantitatively assess the staining, the dyed cells were dissolved in 10% (v/v) acetic acid at room temperature for 20 minutes with periodic shaking, followed by measuring absorbance at 570nm.

M.13. Handing droplet shperoids

CCA spheroids were created by seeding 3,000 human CCA cells in 20µL droplets of their respective culture media on the lid of a Petri dish (Corning). These droplets were incubated for 3 days, and images of the resulting CCA spheroids were captured using a Nikon Eclipse TS-100 light microscope.

M.14. Cancer stem cell sphere formation assay

CCA cells were seeded at a density of 500 cells per well in a special 24-well plate or 10,000 cells in a 60mm plate. They were cultured in serum-free DMEM/F12 medium supplemented with 50x B-27, 100x N2 supplement, 100x non-essential amino acids, 100x sodium pyruvate, 100x penicillin-streptomycin, 5000U/mL hepatin, 100ug/mL human EGF and 20ug/mL FGF-basic. Following a 15-day incubation, pictures of the cell spheres were taken and RNA was subsequently processed for further quantification using q-PCR.

M.15. OCR and ECAR calculation

M.15.1. *In vitro* studies

Oxygen consumption rate (OCR) and extracellular acidification rate (ECAR) was determined as previously describe using a Seahorse XFe24 Analyzer (Seahorse Biosciences)[396]. For that, 50,000 CCA cells or 20,000 primary hepatocytes were plated and incubated with pseudotyped viral particles on a XF24 cell culture microplate (Seahorse Bioscience). Real-time respiration assays were performed after 24 hours (study 1) 48 hours (study 2) using DMEM medium (Thermo Fisher Cat#: 12800017) supplemented with glutamine (1mM), glucose (10mM) and sodium pyruvate (2mM), and lacking bicarbonate. After analysis, cell density was measured by crystal violet for data normalization.

M.15.2. *In vivo* studies

M.15.2.1. Tissue preparation for ECAR determination

After sacrifice, small pieces of livers were trapped in Seahorse plates using islet capture microplates provided by the company and incubated at 37ºC in DMEM medium without bicarbonate and supplemented with 10mM glucose. At the end of experiment, ECAR values were normalized to protein tissue content.

M.15.2.2. Mitochondrial isolation for OCR calculation

First, extracted liver were diluted in 1 mL of MSHE+BSA buffer (70mM sucrose, 210mM mannitol, 5mMm HEPES, 1mM EGTA and 0.5% (w/v) fatty acid-free BSA) at 4ºC, and all subsequent steps of the preparation were performed on ice. Tissue was homogenized 2-3 strokes prior to centrifugation at 800G for 10 minutes at 4ºC. Then, intermediate supernatant is collected and centrifuged again at 8000 g for 10 minutes at 4ºC. The final pellet was resuspended in a minimal volume (15µL) of MSHE+BSA buffer. Total protein (mg/mL) was determined using the Bradford Assay reagent (Bio-Rad Cat#: 5000001). We plated 2µg of protein in 25µL per well and centrifuge the plate at 2000G for 20 minutes at 4ºC. After centrifugation, 155µL of prewarmed (37ºC) 1x MAS buffer (70mM sucrose, 220mM mannitol, 10mM Kh_2PO_4, 5mM $MgCl_2$, 2mM HEPES, 1mM EGTA and 0.2% (w/v) fatty acid-free BSA) + 2µM rotenone + 4µM ADP was added to each well. The mitochondria were briefly observed under a microscope at 20x to ensure consistent adherence to the well. The plate was then transferred to the Agilent Seahorse XFe/XF96 Analyzer, and the experiment initiated. After analysis, cell density was measured by crystal violet for data normalization.

M.16. Metabolic flux analyses

Primary mouse hepatocytes (500.000 cells) were incubated with pseudotyped viral particles expressing the full-length spike of SARS-CoV-2 (MOI: 0.8) or recombinant RBD (20ug/mL) for 48 hours. After that, labelled $^{13}C_6$-glucose was added at a 10mM final concentration for 6 hours. For metabolite extraction, 500µL of cold methanol and water (50/50% v/v) was added to the wells of the culture plates. Plates were left on dry ice for 15 minutes. Subsequently 400µL of the homogenate plus 400µL of chloroform was transferred to a new aliquot and shaken at 1400rpm for 1 hour at 4°C. Aliquots were centrifuged for 30 min at 13000 rpm at 4°C to separate the organic phase from the aqueous phase. A total of 250µL of the aqueous phase was transferred to a fresh aliquot and placed at -80 °C for 20 min. Chilled supernatants were evaporated with a SpeedVac vacuum concentrators (Thermo Fisher) for 2 hours. Resulting pellets were resuspended in 150µL of water/acetonitrile (40/60% v/v). Samples were measured with an UPLC system (Acquity, Waters Inc., Manchester, UK) coupled to a Time-of-Flight mass spectrometer (ToF MS, SYNAPT G2, Waters Inc.). A 2.1 x 100mm, 1.7µm BEH amide column (Waters Inc.), thermostated at 40°C, was used to separate the analytes before entering the MS. Mobile phase solvent A (aqueous phase) consisted of 99.5% water and 0.5% FA and solvent B (organic phase) consisted of 4.5% water, 95% MeCN and 0.5% FA. In order to obtain a good separation of the analytes the following gradient was used: from 10% A to 99.9% A in 2.6 minutes in curved gradient (#9, as defined by Waters), constant at 99.9% A for 1.6 minutes, back to 10% A in 0.3 minutes. The flow rate was 0.250 mL/min, and the injection volume was 4µL. After every 12 injections a QC sample was injected. Samples were injected in duplicate ad random. The MS was operated in negative electrospray ionization full scan mode. The cone voltage was 25V and capillary voltage was 250V. Source temperature was set to 120 °C and capillary temperature to 450 °C. The flow of the cone and desolvation gas (both nitrogen) were set to 5L/h and 600L/h, respectively. A 2ng/mL leucine-enkephalin solution in water/acetonitrile/formic acid (49.9/50/0.1% v/v/v) was infused at 10µL/min and used for a lock mass which was measured each 36 seconds for 0.5 seconds. Spectral peaks were automatically corrected for deviations in the lock mass. Extracted ion traces for relevant analytes were obtained in a 20mDa window in their expected m/z-channels. These traces were subsequently smoothed and peak areas integrated with TargetLynx software. Signals of labelled analytes were corrected for naturally occurring isotopes. The isotope corrected areas were adjusted by median fold-change adjustment. This is a robust adjustment factor for global variations in signal due to e.g. difference in tissue amounts, signal drift or evaporation. The MFC is based on the total amount of detected mass spectrometric features (unique retention time/mass pairs). The calculations and performance of

the median fold-change adjustment factors are described in the following publications[397,398] . Finally, means between duplicates of the adjusted areas were reported.

M.17. Statistics

Statistical analyses were performed using GraphPad PRISM v8 (GraphPad, San Diego, CA, USA). Bar plots show the mean and the standard deviation (SD) or standard error of the mean (SEM), as indicated on each figure legend. Shapiro-Wilk or Kolmogorov-Smirnov tests were used to assess normality. The corresponding statistical test was applied as appropriate and indicated on each figure legend. Outliers were removed using a significance level of 0.05.

Results

1. Silencing CNNM4 halts progression and metastasis in cholangiocarcinoma sensitizing cells to ferroptosis

R.1.1. CNNM4, upregulated in clinical CCA cases and experimental mice model

Our previous findings have highlighted CNNM4's critical role in the progression of various liver diseases[73,74]. To assess its involvement in CCA, we examined expression data from eight independent cohorts of patients comparing resected CCA samples (both iCCA and eCCA) with controls (either normal bile ducts or adjacent liver tissues). *CNNM4* expression exhibited a consistent increase in CCA tumor samples across all cohorts, in comparison to control samples, regardless of their anatomical subtype (**Figure R.1A and R.1B**). Conversely, the expression of *CNNM1-3* did not show consistent patterns in those databases, emphasizing CNNM4's specificity (**Figure R.S1A**). *CNNM4* exhibited higher upregulation in CCA than all the diverse tumor types documented in the TCGA database (**Figure R.S1B**).

Immunohistochemical analysis demonstrated minimal CNNM4 immunoreactivity in non-tumorous tissues but a robust expression in CCA samples. (**Figures R.1C, R.S2A and R.1D** Although CNNM4 was exclusively detected within the tumor, its presence is not restricted to epithelial cancerous cells, as it is also detected in stromal cells in tissues with both low and high CNNM4 expression (**Figure R.S2B**). In samples from iCCA and eCCA patients, CNNM4 was positively correlated with number of von Willebrand Factor (vWF)-positive microvessels and with the proliferation index calculated by immunohistochemistry for Proliferating Cell Nucelar Antigen (PCNA) (**Figure R.S2C**).

To gather further evidence of CNNM4's role in CCA, murine "sleeping beauty" models of CCA were employed[399–401]. These models involve the introduction of transposons capable of triggering mutations that lead to the development of liver-specific tumors. *Cnnm4* was also overexpressed at the transcriptional level in the AKT/NICD model, as confirmed by histological analyses in the AKT/YapS127A and AKT/Fbxw7ΔF models (**Figures R.1E and R.S2D**). Moreover, in a database that compares healthy hepatic organoids with organoids derived from CCA patients, the tumor-derived organoids exhibited higher expression of *CNNM4* (**Figure R.S2E**).

To determine whether changes in *CNNM4* expression are altered at the cellular level as well, we used two human CCA cell lines (EGI-1 and TFK-1) and the non-tumoral immortalized cholangiocyte cell line H69. Analysis revealed elevated *CNNM4* expression in the CCA cell lines compared to H69, at both mRNA and protein levels (**Figures R.1F and R.S2F**). Furthermore, intracellular Mg^{2+} levels decreased in the cytoplasm of CCA cell lines compared to control cells, and within the TFK-1 cell line's mitochondria, evidencing CNNM4's role in Mg^{2+} extrusion in CCA (**Figure R.1G**).

These findings indicate that increased CNNM4 levels are a common characteristic in CCA patients, irrespective of the anatomical subtype.

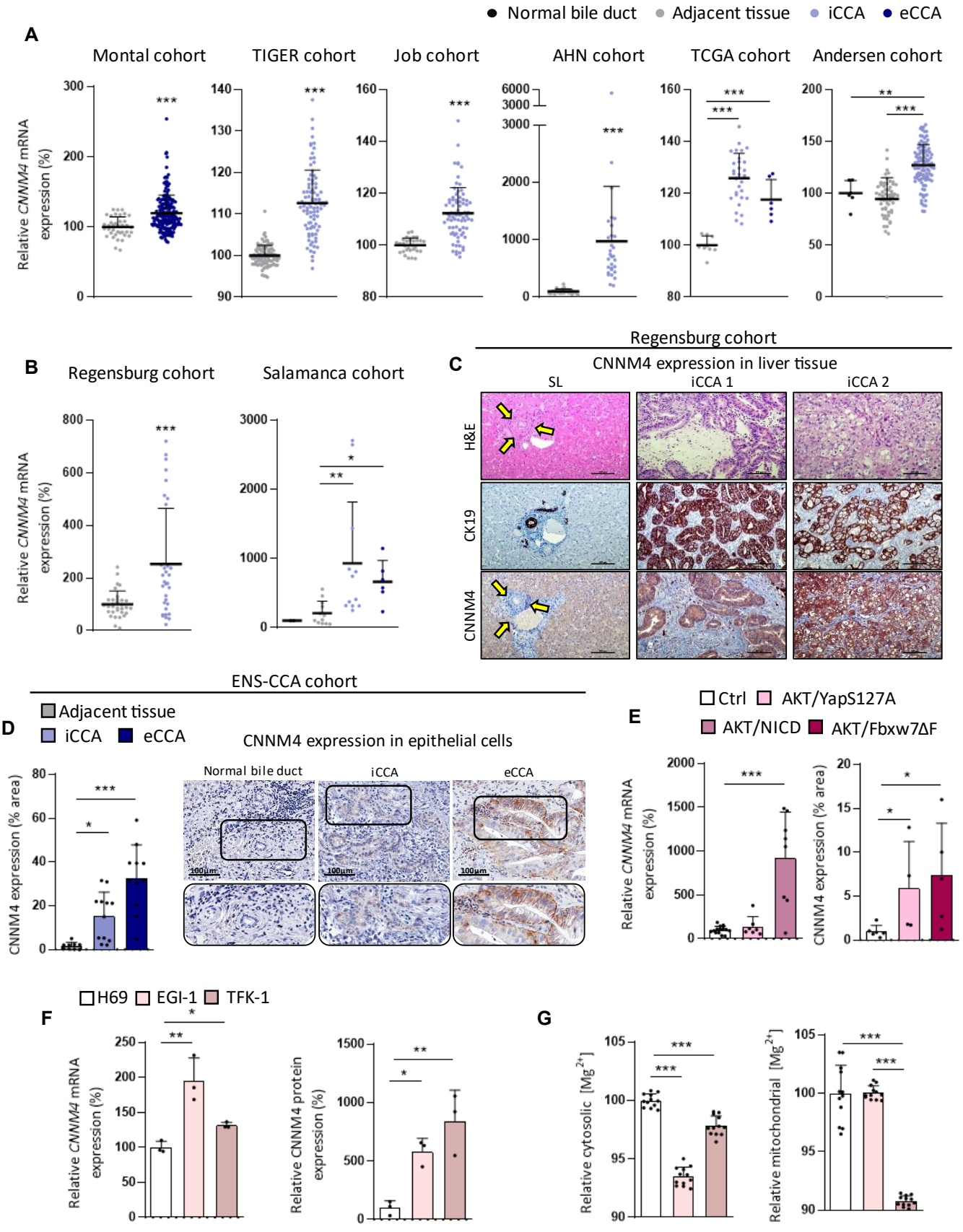
Normal bile duct
Adjacent tissue
iCCA
eCCA
A
Montal cohort
TIGER cohort
Job cohort
AHN cohort
TCGA cohort
Andersen cohort
Relative CNNM4 mRNA expression (%)
B
Regensburg cohort
Salamanca cohort
C
Regensburg cohort
CNNM4 expression in liver tissue
SL
iCCA 1
iCCA 2
H&E
CK19
CNNM4
ENS-CCA cohort
D
Adjacent tissue
iCCA
eCCA
CNNM4 expression in epithelial cells
Normal bile duct
iCCA
eCCA
CNNM4 expression (% area)
E
Ctrl
AKT/YapS127A
AKT/NICD
AKT/Fbxw7ΔF
Relative CNNM4 mRNA expression (%)
CNNM4 expression (% area)
H69
EGI-1
TFK-1
F
Relative CNNM4 mRNA expression (%)
Relative CNNM4 protein expression (%)
G
Relative cytosolic [Mg2+]
Relative mitochondrial [Mg2+]

Figure R.1. Cyclin M4 (CNNM4) overexpression in CCA patients, preclinical models and cell lines. (**A**) *CNNM4* mRNA expression in CCA relative to normal bile duct and/or adjacent normal liver from the Montal, TIGER, Job, AHN, TCGA and Andersen patient cohorts. (**B**) *CNNM4* mRNA expression in CCA relative to adjacent normal liver from the Regensburg and Salamanca CCA cohort. (**C**) CNNM4 immunoreactivity in human non-tumorous (normal biliary cells, indicated by arrows, exhibited very faint immunoreactivity for the protein) and iCCA from the Regensburg cohort. CK19 staining was performed as a marker of benign and malignant biliary cells. Magnification: 200x; scale bar: 100µm. (**D**) CNNM4 immunoreactive in human healthy bile duct, iCCA and eCCA from the ENS-CCA cohort. Magnification: 400x; scale bar: 100µm. (**E**) Transcriptional (*left*) and immunohistochemical (*right*) CNNM4 expression in transposon-based mice models of CCA. (**F**) Transcriptional (*left*) and immunohistochemical (*right*) CNNM4 expression in CCA cell lines compared to a healthy human cholangiocyte cell line (H69). (**G**) Intracellular magnesium determination by cytosolic-specific labeling (*left*) and mitochondrial-specific labeling (*right*) in normal human cholangiocite (H69) and CCA cell lines (EGI-1 and TFK-1). One-way ANOVA, Kruskal-Wallis, Wilcoxon, Mann-Whitney and paired/unpaired Student's t-test were used depending on the normality of the samples. Error bars represent SD and asterisks indicate *p*-values (*<0.05, **<0.01 and ***<0.001). Abbreviations: iCCA: intrahepatic cholangiocarcinoma; eCCA: extrahepatic cholangiocarcinoma; TIGER: The Thailand Initiative in Genomics and Expression Research; TCGA: The Cancer Genome Atlas; SL: surrounding tissue; H&E: hematoxylin and eosin; CK19: cytokeratin 19.

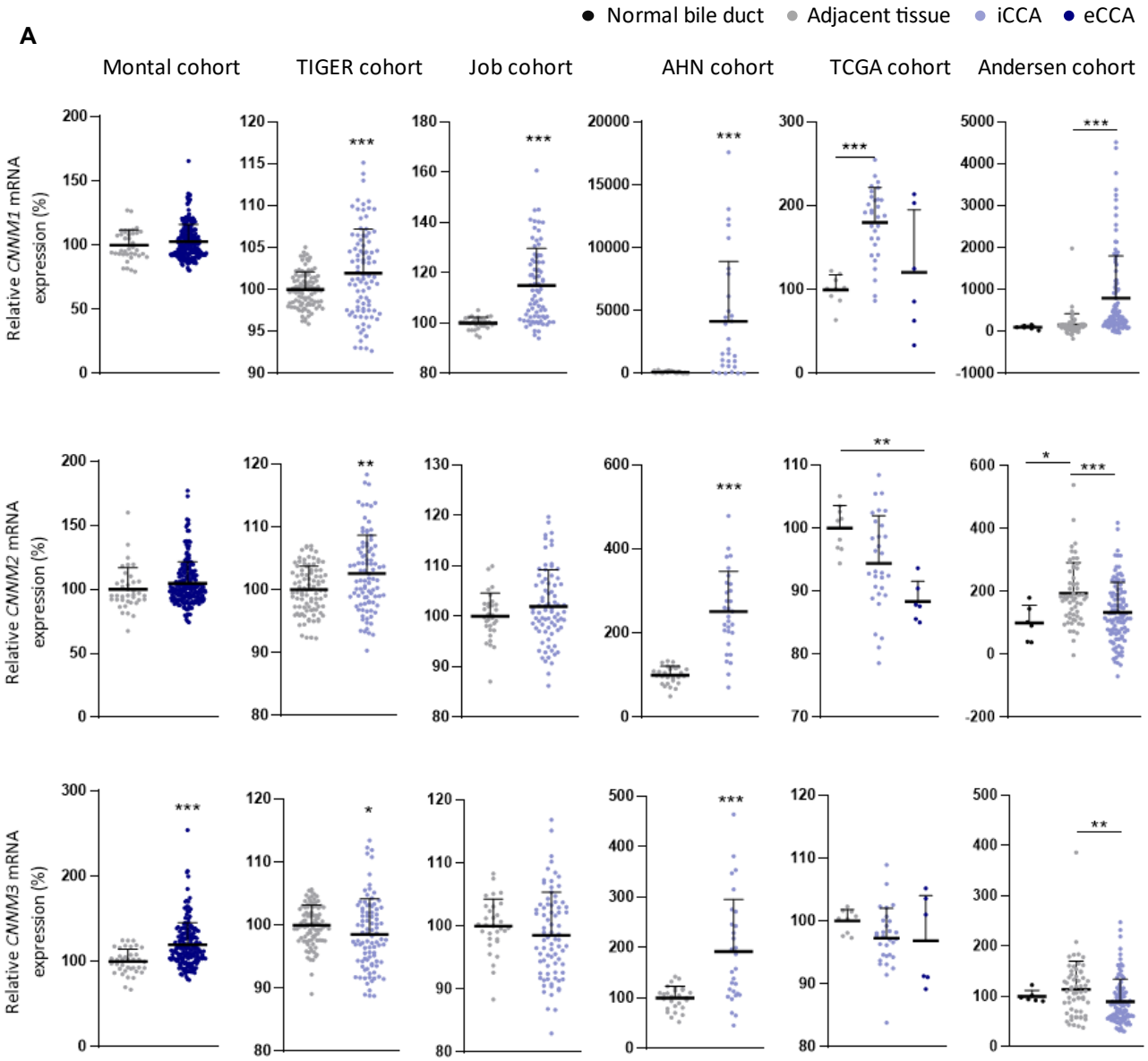

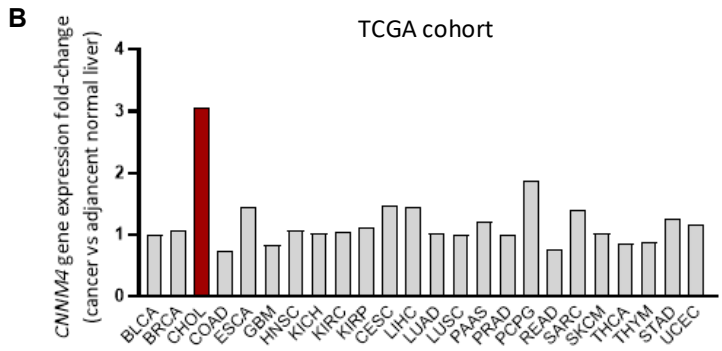

Supplementary Figure R.1. Cholangiocarcinoma exhibits the highest expression of cyclin M4 (CNNM4), which correlates with tumor weight in human samples. (**A**) *CNNM1*, *CNNM2* and *CNNM3* mRNA expression in CCA relative to normal bile duct and/or adjacent normal liver from the Montal, TIGER, Job, AHN, TCGA and Andersen patient cohorts. (**B**) Relative gene expression of *CNNM4* in the CCA TCGA database across various cancer types. Various statistical tests, including one-way ANOVA, Kruskal-Wallis, Mann-Whitney and paired/unpaired Student's t-test were employed based on the normality of the data. Error bars represent SD and asterisks indicate *p*-values (*<0.05, **<0.01 and ***<0.001). Abbreviations: iCCA: intrahepatic cholangiocarcinoma; eCCA: extrahepatic cholangiocarcinoma; TIGER: The Thailand Initiative in Genomics and Expression Research; TCGA: The Cancer Genome Atlas; BLCA: Bladder Urothelial Carcinoma; BRCA: Breast invasive carcinoma; CHOL: Cholangiocarcinoma; COAD: Colon adenocarcinoma; ESCA: Esophageal carcinoma; GBM: Glioblastoma multiforme; HNSC: Head and Neck squamous cell carcinoma; KICH: Kidney Chromophobe; KIRC: Kidney renal clear cell carcinoma; KIRP: Kidney renal papillary cell carcinoma; CESC: Cervical squamous cell carcinoma and endocervical adenocarcinoma; LIHC: Liver hepatocellular carcinoma; LUAD: Lung adenocarcinoma; LUSC: Lung squamous cell carcinoma; PAAD: Pancreatic adenocarcinoma; PRAD: Prostate adenocarcinoma; PCPG: Pheochromocytoma and Paraganglioma; READ: Rectum adenocarcinoma; SARC: Sarcoma; SKCM: Skin Cutaneous Melanoma; THCA: Thyroid carcinoma; THYM: Thymoma; STAD: Stomach adenocarcinoma; UCEC: Uterine Corpus Endometrial Carcinoma.

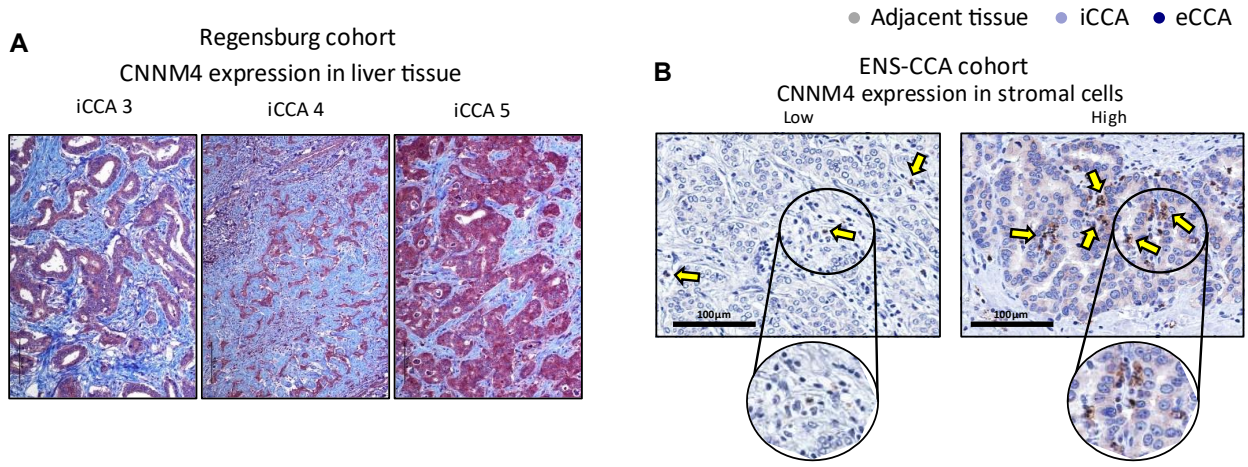

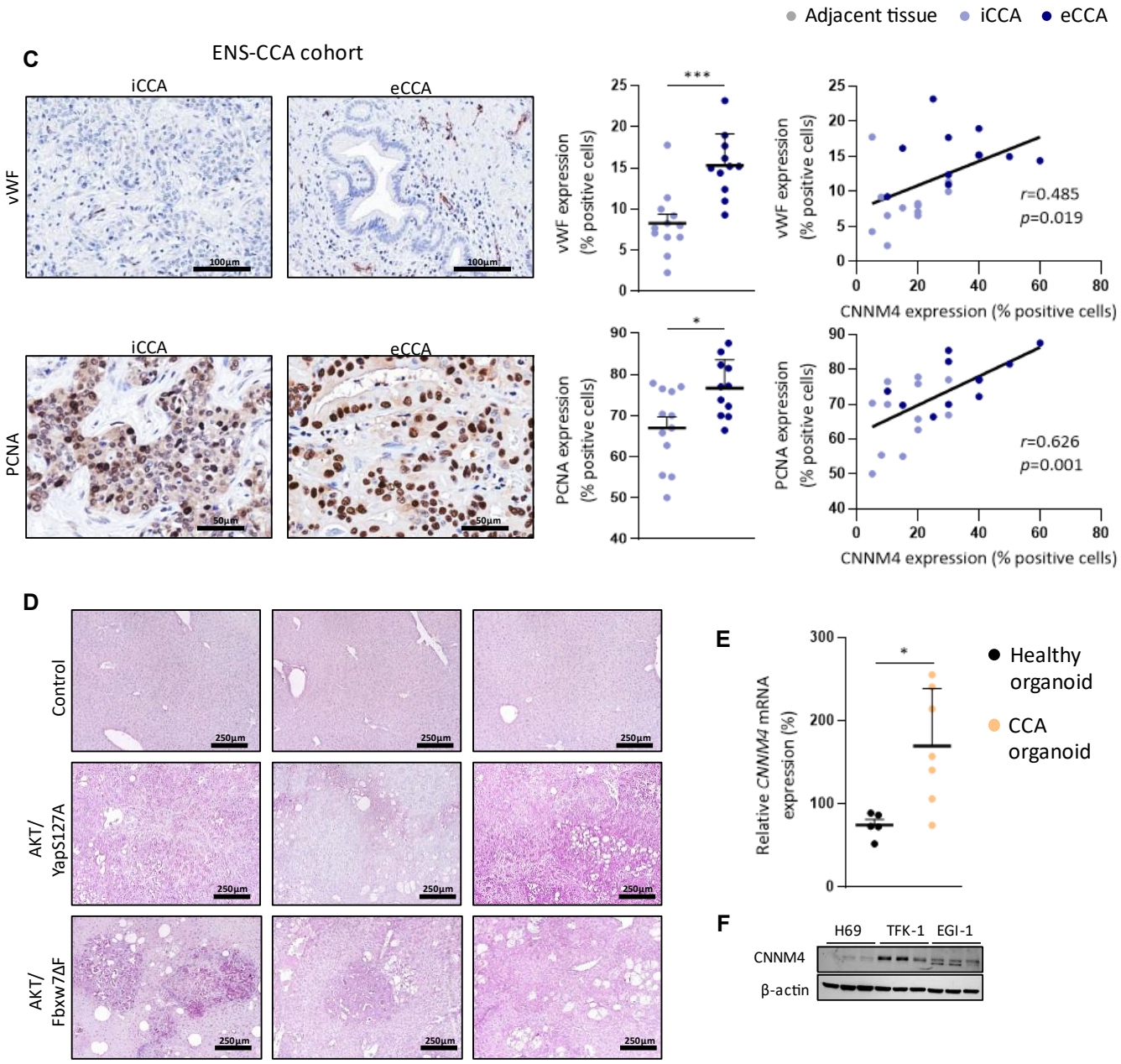

Supplementary Figure R.2. Correlation of CNNM4 with pro-angiogenic and pro-tumoral markers. Expression of CNNM4 in human iCCA samples from the Regensburg cohort and (**A**) in various inflammatory tissues from the ENS-CCA cohort (**B**). (**C**) Immunoreactivity of vWF and PCNA in iCCA and eCCA tissues and its correlation with CNNM4 levels. (**D**) Representative photomicrographs from the CNNM4 immunohistochemistry performed in transposon-based mice models. (**E**) mRNA expresión of CNNM4 in eCCA and healthy organoids. (**F**) Western blot showing the protein expression of CNNM4 in H69, TFK-1 and EGI-1 cells. Mann-Whitney and unpaired Student's t-test and Pearson correlation were employed based on the normality of the data. Error bars represent SD and asterisks indicate *p*-values (*<0.05 and ***<0.001). Abbreviations: iCCA: intrahepatic cholangiocarcinoma; eCCA: extrahepatic cholangiocarcinoma; vWF: von Willebrand Factor; PCNA: Proliferating Cell Nucelar Antigen.

R.1.2. Silencing of CNNM4 results in a less aggressive tumoral phenotype in CCA cell lines

Given CNNM4's potential role in cholangiocarcinogenesis, we investigated its impact on human CCA cell lines by silencing *CNNM4* using five different shRNAs and a control shRNA. Notably, shRNA2 (sh2) and shRNA5 (sh5) exhibited more potent silencing effects (data not shown), so they were those used in upcoming experiments (**Figures R.2A and R.S3A** Noteworthy, a decrease in *CNNM4* mRNA expression was observed, mirroring the protein changes, while the expression of the other Mg^{2+} transporters remained unaltered (**Figure R.S3B**). Further, using selective probes, we detected that the cytoplasmic and mitochondrial Mg^{2+} levels were increased in stable cell lines in which CNNM4 was silenced (**Figure R.2B-C**).

The silencing of CNNM4 expression reduced cell proliferation in all CCA cell lines, as indicated by crystal violet staining assay (**Figure R.2D and R.S3C**). Conversely, siRNA-mediated CNNM4 silencing did not affect the growth rate of the non-tumoral cholangiocyte cell line H69 and the healthy human hepatocyte cell line THLE-2 (**Figures R.S3D and R.S3E**).

To assess the role of Mg^{2+} in this phenomenon, we increased its concentration from the baseline of 1mM to 5mM in both cell lines. Such supplementation did not alter cell proliferation, emphasizing the distinctive impact of CNNM4 (**Figure R.S3F**). As previously described in liver pathologies, overexpression of CNNM4 cancels the effect of Mg^{2+} supplementation due to its role as an extrusor[74].

Exposure of EGI-1 and TFK-1 cells to common CCA chemotherapeutic agents (cisplatin, doxorubicin, gemcitabine and 5-fluorouracil) reveals increased sensitivity when *CNNM4* was silenced (**Figures R.2E**). This altered sensitivity was reflected in changes in expression of genes associated with mechanisms of chemoresistance (MOC), indicating an involvement of CNNM4 in chemoresistant phenotype of CCA (**Figure R.S4A**).

To evaluate energetic metabolism dependency, 2-deoxy-D-glucose (2-DG), a non-metabolizable glucose analog and competitive inhibitor of glycolysis, was administrated which resulted in a reduced proliferation in cells with baseline CNNM4 levels, indicating a greater reliance on glycolysis compared to cells with *CNNM4* silencing (**Figure R.2F**). In addition, CCA cells with silenced *CNNM4* exhibited decreased levels of extracellular lactate (**Figure R.2G**). This finding was confirmed by measuring basal glycolysis and the change in OCR relative to ECAR in stable TFK-1 cells (**Figures R.2H and R.2I**).

In the three-dimensional (3D) CCA cell culture model (hanging drop spheroids), CNNM4 silencing impaired the formation of these structures in both EGI-1 and TFK-1 cells at 72h (**Figure R.2J**). In a different 3D spheroid model, where cancer stem cells (CSCs) or cells with stem cell-related characteristics are enriched, *CNNM4*-silenced cells produced fewer spheres than control cells after 14 days (**Figures R.2K, R.S4D and R.S4C**). In line with this, spheroids derived from *CNNM4*-silenced CCA cells showed reduced expression of CSC markers (**Figure R.S4D**).

In summary, inhibiting CNNM4 in CCA cell culture decreases cell index and results in a less dependent on glycolysis with fewer CSCs and sensitizes these cells to chemotherapy agents.

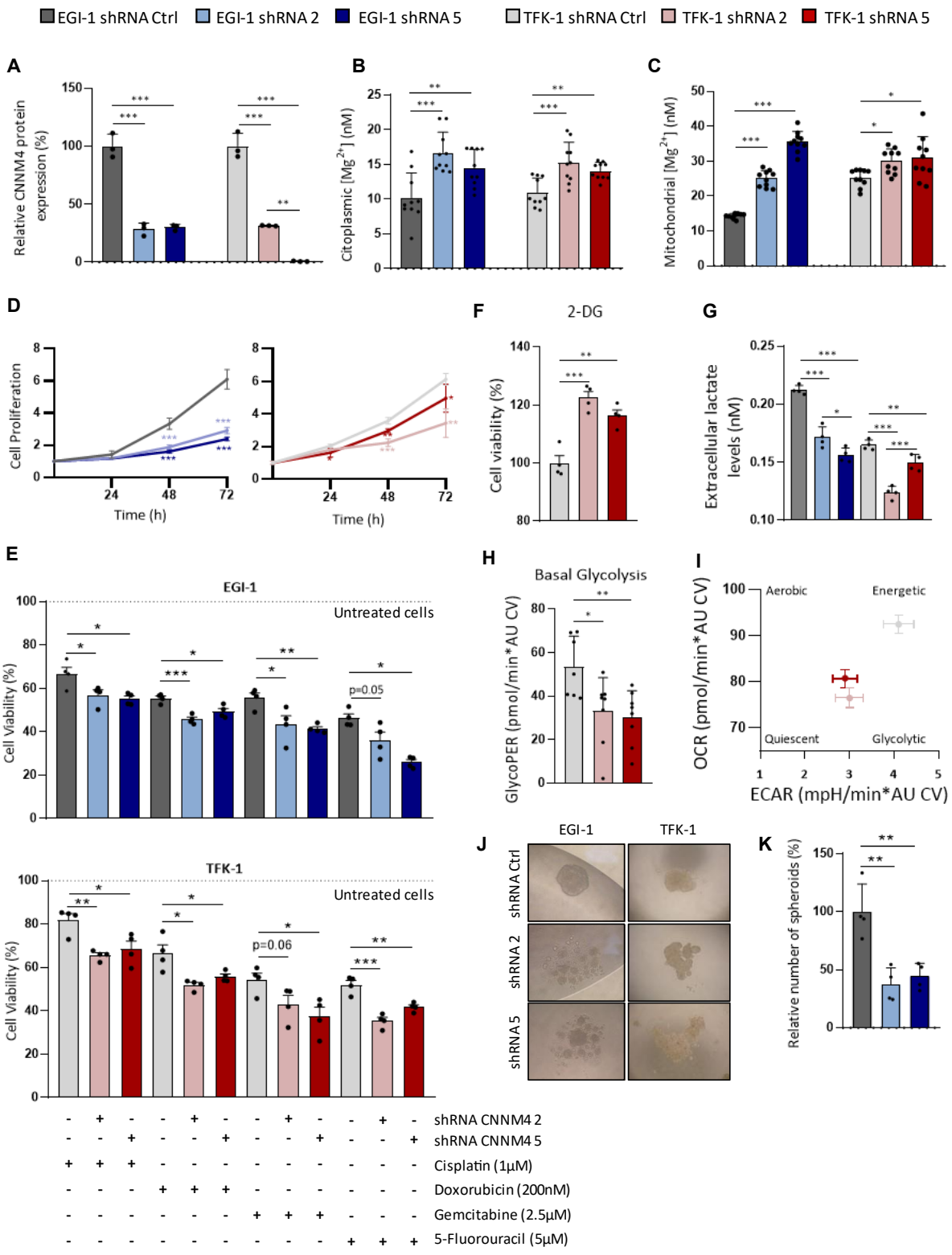

Figure R.2. Silencing of CNNM4 reduces proliferation, chemoresistance, glycolysis and spheroid formation in CCA cell lines. (**A**) Relative CNNM4 protein expression in *CNNM4*-silenced EGI-1 and TFK-1 cell lines (n=3). Intracellular magnesium determination using cytosolic (**B**) and mitochondrial (**C**) labeling in stable *CNNM4*-silenced cells compared to control cells (n=10). (**D**) Proliferation

assessed by crystal violet staining. (**E**) Cell viability in cisplatin, doxorubicin, gemcitabine and 5-fluorouracil-treated EGI-1 and TFK-1 cells with baseline or silenced CNNM4 levels (n=4) evaluated by crystal violet assay. (**F**) Cell viability of CNNM-4 silenced or control TFK-1 cells after administration with 2-deoxy- D-glucose (n=4) evaluated by crystal violet assay. (**G**) Extracellular lactate concentration of CCA cell lines with silencing of CNNM4 or with CNNM4 baseline levels (n=4). Results from seahorse technique showing basal glycolysis (**H**, n=8) and OCR/ECAR in TFK-1 cells (**I**, n=8). Hanging drop spheroid formation at 48h (**J**) and CSC-enriched spheroid formation after 14 days (**K**) in CCA cell lines which baseline or silenced CNNM4 levels (n=4). Statistical significance assessed using one-way ANOVA and Student's t-test. Error bars represent SD and asterisks indicate *p*-values (*<0.05, **<0.01 and ***<0.001). Abbreviations: 2-DG: 2-deoxy-D-glucose; AU CV: arbitrary units from crystal violet quantification; OCR: oxygen consumption rate; ECAR: extracellular acidification rate.

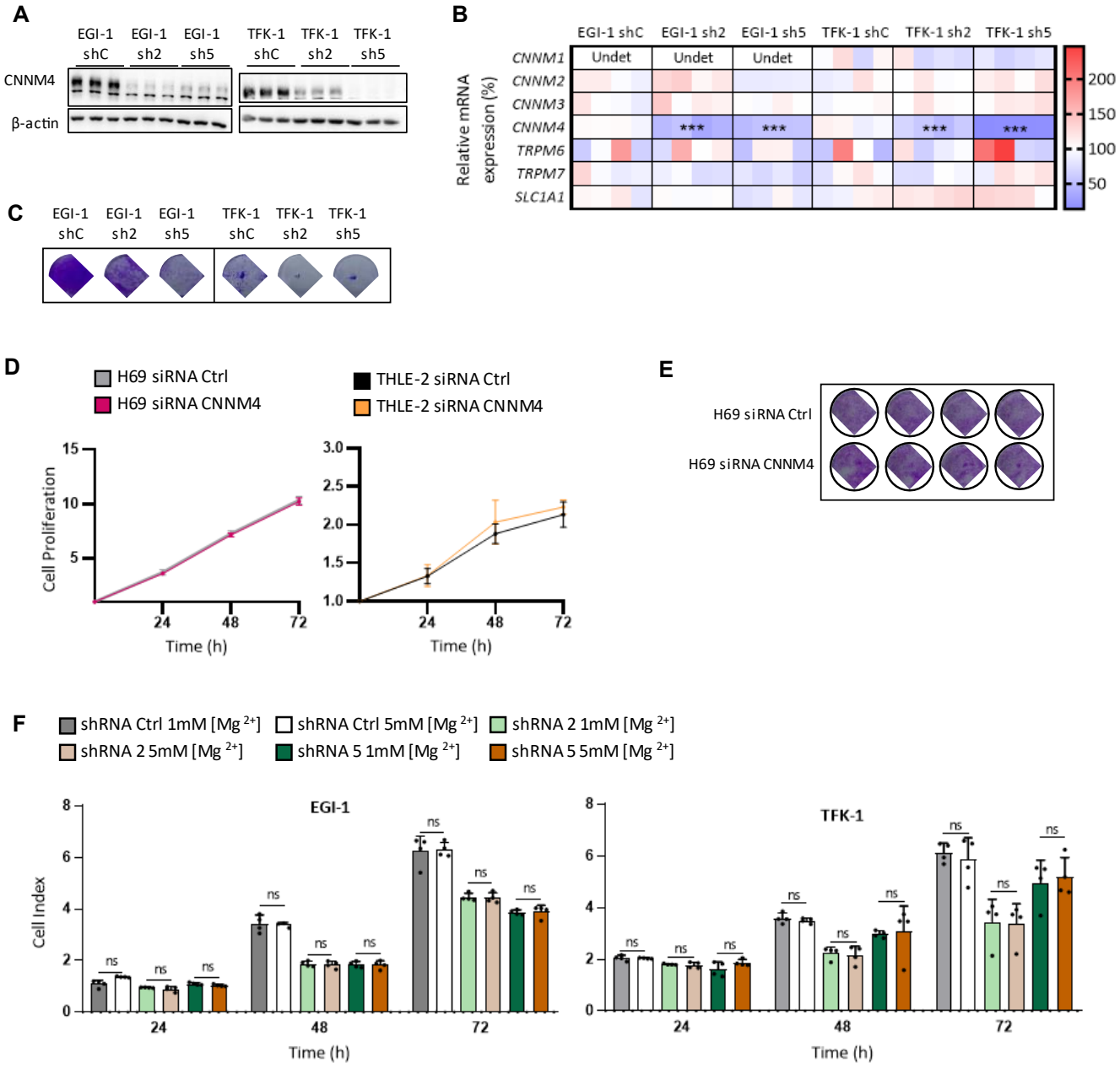

Supplementary Figure R.3. *CNNM4* silencing does not affect healthy hepatocyte and cholangiocyte cells and its overexpression induces pro-oncogenes. (**A**) Western blot showing the protein expression of CNNM4 in CCA stable cell lines with

CNNM4 suppression. (**B**) mRNA expression of magnesium transporters (*CNNM1*, *CNNM2*, *CNNM3*, *TRPM6*, *TRPM7* and *SLC41A1*) in stable cell lines with silencing of CNNM4 (n=4). (**C**) Well scan of fixed CNNM4-silenced EGI-1 and TFK-1 cells stained with crystal violet at 72h. (**D**) Proliferation in healthy cholangiocytes (H69) and hepatocytes (THLE-2) when transfected with siRNA Ctrl or siRNA CNNM4. (**E**) Well scan of fixed control and CNNM4-silenced H69 cells and stained with crystal violet at 72h (n=4). (**F**) Cell viability of EGI-1 and TFK-1 cell lines after supplementing cells with 5mM of magnesium at 24h, 48h and 72h assessed by crystal violet staining (n=4). Statistical significance was assessed using one-way ANOVA and Student's t-test. Error bars represent SD and asterisks indicate *p*-values (*<0.05, **<0.01 and ***<0.001). Abbreviations: Ctrl: control.

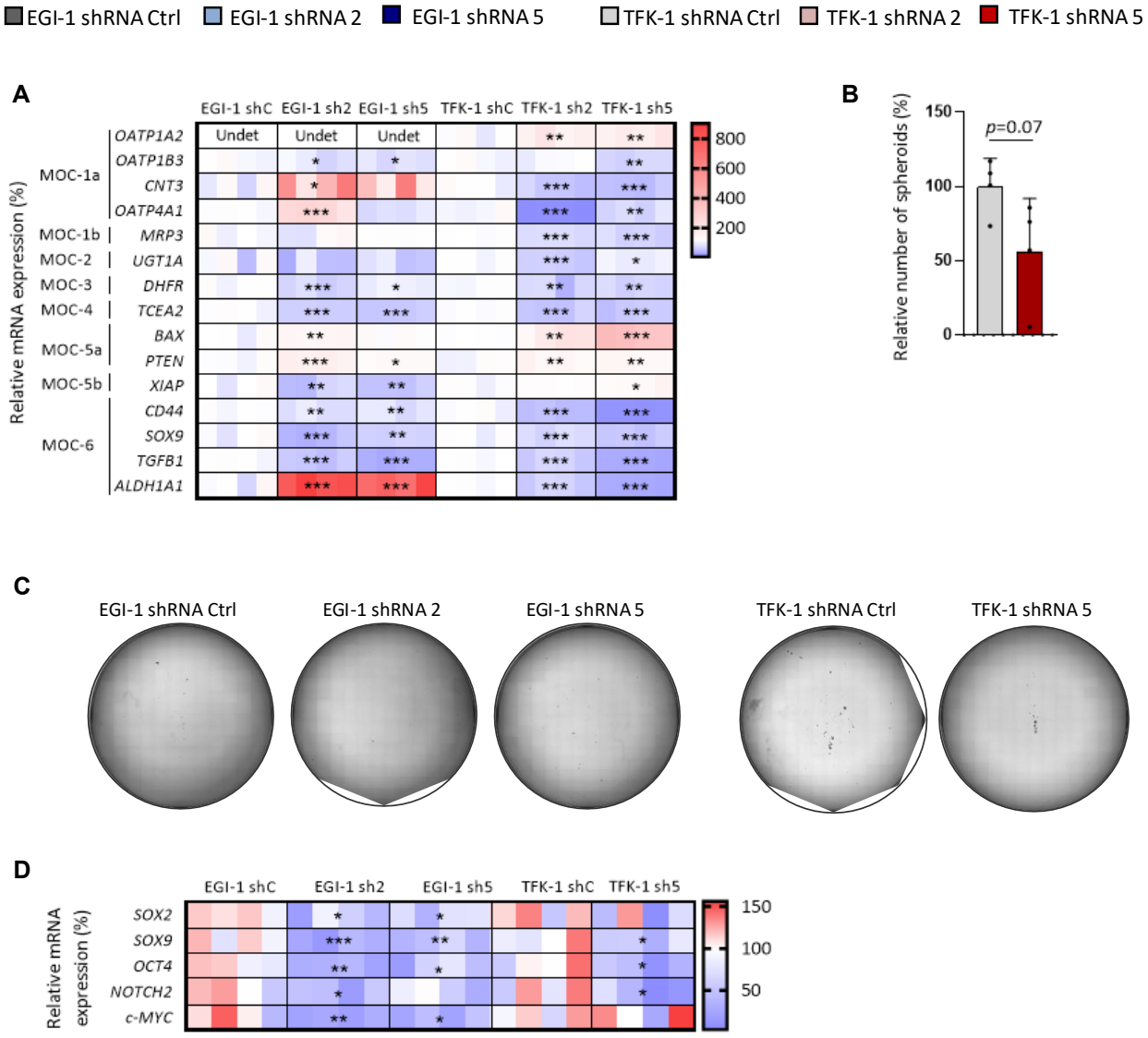

Supplementary Figure R.4. CNNM4 regulates fundamental components of chemoresistance, energy metabolism and cancer stem like phenotype. (**A**) mRNA expression of main indicators of MOC in cells with silencing of CNNM4 compared to control cells (n=4). (**B**) CSC-enriched spheroid formation after 14 days in TFK-1 cell lines which baseline or silenced CNNM4 levels (n=4). (**C**) Representative well scan of CSC-enriched spheroid after 14 days of silenced CNNM4 or control EGI-1 and TFK-1 cells. (**D**) mRNA expression of CSC markers in CSC-enriched spheroids formed after 14 days (n=4). Statistical significance was assessed using one-way ANOVA and Student's t-test. In heatmaps, statistical differences were determined against the controls. Error bars represent SD and asterisks indicate *p*-values (*<0.05, **<0.01 and ***<0.001). Abbreviations: MOC: mechanism of chemoresistance; CSC: cancer stem cell.

R.1.3. CNNM4 knock-down reduces tumour growth, invasion, and metastatic potential of cholangiocarcinoma cells in the CAM assay

CCA is usually diagnosed in advanced stages, with presence of distant metastasis, implying a very poor prognosis. Common sites of metastasis include lymph nodes, peritoneum, and liver, with occasional occurrences in the lungs and bones[402]. Within the TGCA database, we observed a positive correlation between *CNNM4* levels and vascular invasion (**Figure R.3A**). Additionally, the Regensburg cohort showed an almost significant association between *CNNM4* mRNA expression and lung metastasis, with no observed variation in node metastasis (**Figure R.3B**).

To explore the link between CNNM4 and the metastatic process, we employed a well-established model: the *ex ovo* and *in ovo* CAM. Silencing of *CNNM4* dramatically suppressed tumor growth compared to the control group (**Figure R.S5A**). Only cells transfected with control shRNA exhibited profound migration to adjacent CAM (**Figure R.S5B**).

We then focused on exploring CNNM4's role in crucial metastatic stages including intravasation, circulatory migration, extravasation and organ invasion. Tumor growth was assessed through weight and volume measurements and total EGI-1 cell counts in the distal CAM and lungs of the embryos. Cells with silenced *CNNM4* displayed a significant two-fold reduction in the weight and volume of primary tumors compared to the control (**Figure R.3C**). Histopathological examination of excised tumors revealed substantial invasion of cells transfected with shRNA Ctrl into the underlying CAM tissue, a phenomenon not observed in the absence of CNNM4 (**Figure R.3D**).

In the *in ovo* experimental settings, silencing *CNNM4* led to a notable reduction in tumor growth (**Figure R.3E**). Furthermore, analysis of cells migrating into the distal CAM showed a marked decrease in intravasation in the absence of *CNNM4* (**Figure R.3F**). Additionally, examination of extravasation and invasion into the lungs revealed a significant inhibitory effect on these processes due to shRNA-mediated silencing of *CNNM4*. This effect was supported by q-PCR quantification of EGI-1 cells in excised lung tissues (**Figure R.3G**).

According to these data, CNNM4 emerges as a metastasis inducer and a crucial driver of cholangiocarcinogenesis.

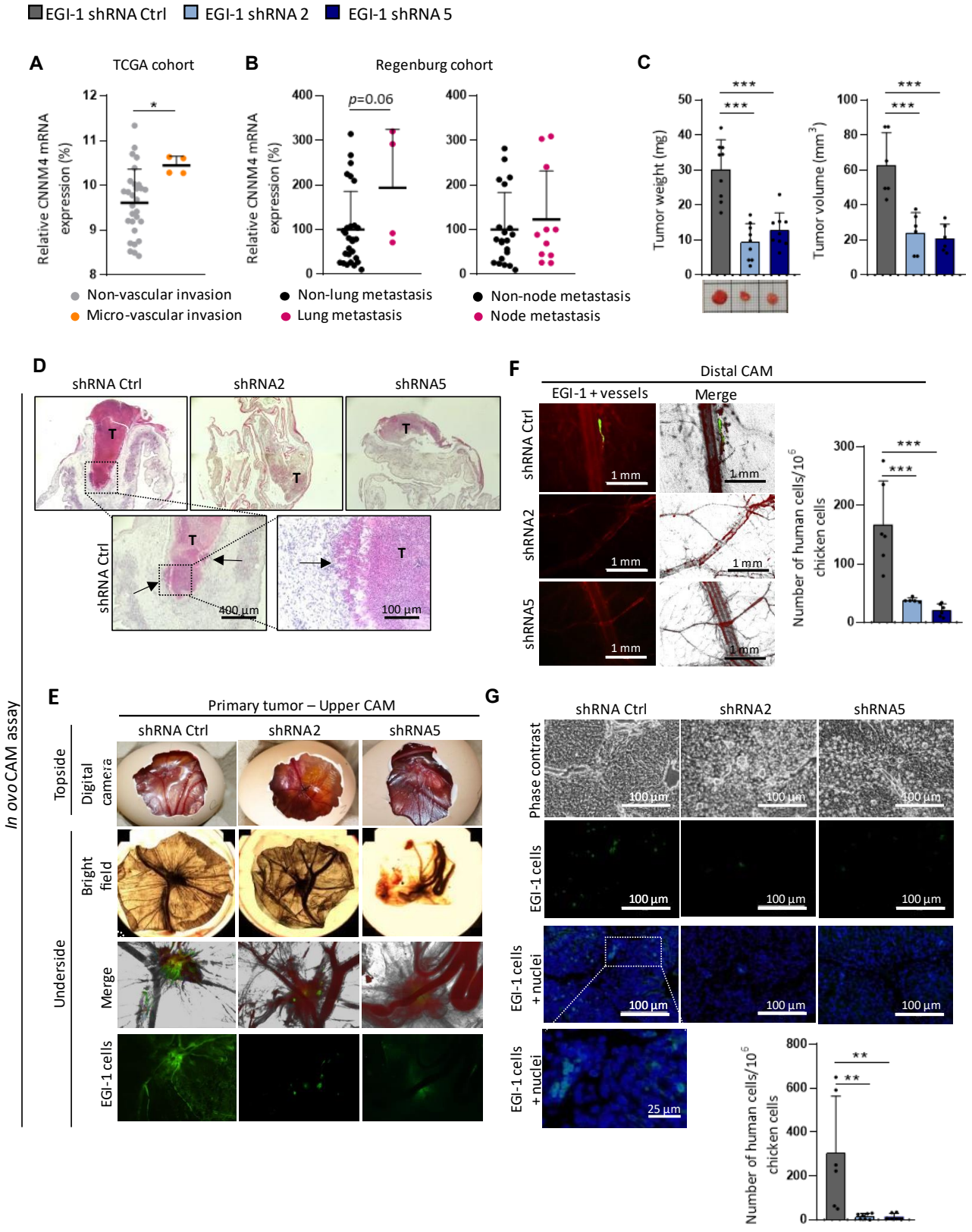

Figure R.3. The inhibitory effects of *CNNM4* silencing on EGI-1 tumor development and invasion by *in ovo* CAM model. *CNNM4* expression in TCGA cohort patients based on vascular invasion (**A**) and in the Regensburg cohort grouped by lung (*left*)

and node metastasis (*right*) (**B**). (**C**) Representative photographs of excised EGI-1 tumors, tumor weights (n=9) and volumes (n=6) from *in ovo* CAM assay. (**D**) Representative micrographs of tumors sections stained with hematoxylin and eosin. Arrows indicate sites of tumor invasion into CAM after shRNA Ctrl transfection. (**E**) Fluorescence micrographs showing inhibitory effects of CNNM4 silencing on EGI-1 cells intravasation to the adjacent CAM. (**F**) Representative micrographs showing EGI-1 cells in the vasculature in the distal CAM and q-PCR quantitation of EGI-1 cell spread to distal CAM. (**G**) Fluorescence micrographs showing inhibitory effects of *CNNM4* silencing on metastatic spread of EGI-1 cells to lungs and q-PCR quantitation of EGI-1 cells spread to lungs. One-way ANOVA, Mann-Whitney and unpaired Student's t-test were used depending on the normality of the samples. Error bars represent SD and asterisks indicate p-values (*<0.05, **<0.01 and ***<0.001). Abbreviations: TCGA: The Cancer Genome Atlas; CAM: chick chorioallantoic membrane; T: tumor area.

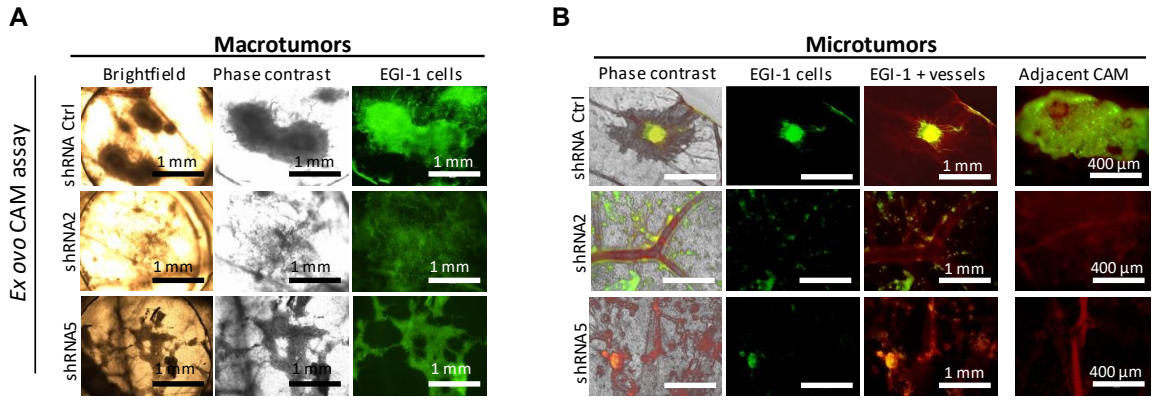

Supplementary Figure R.5. The inhibitory effects of CNNM4 silencing on EGI-1 tumor development and invasion by ex *ovo* CAM model. Fluorescence micrographs of EGI-I cells-forming tumors showing the inhibitory effects of *CNNM4* silencing on formation of (**A**) macrotumors (induced using 500,000 of EGI-1 cells) and (**B**) microtumors (induced using 50,000 EGI-1 cells growth in *ex ovo* CAM conditions. Abbreviations: CAM: chick chorioallantoic membrane.

R.1.4. Inhibition of NUPR-1 following *CNNM4* silencing enhances ferroptosis in CCA cells

To further understand the underlying mechanisms of silencing CNNM4 in CCA tumor growth, we characterized the proteomic changes in EGI-1 and TFK-1 cells after *CNNM4* silencing using liquid chromatography coupled to tandem mass spectrometry (LC-MS/MS).

First, principal component analysis (PCA) effectively discriminated the silenced groups from the control group in both cell lines (**Figure R.S6A**). Fig.S6B shows cell top differentially expressed peptides after *CNNM4* silencing, with samples primarily organized into groups. The major downregulated pathways predominantly involve metabolic processes, but they also comprise chemotherapeutic processes, inflammatory processes, and cancer proliferation and EMT pathways (**Figures R.4A and R.S6C**). However, the antioxidant system-related pathways were consistently the most affected among the four comparisons, indicating an inhibitory effect of these pathways due to *CNNM4* silencing.

NUPR-1, a ferroptosis inhibitor, exhibited the most negative activation z-score as the upstream regulator in *CNNM4*-silenced TFK-1 cells compared to controls (**Figure R.4B**). This was confirmed by observing decrease in NUPR-1 levels and other ferroptosis-associated markers, including GPX-4, ALOX5 and 4-HNE in EGI-1 cells (**Figures R.4C, R.S7A and R.S7B**).

Dysregulation of gene expression related to ferroptosis and iron metabolism markers due to *CNNM4* silencing in CCA cells (**Figure R.S7C**) and CCA cells-derived spheroids (**Figure R.S7D**) suggested an enhanced ferroptotic activity, altogether with an increase in iron uptake and storage. No changes in iron metabolism markers in the healthy cholangiocyte H69 cell line after silencing *CNNM4* were observed (**Figure R.S7E**). In contrast, in *CNNM4*-silenced CCA cells increased intracellular iron levels (**Figure R.4D**) along with one of the final products of lipid peroxidation, MDA (**Figure R.4E**) were detected. Moreover, *CNNM4* silencing in CCA cells resulted in increased mitochondrial ROS (**Figures R.4F and R.S7F**).

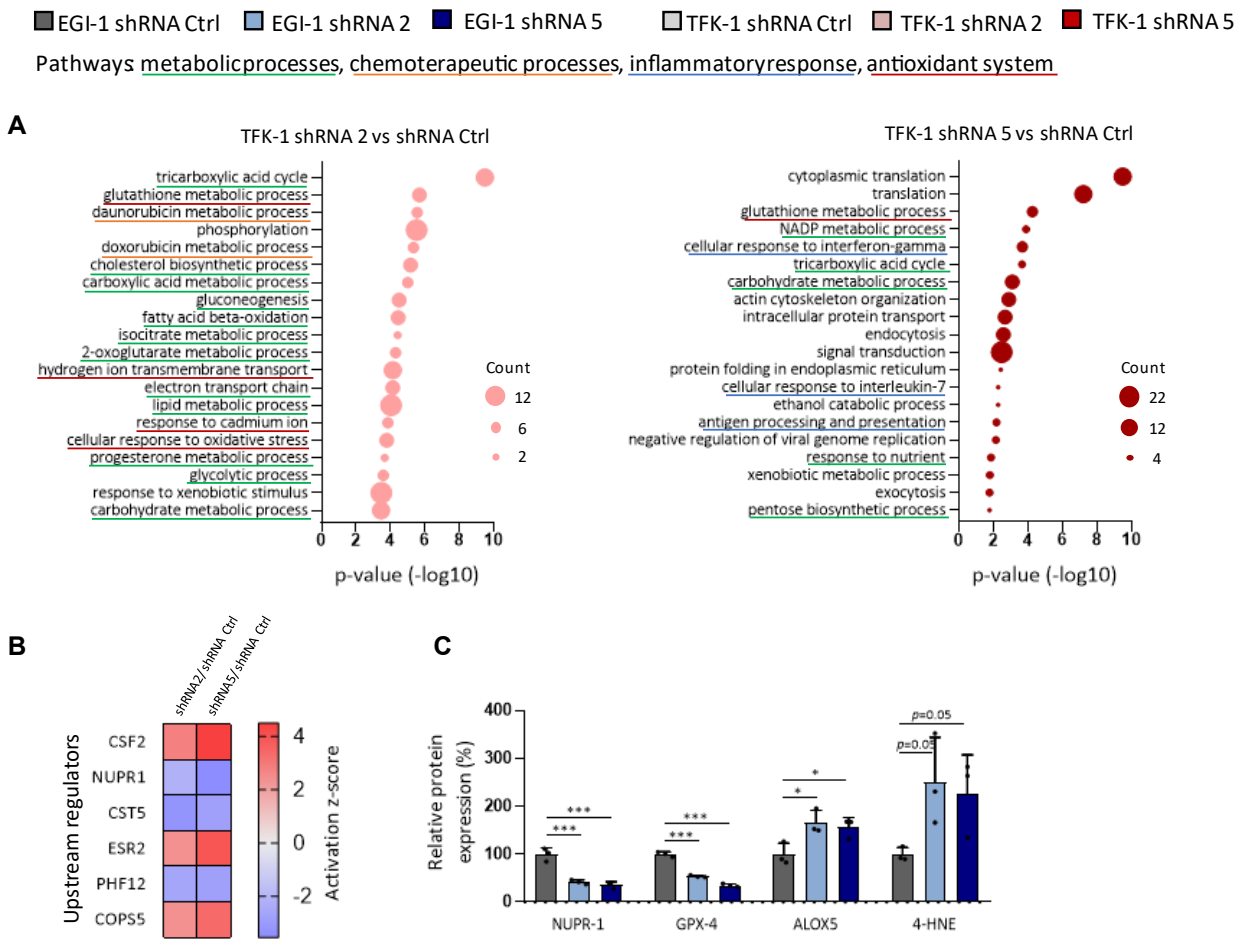

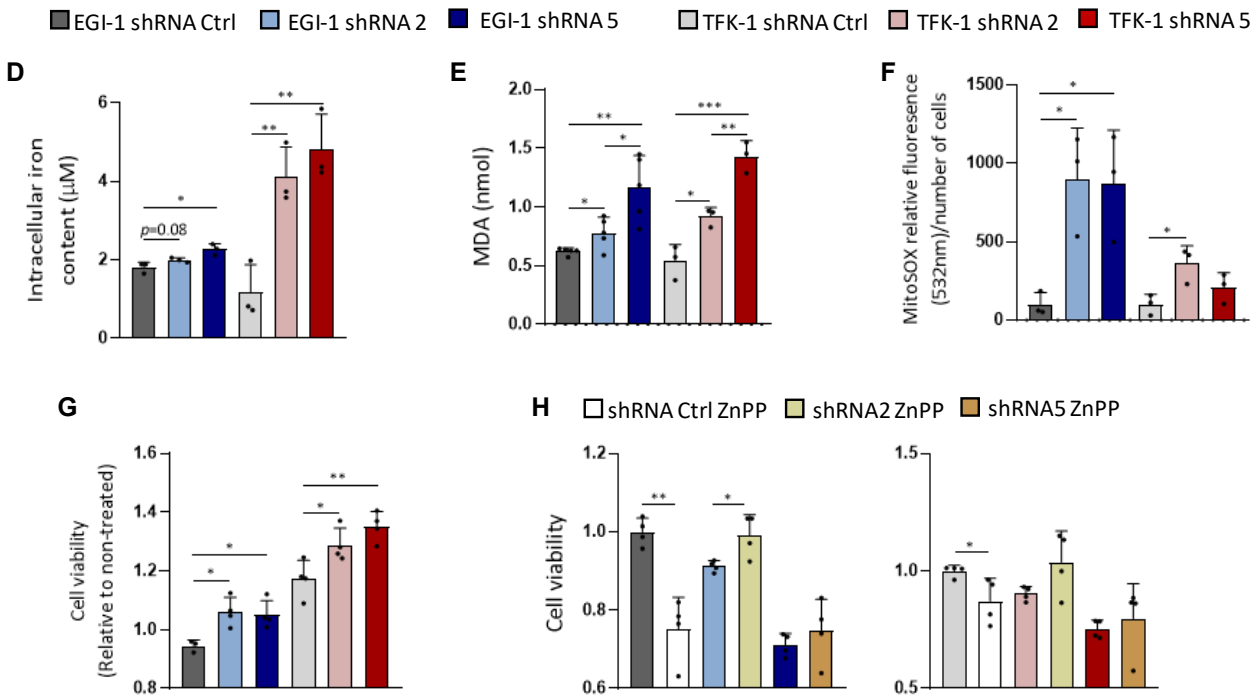

Figure R.4. Ferroptosis inhibition in *CNNM4*-silenced CCA cells. (**A**) Top-20 downregulated gene ontology term-enriched pathways representing the unique differentially expressed peptides in *CNNM4*-silenced TFK-1 compared to control TFK-1 cells (n=3). The number of proteins belonging to the identified dysregulated pathways is shown by the diameter measure. (**B**) Common upstream regulators in TFK-1 cells with CNNM4 silencing (n=3). (**C**) Protein quantification of NUPR-1, GPX-4, ALOX5 and 4-HNE in stable EGI-1 cells with or without CNNM4 silencing (n=3). (**D**) Intracellular iron content in CCA cells with CNNM4 silencing (n=3). (**E**) MDA determination in control and CNNM4-silenced CCA cells (n=5 in EGI-1 and n=3 in TFK-1). (**F**) Relative MitoSOX fluorescence of the indicated groups (n=3). (**G**) Relative cell viability after 48h treatment with 50µM deferiprone (n=4) normalized to untreated cells using crystal violet staining. (**H**) Cell viability in stable EGI-1 cells (*left*) and TFK-1 cells (*right*) after 48h administration of 25µM Zinc Protoporphyrin (n=4). Statistical significance was assessed using one-way ANOVA and Student's t-test. Error bars represent SD and asterisks indicate *p*-values (*<0.05, **<0.01 and ***<0.001). Abbreviations: MDA: Malondialdehyde; ZnPP: Zinc Protoporphyrin.

Remarkably, patient-derived xenograft (PDX) models from a cohort of patients with diverse clinical features demonstrated a trend toward a decrease in CNNM4 positivity in cells harboring mutated IDH1, known for sensitizing cells to ferroptosis (**Figure R.S7G**)[403]. These findings unequivocally corroborated the association between reduced CNNM4 expression and molecular pathways driving ferroptosis.

To understand ferroptosis importance for CCA cells with reduced CNNM4 expression, cells were exposed to the iron chelator deferiprone. After normalizing the data to untreated cells, we observed enhanced growth of *CNNM4*-silenced cells (**Figure R.4G**), effectively reversing the observed phenotype (**Figure R.2D**).). Furthermore, the addition of Zinc Protoporphyrin (ZnPP), an inhibitor of heme oxygenase-1 (HO-1), affected the proliferative rate of CCA cells with normal CNNM4 levels but had no effect on cell growth when CNNM4 was silenced (**Figure R.4H**).

In conclusion, ferroptosis is crucial in driving the observed effects in CCA cells when CNNM4 levels are decreased.

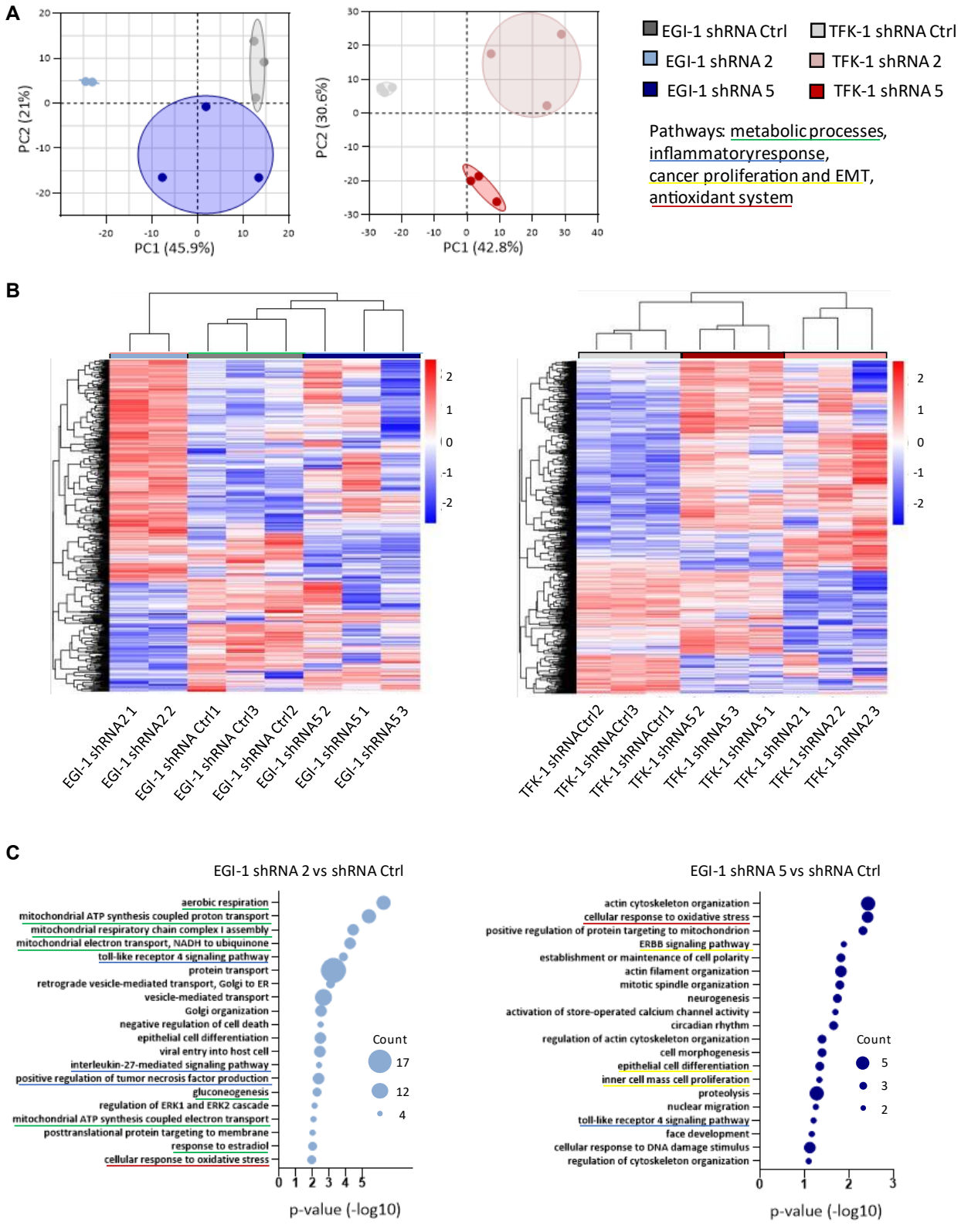

Supplementary Figure R.6. Proteomic analyses reveal changes in CCA cells after silencing *CNNM4*. (**A**) Principal component analysis of proteomic results for EGI-1 (*left*) and TFK-1 (*right*) cells after *CNNM4* silencing. (**B**) Heatmap showing the differentially

expressed proteins between control and CNNM4 silenced EGI-1 (*left*) and TFK-1 (*right*) cells. (**C**) Top-20 downregulated gene ontology term-enriched pathways representing the unique differentially expressed peptides in CNNM4-silenced EGI-1 compared to control EGI-1 cells (n=3). The number of proteins belonging to the identified dysregulated pathways are shown by the diameter measure.

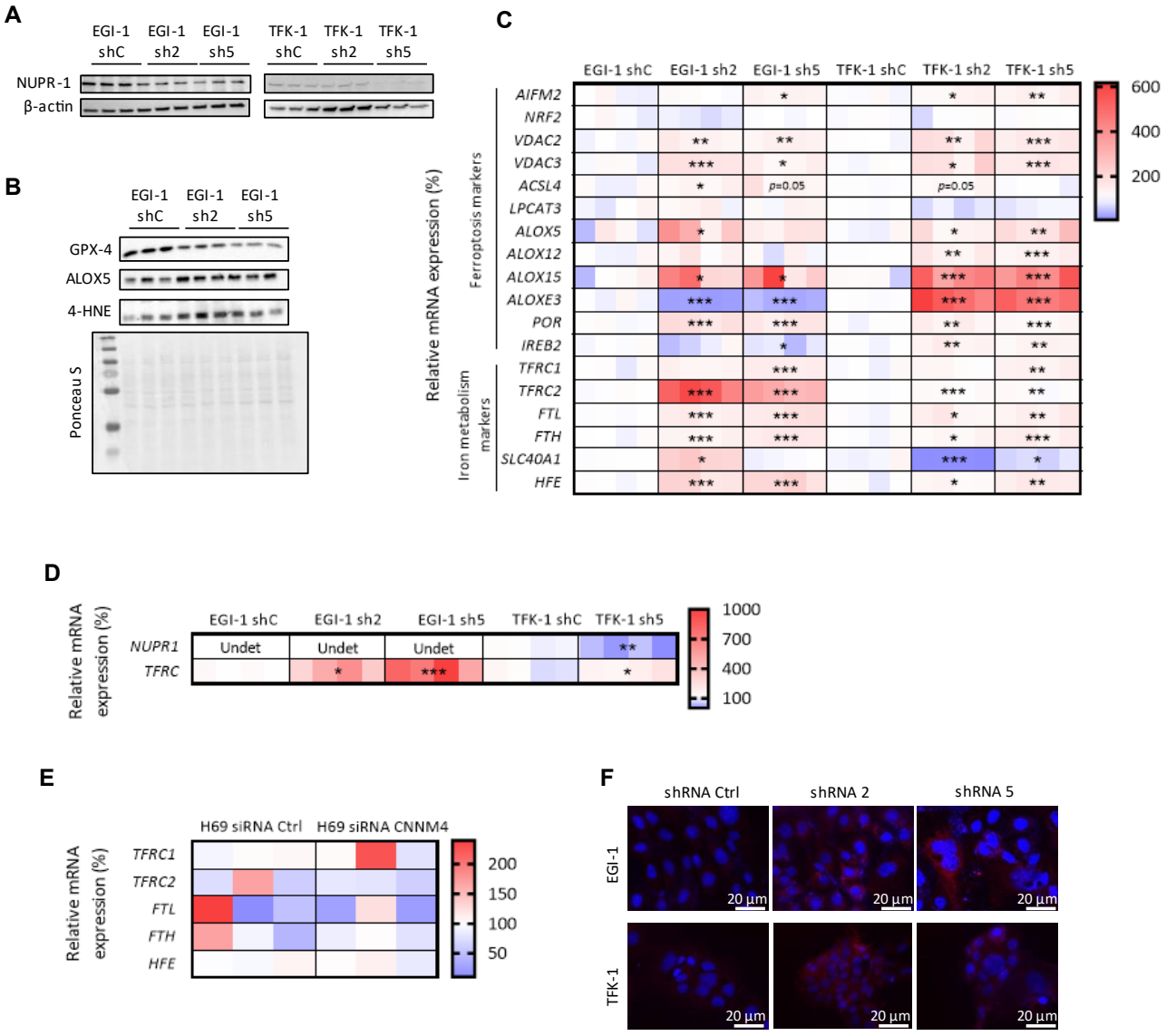

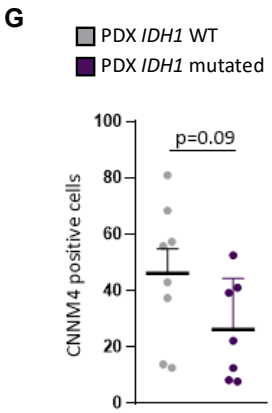

Supplementary Figure R.7. Ferroptosis is inhibited in *CNNM4*-silcenced CCA cells. Western blot displaying NUPR-1 (**A**) and GPX-4, ALOX5 and 4-HNE (**B**) protein expression in CNNM4-silenced CCA cell lines compared to controls (n=3). (**C**) mRNA expression of key ferroptosis regulators and iron metabolism markers in stable CCA cells. (**D**) mRNA expression of *NUPR-1* and *TRFC* in CSC-enriched spheroids (n=4). (**E**) mRNA expression of iron metabolism markers in healthy cholangiocyte cells after silencing CNNM4 (n=3). (**F**) Representative confocal micrographs of fixed CCA cells stained with fluorescent MitoSOX dye. Magnification: 100x; scale bar: 20µm. (**G**) CNNM4 positive cell quantification in patient-derived xenografts (PDXs) grouped based on the *IDH1* mutation status. Statistical significance was assessed using one-way ANOVA and Student's t-test. In heatmaps, statistical differences were determined against the controls. Error bars represent SD and asterisks indicate *p*-values (*<0.05, **<0.01 and ***<0.001).

R.1.5. Silencing *CNNM4* mitigates tumorigenicity by inducing ferroptosis in a murine model

Based on the obtained data, the AKT/YapS127A sleeping beauty mice model was further employed to shed light onto importance of CNNM4 for CCA biology (**Figure R.1E**)[404–406]. After inducing the tumors, *Cnnm4* was silenced by treatment with CNNM4-targeting siRNA conjugated to GalNAc ligand for liver-specific targeting. Both CCA-induced groups showed similar echographic manifestations prior to siRNA treatment (**Figure R.S8A**). However, at the time of sacrifice, only the CCA mice treated with siRNA Ctrl demonstrated an increased liver-to-body weight ratio compared to control mice (**Figure R.S8B**).

Based on an independent pathologist's tumorigenicity assessment, *CNNM4* siRNA-treated mice exhibited a substantial decrease in the tumor score. No tumors were detected in other organs of CCA-induced mice. As expected, CNNM4 immunoreactivity decreased in CNNM4 siRNA-treated mice (**Figure R.5A**), accompanied by reduced transcriptional levels, while other Mg^{2+} transporters' expression remained unchanged (**Figure R.S8C**). Moreover, a decrease in expression of SOX9, glutamine synthetase (GS) and epithelial cell adhesion molecule (EpCAM) was observed in tumors excised from CNNM4 siRNA-treated mic (**Figure R.5A**).

In the next step, we aimed to determine the effect of CNNM4 downregulation on energy metabolism *in vivo*. Basal glucose levels in control siRNA treated CCA-induced mice were elevated compared to healthy control and CNNM4 siRNA treated CCA-induced mice (**Figure R.5B**). Besides, control siRNA treated mice showed increased ECAR in fresh liver tissue (**Figure R.5C**) and OCR in freshly isolated mitochondria

(**Figure R.5D**) in comparison to *CNNM4*-silenced CCA mice.

Concerning ferroptosis, the expression of NUPR-1 and GPX4 was downregulated in *CNNM4*-silenced treated livers (**Figures R.5E and R.S8D**) with a greater tendency to increase iron and MDA content (**Figure R.5F-H**). Finally, immunoreactivity of the key lipid peroxidation by-product 4-HNE was increased in *CNNM4*-silenced livers from animals with CCA, compared with healthy control and control siRNA treated CCA (**Figures R.5I and R.S8E**).

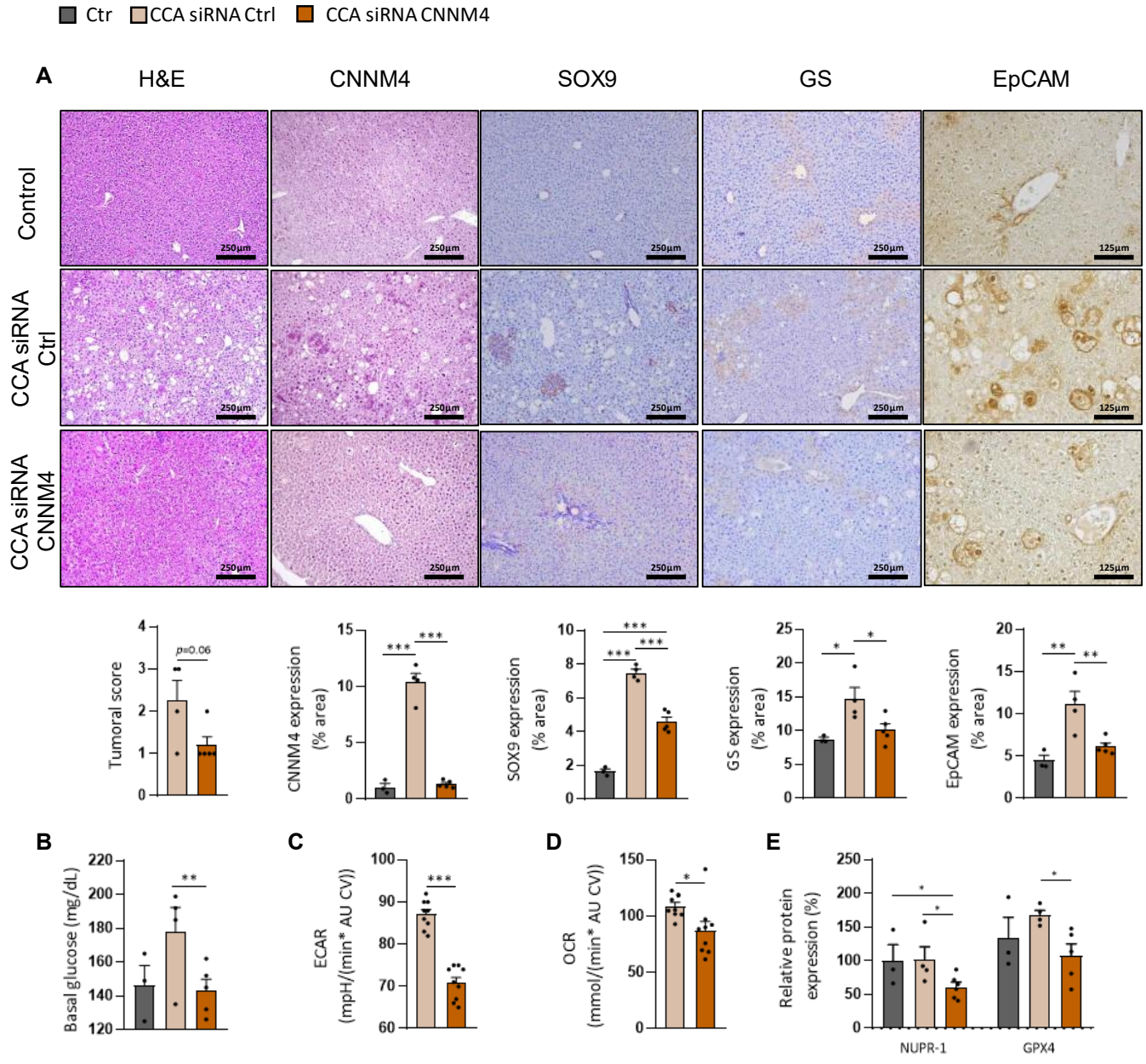

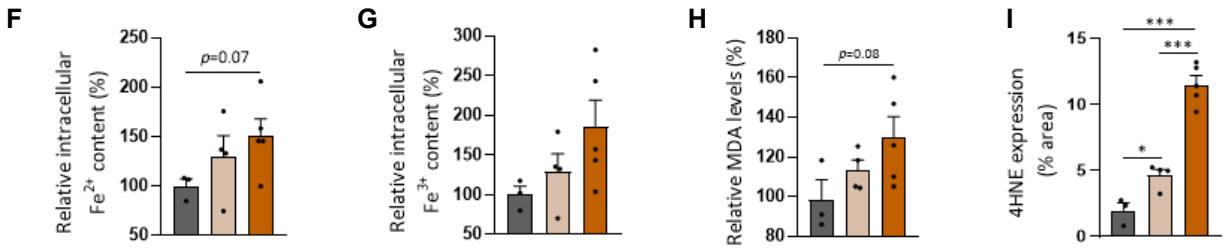

Figure R.5. Transposon-induced CCA mice model treated with *CNNM4* silencing showed a less tumoral phenotype. (**A**) Histological characterization of CNNM4, SOX9, GS and EpCAM in livers from control mice and transposon-induced CCA mice with siRNA control or *CNNM4* treatment and respective quantification. Magnification: 200x and 400x; scale bar: 250µm and 125µm. (**B**) Glucose levels in serum, (**C**) ECAR in fresh liver slices and (**D**) OCR in fresh isolated mitochondria from those mice. (**E**) NUPR-1 and GPX4 protein expression from hepatic homogenates of control mice and untreated and *CNNM4*-silenced CCA-induced mice. Relative determination of ferrous (**F**), ferric (**G**) and MDA (**H**) content in those mice. (**I**) Immunohistochemical 4-HNE expression in livers from control mice and transposon-induced CCA mice with or without CNNM4 siRNA treatment. Statistical significance was assessed using one-way ANOVA and Student's t-test. Error bars represent SEM and asterisks indicate *p*-values (*<0.05, **<0.01 and ***<0.001). Abbreviations: CCA: cholangiocarcinoma; H&E: Hematoxylin and Eosin; GS: glutamine synthetase; EpCAM: Epithelial Cell Adhesion Molecule; ECAR: Extracellular Acidification Rate; OCR: Oxygen Respiratory Rate; Fe^{2+}: ferrous iron; Fe^{3+}: ferric ion; MDA: Malondialdehyde; 4-HNE: 4-Hydroxynonenal.

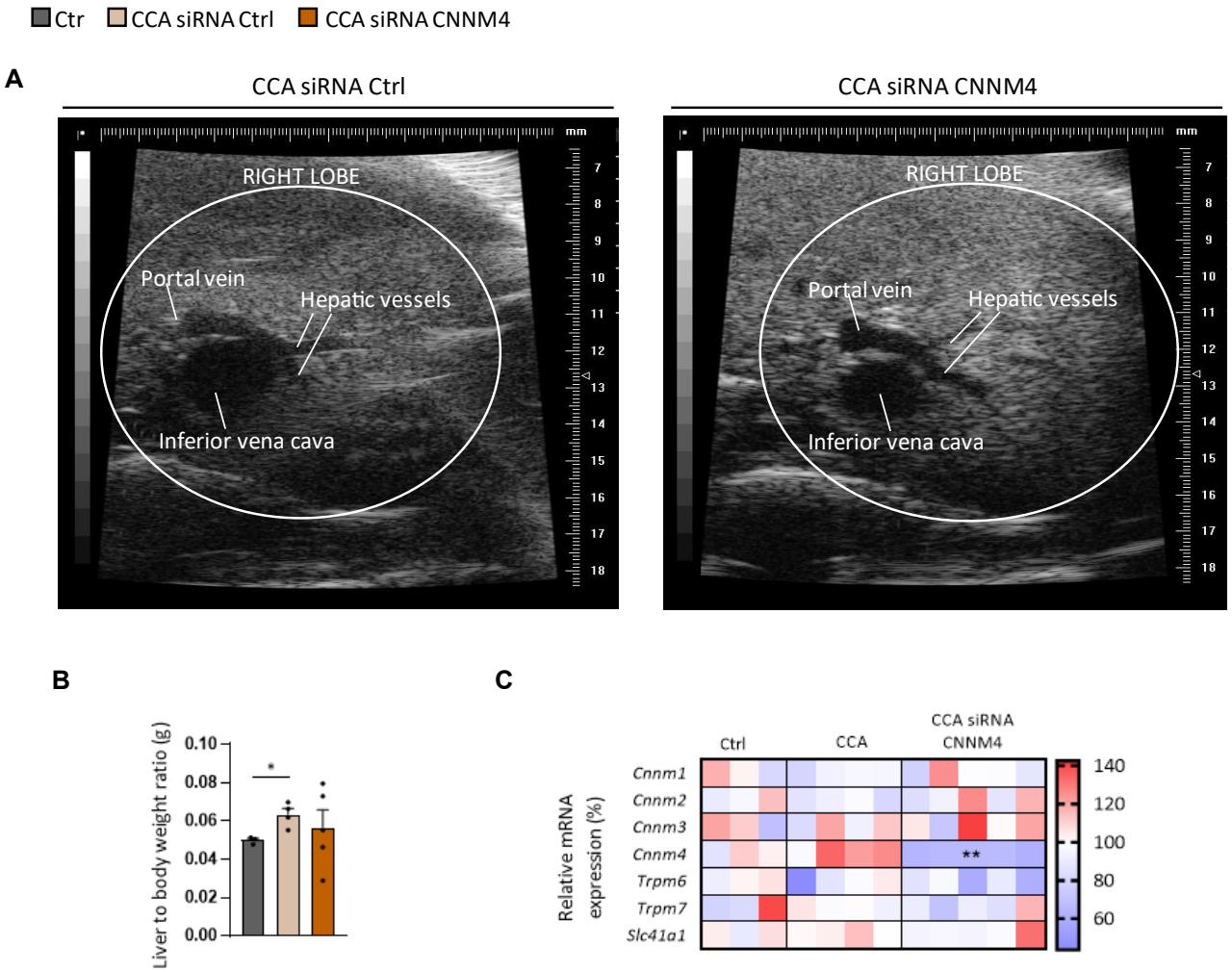

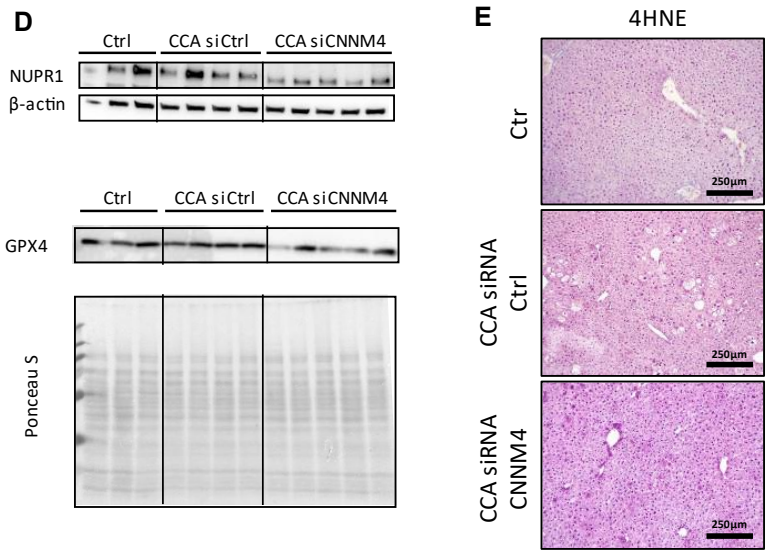

Supplementary Figure R.8. Transposon-induced CCA mice model treated with *CNNM4* silencing showed a less tumoral phenotype. (**A**) Representative liver echography and (**B**) liver-to-body weight ratio in control mice and transposon-induced CCA mice with treatment of siRNA control or CNNM4. (**C**) mRNA expression of magnesium transporters and (**D**) NUPR-1 and GPX4 protein expression in livers from those mice. Statistical differences were determined against the controls. (**E**) Representative photomicrographs from the 4-HNE immunohistochemistry performed in transposon-based mice models. Magnification: 200x; scale bar: 100µm. Error bars represent SEM and asterisks indicate *p*-values (*<0.05 and **<0.01). Abbreviations: Ctrl: Control; CCA: Cholangiocarcinoma.

2. Study 2

R.2.1. Obese patients with MASH have increased hepatic expression of SARS-CoV-2 critical entry points.

Journal of Hepatology, 2020 Oct 20: *doi.org/10.1016/j.jhep.2020.09.027*

To the Editor:

We read with great interest the article published by Biquard and colleagues showing that, according to public transcriptomic data, the hepatic expression of ACE and the cellular TMPRSS2 remains unchanged in patients with MASLD[407]. SARS-CoV-2 attaches to cells by binding to its receptor ACE2. TMPRSS2 then cleaves the SARS-CoV-2 spike protein, allowing fusion of cellular and viral membranes[408]. Despite this retrospective study, there is growing evidence that patients with MASLD are at higher risk of COVID-19 disease progression[409–411].

Given the ongoing discussion, we have assessed the expression of SARS-CoV-2 cell entry molecules in the liver of obese patients with MASLD and/or T2D (see **Table M.2** for detailed characteristics), since this information seems crucial to understand and prevent cell infection. Considering that T2D has been associated with a worse prognosis in patients with COVID-19 and that well-controlled glycemia was associated with a markedly improved outcome[412], we first focused on patients with T2D. Liver mRNA expression of ACE2 was significantly lower in patients with T2D while TMPRSS2 also tended to decrease but was not statistically significant (**Figure R.9A**). Then, we analysed separately men and women. In men, hepatic ACE2 and TMPRSS2 expression remained unchanged between the 2 groups (**Figure R.9B**). However, in women with T2D, ACE2 was significantly lower while TMPRSS2 gene expression tended to decrease compared to women without T2D **(Figure R.9B**). These results indicate that while the cell entry machinery of SARS-CoV-2 is not majorly altered in the liver of obese men with T2D, its downregulation in women might indicate a lower susceptibility to liver injury. These findings are in consonance with the well-established protective role of estrogens in dysmetabolism[413].

Next, we measured the expression of these genes in the liver according to the presence of MASLD. Liver mRNA expression of both ACE2 and TMPRSS2 did not show differences between individuals without liver injury and patients with only steatosis, but these genes were upregulated in obese patients with metabolic dysfunction-associated steatohepatitis (MASH) (**Figure R.9C**). Moreover, ACE2 and TMPRSS2 were positively correlated with MASLD activity score (**Figure R.1D**). Of note, TMPRSS2 was also positively correlated with weight, BMI and cholesterol (data not shown).

In summary, our results indicate that in the livers of obese patients, SARS-CoV-2 entry factors are differently affected by T2D and MASLD. While obese women with T2D have unexpectedly lower levels of ACE2 and TMPRSS2 than obese normoglycemic women, obese patients with MASH show markedly higher expression of these genes, suggesting that advanced stages of MASLD might predispose individuals to COVID-19.

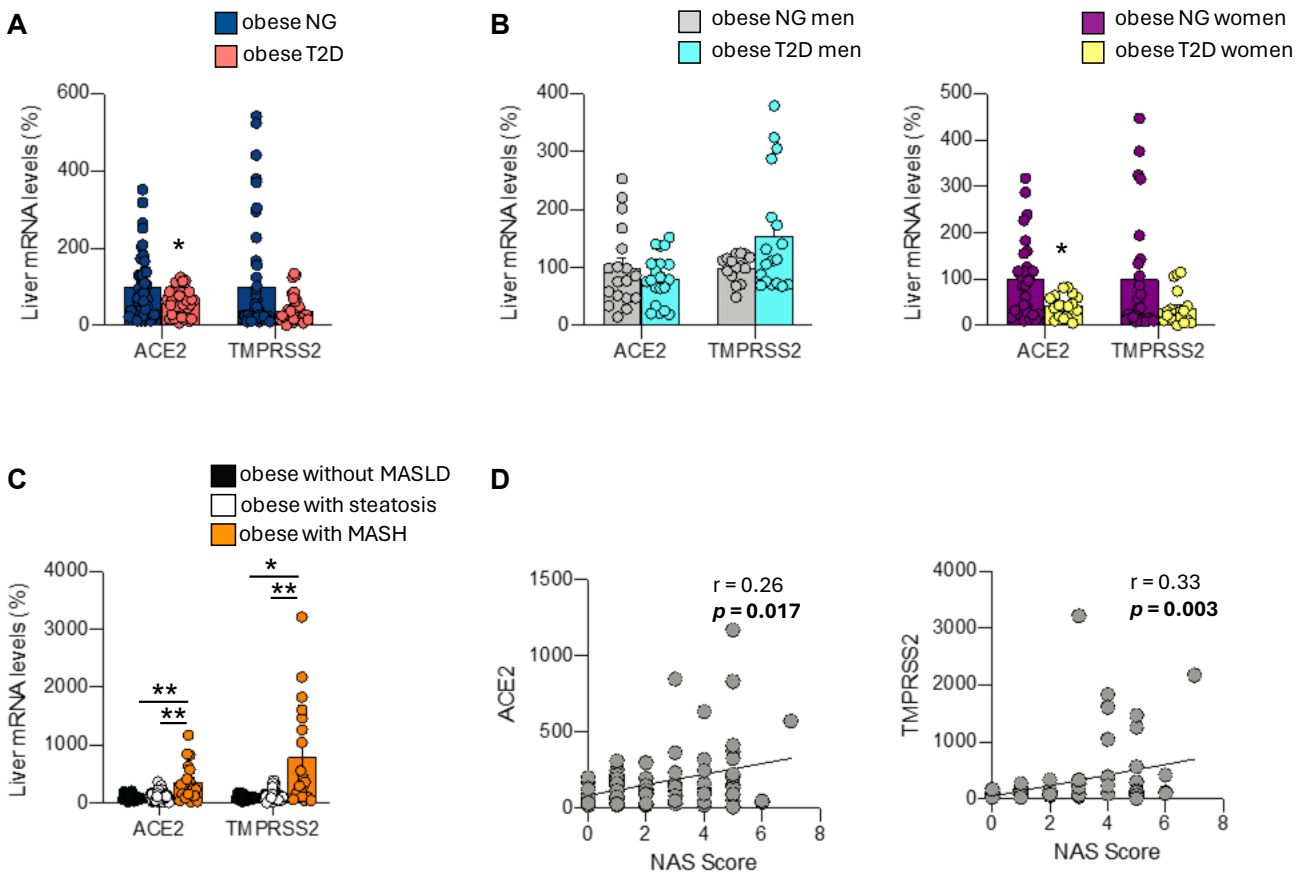

Figure R.9. *ACE2* and *TMPRSS2* hepatic mRNA levels in patients with T2D or MASLD. (**A**) *ACE2* and *TMPRSS2* expression in obese patients with T2D (n = 43) or NG (n = 51); and (**B**) separately by men and women with T2D or NG. (**C**) *ACE2* and *TMPRSS2* expression in obese patients without MASLD (n = 17), steatosis (n = 57), MASH (n = 20). (**D**) Correlation between *ACE2* and *TMPRSS2* with NAS score. $*p$ <0.05, $**p$ <0.01, Mann-Whitney *U* test (**A, B**), Krustal-Wallis followed by Dunn *post-hoc* test (**C**). ACE2, angiotensin converting enzyme 2; MASLD, metabolic dysfunction-associated steatotic liver disease; MASH, metabolic dysfunction-associated steatohepatitis; NG, normoglycemia; T2D, type 2 diabetes; TMPRSS2, transmembrane protease serine 2.

R.2.2. The spike of SARS-CoV-2 binds to human hepatocytes and hepatocytes derived from humanized ACE2 (hACE2) mice

In order to determine if the spike of SARS-CoV-2 could directly interact with human hepatocytes, the binding capacity of the S1 or the RBD were measured by flow cytometry in THLE-2 cells, a human hepatocyte cell line expressing ACE2, TMPRSS2 and NRP1 (**Figure R.10A**). **Figure R.10B and R.10C** show that RBD interacts with human hepatocytes. Under these conditions, the binding capacity was comparable to that observed on Vero E6 cells[392], a widely used kidney epithelial cell model in SARS-CoV-2 biology research[414]. In order to confirm that this interaction was mediated by ACE2, we carried out pull-down experiments with S1 or RBD proteins in THLE-2 human hepatocytes (**Figure R.10D**). This approach confirmed the binding of S1 and RBD to ACE2 in human hepatocytes. We then evaluated the ability of pseudotyped lentiviral particles that express the full-length spike of SARS-CoV-2[385] to infect human hepatocytes. THLE-2 cells cultured in the presence of pseudotyped viral particles are susceptible to be infected, as detected by flow cytometry (**Figure R.10E**). Our findings indicating that human hepatocytes could be a relevant cell target for SARS-CoV-2 prompted us to study its infectivity in relevant primary cell models. For this purpose, we used transgenic mice that express human ACE2 (hACE2) and are therefore SARS-CoV-2 susceptible[415]. We assessed the expression of ACE2 and NRP1, an important factor that mediates the initial steps of SARS-CoV-2 infection, in hACE2- and wild-type (WT)-derived primary hepatocytes by immunoblotting. Both ACE2 and NRP1 protein levels were upregulated in hACE2-derived hepatocytes compared to control hepatocytes (Fig. 1f). Pulldown assays confirmed that S1 and RBD directly bind to ACE2 expressed on primary hepatocytes (Fig. 1g). In order to determine the susceptibility to infection, hACE2 primary hepatocytes were exposed to pseudotyped viral particles expressing the full-length spike of SARS-CoV-2 and pseudotyped viral particles without spike as a negative control. Flow cytometry experiments revealed that hACE2 primary hepatocytes, but not WT mouse hepatocytes, are infected by pseudotyped viral particles expressing the SARSCoV-2 spike while pseudotyped control viral particles did not show any effect (**Figure R.10H**). Remarkably, we demonstrate that upcyte second-generation human hepatocytes are also susceptible to infection with pseudotyped viral particles, whereas the control virus had no effect (**Figure R.10I**). Consistent with these results, we observed that in primary hACE2 hepatocytes, ACE2 levels measured by western blot were decreased in the presence of pseudotyped viral particles, but no modulation was detected upon infection with the control virus (**Figure R.S9A**). In human primary hepatocytes, changes in the pattern of ACE2 expression were observed after infection (**Figure R.S9B**). NRP1 is another receptor known to enhance viral infection[416]. In this context, we explored NRP1 expression in hACE2 and human primary hepatocytes after infection (**Figure R.S9A and R.S9B**). Finally, to

assess whether infection renders primary mouse and human hepatocytes susceptible to apoptotic processes, we measured caspase-3 activity by fluorimetry in the presence of pseudotyped viral particles. Infection induced an apoptotic response that was dependent on the presence of the spike (**Figure R.S9C**).

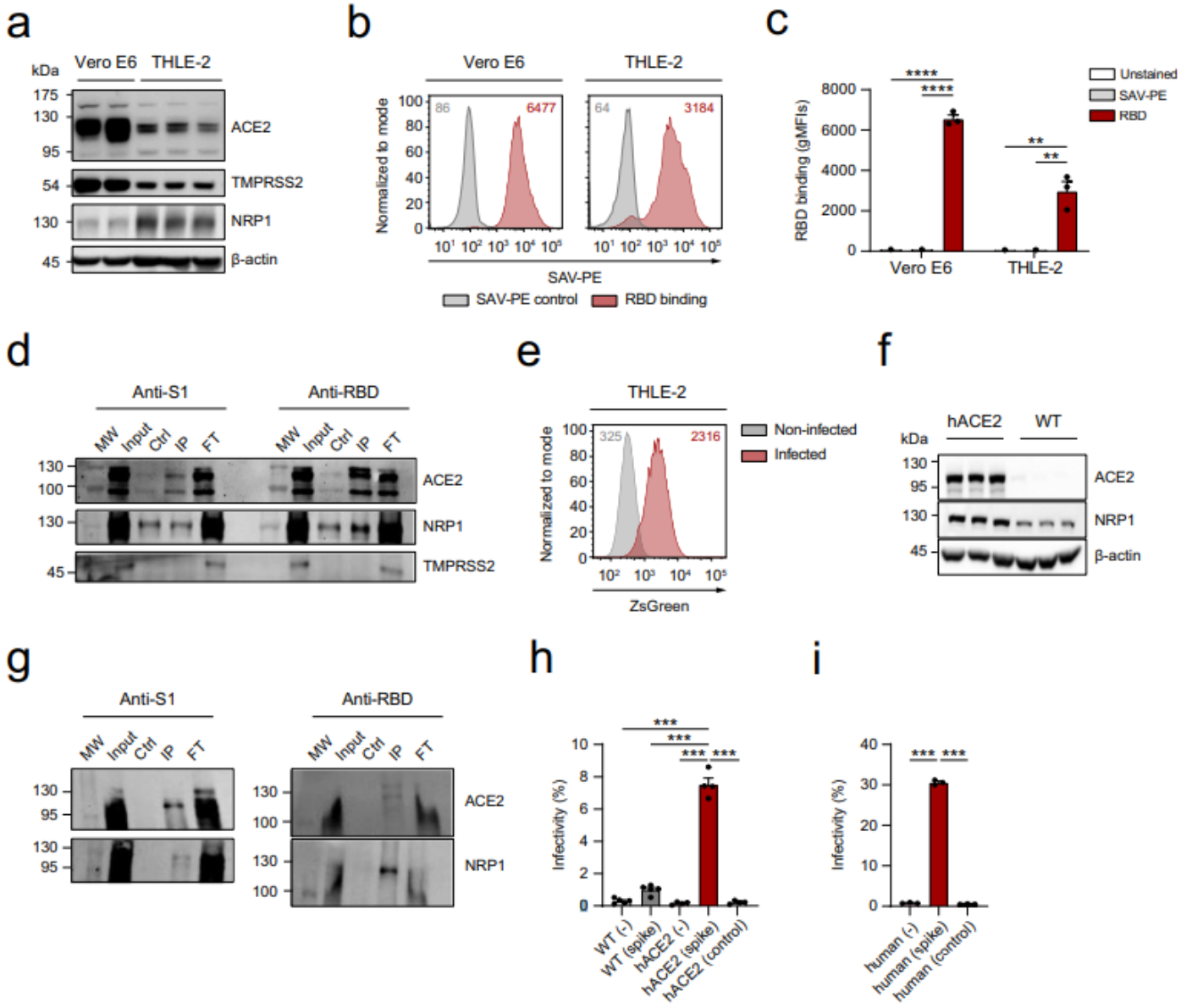

Figure R.10. The spike of SARS-CoV-2 binds to human hepatocytes and hepatocytes derived from humanized ACE-2 (hACE2) mice. (**a**) Western blot showing the expression of ACE2, TMPRSS2 and NRP1 proteins on Vero E6 cells (*left*) or THLE-2 human hepatocytes (*right*). (**b**) A representative flow cytometry histogram showing the binding of the RBD to Vero E6 cells (*left*) or THLE-2 human hepatocytes (*right*). (**c**) Binding of the RBD to Vero E6 cells or THLE-2 cells (n=3, unpaired t-test), measured by flow cytometry. (**d**) Western blot showing the expression of ACE2, NRP1 and TMPRSS2 on different fractions of the immunoprecipitation assay (input, control, immunoprecipitated and flowthrough) with S1 (*left*) or RBD (*right*) on THLE-2 human hepatocytes. (**e**) A representative histogram representing the infection rate of THLE-2 cells measured by flow cytometry (ZsGreen expression) 48 hours after addition of the pseudotyped viral particles expressing the full-length spike of SARS-CoV-2. (**f**) Western blot showing the expression of ACE2,

NRP1 and β-actin on hACE2 (*left*) or WT (*right*) primary mouse hepatocytes. (**g**) Western blot showing the expression of ACE2 and NRP1 on the different fractions after the immunoprecipitation assay (input, control, immunoprecipitated and flowthrough) with S1 (*left*) or RBD (*right*) on hACE2 primary mouse hepatocytes. (**h**) Infection rate of hACE2 or WT primary mouse hepatocytes measured by flow cytometry (n=5, one-way ANOVA test). (**i**) Infection rate of upcyte second-generation human hepatocytes measured by flow cytometry (n=3, one-way ANOVA test). Error bars represent SEM and asterisks represent p-values (****<0.01, ***<0.001 and ****<0.0001). Abbreviations: FT: flowthrough in the immunoprecipitation assay; hACE2: humanized angiotensin-converting enzyme 2; IP: immunoprecipitated fraction; MW: molecular weight marker; SAV-PE: Streptavidin-phycoerythrin; WT: wild type.

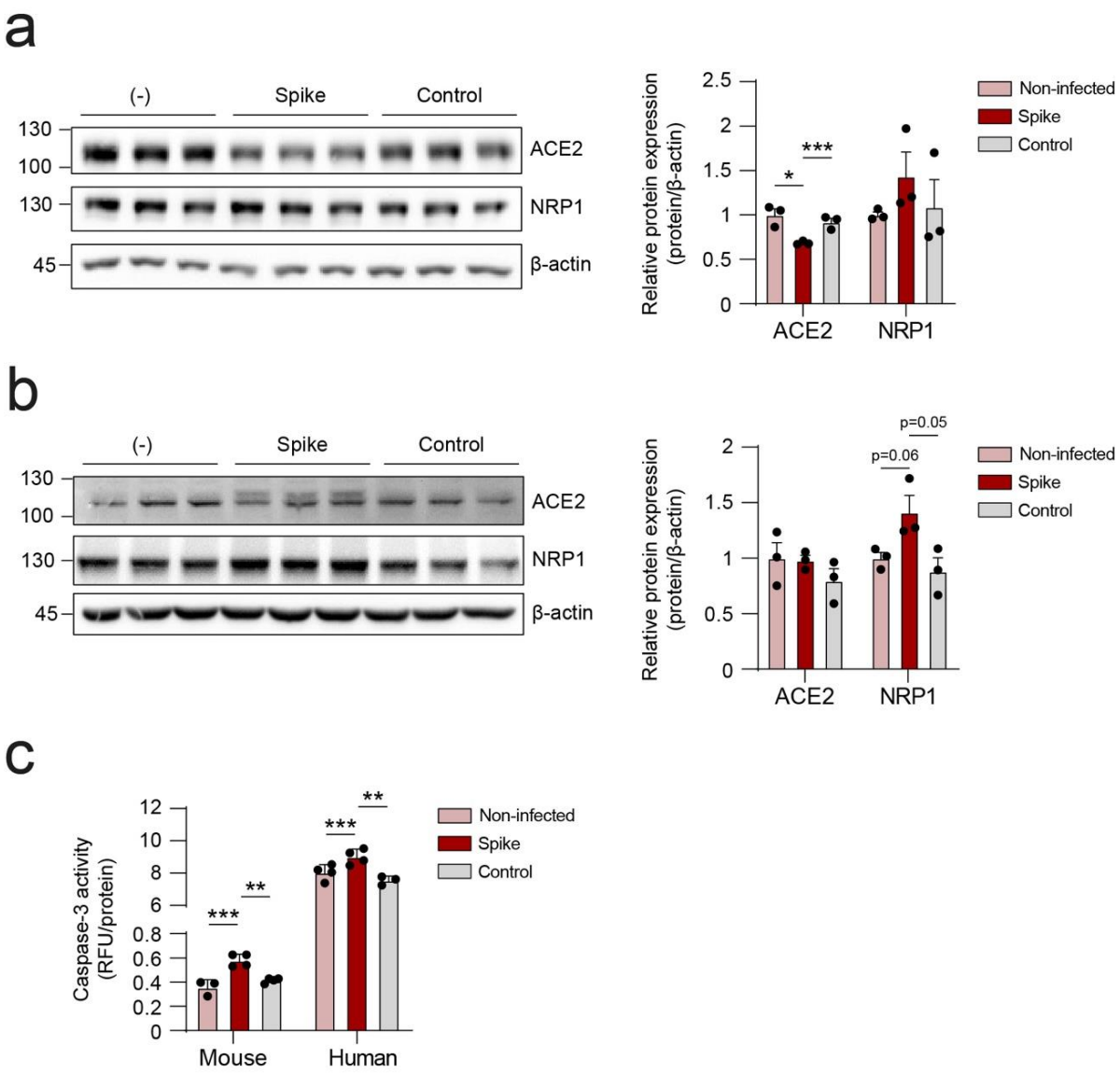

Supplementary Figure 9. Binding of pseudotyped viral particles expressing the SARS-CoV-2 spike alters the expression of ACE2 and NRP1 proteins and induces apoptosis in hepatocytes. (**a, b**) Western blot showing the expression of ACE2 and NRP1 proteins on primary hACE2 mouse hepatocytes (***a***) or upcyte second-generation human hepatocytes (***b***) infected with lentiviral particles expressing the spike protein or control (n=3, one-way ANOVA test). (**c**) Caspase-3 activity measured by fluorimetry in mouse and human primary hepatocytes treated with lentiviral particles expressing the spike protein or control (n=4, one-way ANOVA test). Error bars represent SEM and asterisks represent p-values (*<0.05, **<0.01, ***<0.001).

R.2.3. Proteomic analyses reveal changes in hACE2 mouse hepatocytes after infection with pseudotyped viral particles expressing the spike of SARS-CoV-2.

Significant molecular changes have been reported in cells that have been infected with SARS-CoV2[417]. In the context of liver infection, we characterized changes at the proteome level that result from the interaction of the full-length spike of SARS-CoV-2 with hACE2 primary hepatocytes. First, we examined the proteomic changes induced by pseudotyped viral particles expressing the full-length spike of SARS-CoV-2 on primary mouse hepatocytes expressing humanized hACE2 (**Figure R.11A**) or WT mouse hepatocytes (**Figure R.11B**). Consistent with the rather absence of infection of WT hepatocytes in comparison with that of the humanized hACE2 model (**Figure R.10H**), WT hepatocytes presented a lower number of differentially expressed peptides than the humanized hACE2 model (**Figure R.11C**). In order to focus on changes derived from the binding of the spike of SARS-CoV-2, 13 common peptides that were found significantly dysregulated in an ANOVA + Tukey test ($p < 0.05$) in both WT and hACE2 hepatocytes after exposure to pseudotyped viral particles were discarded in downstream analyses (**Figure R.11C**). **Figure R.11D** shows the list of the top-25 up- and down-regulated specific peptides in hACE2 hepatocytes after exposure to pseudotyped viral particles. The Database for Annotation, Visualization and Integrated Discovery (DAVID) was used to identify the major pathways altered as a result of the infection. We considered those pathways that were found altered in the hACE2 model but not in the WT model (**Figure R.11E**). Identified dysregulated pathways included viral-related responses: response to the virus, inflammatory and immune-related signals against infection, receptor-mediated endocytosis and mitochondrial translation. In the context of liver-related pathways, the cholesterol steroids pathway was significantly altered on hACE2 hepatocytes. Moreover, two pathways related to iron homeostasis were significantly upregulated in infected hACE2 hepatocytes compared to control hepatocytes (**Figure R.11E**). Iron-trafficking proteins such as neutrophil gelatinase-associated lipocalin (NGAL), transferrin endocytosis, and recycling molecules, such as transferrin receptor protein 2 (TFR2) and the transmembrane protease serine 6 (TMPS6), among others, were greatly representative in hACE2 hepatocytes exposed to the pseudotyped viral model. These results are in line with previous studies describing the role of iron metabolism in COVID-19 patient progression[418–422]. Additionally, KEGG pathways represent the unique peptides in the infected hACE2 hepatocytes compared to control hepatocytes identified ribosome- and COVID-19-related processes (**Figure R.S10A**).

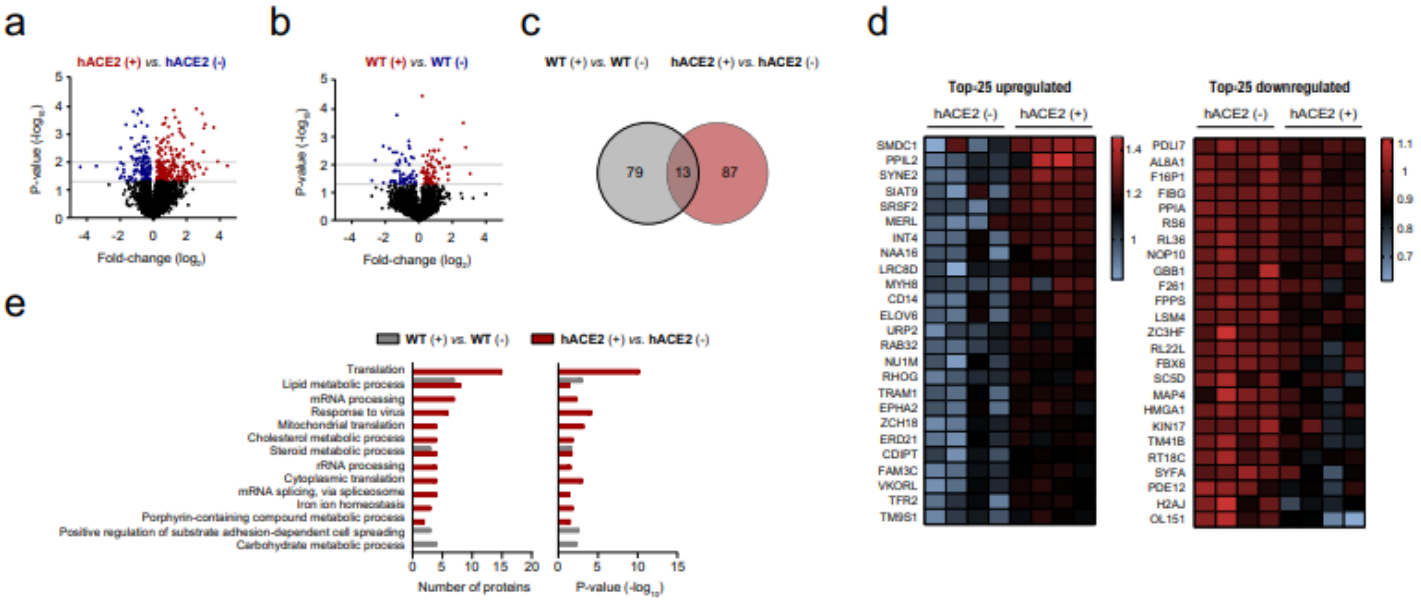

Figure R.11. Proteomic analyses reveal changes in hACE2 mouse hepatocytes after infection with pseudotyped viral particles expressing the spike of SARS-CoV-2. (**a**) Volcano plot showing the 354 differentially expressed peptides between hACE2 mouse hepatocytes in presence (+) or absence (-) of pseudotyped viral particles after 48 hours. (**b**) Volcano plot showing the 132 differentially expressed peptides between WT mouse hepatocytes in presence (+) or absence (-) of pseudotyped viral particles. For a detailed list of all peptides including their fold-change and p-values refer to the Supplementary Data 1. (**c**) Venn diagram showing common peptides between hACE2 (+ *vs*. -) and WT (+ *vs*. -) mouse hepatocyte comparisons. (**d**) Heatmap showing the top-25 up- or downregulated peptides between hACE2 mouse hepatocytes in presence (+) or absence (-) of pseudotyped viral particles. (**e**) Gene ontology term enriched pathways representing the unique differentially expressed peptides in the WT (+ *vs*. -) or hACE2 (+ *vs*. -) mouse hepatocyte comparisons. Number of proteins belonging the identified dysregulated pathways (*left*) and their corresponding p-values (*right*) are shown.

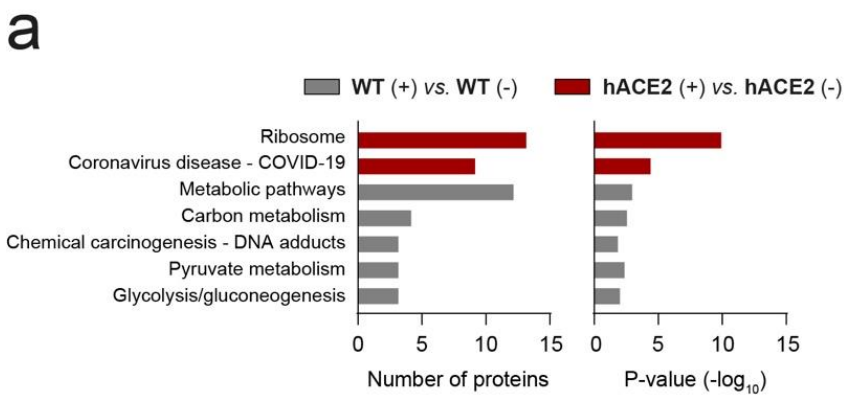

Supplementary Figure 10. Infection with pseudotyped viral particles alters ribosome- and COVID-19-related processes on hACE2 hepatocytes compared to control hepatocytes. (**a**) KEGG pathways representing the unique differentially expressed peptides in WT or hACE2 mouse hepatocytes either treated with pseudotyped lentiviral particles expressing the spike or SARS-CoV-2 (+) or control viral particles (-). Number of proteins belonging the identified dysregulated pathways (left) and their corresponding p-values (right) are shown.

R.2.4. Binding of the spike of SARS-CoV-2 alters mitochondrial activity and glucose homeostasis in mouse and human primary hepatocytes

Iron uptake is essential for the correct functioning of mitochondria; therefore, accumulation of this ion usually leads to oxidative stress[423,424]. In order to clarify whether the infection of hACE2 hepatocytes by pseudotyped viral particles expressing the full-length spike of SARS-CoV-2 affected mitochondrial function, we performed metabolic analyses to evaluate alterations in energy production pathways.

Figure R.12A shows changes in the OCR and ECAR after infection of hACE2 hepatocytes by pseudotyped viral particles compared to controls, measured by extracellular flux analysis. These results showed a shift towards enhanced glycolysis. Viral infection also enhanced the OCR, suggesting increased mitochondrial activity (**Figure R.12A**). Importantly, upcyte second-generation human hepatocytes showed a similar metabolic switch characterized by a more energetic state upon infection (**Figure R.12B**). In this context, the activity of AMP kinase, a major hub for metabolic control in the cell, was examined by immunoblotting in hACE2 and human primary hepatocytes, resulting in an increase in AMPKα phosphorylation in Thr172. No effect was observed after infection with control viral particles (**Figures R.12C and R.S11A**). These metabolic changes could result from the direct interaction of the SARS-CoV-2 spike with the ACE2 receptor on the surface of hACE2 and human hepatocytes. In this context, it is known that ACE2 can regulate mitochondrial function and that ACE2-knockout mice show impaired mitochondrial respiration[425–427]. Moreover, exacerbated mitochondrial activity could alter the cell oxidative state, leading to cell death[428,429]. We also measured the content of mitochondrial ROS in hACE2 and human primary hepatocytes, showing that infection with pseudotyped viral particles increased ROS production (**Figures R.12D and R.S11B**). Consistently *Tnf* and *Il6* in primary hACE2 hepatocytes (**Figure R.S12A**) and *TNF* in case of human primary hepatocytes (**Figure R.S12B**) were significantly modulated under pseudovirus S1 infection while no regulation was identified with the control virus. Importantly, iron metabolism was also modulated in response to the lentiviral particles expressing spike. Iron transporters (*TRFC1* and *TRFC2*) were upregulated while *FTL* expression was reduced suggesting a higher iron utilization by the mice and human primary hepatocytes (**Figure R.S12A and R.S12B**).

Finally, these circumstances, extracellular ATP levels were significantly increased in infected primary hepatocytes (**Figure R.12E**), whereas intracellular ATP levels remained unaltered (**Figure R.S11C**).

In order to further understand the rewiring of energy metabolism produced by the binding of the spike of SARS-CoV-2, we performed metabolic flux experiments employing labeled [U-^{13}C]-glucose analyzed by high resolution mass spectrometry on hACE2 hepatocytes. Determination of isotopic enrichment labeled tracer of [U-^{13}C]-glucose revealed an increase of the glycolytic flux into the tricarboxylic

acid (TCA) cycle in hACE2 hepatocytes after infection with pseudotyped viral particles or binding of recombinant RBD (**Figure R.12F**). **Figure R.S13A** shows that binding of the spike or RBD to hepatocytes increases cellular consumption of labelled glucose, resulting in the activation of downstream energy pathways characterized by accumulation of labelled metabolites that include citrate, fumarate and malate. The observed increase of glutamate levels probably acts to potentiate the activity of the TCA through α-ketoglutarate (α-KG) (**Figure R.12F**). We also analyzed each labelled carbon independently (**Figure R.S13B**), further confirming the findings on rewiring at the mitochondrial level and a shift towards the glycolytic processes shown in Fig. 3a. TCA cycle activity could also be evaluated by measuring the ratio between the labelled citrate on different carbons and the sixth labelled carbon of glucose ([U-$^{13}C_6$]-glucose). Notably, citrate/glucose ratios in hACE2 hepatocytes in presence of pseudotyped viral particles were significantly increased compared to non-infected cells (**Figure R.S13C**), confirming a boosted activity of TCA on hepatocytes upon interaction with the spike of SARS-CoV-2. To confirm these data, glucose and lactate levels were examined under infection with pseudotyped and control viral particles in hACE2 and in human primary hepatocytes. The extracellular lactate levels were upregulated in hepatocytes upon infection compared to controls (**Figure R.12G**). In addition, a reduction in the levels of intracellular glucose was detected (**Figure R.12H**), consistent with a more pronounced glycolytic phenotype. Furthermore, gene expression of glycolytic enzymes, lactate and glutamine metabolism (*G6PDH*, *PKLR*, *PFKL*, *LDHA*, *LDHB*, *GLS1*, *GLS2* and *GLUL*), were upregulated in primary mouse (hACE2) and human hepatocytes upon infection compared to controls (**Figures R.S12A and R.S12B**).

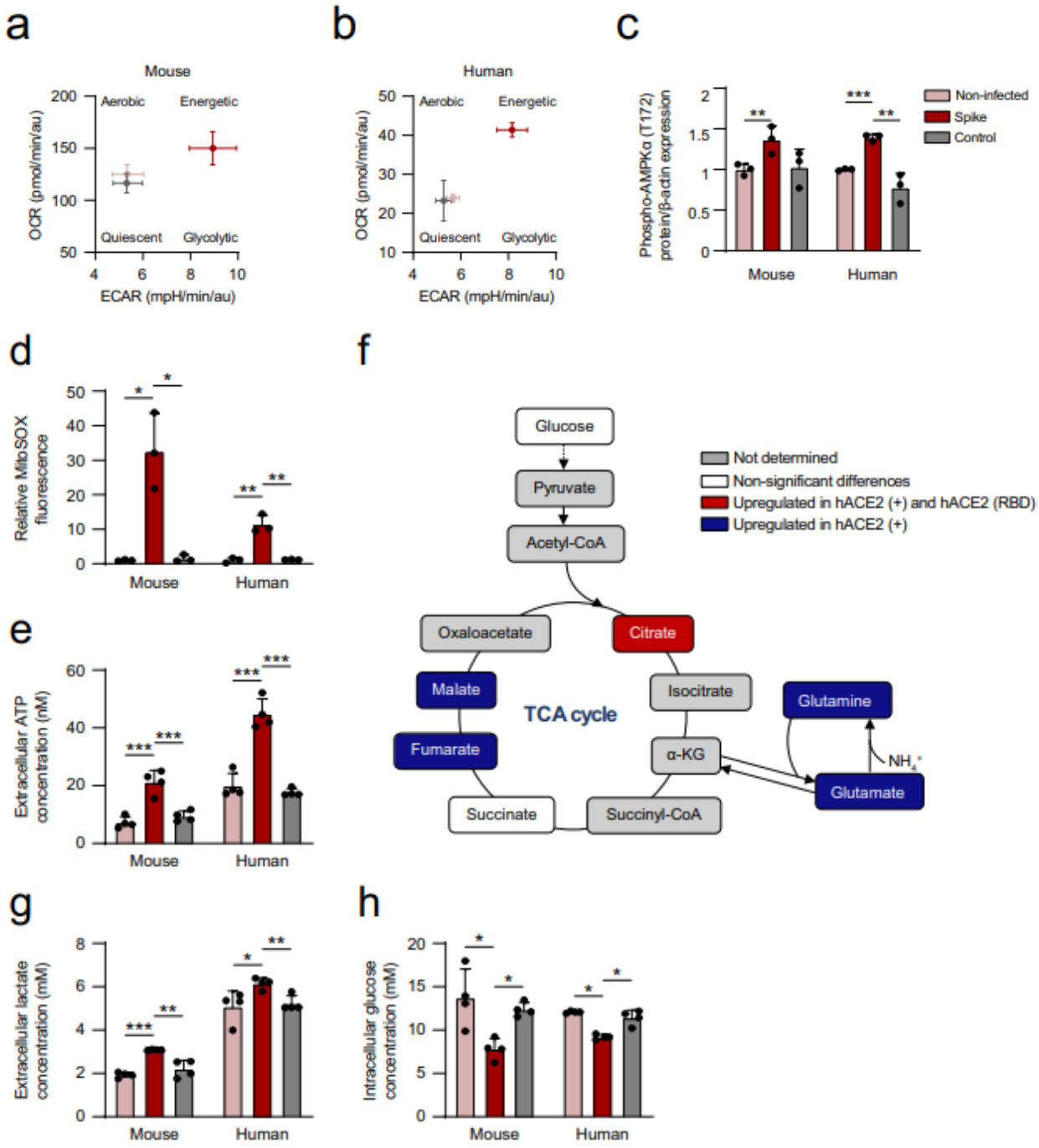

Figure R.12. Binding of the spike of SARS-CoV-2 alters mitochondrial activity and glucose homeostasis in hACE2 and human primary hepatocytes. (**a, b**) Oxygen consumption rate (OCR) and extracellular acidification rate (ECAR) after infection with pseudotyped viral particles expressing the spike protein or control of hACE2 hepatocytes (n= 6) (*a*) or human primary hepatocytes (n=6) (*b*) measured by extracellular flux analyses. (**c**) Relative quantification of phospho-AMPKα (T172) levels measured by immunoblotting on primary hACE2 hepatocytes or primary human hepatocytes infected with pseudotyped lentiviral particles (n=3, one-way ANOVA test). (**d**) Relative MitoSOX fluorescence (n=3, one-way ANOVA test) and (**e**) extracellular ATP concentration (n=4, one-way ANOVA test) of the indicated groups. (**f**) Schematic representation showing the up- or down-regulation of metabolites of the TCA cycle after hepatocyte infection with lentiviral particles or in the presence of recombinant RBD (n= 3, one-way ANOVA). (**g**)

Extracellular lactate concentration (n=4, one-way ANOVA test) and (**h**) intracellular glucose concentration (n=4, one-way ANOVA test) of the indicated groups. Asterisks represent p values (*<0.05, **<0.01 and ***<0.001).

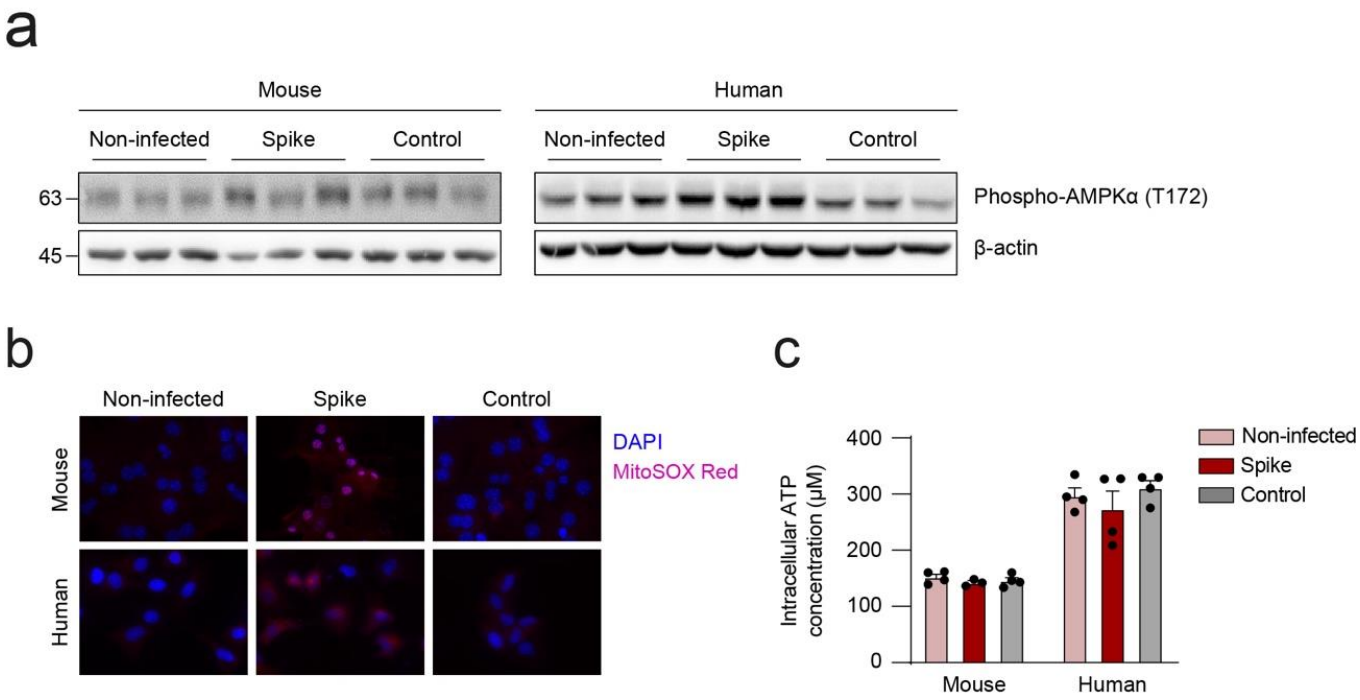

Supplementary Figure 11. Binding of the spike of SARS-CoV-2 alters mitochondrial activity and glucose homeostasis in hACE2 and human primary hepatocytes. (**a**) Western blot showing the expression of phospho-AMPKα (T172) protein on hACE2 (*left*) and primary human hepatocytes (*right*) infected with lentiviral particles expressing the spike protein or control. (**b**) Representative images of hACE2 and human hepatocytes labelled with MitoSOX for the indicated conditions. (**c**) Intracellular ATP concentration in both mouse (hACE2) and human primary hepatocytes after infection with the indicated lentiviral particles (n= 4, one-way ANOVA).

a

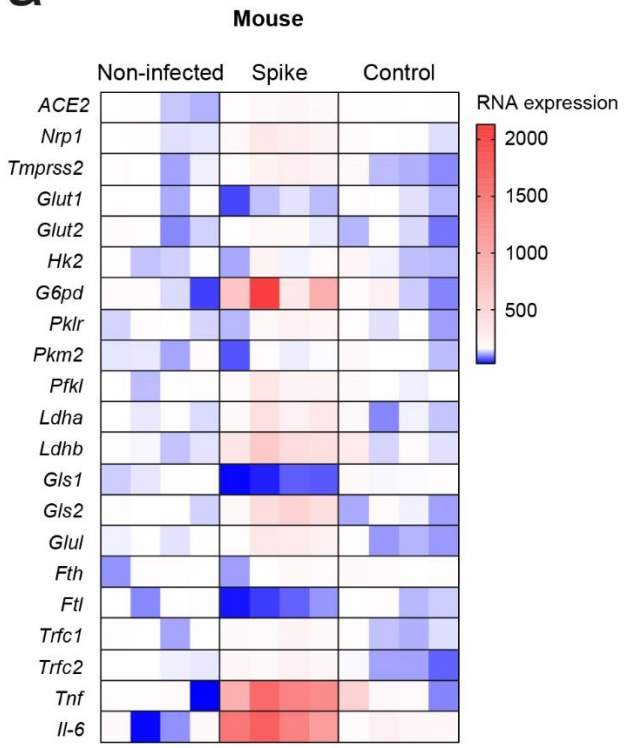

	Non-infected *vs.* Spike	Control *vs.* Spike	Non-infected *vs.* Control
ACE2	*	*	ns
Nrp1	**	*	ns
Tmprss2	*	*	ns
Glut1	ns	ns	ns
Glut2	ns	ns	ns
Hk2	ns	ns	ns
G6pd	p=0.05	ns	ns
Pklr	p=0.07	p=0.06	ns
Pkm2	ns	ns	ns
Pfkl	*	p=0.06	ns
Ldha	*	*	ns
Ldhb	*	**	ns
Gls1	***	***	ns
Gls2	*	*	ns
Glul	*	*	ns
Fth	ns	ns	ns
Ftl	*	*	ns
Trfc1	**	**	ns
Trfc2	**	***	ns
Tnf	***	***	ns
Il-6	ns	ns	ns

b

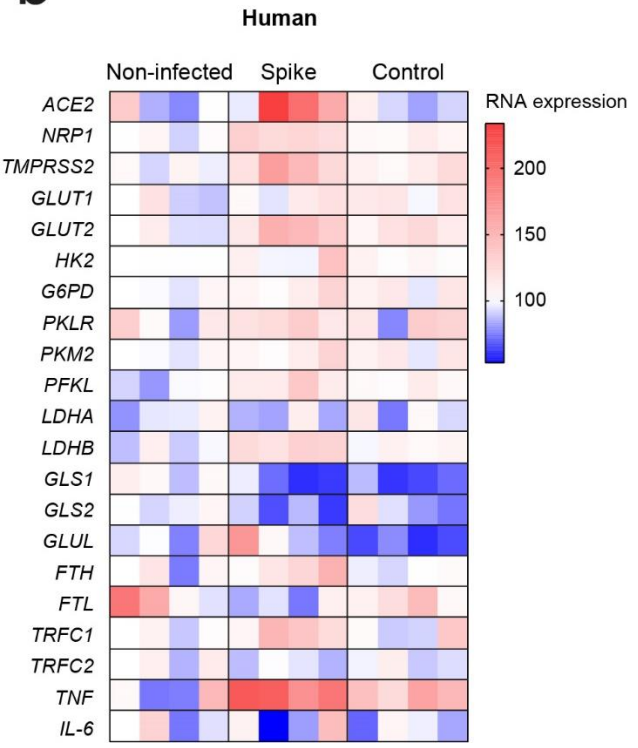

	Non-infected *vs.* Spike	Control *vs.* Spike	Non-infected *vs.* Control
ACE2	p=0.06	ns	ns
NRP1	***	***	ns
TMPRSS2	**	*	ns
GLUT1	ns	ns	ns
GLUT2	*	ns	ns
HK2	ns	ns	ns
G6PD	p=0.06	ns	ns
PKLR	p=0.06	ns	ns
PKM2	ns	ns	ns
PFKL	ns	ns	ns
LDHA	ns	ns	ns
LDHB	**	**	**
GLS1	**	ns	**
GLS2	*	ns	ns
GLUL	*	ns	*
FTH	ns	*	ns
FTL	ns	ns	ns
TRFC1	*	ns	ns
TRFC2	ns	ns	ns
TNF	**	*	ns
IL-6	ns	ns	ns

Supplementary Figure 12. Binding of the spike of SARS-CoV-2 alters mitochondrial activity and glucose homeostasis in hACE2 and human primary hepatocytes. (**a, b**) RNA expression of genes related to SARS-CoV-2 infection and inflammatory

responses, as well as other related with glucose, lactate and glutamine metabolism on mouse (*a*) and human (*b*) hepatocytes after infection with pseudotyped viral particles expressing the spike of SARS-CoV-2 or controls (n=4, one-way ANOVA). Asterisks represent p-values (*<0.05, **<0.01 and ***<0.001).

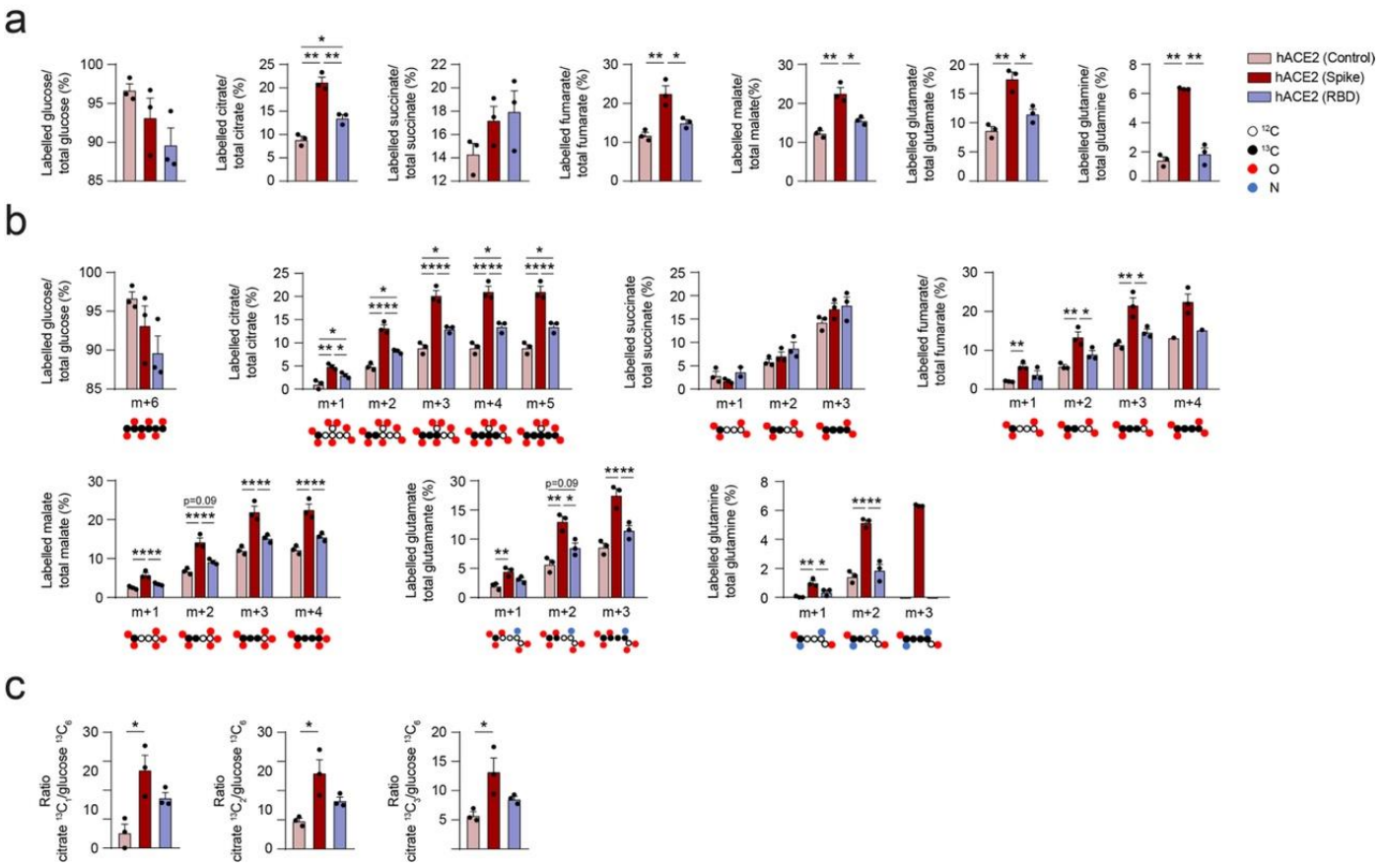

Supplementary Figure 13. Binding of the spike of SARS-CoV-2 alters mitochondrial activity and glucose homeostasis in hACE2 and human primary hepatocytes. (**a**) Percentage of total labelled carbons of each metabolite (glucose, citrate, succinate, fumarate, malate, glutamate and glutamine) related to their total levels measured on hACE2 hepatocytes exposed to pseudotyped viral particles or recombinant RBD (n=3, one-way ANOVA). (**b**) Percentage of every labelled carbon (^{13}C) of the metabolites analyzed related to their total amount (n= 3, one-way ANOVA). (**c**) Ratios between 1/2/3-^{13}C (citrate) related to 6-^{13}C (glucose) (n= 3, one-way ANOVA). Abbreviations: α-KG: α-ketoglutarate; ^{12}C: carbon-12 molecule; ^{13}C: carbon-13 isotope; O: oxygen molecule; N: nitrogen molecule. Asterisks represent p values (*<0.05 and **<0.01).

R.2.5. Infection of primary hepatocytes regulates the renin-angiotensin system

ACE2 is a key enzyme of the RAS that converts angiotensin AngII to Ang 1-7. A reduction in the presence of ACE2 in the cell membrane alters the balance of RAS toward an increase in AngII. Therefore, the activation of the Ang 1-7/Mas receptor is an important mechanism for counteracting the deleterious effects induced by inappropriate increases in the AngII/AT1 receptor in several diseases[430].

Remarkably, Ang 1-7 levels were significantly reduced in human primary hepatocytes after infection (**Figure R.13A**), corresponding to ACE2 inhibition after the binding of the spike. Treatment with A779, a pharmacological inhibitor of the ACE2/Ang 1-7/Mas

axis, increased the susceptibility of mouse and human primary hepatocytes to infection (**Figures R.13B and R.13C**). No apoptotic response was detected at 0.1 and 1μM concentrations of A779 (**Figures R.S14A and R.S14B**). These results are consistent with previously observed data showing that an imbalance of AngII/ Ang1-7 influences susceptibility to SARS-CoV-2 infection[431]. Treatment with A779 increased mitochondrial ROS in mouse and human hepatocytes upon infection (**Figures R.13D and R.S14C**). Accordingly, significant changes were also observed in the level of ATP production upon treatment with A779 (**Figure R.13E**). The blockade of the RAS system in primary hepatocytes by using the Mas inhibitor A779 showed comparable metabolic effects to those observed upon infection with pseudotyped lentiviral particles expressing the spike of SARS-CoV-2 (**Figures R.12D and R.12E**). During infection, an interaction between the spike and ACE2 occurs, inhibiting RAS signal transduction. Thus, activation of the Mas receptor may counteract the inflammatory response mediated by SARS-CoV-2 infection in primary hepatocytes.

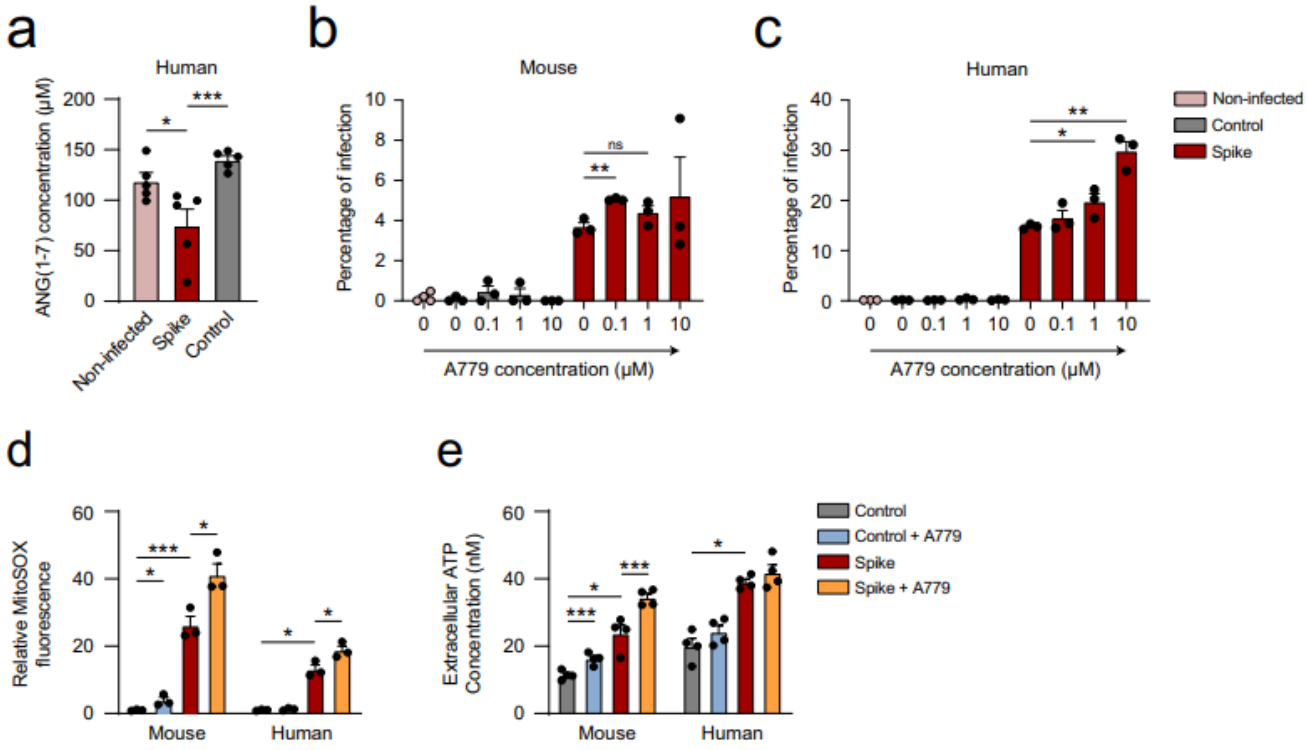

Figure R.13. Infection of primary hepatocytes regulates the renin-angiotensin system. (**a**) Extracellular levels of Ang 1-7 secreted by human primary hepatocytes after infection with pseudotyped viral particles compared to controls, measured by ELISA (n=5, one-way ANOVA). (**b**, **c**) Percentage of infected hACE2 (*b*) or human (*c*) primary hepatocytes after infection with pseudotyped viral particles or controls in the presence of different doses of A779, measured by flow cytometry (n=3, one-way ANOVA). (**d**) Relative MitoSOX fluorescence (n=3, one-way ANOVA) and (**e**) extracellular ATP concentration (n=4, one-way ANOVA test) of the indicated groups. Error bars represent SEM and asterisks represent p-values (*<0.05, **<0.01 and ***<0.001).

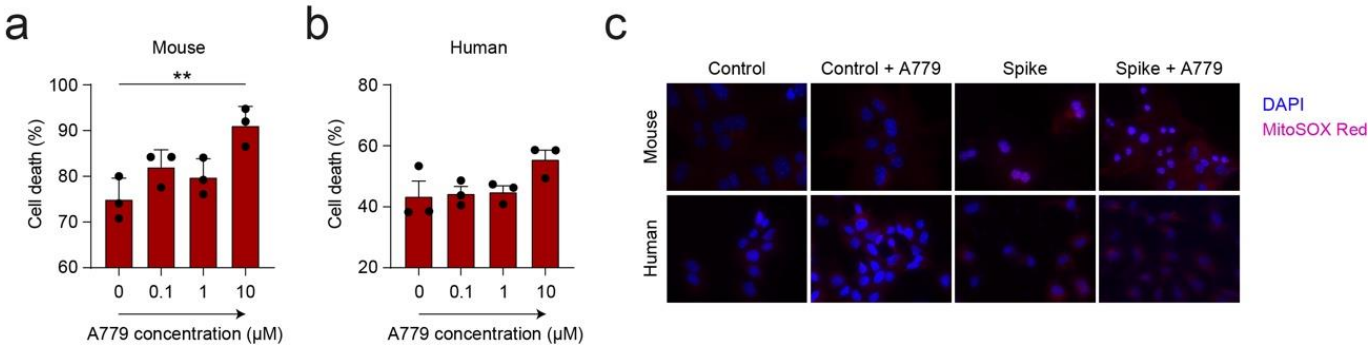

Supplementary Figure 14. Infection of primary hepatocytes regulates the renin-angiotensin system. (**a, b**) Percentage of cell death corresponding to hACE2 (*a*) and human (*b*) primary hepatocytes after infection with pseudotyped lentiviral particles expressing the spike of SARS-CoV-2 in the presence of the indicated doses of A779 or vehicle control, measured by flow cytometry (n=3, one-way ANOVA). (**c**) Representative images of hACE2 and human hepatocytes labelled with MitoSOX after infection with pseudotyped viral particles or controls in the presence or absence of A779 (mouse: 0.1 μM; human: 1μM). Error bars represent SEM and asterisks represent p-values (**<0.01).

R.2.6. Dysregulation of hepatocyte mitochondrial activity modulates ACE2 levels and increases susceptibility to infection

Metabolic alterations associated with obesity, fatty liver disease and T2D have been described as risk factors for COVID-19[432]. In this context, understanding the broad spectrum of factors that shape SARS-CoV-2 pathophysiology in patients with MASLD remains a pressing issue. We have recently reported that the liver of patients with MASLD presents increased levels of *ACE2* and *TMPRSS2*[433].

In order to provide new insights related to the regulation of the viral entry points in the liver, primary hepatocytes isolated from a humanized ACE2 mouse model were exposed to steatotic insults. ACE2 levels were significantly elevated in a time-dependent manner in hACE2 hepatocytes cultured in medium deficient in methionine and choline (MCD) that triggers the accumulation of lipids and the production of ROS, generating mitochondrial dysfunction[434]. Additionally, NRP1, which is known to bind furin-cleaved substrates and potentiates SARS-CoV-2 infectivity, was also induced in steatotic hepatocytes (**Figure R.14A**). Indeed, NRP1 has a critical role in liver fibrosis and cirrhosis pathogenesis[435,436].

Metformin is an antidiabetic drug widely used in patients with MASLD[437]. Metformin acts by inhibiting the activity of Complex I of the mitochondrial respiratory chain directly modulating ATP production in the cell[438,439]. Recently, metformin has been proposed as a potential therapy for COVID-19 patients[440,441], although its role in clinical disease progression remains controversial. Therefore, we have evaluated if metformin has any impact on the success of viral entry in hACE2 hepatocytes. Treatment with metformin significantly reduced the levels of ACE2 and NRP1 proteins in hACE2 hepatocytes in a time dependent manner (**Figure R.14B**). Notably, metformin was able to diminish the levels of ACE2 and NRP1 in stimulated steatotic hepatocytes to a similar content of that of healthy hACE2 liver cells (**Figure R.14C**). A similar result was observed at the transcriptional level of *Ace2* and *Nrp1* (**Figure R.S15A**). Importantly, the expression of *Tmprss2* was induced in steatotic conditions and reduced upon treatment with metformin (**Figure R.S15A**). These results were also examined in human primary hepatocytes under steatotic conditions and in the presence or absence of metformin (**Figure R.S15B**). Induction of *ACE2, NRP1 and TMPRSS2* expression under steatotic conditions were identified, as described previously (**Figure R.S15B**)[433]. In these conditions, metformin was able to reduce *their* expression (**Figure R.S15B**).

Steatotic hACE2 hepatocytes exposed to pseudotyped viral particles expressing the spike of SARS-CoV-2 showed higher susceptibility to infection compared to healthy cells (**Figure R.14D**). Metformin is able to significantly reduce the increased infection rate observed in metabolically compromised hepatocytes. Human primary hepatocytes showed a similar response in cells treated with MCD in the presence or absence of metformin (**Figure R.14D**). Finally, we studied the effect of metformin on the RAS system

upon infection with pseudotyped lentiviral particles expressing the spike of SARS-CoV-2 (**Figure R.14E**). Levels of Ang 1-7 measured by ELISA were upregulated under steatotic conditions (**Figure R.14E**). Activation of the counterregulatory ACE2/Ang1-7/Mas axis has been shown to prevent liver injury[442]. Therefore, metformin significantly reduced Ang 1-7, likely due to the reduction in oxidative stress and thus reduced liver injury (**Figures R.14E, R.S15A and R.S15B**). According to this, *TNF* and *IL-6* gene expression were upregulated when metformin was present (**Figures R.S15A and R.S15B**).

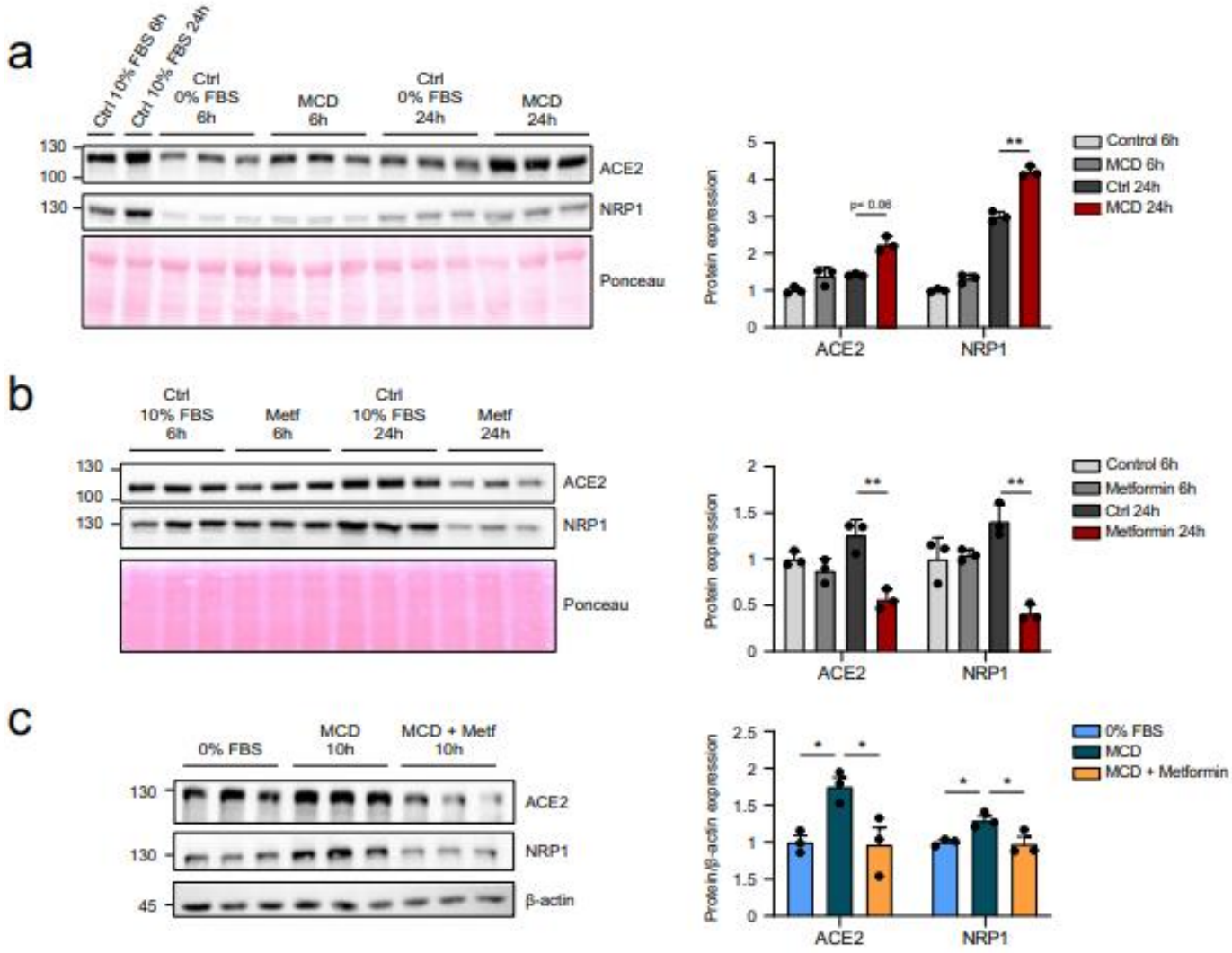

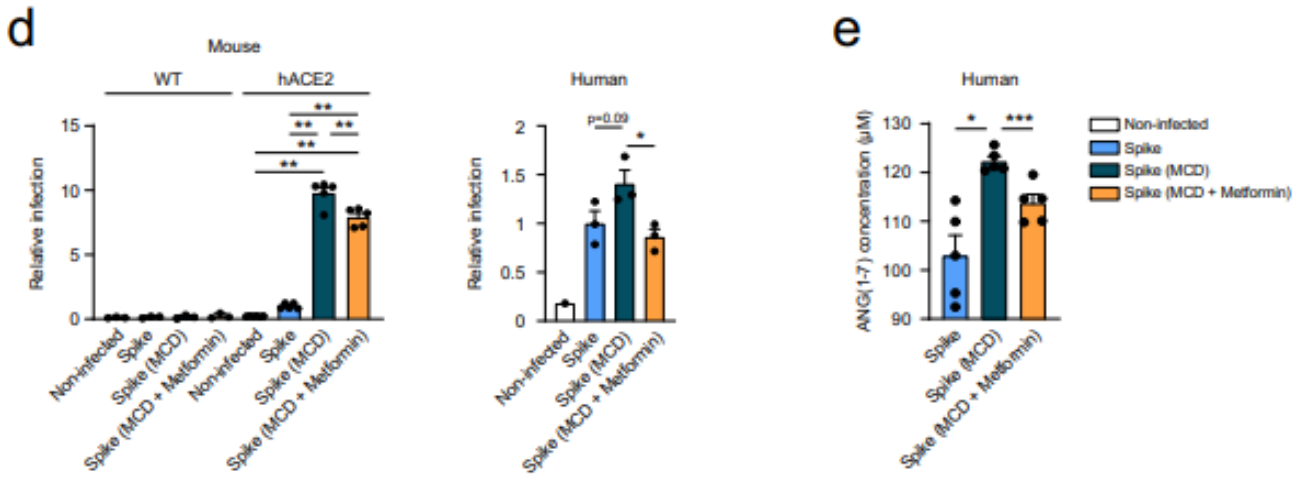

Figure R.14. Dysregulation of hepatocyte mitochondrial activity modulates ACE2 levels and increases susceptibility to infection. (**a**) Western blot showing the modulation of ACE2 and NRP1 protein expression when incubated with methionine-choline deficient (MCD) medium for 6 hours and 24 hours (along with their respective controls. Quantification of ACE2 or NRP1 protein expression by densitometry is also shown (n=3, unpaired t test). (**b**, **c**) Western blot showing the expression of ACE2 and NRP1 protein expression when treated with 1mM metformin for 6 or 24 hours (n=3, unpaired t test) (*b*) or with MCD or MCD plus 1mM metformin for 10 hours (n=3, one-way ANOVA) (*c*) as well as their respective controls. Relative quantification of ACE2 or NRP1 protein expression (related to β-actin) is also shown. (**d**) Relative infection with pseudotyped viral particles or controls of WT or hACE2 mouse hepatocytes (*left*) or upcyte second-generation human hepatocytes (*right*) upon treatment with MCD or MCD and metformin, measured by flow cytometry (one-way ANOVA). (**e**) Extracellular levels of Ang 1-7 secreted by human primary hepatocytes after infection with pseudotyped viral particles upon treatment with MCD or MCD and metformin, measured by ELISA (n=5, one-way ANOVA). Error bars represent SEM and asterisks represent p-values (*<0.05, **<0.01 and ***<0.001).

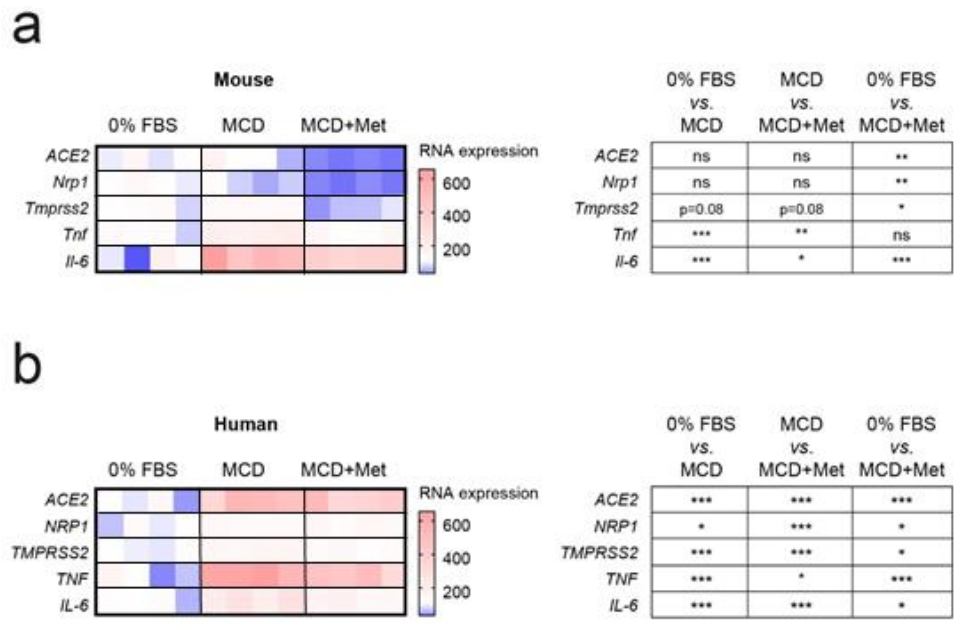

Supplementary Figure 15. Dysregulation of hepatocyte mitochondrial activity modulates ACE2 levels and increases susceptibility to infection. (**a, b**) RNA expression of the indicated genes on mouse (*a*) and human (*b*) hepatocytes treated with MCD or MCD+Meftormin (Met) compared to controls (0% FBS). Asterisks represent p-values (*<0.05, **<0.01 and ***<0.001).

Discussion

D.1. Study 1

In the first study, we have explored the therapeutic potential of silencing CNNM4 as an oncogenic driver in CCA, a malignancy characterized by its aggressive nature and limited treatment options. Over recent years, advancements in cancer research have led to a growing interest in the development of novel and targeted therapeutic approaches for this malignant biliary tract cancer. Our findings demonstrated a general increase in CNNM4 expression in CCA tumors from 8 independent cohorts as well as in 2 mouse models and in 2 CCA cell lines when compared to respective control. For the first time, we have described the effluxer capacity of CNNM4 in cholangiocytes. Silencing of CNNM4 inhibited cholangiocarcinogenesis in various CCA models, including in *in vitro*, in the CAM, and in *in vivo* studies. Moreover, spectrometry analysis following CNNM4 silencing revealed an enhanced ferroptosis pathway attributed to the downregulation of NUPR-1.

Mg^{2+} plays a crucial role in cancer physiopathology, contributing to metabolic and physiological functions that can influence carcinogenesis. Epidemiological studies have identified Mg^{2+} deficiency as a risk factor for certain human cancers, including CCA.[443]. Furthermore, *in vivo* studies demonstrate that animals fed an Mg^{2+}-deficient diet developed more lung metastases than controls[444]. This could be attributed to the intense inflammatory response triggered by Mg^{2+} deficiency, which may promote cancer progression by fostering the presence of inflammatory cells and mediators in the tumor microenvironment[445]. Accordingly, our study reveals that silencing *CNNM4* is associated with a decrease in inflammation-related pathways. Moreover, Mg^{2+} is indispensable for activating the NOX, a primary source of ROS[446]. Conversely, lowering cellular Mg^{2+} has been associated with decreased ROS in a TRPM7 knock-down neuronal model[447]. Mg^{2+} serves as a cofactor for over 600 enzymes and an activator of an additional 200 enzymes, including ATP, which is only active when bound to Mg^{2+}[10]. ATP is crucial for iron receptor-mediated endocytosis, as it acidifies the lumen of the endocytic vesicle through the action of H^{+}-ATPase, releasing iron from transferrin. Therefore, elevated intracellular Mg^{2+} levels may potentiate iron uptake by the cell, thereby enhancing ROS production via the Fenton reaction[448].

Silencing of *CNNM4* in two CCA cell lines reduces their cell density, regardless of the addition of magnesium in medium. In contrast, when silencing CNNM4 in a normal cholangiocyte cell line, there was no significant change in proliferation. Furthermore, CNNM4-silenced CCA cell lines showed increased levels of *PTEN* expression. These data are consistent with previous findings showing how inhibiting miR-10a-5p, whose predictor target is CNNM4, can interact with PTEN, ultimately suppressing the growth of cholangiocarcinoma cells[449]. In turn, several studies have demonstrated the suppressive effect of the AKT signaling pathway on

ferroptosis via SREBP-mediated lipogenesis[450–453], in hepatocellular carcinoma as well[454]. Indeed, the AKT pathway prevents ferroptosis-induced cell death in IDH-mutated glioma cells, a mutation reported in 15-20% of iCCA patients and currently considered a potential therapeutic target[455,456]. In our study, the downstream effects of silencing CNNM4 on ferroptosis are mediated by a reduction in NUPR-1 levels, mechanism under scrutiny for their multiple beneficial impacts on cancer.

The effects induced by *CNNM4* silencing are interconnected and driven by the increased production of ROS resulting from ferroptosis. Currently, cancer polytherapy, which includes radiotherapy, chemotherapy, immunotherapy and molecular targeted therapy represents the standard approach to unresectable CCA treatment[457]. However, the long-term survival of patients is significantly hindered by tumor drug resistance[458]. Ferroptosis has recently been associated with drug resistance in tumors[459]. Tumor cells maintain a precise balance in the generation of ROS, which is often influenced by iron overload. When these tumor cells are exposed to drugs, such as cisplatin in the case of CCA, they trigger the production of large amounts of ROS, representing a significant challenge to their survival. Subsequently, tumor cells activate specific mechanisms to alter their metabolic microenvironment and suppress ROS formation, ultimately leading to the development of drug resistance[460]. Therefore, ferroptosis plays a pivotal role in resistance of tumoral cells to drugs by producing ROS, consequently increasing their sensitivity to chemotherapeutic treatments[461]. In our study, silencing of *CNNM4*-induced ferroptosis not only sensitizes CCA cells to cisplatin, doxorubicin, gemcitabine and 5-fluorouracil, the most used drugs in CCA treatment, but also results in an increased generation of ROS in the mitochondria. A similar outcome was observed when genetic and pharmacological inhibition of HO-1, a crucial cytoprotective enzyme in ferroptosis, made CCA cell lines more susceptible to the cytotoxicity of gemcitabine and doxorubicin, along with induction of intracellular ROS generation[462]. It is believed that this tumor chemoresistance is attributed to different factors: tumor heterogeneity, the tumor microenvironment, and potentially its origin, CSCs[461].

CSCs or tumor-initiating cells (TICs), a small but essential subpopulation of cells, preside over the hierarchy within the tumor and possess the capacity for self-renewal, proliferation and differentiation into diverse cell populations that constitute the tumor[463]. CSCs particularly depend on iron, requiring it more than non-CSCs[464]. Consistently, iron supplementation promotes CSC-like features in CCA cells whereas iron chelator treatment impairs their ability to form spheroids[465]. However, maintaining ROS balance plays a crucial role for CSCs integrity, since elevated ROS levels result in the impairment of self-renewal and differentiation and increases the sensitivity of CSCs to radiotherapy in different cancer types[464]. Our results demonstrated that baseline

CNNM4 levels in CCA cells correlate with enhanced spheroid-forming ability (a capacity used by many groups to assess CSC activity[466]) and higher CSCs markers, compared to silenced *CNNM4* cells. Additionally, in 2D culture, *CNNM4*-silenced CCA cells also exhibit lower levels of CSCs markers compared to control cells. Accordingly, Zhu *et al.* demonstrated that FBXO31 promotes cisplatin-induced ferroptosis in CCA and in CSC-like cells[467].

Fewer than 1% of cells in a tumor possess the ability to trigger angiogenesis and eventually form metastases in distant organs. Metastatic cancer stem cells (MCSCs), a subgroup of CSCs, have been proposed as potential candidates responsible for metastasis due to the stem cell properties and invasion abilities that facilitate cancer metastasis[468,469]. Regarding CNNM4's role in metastasis, lower CNNM4 levels in CCA cells showed no invasion into the subjacent tissue, migrated less into the vessels and hardly any cell was observed forming metastasis in the lungs in *ex ovo* and *in ovo* CAM model, relative to CCA cells with normal CNNM4 levels. Furthermore, proteomic analysis revealed a downregulation of pathways related to cell proliferation, EMT and tumor invasion in *CNNM4*-silenced CCA cells. Importantly, liver tissue of mice exposed to *CNNM4* siRNA exhibited decreased SOX9 and EpCAM immunoreactivity. SOX9 and EpCAM, CSC markers, are associated with cell migration and invasion through EMT in various cancers[470]. Several studies highlighted the vulnerability of cancer cells resistant to conventional treatments or prone to metastasize to ferroptosis[471–473]. Ferroptosis is inversely correlated with metastasis across multiple cancer types, inhibiting cell proliferation, migration and invasion [474–476]. In the context of esophageal squamous cell carcinoma, ferroptosis inhibits cell proliferation, migration, and invasion [474]. Similarly, the overexpression of SLC7A11, a key component of the ferroptosis pathway responsible for the cystine-glutamate exchange, is associated with a higher tumor-nodule-metastasis stage and a poorer prognosis in human HCC[475]. Moreover, neratinib has been shown to trigger ferroptosis and prevent brain metastasis in a novel syngeneic model of spontaneous HER 2-positive breast cancer brain metastasis[476]. Inhibition of metastasis process may be attributed to ROS-mediated damage, as demonstrated by 2,2'-dipyridone hydrazone dithiocarbamic acid and by HDAC inhibitor[477,478]. This evidence supports the role of ferroptosis in preventing tumor metastasis.

The Warburg effect is a characteristic feature of cancer, describing the metabolic shift that occurs when a cell transforms into a cancerous state, and has been linked to metastasis, as it facilitated its progression[479,480]. This shift is driven by the increased proliferation of cancer cells, resulting in elevated demands for both anabolic and bioenergetic processes. To meet these increased requirements, cancer cells exhibit higher rates of glucose uptake and glycolysis, and cancer cells preferentially convert pyruvate into lactate, even in the presence of

oxygen, primarily by LDH[480]. In the context of CCA, several potential therapeutic targets have been identified with a focus on disrupting the upregulation of glycolysis and altering mitochondrial energy metabolism to impede disease progression[481]. To investigate the contribution of CNNM4 in this metabolic effect, our study employed a multi-faceted approach. Administration of a glucose competitive analogue, Seahorse Extracellular Flux Analyzer and lactate production analyses showed that silencing *CNNM4* effectively suppressed the Warburg effect in CCA cells. Moreover, our approach by mass spectrometry assays revealed a downregulation in several key energetic metabolic pathways. In TFK-1 cells, this primarily affected glucose catabolism pathways, possibly influenced by *TP53* gene mutations that, in part, regulates energy metabolism by promoting glycolysis in cancer[482]. Simultaneously, EGI-1 cells exhibited a downregulation in oxidative respiration. Recently, CCA has been proposed to depend on mitochondrial oxidative phosphorylation, contributing to the CSC phenotype[483]. Furthermore, the metabolic shift was mirrored in our *in vivo* model, with mice treated with siRNA for *CNNM4* showing reduced serum glucose levels, a known driver of cell proliferation in patients with CCA[484]. Fresh liver and isolated mitochondria from these animals showed less glycolytic and energetic phenotype, respectively. Cellular metabolic reprogramming shares common features with ferroptosis, including glutamate, NADPH, GSH or ROS[485]. Glutaminolysis, the process in which glutamine is converted into glutamate by glutaminase (GLS) to ultimately produce α-KG for supplying energy in the TCA cycle, has been shown to promote ferroptosis since glutamate is essential for the SLC7A11/GHS/GPX4 pathway[486]. Indeed, glutamine synthase 2 (GLS2) induces ferroptosis by depleting the available glutamate[487]. Several intermediates from the TCA cycle, including IDH1, inhibit tumor progression in CCA by making cells more susceptible to ferroptosis[488]. Reduction power is crucial in the three ferroptosis antioxidant axes and is also associated with other ferroptosis inhibitors such as *de novo* synthesis and fatty acid elongation. The generation of NADPH involves metabolic processes like the pentose phosphate pathway (PPP) and isocitrate conversion to α-KG[486]. Interestingly, these processes are downregulated in *CNNM4*-silenced cells, as revealed by proteomic analysis. Furthermore, during ferroptosis, glycolysis decreases concomitantly with the irreversible mitochondrial damage caused by oxidative stress, compromising organelle integrity, ultimately leading to energy depletion and cell death[486].

In brief, cancer cells generate elevated ROS levels due to their increased metabolic needs. Moderately increased levels of ROS can induce the activation of receptors, oncogenes and growth factor-dependent pathways, ultimately leading to the activation of oxidizing enzymes and causing genetic instability. Moreover, elevated ROS levels can influence the mobility and invasiveness of cancer cells, participate in remodeling the

extracellular matrix, enhance neo-angiogenesis and induce metabolic changes in both cancer and stromal cells[489,490]. However, oxidative stress is commonly recognized as the "double-edged sword" in cancer, as overwhelming levels of ROS make cancer cells more susceptible to death[490]. Hence, ferroptosis could be a potential tumor suppressor event in CCA that could be used in combination with other anticancer therapies[491]. Specifically, siRNA targeting *CNNM4* promotes ferroptosis by downregulating NUPR-1 in CCA cells, which is accompanied by increased ROS production.

In the iCCA-induced mice model of this study, GalNAc-*CNNM4* siRNA, a molecule that specifically targets the ASGPR found exclusively in hepatocytes, was employed to target CNNM4 expression. GalNAc siRNA technology is now being successfully employed used in clinical praxis, with even more compounds in clinical development[492]. It offers stability, favourable pharmacokinetics, liver -specificity, durable target gene inhibition with infrequent dosing, easy administration and low immunogenicity[493]. Why do we see differences in cholangiocarcinoma, a disease that occurs in the bile duct, when treating hepatocytes? Initial evidence emerged from viral hepatitis patients who often develop iCCA[494–497]. Then, Sekiya *et al.* showed that some CCA cells potentially arise though hepatocytes dedifferentiation via *NOTCH* activation[498]. In line with this, iCCA's origins in fully differentiated hepatocytes were shown when *Notch* and *Akt* were induced in mouse model using the sleeping-beauty transposon system[404]. Two more sleepy-beauty mouse models have been established for studying CCA, one of which was utilized in this study[405,406]. Additionally, some authors successfully transformed iCCA cells into functional hepatocytes using organoid cultures, supporting the hypothesis that iCCA may derive from hepatocytes[499]. While this theory is gaining support, the exact percentage of CCA patients whose condition originates from hepatocytes remains unknown. It represents a mystery and further evaluation could aid in the discovery of additional drugs for this disease.

Broadly translated, our findings reveal a novel therapy for CCA: silencing of *CNNM4* inhibits progression and growth by reversing key cancer hallmarks. This approach induces ferroptosis-mediated ROS production, enhancing CCA cells sensitivity to chemotherapy, reducing CSC population, halting metastasis and preventing metabolic reprogramming alterations. We suggest further investigating GalNAc CNNM4 siRNA as a potent, long-lasting, and well tolerated compound targeting CNNM4 to the liver for treatment of CCA patients.

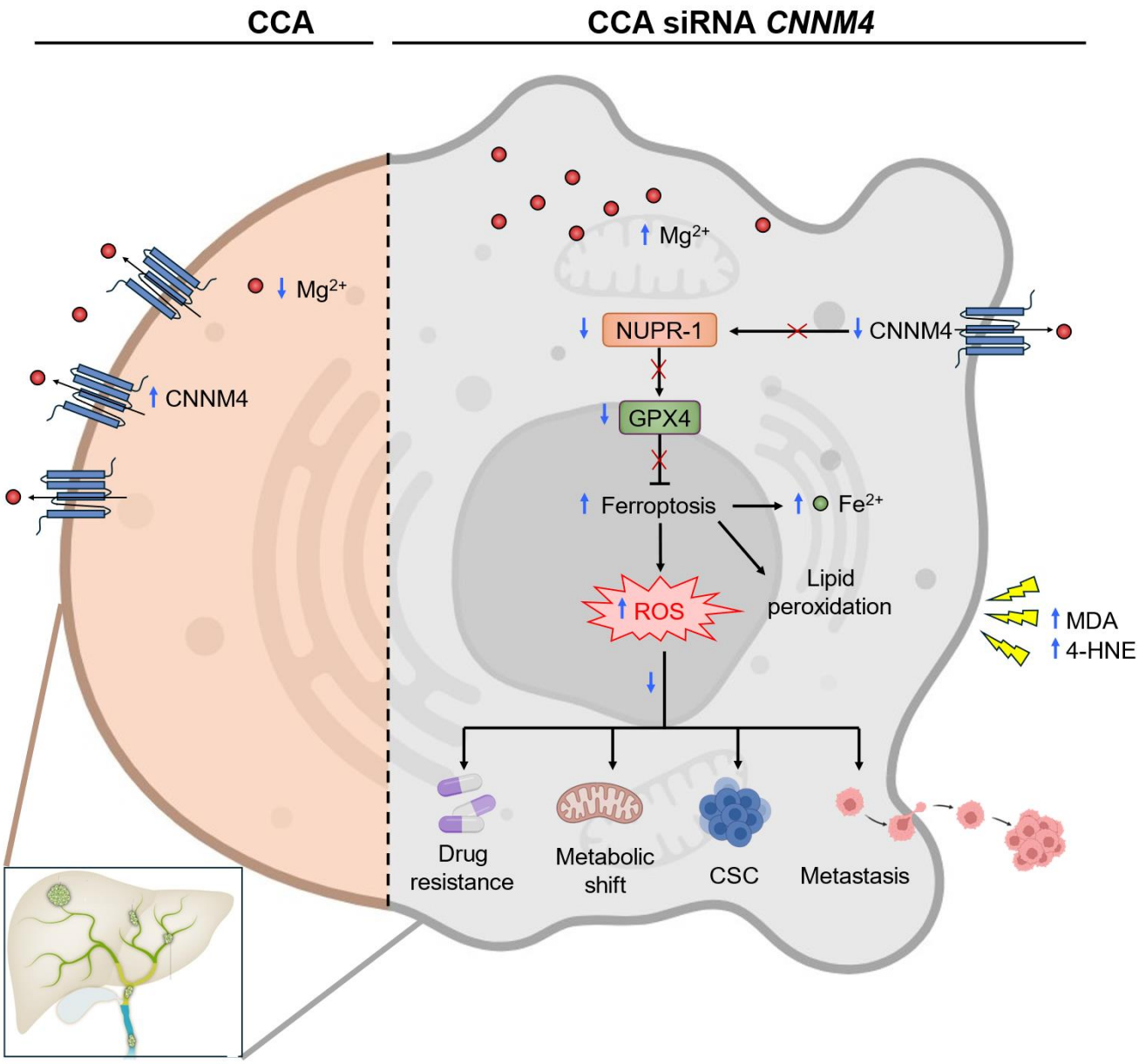

Figure D.1. Graphical abstract from study 1. Liver-targeted silencing of CNNM4 leads to the downregulation of NUPR-1 levels, impairing the cell's antioxidant capacity. This results in increased ROS production via the Fenton reaction, driven by an accumulation of reactive labile iron ions, causing membrane peroxidation and ultimately leading to ferroptosis. This process decreases tumor-related phenomena, including drug resistance, metabolic shifts, cancer stem cell capacity, and metastasis. Abbreviations: Mg^{2+}, magnesium ion; CNNM4, cyclin M4; NUPR-1, nuclear protein 1; GPX4, glutathione peroxidase 4, Fe^{2+}, ferrous ion; ROS, reactive oxygen species; MDA, malondialdehyde; 4-HNE, 4-hydroxynonenal.

D.2. Study 2

The impact of SARS-CoV-2 on the liver has been extensively debated. The high incidence of COVID-19 patients with elevated transaminases may be due to a compromised detoxifying capacity of the liver in these poly-treated patients, the response to a proinflammatory environment, the hypoxia state of hepatocytes due to a reduction in the hepatic blood flow or the possible tropism of SARS-CoV-2 to the liver. On the other hand, liver disease is a risk factor for severe COVID-19 pathology as described in MASLD patients[500]. Given the controversial information of SARS-CoV-2 tropism to the liver, we have demonstrated that pseudotyped viral particles expressing the full-length spike of SARS-CoV-2 were able to infect human primary hepatocytes as well as hepatocytes isolated from a humanized hACE2 mouse model. Mass spectrometry analysis revealed that in primary hepatocytes infected with pseudotyped lentiviral particles expressing the spike of SARS-CoV-2, the main molecular processes dysregulated were mitochondria-dependent. Specifically, fluxomics analyses revealed an increase in the TCA activity in hACE2 and human primary hepatocytes as a result of infection with pseudotyped viral particles or binding of recombinant RBD, indicating a shift to a glycolytic phenotype induced by ACE2 after binding of the spike. In the present study we have also dissected hepatic expression patterns of SARS-CoV-2 viral entry points under steatotic conditions, demonstrating a higher susceptibility to infection of steatotic hepatocytes. Finally, we have reported new insights in the beneficial effects of metformin treatment in patients with MASLD as a result of a significant reduction of hepatic ACE2 content and reduced predisposition to infection.

Several reports provided the first data supporting the notion that hepatic cells are permissive for SARS-CoV-2 infection and viral replication, but the usage of immortalized hepatoma cell models instead of primary hepatocytes limited the depth of their findings[501–503]. More recently, several studies have provided further evidence by using organoids derived from human hepatocytic stem cells demonstrating that the liver could be a potential target of SARS-CoV-2[504–506]. Although other hepatic cell types like cholangiocytes showed higher expression of ACE2 than hepatocytes, no direct evidence of infection in these cells have been reported in the liver of patients with COVID-19 in spite of the fact that viral particles compatible with SARS-CoV-2 were identified by electron microscopy techniques in the hepatocytes from COVID-19 autopsies[318,506]. These data encourage a rigorous study of the permissiveness of the liver to SARS-CoV-2 infection and its potential cytopathic effect that could explain the deleterious effects identified in COVID-19 patients. The models presented in this study include a non-transformed human hepatocyte cell line, primary hepatocytes obtained from humanized hACE2 transgenic mice and upcyte second-generation human hepatocytes. These

approaches demonstrate that the spike of SARS-CoV-2 binds to ACE2 expressed in primary hepatocytes and identify the hepatocyte as a susceptible cell target for SARS-CoV-2 infection. This information may be relevant for clinical treatment of COVID-19 patients, considering that liver functionality may be compromised by infectivity.

Furthermore, our approach by mass spectrometry analysis revealed a molecular mechanism in hACE2 hepatocytes that compromised mitochondrial activity as a result of infection. Previous data have shown that the depletion of the Ang 1-7 receptor *Mas* in hepatocytes aggravates mitochondrial dysfunction, increased mitochondrial ROS, induced fatty acid synthesis and impaired cholesterol synthesis/efflux[426]. Hence, lipid alteration and insulin resistance in the hepatocytes, concomitant with an apoptotic process was observed in the hepatocytes *Mas*$^{-/-}$. These data are consistent with our proteomics results where a possible ACE2 inhibition mediated mitochondrial dysfunction has been detected. Indeed, iron metabolism appeared significantly overrepresented in infected hACE2 hepatocytes. Increased iron uptake upon viral infection would increase mitochondrial ROS[424]. Accordingly, Saleh *et al.* described that severity in COVID-19 patients was associated with a hyperferritinemia[507]. Our data sustain the idea that this misbalance in iron metabolism and mitochondrial ROS production could partly result from the alteration in the cellular oxidative homeostasis promoted by an exacerbated mitochondrial activity in infected mouse and human primary hepatocytes, triggering an apoptotic response.

A metabolic reprogramming similar to Warburg effect in cancer cells has been previously identified in the host cells under SARS-CoV-2 infection[508]. Fluxomics analyses revealed that infected hACE2 hepatocytes present a glycolytic phenotype characterized by higher production of lactic acid and a more active TCA. Experiments performed in human primary hepatocytes further evidenced a modulation of intracellular glucose and extracellular lactate upon infection. These data are consistent with previous work showing that viral infection promotes glycolysis[509]. Remarkably, in our fluxomics results performed with the primary hepatocytes, infection resulted in an increase of fumarate and malate. This altered glycolytic metabolism could support the replication of the virus in the liver and may also contribute to evade cytotoxic immune responses by acidifying the extracellular compartment.

Infection of hACE2 hepatocytes resulted in disturbances in glucose and glutamine metabolism. In these circumstances, enhancement of glutaminolysis metabolism with upregulation of glutamate levels and triggering of TCA was also detected. This metabolic pathway has been identified as a key player in infected

host cells, as previously reported for other viruses, and may trigger replication of SARS-CoV-2[510]. Our group has previously described the alteration of this anaplerotic pathway with upregulation of the enzyme glutaminase 1, which is responsible for glutamine catabolism in the liver of patients with MASLD[511]. Therefore, there might be a glutamine-dependent link between liver disease and SARS-CoV-2 infection.

The described metabolic switch was mediated in part by inhibition of the RAS system through the interaction between the spike and ACE2. Indeed, inhibition of the Mas receptor with A779 amplified the observed phenotype. MASLD patients showed elevated levels of *ACE2* and *TMPRSS2* in the liver[433,512]. Interestingly, high levels of Ang 1-7, the product of ACE2, were able to revert MASLD through the activity of its receptor *Mas*, modulating hepatic mitochondrial function. Our data suggests a compensatory mechanism that may help to prevent impaired mitochondrial activity and liver damage. Although this response may initially be beneficial for the hepatocyte, our results identified a higher susceptibility to infection. These data support the predisposition of MASLD patients to a more severe COVID-19 prognosis.

Metformin is a widely used pharmacological choice for the treatment of hyperglycemia in MASLD patients. Beyond its effect in glucose metabolism, metformin improves mitochondrial respiration, reducing Complex I activity through the activation of 5' AMP-activated protein kinase (AMPK)[513]. Additionally, metformin has been associated to modulation of post-translational modifications, including ubiquitination of several target proteins[514,515]. Thus, the effects of metformin were evaluated in human and hACE2 primary hepatocytes under steatotic conditions. This approach revealed a downregulation of ACE2 levels in hepatocytes treated with metformin, resulting in resistance to infection. Importantly, Ang 1-7 levels were reduced under metformin treatment, probably as a reduction of oxidative stress and reduced ACE2 levels. These data suggest that metformin treatment could be beneficial for COVID-19 patients previously diagnosed with MASLD and T2D.

In summary, our findings obtained from different models demonstrate that hepatocytes are susceptible to infection and upon entrance of the virus, they experience a metabolic reprogramming towards glycolysis but also mitochondrial dysfunction. Steatotic hepatocytes are more vulnerable to infection, and under this context, metformin might prevent liver dysfunction caused by SARS-CoV-2.

D.3. Intersecting insights from study 1 and study 2

The main topic of this doctoral thesis was initially intended to explore the role of magnesium homeostasis in CCA and the potential involvement of its transporters. However, due to the emergence of the COVID-19 pandemic during this research and the urgent need for scientific contributions to combat this global health crisis, we redirected our focus towards investigating the impact of COVID-19 on the liver. Although CCA and COVID-19 appear to be completely distinct diseases, our research has identified three common traits shared by both areas of investigation: (1) mitochondrial dysfunction and metabolic reprogramming, (2) increased oxidative stress and (3) alterations in iron metabolism.

In the contexts of both CCA and COVID-19 infection, mitochondria functions are altered resulting in a metabolic shift. Mitochondria are intracellular organelles responsible for metabolizing nutrients, generating free radicals, maintaining calcium homeostasis and regulating cell survival and death. Importantly, mitochondria synthetize ATP via oxidative phosphorylation, a process driven by the oxidation of metabolites through the Krebs cycle and β-oxidation of fatty acids[516]. Pathophysiological alterations in mitochondria, such as those observed in cancer and virus-related infections, are associated with increased glycolysis, the phenomenon known as the Warburg effect. In tumoral cells, this metabolic promotes cellular invasiveness, aggressiveness and drug resistance[517]. In our study, we observed that these cancerous behaviors can be reversed by silencing *CNNM4* in CCA. Lactate, a byproduct of this metabolic shift, is expelled into the microenvironment, promoting tissue acidity and immune cells exhaustion[518]. Our study found that silencing *CNNM4* in CCA cells resulted in lower lactate levels, providing further evidence that this therapeutic approach could reverse the Warburg effect. Similarly, many viruses induce alterations in host cell metabolism reminiscent of the Warburg effect, characterized by enhanced glycolysis. This metabolic reprogramming facilitates rapid energy production and provides essential precursors for nucleotide synthesis and specific protein production necessary for viral replication. In some viruses, enhanced aerobic glycolysis is evidenced by the upregulation of glycolytic genes, including glucose transporters and several glycolytic enzymes[519]. Likewise, exposure to spike protein particles upregulates intermediates involved in glycolysis, lactate and glutamine metabolism. This process also increases acidification of the extracellular matrix, decreases intracellular glucose and raises extracellular lactate concentrations, all in one indicating an enhancement of glycolytic activity.

Another shared pathological mechanism observed in both studies is the increased production of ROS within mitochondria. ROS are independently existing molecules that contain at least one oxygen atom and one or

more unpaired electrons, encompassing both oxygen and nitrogen free radicals. These ROS can be produced through enzymatic pathways, such as via lipoxygenase, as well as non-enzymatic processes like the iron-dependent Fenton reaction. The elimination of ROS is primarily managed by glutathione peroxidase (GPX) and other antioxidant mechanisms[520]. Under physiological conditions, ROS are generated in small quantities as byproducts of cellular processes. Oxidative stress arises when there is an imbalance between increased production of ROS and reduced antioxidant responses. In cancer, low levels of ROS can initiate or promote tumorigenesis by supporting cellular transformation and proliferation, whereas elevated levels of ROS can induce programmed cell death[521]. In our first study, we demonstrate that ROS plays a central role in the therapeutic effects of *CNNM4* silencing in CCA. Excessive ROS production induced by depletion of *CNNM4* triggers ferroptosis in tumoral cells, effectively reversing cell viability, chemoresistance, cancer stem cell capacity, and metastatic potential. ROS also exhibits a paradoxical effect on viral infection, particularly in the context of SARS-CoV-2 During the early stages of infection, ROS facilitates the activation of immune cells and inhibits viral replication. However, in severe cases of COVID-19, uncontrolled ROS production exacerbates inflammation, leading to tissue damage and multiple organ failure[522]. The interaction of the spike protein with hepatocytes resulted in elevated mitochondrial ROS production, which subsequently induced apoptosis, evidenced by increased caspase 3 levels. Additionally, inhibition of the Mas receptor within the renin-angiotensin system exacerbated this effect.

Iron overload can contribute to oxidative stress through the Fenton reaction, in which hydrogen peroxide (H_2O_2) reacts with Fe^{2+} and Fe^{3+} to produce ROS. To prevent toxicity from increased ROS via the Fenton reaction, iron is stored as ferritin intracellularly and bound to transferrin extracellularly. However, an accumulation of excess iron within the cell can lead to an increase in the labile iron pool of redox-active Fe^{2+}, which may further contribute to the formation of reactive free radicals[523]. Following *CNNM4* silencing treatment in CCA models, there was a marked increase in iron content, a characteristic hallmark of ferroptosis. In addition, the binding of spike protein particles to hepatocytes disrupts iron metabolism intermediates. Some studies suggest that dysregulated iron may be a critical factor contributing to hepatic failure in COVID-19 patients[422].

Overall, both pathologic conditions, ferroptosis in CCA cells induced by *CNNM4* depletion and SARS-CoV-2 binding to hepatocytes, result in excessive ROS production driven by dysregulated iron metabolism, which triggers the Fenton reaction and disrupts mitochondrial function and energy metabolism.

Conclusions

Based on Hypothesis and Objectives, Results and the Discussion, the following can be concluded:

C.1. Study 1

1- CNNM4 is upregulated in clinical and preclinical models of CCA, regardless of the anatomical subtype, suggesting a potential role of CNNM4 in cholangiocarcinogenesis.

2- CNNM4 functions as a Mg^{2+} extruder in the plasmatic and mitochondrial membranes of cholangiocytes, since higher CNNM4 levels correlate with reduced Mg^{2+} levels in the cytoplasm and mitochondria.

3- Silencing *CNNM4* halts key cancer hallmarks in CCA:

   a. Silencing *CNNM4* diminishes cell proliferation in human CCA cell lines without affecting non-tumoral hepatocyte and cholangiocyte cell lines. Additionally, it decreases tumoral growth of CCA murine livers *in vivo* and in the well-established angiogenic *in ovo* and *ex ovo* CAM model.
   b. Silencing *CNNM4* sensitizes cells to commonly used chemotherapeutic drugs in CCA: cisplatin, doxorubicin, gemcitabine and 5-fluorouracil.
   c. In *in vitro* and *in vivo* CCA models, silencing *CNNM4* reduces cellular dependence on energy metabolism via both glycolysis and oxidative respiration, thereby inhibiting the metabolic reprogramming observed in CCA.
   d. Silencing *CNNM4* decreases self-renewal and multipotent nature of the cancer stem cell subpopulations in tumor spheroids formed from CCA cell lines.
   e. Silencing *CNNM4* inhibits migration into adjacent tissue, intravasation, extravasation and invasion into the lungs in *in ovo* and *ex ovo* CAM model.

4- Silencing *CNNM4* alters cellular signaling in CCA:

   a. Silencing *CNNM4* downregulates signaling pathways including metabolic, chemotherapeutic and inflammatory processes altogether with cancer proliferation, EMT and antioxidant system-related pathways.

b. Silencing *CNNM4* induces ferroptosis-mediated ROS production through NUPR-1 inhibition, that may exert its effects on *CNNM4* silencing in enhancing CCA cells sensitivity to chemotherapy, reducing CSC population, halting metastasis and preventing metabolic reprogramming alterations.

5- Modulation of CNNM4 levels represents a potential target to inhibit CCA progression and metastasis.

C.2. Study 2

1- Healthy hepatocytes express critical entry points for SARS-CoV-2, including ACE2, NRP1 and TRPMSS2.

2- Hepatocytes are susceptible to SARS-CoV-2 infection through the binding of the RBD of the S1 protein to ACE2 receptor in both in human primary hepatocytes and non-tumoral hepatocyte cell line.

3- Binding of spike protein induces profound proteomic changes in primary hepatocytes derived from humanized ACE2 mice:

a. Primary hepatocytes from humanized ACE2 mice exhibited a higher number of differentially expressed peptides compared to primary hepatocytes from WT mice lacking ACE2 expression, which are not susceptible to infection by lentiviral particles expressing the spike protein of SARS-CoV-2. Therefore, subsequent experiments were performed using hepatocytes from humanized ACE2 mice.
b. Primary hepatocytes exposed to pseudotyped viral particles expressing the spike protein showed dysregulated pathways, including those related to viral response, metabolic processes and iron homeostasis.

4- Mitochondrial function is altered after infection of hepatocytes by pseudotyped viral particles expressing spike protein of SARS-CoV-2:

a. Key players in iron homeostasis are dysregulated upon infection of hepatocytes with lentiviral particles expressing spike protein which leads to oxidative stress, resulting in mitochondrial malfunction.

b. A similar alteration in energy production pathways to the Warburg effect is observed in human and mouse primary hepatocytes infected by lentiviral particles, characterized by a shift to enhanced glycolysis and increased mitochondrial activity.
c. Infection of hepatocytes with pseudotyped viral particles increases mitochondrial ROS production, demonstrating an elevated oxidative state in the cells.
d. Major inflammatory mediators in COVID-19 are upregulated in the primary hepatocytes under lentiviral particles infection.

5- Hepatocytes subjected to methionine-choline deficient (MCD) medium, a model mimicking MASH condition, exhibit increased susceptibility to SARS-CoV-2:

a. ACE2 and NRP1 protein levels are elevated primary hepatocytes cultured in MCD medium.
b. Metabolically compromised hepatocytes demonstrate higher susceptibility to infection by pseudotyped viral particles expressing the spike protein of SARS-CoV-2.
c. Levels of Ang1-7 measured are upregulated under steatotic conditions, probably as a compensatory mechanism to ameliorate liver damage.

6- Metformin treatment may offer therapeutic benefits for COVID-19 patients previously diagnosed with MASLD and T2D:

a. The addition of metformin to primary hepatocytes, both under physiological conditions and in MCD medium, reduces the expression of the key entry points at both protein and transcriptional levels.
b. Metformin treatment reduces the infection rates in MASH-induced hepatocytes.
c. Metformin administration to MASH-induced primary hepatocytes reverses the increased expression of Ang1-7 caused by MCD medium, likely due to the reduction of oxidative stress and ACE2 levels.

Summary in Spanish

S.S.1. Estudio 1

S.S.1.1. Introducción

El magnesio (Mg^{2+}) es un micronutriente esencial, ubicado principalmente en el espacio intracelular, donde representa el principal catión divalente intracelular[2,3]. Mantener la homeostasis de Mg^{2+} es crucial para varios procesos fisiológicos, incluyendo el metabolismo, la proliferación celular y la integridad estructural[5]. Para mantener una regulación precisa de esta homeostasis las células de mamífero disponen de diferentes mecanismos: moléculas de unión a Mg^{2+}, almacenamiento de Mg^{2+} en orgánulos y seis familias de canales y transportadores de Mg^{2+}: TRPM, SLC41A, MMgT1, CNNM, MRS1 y MagT1. En particular, la familia de los CNNMs es la menos estudiadad[16].

La familia de los CNNMs está compuesta por cuatro proteínas (CNNM1-4), capaces de transportar el Mg^{2+} a través de las membranas celulares, incluyendo la membrana plasmática, el retículo endoplasmático y el aparato de Golgi, regulando la homeostasis de Mg^{2+} dentro de la célula[16,69,77]. La distribución las isoformas de los CNNMs varía entre los diferentes tejidos del cuerpo. En condiciones fisiológicas, CNNM2 y CNNM3 se expresan en todos los tejidos, mientras que CNNM1 es más abundante en el testículo y el cerebro, y CNNM4 tiene mayor expresión en varias regiones del cerebro, el testículo y el tracto digestivo[16,57,78].

Varios estudios han observado una asociación entre la deficiencia de Mg^{2+} y varias enfermedades hepáticas. Anteriormente, nuestro grupo, el Laboratorio de Enfermedades Hepáticas de CIC bioGUNE, identificó que el transportador de Mg^{2+} CNNM4 tiene un papel fundamental en enfermedades hepáticas como enfermedad hepática esteatósica asociada a disfunción metabólica (MASLD, en inglés *metabolic dysfunction-associated steatotic liver disease*) y en daño hepático inducido por medicamentos (DILI, en inglés *drug-induced liver injury*)[434,524]. La deficiencia de Mg^{2+} también está asociada a otras enfermedades, incluido el cáncer de manera bidireccional: la hipomagnesemia aumenta el riesgo de cáncer debido a la presencia de inflamación crónica, mientras que los tratamientos específicos para el cáncer han demostrado inducir hipomagnesemia[109–111]. Los datos epidemiológicos sugieren que la ingesta de magnesio, que se encuentra predominantemente en granos sin procesar y vegetales de hoja verde, está asociada a un menor riesgo de varios tipos de cáncer, como el de mama, pulmón, colorrectal y de hígado, incluido el colangiocarcinoma (CCA)[100–104].

El CCA es un proceso tumoral de carácter maligno que afecta a las células de los conductos biliares llamadas colangiocitos[130]. Es el tipo de cáncer más del tracto biliar y el segundo tumor primario de hígado más

prevalente después del carcinoma hepatocelular (HCC, en inglés *hepatocellular carcinoma*), y representa el ~ 15% de todos los cánceres primarios de hígado y el ~3% de los tumores gastrointestinales. A pesar de ser un tumor poco frecuente (0.3-6/100,000 habitantes al año), es muy agresivo y tiene un alto riesgo de recurrencia, con una tasa de supervivencia a cinco años de solo el 5%, representando el 2% de todas las muertes relacionadas con el cáncer. La elevada letalidad de esta enfermedad puede atribuirse a su sintomatología asintomática en estadios iniciales, su naturaleza altamente agresiva y su elevada resistencia a la quimioterapia[133,134]. Hoy en día, la resección quirúrgica es el único tratamiento curativo para pacientes con CCA, lo que es posible en solo el 30% de los pacientes debido a la presencia de metástasis, crecimiento del tumor extensivo o estado clínico desfavorable[192].

Una de las dianas más comúnmente utilizadas en el tratamiento del cáncer son los procesos de muerte celular, dado que el cáncer se caracteriza por una desregulación de la división y la muerte celular[211,212]. Se define como muerte celular al deterioro irreversible de las funciones vitales de la célula y puede clasificarse como muerte celular accidental, si ocurre instantánea e incontroladamente debido a un daño físico, químico o mecánico; o regulada, cuando la muerte depende de una señalización molecular sofisticada que puede ser modulada genéticamente o farmacológicamente[219,221]. Diferentes tipos de muerte han sido descubiertos, incluyendo los clásicos como apoptosis, autofagia o necrosis; así como los más recientemente descubiertos como necroptosis, mitoptosis, paraptosis, ferroptosis[223]…

La ferroptosis es un tipo de muerte celular caracterizada por la presencia de estrés oxidativo causado por un aumento de hierro celular, lo que resulta en la peroxidación lipídica en la membrana celular[225]. La selenoproteína glutatión peroxidasa 4 (GPX4) actúa como un represor central de la ferroptosis utilizando el poder reductor del glutatión reducido (GSH) proveniente del del sistema x_c- (SLC7A11) para transformar los hidroperóxidos de ácidos grasos poliinsaturados (PUFA-PL-OOH), unos compuestos reactivos, en alcoholes de fosfolípidos de ácidos grasos poliinsaturados (PUFA-PL-OH), compuestos no reactivos y no letales[218]. Las enzimas dependientes de hierro como ALOX, NOX y POR oxidan los PUFA-PLs comprometiendo la integridad de la membrana plasmática y generando aldehídos tóxicos como 4-hidroxinonenal (4-HNE) y malondialdehído (MDA)[227,228]. La ferroptosis también se ve significativamente influenciada por el metabolismo del hierro, incluyendo su absorción, almacenamiento, exportación y utilización[229]. En definitiva, la ferroptosis se caracteriza por un aumento de la peroxidación lipídica, una acumulación de hierro y una disminución en la actividad antioxidante de la célula. Recientemente, se ha sugerido que la inactivación de la proteína nuclear 1 (NUPR-1) deteriora la función mitocondrial y el metabolismo energético en las células cancerosas y

desencadena ferroptosis mediante la modulación del metabolismo del hierro, la homeostasis de especies reactivas de oxígeno (ROS, en inglés *reactive oxygen species*) y la vía GSH/GPX4[231,232].

S.S.1.2 Hipótesis y objetivos

En este trabajo, postulamos la hipótesis de que el transportador de Mg^{2+} CNNM4 representa un mecanismo subyacente en la patogénesis del CCA y una posible diana terapéutica para el tratamiento de esta enfermedad mediante el silenciamiento con terapia dirigida utilizando la molécula GalNAc-CNNM4 siRNA. Para ello se han planteado los siguientes objetivos:

I. Caracterizar la contribución de CNNM4 a la patogénesis del CCA mediante el análisis de su expresión en tejido de pacientes con CCA, así como su impacto en rasgos características claves asociadas al CCA.
II. Determinar el impacto del silenciamiento genético de *CNNM4* en la proliferación celular, la quimioresistencia, el metabolismo energético y la formación de esferoides en líneas celulares de CCA.
III. Evaluar el impacto del silenciamiento genético de *CNNM4* en la metástasis en un modelo de membrana corioalantoideas de pollo (CAM, en inglés *chick chorioallantoic membrane*) *ex ovo* e *in ovo*.
IV. Identificar los mecanismos mediante los cuales CNNM4 ejerce sus funciones en la patogénesis del CCA
V. Analizar los efectos del silenciamiento genético de CNNM4 en la progresión del CCA en modelos *in vivo*.

S.S.1.3. Resultados y discusión

Inicialmente, se evaluó la expresión de *CNNM4* en 8 cohortes independientes de pacientes para comparar muestras de CCA resecadas con tejido control (ya sea tejido hepático adyacente no tumoral o tejido biliar sano). Se observó un aumento de la expresión de *CNNM4* en todas las cohortes, mientras que la expresión de *CNNM1-3* no mostró tendencias consistentes, lo que resalta la especificidad de CNNM4. Estos resultados fueron confirmados mediante análisis de inmunohistoquímica en pacientes humanos con CCA. El aumento en la expresión de *CNNM4* se asoció además con factores proliferación (PCNA) y de conteo de microvasos positivos (vWF). Además, se detectó una mayor expresión de *CNNM4* en modelos animales de CCA respecto

animales sanos, así como en colangioctios humanos tumorales en comparación con colangiocitos normales en cultivo.

Mediante estudios mecanísticos descritos en esta tesis, identificamos por primera vez a CNNM4 como un extrusor de Mg^{2+} en un contexto de CCA. Observamos que tanto el silenciamiento genético de CNNM4 mediante shRNA como la comparación de líneas celulares de colangiocitos humanos normales con líneas de colangiocitos humanos tumorales, mostraban un aumento de la concentración citoplasmática y mitocondrial de Mg^{2+}, respaldando el papel de CNNM4 como extrusor.

Importante destacar que el silenciamiento de *CNNM4* en líneas celulares de colangiocitos tumorales inhibió características claves del cáncer, incluyendo la proliferación, la resistencia a los tratamientos quimioterapéuticos comúnmente utilizados en CCA (cisplatino, doxorrubicina, gemcitabina y 5-fluorouracilo), la transformación metabólica hacia un estado más glicolítico , llamado efecto Warburg, y la formación de esferoides, utilizado por varios autores para analizar la capacidad de célula madre de cáncer (CSC, en inglés *cancer stem cell*). Los estudios realizados con modelos *ex ovo* e *in ovo* demostraron un menor potencial metastásico tras en silenciamiento de CNNM4 en células de CCA.

A través de estudios proteómicos, identificamos a NUPR-1 como un regulador aguas debajo de CNNM4, lo que indicaba que el silenciamiento de CNNM4 inhibe esta proteína promoviendo la ferroptosis en las células de CCA. El incremento excesivo de ROS inducido por el proceso de ferroptosis se relaciona con todos los procesos observados anteriormente tras el silenciamiento de CNNM4 (resistencia a quimioterapia, efecto Warburg, capacidad CSC y metástasis), sugiriendo así que la ferroptosis podría ser un evento supresor de tumores potencialmente útil en CCA, y que el silenciamiento de CNNM4 podría ser usado en combinación con otras terapias anticancerígenas.

Finalmente, estos resultados se confirmaron en modelos murinos de CCA, donde el silenciamiento efectivo de CNNM4 se realizó utilizando una molécula de GalNAc-CNNM4 siRNA, que ofrece diversas ventajas: estabilidad, farmacocinética favorable, especificidad hepática, efecto prolongado con dosis infrecuentes, administración fácil y baja inmunogenicidad.

S.S.1.4. Conclusiones

1- CNNM4 se encuentra sobreexpresado en modelos clínicos y preclínicos de CCA lo que sugiere un posible papel de CNNM4 en la carcinogénesis de CCA.
2- CNNM4 funciona como un extrusor de Mg^{2+} en las membranas plasmáticas y mitocondriales de los colangiocitos, ya que niveles más altos de CNNM4 se correlacionan con niveles reducidos de Mg^{2+} en el citoplasma y las mitocondrias.
3- El silenciamiento de CNNM4 inhibe características cruciales del cáncer en el CCA:
    a. El silenciamiento de *CNNM4* disminuye la proliferación celular en líneas celulares humanas de CCA sin afectar a líneas celulares no tumorales de hepatocitos y colangiocitos. Además, reduce el crecimiento tumoral de hígados murinos de CCA *in vivo* y del modelo angiogénico *in ovo* y *ex ovo* CAM.
    b. El silenciamiento de *CNNM4* sensibiliza a las células a fármacos quimioterapéuticos comúnmente utilizados en CCA: cisplatino, doxorrubicina, gemcitabina y 5-fluorouracilo.
    c. En modelos de CCA *in vitro* e *in vivo*, el silenciamiento de *CNNM4* reduce la dependencia celular del metabolismo energético tanto a través de la glucólisis como de la respiración oxidativa, inhibiendo así la reprogramación metabólica observada en el CCA.
    d. El silenciamiento de *CNNM4* disminuye la auto-renovación y la pluripotencia de las subpoblaciones de células madre cancerosas en esferoides tumorales formados a partir de líneas celulares de CCA.
    e. El silenciamiento de *CNNM4* inhibe la migración hacia el tejido adyacente, la intravasación, la extravasación y la invasión en los pulmones en el modelo *in ovo* y *ex ovo* CAM.
4- El silenciamiento de *CNNM4* altera la señalización celular en el CCA:
    a. El silenciamiento de *CNNM4* reduce vías de señalización, incluyendo procesos metabólicos, quimioterapéuticos e inflamatorios junto con la proliferación del cáncer, transición epitelio-mesénquima y vías relacionadas con el sistema antioxidante.
    b. El silenciamiento de *CNNM4* induce la producción de ROS mediada por ferroptosis a través de la inhibición de NUPR-1, que ejerce sus efectos en el silenciamiento de CNNM4 mejorando la sensibilidad de las células de CCA a la quimioterapia, reduciendo la población de CSC, deteniendo la metástasis y previniendo la reprogramación metabólica.

5- La modulación de CNNM4 representa una potencial diana terapéutica para inhibir la progresión y metástasis del CCA.

S.S.2. Estudio 2

Esta tesis inicialmente tuvo como objetivo explorar el papel del transportador de Mg^{2+} CNNM4 en CCA. Sin embargo, la emergencia de la pandemia de COVID-19 desvió nuestro enfoque hacia la investigación del impacto del virus en el hígado.

S.S.2.1. Introducción

La enfermedad por coronavirus 2019 (COVID-19), causada por el coronavirus del síndrome respiratorio agudo severo 2 (SARS-CoV-2), es una enfermedad altamente contagiosa y patogénica en los seres humanos, que a menudo resulta en infecciones graves del tracto respiratorio inferior y un alto riesgo de enfermedades respiratorias mortales[242,243]. En marzo de 2020, la Organización Mundial de la Salud (OMS) lo declaró una pandemia global, con un posterior impacto devastador en todo el mundo, causando más de 7 millones de muertes[245,246].

El SARS-CoV-2 pertenece a la familia de los coronavirus, los cuales se caracterizan por ser virus con cubierta, de ARN monocatenario de sentido positivo y poliadenilado que infectan a mamíferos, incluyendo a los humanos, y causan una amplia variedad de enfermedades[251]. Expresa cuatro proteínas estructurales incluyendo la proteína nucleocápsida (N), la proteína spike (S), la proteína de membrana (M) y la proteína de envoltura (E)[252]. La proteína spike es fundamental para la unión viral y la internalización en las células huéspedes[254]. Está compuesta por dos subunidades: la subunidad de unión al receptor (S1) y la subunidad de fusión a la membrana (S2).

Tras la interacción del SARS-CoV-2 con la célula huésped mediante el principal receptor, la enzima convertidora de angiotensina 2 (ACE2), el virus sigue dos rutas de entrada. En la primera y preferida ruta, la proteasa transmembrana del huésped, serina 2 (TMPRSS2) corta la proteína spike en dos puntos lo que facilita la fusión de las membranas para la entrada a la célula[256,257]. En la segunda ruta, cuando la célula no expresa suficiente TMPRSS2 o cuando la interacción con esta falla, el virus se internaliza mediante endocitosis mediada por clatrina. A parte de ACE2 y TMPRSS2, existen otros factores que facilitan la unión de SARS-CoV-2 a la membrana como NRP-1[258] .

Después de su entrada en la célula, el SARS-CoV-2 activa el sistema inmunitario innato, provocando la liberación de citocinas[259]. Posteriormente, los linfocitos B y T se activan para iniciar la memoria inmunológica[260]. En los casos severos de COVID-19, se produce una liberación excesiva y desregulada de citoquinas, lo que contribuye a una condición fatal llamada tormenta de citoquinas, que conduce a una hiperinflamación y un fallo multiorgánico[261]. La entrada de SARS-CoV-2 también induce cambios en el sistema renina-angiotensina. En un contexto fisiológico, el RAS presenta dos vías: la vía clásica, que ejerce efectos proinflamatorios, proapoptóticos y prooxidantes, y la vía alternativa, que, con la presencia de ACE2, desempeña un papel contrario a la ruta clásica[269]. En la vía alternativa, ACE2 actúa como enzima para la producción de Ang1-7, la cual se une al receptor *Mas* para promover estos efectos protectores. Dado que SARS-CoV-2 utiliza ACE2 como receptor de entrada a la célula, podría alterar la actividad catalítica de ACE2 y por lo tanto promover la vía clásica con sus devastadores efectos [270].

Existen diversas evidencias que implican al COVID-19 en el daño hígado, tales como el incremento de enzimas hepáticas tras la infección, la aparición de esteatosis en biopsias post-mortem de pacientes fallecidos por COVID-19 y la observación de que las enfermedades hepáticas preexistentes predisponen a un peor pronóstico y mayor mortalidad en pacientes con COVID-19[279,314,327,328]. En estos estudios, la principal etiología entre los pacientes con enfermedades hepáticas crónicas son MASLD y esteatohepatitis asociada a disfunción metabólica (MASH, en inglés *metabolic dysfunction-associated steatohepatitis*)[338]. MASLD abarca un espectro de enfermedades que va desde la esteatosis hepática hasta el daño hepatocelular, denominado MASH y fibrosis que puede progresar a cirrosis y eventualmente a HCC[362,363].

Han surgido múltiples hipótesis para explicar los mecanismos subyacentes a los efectos hepáticos de la COVID-19. Además del daño hepático directo inducido por el virus, los posibles mecanismos incluyen daño mediado por el sistema inmune, lesión por isquemia y reperfusión hipóxica, y hepatotoxicidad relacionada con medicamentos, todos los cuales contribuyen a la lesión hepática en pacientes con COVID-19[525].

S.S.2.2. Hipótesis y objetivos

En este estudio, proponemos que la unión de SARS-CoV-2 a las células hepáticas induce daño en el hígado, disfunción mitocondrial y alteraciones metabólicas. Asimismo, planteamos la hipótesis de que los individuos con MASLD tienen un mayor riesgo de padecer COVID-19 severo y que la metformina, un fármaco

ampliamente prescrito para la hiperglucemia en pacientes con MASH, puede mitigar la infección de SARS-CoV-2 en estos pacientes. Para ello se han planteado los siguientes objetivos:

I. Evaluar la potencial unión e infectividad de los hepatocitos, tanto en hepatocitos primarios como en líneas celulares, utilizando partículas virales que expresan la proteína spike del SARS-CoV-2.
II. Identificar los cambios celulares a nivel proteómico y metabólico en hepatocitos primarios después de la infección con partículas virales pseudotipadas que expresan la proteína spike del SARS-CoV-2.
III. Caracterizar la regulación del sistema renina-angiotensina en hepatocitos primarios tras la infección con SARS-CoV-2.
IV. Analizar la susceptibilidad de pacientes obesos con MASH al SARS-CoV-2 y evaluar los efectos beneficiosos de la metformina en pacientes con MASH infectados con SARS-CoV-2.

S.S.2.3. Resultados y discusión

En nuestro trabajo, observamos que una línea celular de hepatocitos humanos no tumorales (THLE-2) y hepatocitos primarios provenientes de ratones humanizados con ACE2 (hACE2) que expresan ACE2, TMPRSS2 y NRP-1, eran capaces de unirse a la proteína spike. Además, las THLE-2, los hepatocitos primarios hACE2 y hepatocitos primarios humanos eran susceptibles de ser infectados con partículas lentivirales que expresaban la proteína spike del SARS-CoV-2. Estos resultados son consistentes con la bibliografía existente, donde se ha observado infección de hepatocitos por SARS-CoV-2 en modelos celulares tumorales, en organoides humanos de células madre hepáticas y en hígados de autopsias de COVID-19[318,501–506]. Estos datos muestran el potencial efecto citopático de SARS-CoV-2 en el hígado, lo que podría explicar los efectos perjudiciales identificados en pacientes con COVID-19.

En análisis de espectrometría de masas observamos las vías de señalización específicamente moduladas en los hepatocitos primarios de ratón infectados con las partículas virales que expresan la proteína spike. Estas vías pueden resumirse en respuesta al virus, alteración mitocondrial y modulación del metabolismo del hierro. El aumento del hierro intracelular, observado en pacientes de COVID-19, causaría un estado de hiperferritina que podría incrementar la concentración de ROS mitocondrial, generando una alteración de la homeostasis oxidativa celular y un aumento de la actividad mitocondrial[424,507].

Una reprogramación metabólica similar al efecto Warburg de las células tumorales se ha identificado previamente en células tras la infección del SARS-CoV-2[508]. Los hepatocitos infectados con partículas lentivirales que contenían la proteína spike presentaron una mayor acidificación del medio y un aumento en el consumo de oxígeno, lo que indicó un cambio metabólico hacia un fenotipo más energético y glicolítico. Asimismo, los análisis de fluxómica revelaron que los hepatocitos infectados con las partículas lentivirales presentaban una mayor producción de lactato y un ciclo de Krebs más activado. En particular, se observó un aumento de malato y fumarato tras la infección que podrían contribuir a evadir la respuesta inmune acidificando el compartimento extracelular.

Por otro lado, el sistema renina-angiotensina también se vio afectado tras la exposición de los hepatocitos primarios a las partículas lentivirales que contiene la proteína spike. La unión de spike a los hepatocitos provocó la disminución de ACE2, lo que resultó en una reducción de Ang1-7. Por el contrario, la inhibición del receptor *Mas* por su antagonista A779, predispuso a los hepatocitos a una mayor susceptibilidad a ser infectadas por las partículas lentivirales de manera dependiente de ROS.

En hepatocitos sometidos a una dieta que mimetiza una condición de MASH, la expresión de ACE2 y Ang1-7 están aumentados. Aunque inicialmente estos efectos podrían ser beneficiosos para el hepatocito, nuestros resultados muestran una mayor susceptibilidad a la infección en hepatocitos tratados con dieta esteatósica, Esto sugiere un mecanismo compensatorio que podría ayudar a prevenir la alteración de la actividad mitocondrial y el daño hepático[442].

La metformina, un fármaco utilizado para el tratamiento de la hiperglicemia en pacientes con MASLD, tiene efectos más allá del metabolismo de la glucosa, incluyendo la mejora de la respiración mitocondrial y la modulación de modificaciones postraduccionales[514,515]. En los hepatocitos primarios humanos y de ratón bajo un contexto de MASH, la administración de metformina disminuyó la expresión de ACE2, lo que resultó en una menor infección a las partículas lentivirales con spike. Además, se redujo la expresión de Ang1-7, probablemente por una reducción del estrés oxidativo y de la concentración de ACE2. Estos resultados sugieren que el tratamiento con metformina podría ser beneficioso para pacientes con COVID-19 que previamente han sido diagnosticados con MASLD y diabetes de tipo 2.

S.S.2.3. Conclusiones

1- El hepatocito sano expresa las proteínas esenciales para la entrada del SARS-CoV-2, incluidas ACE2, NRP1 y TMPRSS2.
2- Tanto los hepatocitos humanos primarios como la línea celular humana no tumoral son susceptibles a la infección por SARS-CoV-2 a través de la unión del RBD de la proteína S1 al receptor ACE2.
3- La unión de la proteína spike produce cambios proteómicos en los hepatocitos primarios derivados de ratones humanizados con ACE2:
    a. Los hepatocitos primarios de ratones humanizados con ACE2 exhibieron un mayor número de péptidos diferencialmente expresados en comparación con los hepatocitos primarios de ratones WT que carecen de la expresión de ACE2, los cuales no son susceptibles a la infección por partículas lentivirales que expresan la proteína spike del SARS-CoV-2. Por lo tanto, a continuación, los experimentos se realizaron utilizando hepatocitos de ratones humanizados con ACE2.
    b. Los hepatocitos primarios expuestos a partículas virales pseudotipadas que expresan la proteína spike mostraron vías proteómicas alteradas, incluidas las relacionadas con la respuesta viral, los procesos metabólicos y la homeostasis del hierro.
4- La función mitocondrial se ve alterada tras la infección de hepatocitos por partículas virales pseudotipadas que expresan la proteína spike del SARS-CoV-2:
    a. La infección de hepatocitos con partículas lentivirales que expresan la proteína spike provoca la alteración de mediadores clave en la homeostasis del hierro, lo que lleva a estrés oxidativo, resultando en un mal funcionamiento mitocondrial.
    b. Los hepatocitos primarios infectados por las partículas lentivirales muestran una reprogramación metabólica caracterizada por una glicólisis aumentada y una mayor actividad mitocondrial.
    c. La producción de ROS mitocondrial se ve aumentado tras la infección de hepatocitos con partículas virales pseudotipadas, demostrando un estado oxidativo elevado en las células.
    d. Los principales mediadores inflamatorios en COVID-19 están regulados al alza en los hepatocitos primarios bajo la infección por partículas lentivirales.

5- Los hepatocitos sometidos a medio deficiente en metionina y colina (MCD, en inglés *methionine-choline deficient*), un modelo que imita la condición de MASH, exhiben una mayor susceptibilidad al SARS-CoV-2:
    a. Los niveles de proteínas ACE2 y NRP1 están elevados en hepatocitos primarios cultivados en medio MCD.
    b. Los hepatocitos metabólicamente comprometidos demuestran una mayor susceptibilidad a la infección por partículas virales pseudotipadas que expresan la proteína spike del SARS-CoV-2.
    c. Los niveles de Ang1-7 están aumentados bajo condiciones esteatósicas, probablemente como un mecanismo compensatorio para mitigar el daño hepático.
6- El tratamiento con metformina puede ofrecer beneficios terapéuticos para los pacientes con COVID-19 previamente diagnosticados con MASLD y T2D:
    a. La adición de metformina a los hepatocitos primarios, tanto en condiciones fisiológicas como en medio MCD, reduce la expresión de las proteínas esenciales de entrada del virus tanto a nivel proteico como transcripcional.
    b. El tratamiento con metformina reduce las tasas de infección en hepatocitos con MASH.
    c. La administración de metformina a hepatocitos primarios con MASH revierte la expresión aumentada de Ang1-7 causada por el medio MCD, probablemente debido a la reducción del estrés oxidativo y de los niveles de ACE2.

References

1. Aikawa, J. K. *Magnesium: Its Biologic Significance*. (CRC Press, 2019).
2. F de Baaij, J. H., J Hoenderop, J. G. & M Bindels, R. J. Magnesium in Man: Implications for Health and Disease. *Physiol Rev* **95**, 1–46 (2015).
3. Barbagallo, M., Veronese, N. & Dominguez, L. J. Magnesium in Aging, Health and Diseases. (2021) doi:10.3390/nu13020463.
4. Liu, M., Yang, H. & Mao, Y. Magnesium and liver disease. *Ann Transl Med* **7**, 578–578 (2019).
5. Razzaque, M. S. Magnesium: Are We Consuming Enough? (2018) doi:10.3390/nu10121863.
6. Feeney, K. A. *et al.* Daily magnesium fluxes regulate cellular timekeeping and energy balance. *Nature* **532**, 375 (2016).
7. Li, F. Y. *et al.* Second messenger role for Mg2+ revealed by human T-cell immunodeficiency. *Nature 2011 475:7357* **475**, 471–476 (2011).
8. Hou, H. *et al.* Magnesium acts as a second messenger in the regulation of NMDA receptor mediated CREB signaling in neurons. *Mol Neurobiol* **57**, 2539 (2020).
9. Daw, C. C. *et al.* Lactate Elicits ER-Mitochondrial Mg 2+ Dynamics to Integrate Cellular Metabolism. *Cell* **183**, 474–489 (2020).
10. Anastassopoulou, J. & Theophanides, T. Magnesium-DNA interactions and the possible relation of magnesium to carcinogenesis. Irradiation and free radicals. *Crit Rev Oncol Hematol* **42**, 79–91 (2002).
11. FI, W. & A, C. Magnesium in cell proliferation and differentiation. *Front Biosci* **4**, D607-17 (1999).
12. De Baaij, J. H. F., Hoenderop, J. G. J. & Bindels, R. J. M. Regulation of magnesium balance: lessons learned from human genetic disease. *Clin Kidney J* **5**, i15 (2012).
13. Dietary Reference Intakes for Calcium, Phosphorus, Magnesium, Vitamin D, and Fluoride. *Dietary Reference Intakes for Calcium, Phosphorus, Magnesium, Vitamin D, and Fluoride* (1997) doi:10.17226/5776.
14. Al Alawi, A. M., Majoni, S. W. & Falhammar, H. Magnesium and Human Health: Perspectives and Research Directions. *Int J Endocrinol* **2018**, (2018).
15. Rosanoff, A. *et al.* Recommendation on an updated standardization of serum magnesium reference ranges. *Eur J Nutr* **61**, 3697 (2022).
16. Chen, Y. S. & Gehring, K. New insights into the structure and function of CNNM proteins. *FEBS J* **290**, 5475–5495 (2023).
17. Clapham, D. E. TRP channels as cellular sensors. *Nature 2004 426:6966* **426**, 517–524 (2003).
18. Runnels, L. W., Yue, L. & Clapham, D. E. TRP-PLIK, a bifunctional protein with kinase and ion channel activities. *Science (1979)* **291**, 1043–1047 (2001).
19. Hardy, S. *et al.* PRL-1/2 phosphatases control TRPM7 magnesium-dependent function to regulate cellular bioenergetics. *Proc Natl Acad Sci U S A* **120**, e2221083120 (2023).
20. Schmitz, C. *et al.* The Channel Kinases TRPM6 and TRPM7 Are Functionally Nonredundant *. (2005) doi:10.1074/jbc.M509175200.
21. Schlingmann, K. P. *et al.* Hypomagnesemia with secondary hypocalcemia is caused by mutations in TRPM6, a new member of the TRPM gene family. *Nature Genetics 2002 31:2* **31**, 166–170 (2002).
22. Zhang, S., Cao, F., Li, W. & Abumaria, N. TRPM7 kinase activity induces amyloid-β degradation to reverse synaptic and cognitive deficits in mouse models of Alzheimer's disease. *Sci Signal* **16**, (2023).
23. Meng, Z., Wang, X., Yang, Z. & Xiang, F. Expression of transient receptor potential melastatin 7 up-regulated in the early stage of renal ischemia-reperfusion. *Transplant Proc* **44**, 1206–1210 (2012).
24. Du, J. *et al.* TRPM7-mediated Ca2+ signals confer fibrogenesis in human atrial fibrillation. *Circ Res* **106**, 992–1003 (2010).
25. Middelbeek, J. *et al.* TRPM7 is required for breast tumor cell metastasis. *Cancer Res* **72**, 4250–4261 (2012).
26. Nemoto, T., Tagashira, H., Kita, T., Kita, S. & Iwamoto, T. Functional characteristics and therapeutic potential of SLC41 transporters. (2022) doi:10.1016/j.jphs.2022.12.003.
27. Kolisek, M., Nestler, A., Vormann, J., Schweigel-Röntgen, M. & Hu, S.-R. M. Human gene SLC41A1 encodes for the Na /Mg 2 exchanger. *Am J Physiol Cell Physiol* **302**, 318–326 (2012).

28. Mastrototaro, L., Smorodchenko, A., Aschenbach, J. R., Kolisek, M. & Sponder, G. Solute carrier 41A3 encodes for a mitochondrial Mg 2+ efflux system. (2016) doi:10.1038/srep27999.
29. Sahni, J., Nelson, B. & Scharenberg, A. M. SLC41A2 encodes a plasma-membrane Mg2+ transporter. *Biochemical Journal* **401**, 505 (2007).
30. Cibulka, M. *et al.* Alzheimer's Disease-Associated SNP rs708727 in SLC41A1 May Increase Risk for Parkinson's Disease: Report from Enlarged Slovak Study. *Int J Mol Sci* **23**, 1604 (2022).
31. Bai, Y. *et al.* Associations of rs823128, rs1572931, and rs823156 polymorphisms with reduced Parkinson's disease risks. *Neuroreport* **28**, 936 (2017).
32. Kolisek, M. *et al.* Substitution p.A350V in Na+ /Mg2+ Exchanger SLC41A1, Potentially Associated with Parkinson's Disease, Is a Gain-of-Function Mutation. (2013) doi:10.1371/journal.pone.0071096.
33. Lin, C. H. *et al.* Variant R244H in Na+/Mg2+ exchanger SLC41A1 in Taiwanese Parkinson's disease is associated with loss of Mg2+ efflux function. *Parkinsonism Relat Disord* **20**, 600–603 (2014).
34. Hurd, T. W. *et al.* Mutation of the Mg2+ transporter SLC41A1 results in a nephronophthisis-like phenotype. *Journal of the American Society of Nephrology* **24**, 967–977 (2013).
35. Kolisek, M. *et al.* SLC41A1 is the only magnesium responsive gene significantly overexpressed in placentas of preeclamptic women. *Hypertens Pregnancy* **32**, 378–389 (2013).
36. Njiaju, U. O. *et al.* Whole Genome Studies Identify Solute Carrier Transporters in Cellular Susceptibility to Paclitaxel. *Pharmacogenet Genomics* **22**, 498–507 (2012).
37. Shindo, Y., Yamanaka, R., Suzuki, K., Hotta, K. & Oka, K. Altered expression of Mg(2+) transport proteins during Parkinson's disease-like dopaminergic cell degeneration in PC12 cells. *Biochim Biophys Acta* **1863**, 1979–1984 (2016).
38. Li, Q. *et al.* High expression of slc41a3 correlates with poor prognosis in hepatocellular carcinoma. *Onco Targets Ther* **14**, 2975–2988 (2021).
39. He, Z. *et al.* Structure and function of the human mitochondrial MRS2 channel. doi:10.1101/2023.08.12.553106.
40. Kuramoto, T., Kuwamura, M., Tokuda, S., Izawa, T. & Nakane, Y. A Mutation in the Gene Encoding Mitochondrial Mg 2+ Channel MRS2 Results in Demyelination in the Rat. *PLoS Genet* **7**, 1001262 (2011).
41. Yamanaka, R. *et al.* Mitochondrial Mg2+ homeostasis decides cellular energy metabolism and vulnerability to stress. *Sci Rep* **6**, (2016).
42. Piskacek, M., Zotova, L., Zsurka, G. & Schweyen, R. J. Conditional knockdown of hMRS2 results in loss of mitochondrial Mg + uptake and cell death. *J Cell Mol Med* **13**, 693–700 (2009).
43. Chen, Y. *et al.* Human mitochondrial Mrs2 protein promotes multidrug resistance in gastric cancer cells by regulating p27, cyclin D1 expression and cytochrome C release. *Cancer Biol Ther* **8**, 1–8 (2009).
44. Castiglioni, S. *et al.* The Interplay between TRPM7 and MagT1 in Maintaining Endothelial Magnesium Homeostasis. *Membranes (Basel)* **13**, (2023).
45. Blommaert, E. *et al.* Mutations in MAGT1 lead to a glycosylation disorder with a variable phenotype. **116**, (2019).
46. Matsuda-Lennikov, M. *et al.* Magnesium transporter 1 (MAGT1) deficiency causes selective defects in N-linked glycosylation and expression of immune-response genes. *Journal of Biological Chemistry* **294**, 13638–13656 (2019).
47. Goytain, A. & Quamme, G. A. Identification and characterization of a novel family of membrane magnesium transporters, MMgT1 and MMgT2. *Am J Physiol Cell Physiol* **294**, 495–502 (2008).
48. Kalam, H. *et al.* Identification of host regulators of Mycobacterium tuberculosis phenotypes uncovers a role for the MMGT1-GPR156 lipid droplet axis in persistence. *Cell Host Microbe* **31**, 978-992.e5 (2023).
49. Ishii, T. *et al.* Mg2+ Extrusion from Intestinal Epithelia by CNNM Proteins Is Essential for Gonadogenesis via AMPK-TORC1 Signaling in Caenorhabditis elegans. *PLoS Genet* **12**, e1006276 (2016).
50. Huang, Y. *et al.* Ginsenoside Rh2 Inhibits Angiogenesis in Prostate Cancer by Targeting CNNM1. *J Nanosci Nanotechnol* **19**, 1942–1950 (2019).

51. Xie, Y. *et al.* SNHG7 Facilitates Hepatocellular Carcinoma Occurrence by Sequestering miR-9-5p to Upregulate CNNM1 Expression. *Cancer Biother Radiopharm* **35**, 731–740 (2020).
52. Asiedu, M. K. *et al.* Pathways Impacted by Genomic Alterations in Pulmonary Carcinoid Tumors. *Clin Cancer Res* **24**, 1691–1704 (2018).
53. Jayathirtha, M. *et al.* Investigating the Function of Human Jumping Translocation Breakpoint Protein (hJTB) and Its Interacting Partners through In-Solution Proteomics of MCF7 Cells. *Molecules* **27**, (2022).
54. Wang, M., Miao, Z., Cen, H., He, J. & Wei, C. Long non-coding RNA (LncRNA) CHROMR promotes the expression of the CNNM1 gene by adsorbing hsa-miR-1299 to obtain drug resistance in diffuse large B lymphoma cells. *Transl Cancer Res* **11**, 1362–1371 (2022).
55. Chandran, U. *et al.* Expression of cnnm1 and its association with stemness, cell cycle, and differentiation in spermatogenic cells in mouse testis. *Biol Reprod* **95**, 1–12 (2016).
56. Stuiver, M. *et al.* CNNM2, encoding a basolateral protein required for renal Mg2+ handling, is mutated in dominant hypomagnesemia. *Am J Hum Genet* **88**, 333–343 (2011).
57. De Baaij, J. H. F. *et al.* Membrane Topology and Intracellular Processing of Cyclin M2 (CNNM2). (2012) doi:10.1074/jbc.M112.342204.
58. García-Castaño, A. I. *et al.* Novel variant in the CNNM2 gene associated with dominant hypomagnesemia. (2020) doi:10.1371/journal.pone.0239965.
59. Zhou, D. Y. *et al.* Decreased CNNM2 expression in prefrontal cortex affects sensorimotor gating function, cognition, dendritic spine morphogenesis and risk of schizophrenia. *Neuropsychopharmacology 2023 49:2* **49**, 433–442 (2023).
60. Li, X. *et al.* Case Report: CNNM2 Mutations Cause Damaged Brain Development and Intractable Epilepsy in a Patient Without Hypomagnesemia. *Front Genet* **12**, 705734 (2021).
61. Gui, J. *et al.* Identification of novel proteins for sleep apnea by integrating genome-wide association data and human brain proteomes. *Sleep Med* **114**, 92–99 (2024).
62. Matsumoto, Y. *et al.* Detection of novel and recurrent conjoined genes in non-Hodgkin B-cell lymphoma. *J Clin Exp Hematop* **61**, 71–77 (2021).
63. Győrffy, B. Discovery and ranking of the most robust prognostic biomarkers in serous ovarian cancer. *Geroscience* **45**, 1889–1898 (2023).
64. Xie, M. *et al.* Identification of genes contributing to cisplatin resistance in osteosarcoma cells. *FEBS Open Bio* **13**, 164–173 (2023).
65. Wang, Y., Wang, L., Wang, W. & Guo, X. Overexpression of circular RNA hsa_circ_0001038 promotes cervical cancer cell progression by acting as a ceRNA for miR-337-3p to regulate cyclin-M3 and metastasis-associated in colon cancer 1 expression. *Gene* **733**, (2020).
66. Hu, T. *et al.* PDK2 induces cisplatin-resistance in lung adenocarcinoma via transcriptional regulation of CNNM3. *J Drug Target* **27**, 460–465 (2019).
67. Bidinotto, L. T. *et al.* Molecular Profiling of a Rare Rosette-Forming Glioneuronal Tumor Arising in the Spinal Cord. *PLoS One* **10**, (2015).
68. Jang, S. Il, Lee, Y. W., Cho, C. K., Yoo, H. S. & Jang, J. H. Identification of Target Genes Involved in the Antiproliferative Effect of Enzyme-Modified Ginseng Extract in HepG2 Hepatocarcinoma Cell. *Evid Based Complement Alternat Med* **2013**, (2013).
69. Zolotarov, Y. *et al.* ARL15 modulates magnesium homeostasis through N-glycosylation of CNNMs. **1**, 3.
70. Daneshmandpour, Y., Darvish, H., Pashazadeh, F. & Emamalizadeh, B. Features, genetics and their correlation in Jalili syndrome: a systematic review. *J Med Genet* **56**, (2019).
71. Jalili, I. K. & Smith, N. J. D. A progressive cone-rod dystrophy and amelogenesis imperfecta: a new syndrome. *J Med Genet* **25**, 738–740 (1988).
72. Li, H., Huang, Y., Li, J. & Xie, M. Novel homozygous nonsynonymous variant of CNNM4 gene in a Chinese family with Jalili syndrome. *Mol Genet Genomic Med* **10**, (2022).

73. Simón, J. *et al.* Magnesium accumulation upon cyclin M4 silencing activates microsomal triglyceride transfer protein improving NASH. *J Hepatol* **75**, 34 (2021).
74. González-Recio, I. *et al.* Restoring cellular magnesium balance through Cyclin M4 protects against acetaminophen-induced liver damage. *Nat Commun* **13**, (2022).
75. Funato, Y. *et al.* Membrane protein CNNM4-dependent Mg2+ efflux suppresses tumor progression. *J Clin Invest* **124**, 5398–5410 (2014).
76. Rhodes, D. R. *et al.* Oncomine 3.0: genes, pathways, and networks in a collection of 18,000 cancer gene expression profiles. *Neoplasia* **9**, 166–180 (2007).
77. Funato, Y. & Miki, H. The emerging roles and therapeutic potential of cyclin M/CorC family of Mg2+ transporters. *J Pharmacol Sci* **148**, 14–18 (2022).
78. The Human Protein Atlas. https://www.proteinatlas.org/.
79. Sponder, G. *et al.* Human CNNM2 is not a Mg(2+) transporter per se. *Pflugers Arch* **468**, 1223–1240 (2016).
80. Yamazaki, D. *et al.* Basolateral Mg2+ Extrusion via CNNM4 Mediates Transcellular Mg2+ Transport across Epithelia: A Mouse Model. *PLoS Genet* **9**, e1003983 (2013).
81. Arjona, F. J. *et al.* CNNM2 mutations cause impaired brain development and seizures in patients with hypomagnesemia. *PLoS Genet* **10**, (2014).
82. Bai, Z. *et al.* CNNM proteins selectively bind to the TRPM7 channel to stimulate divalent cation entry into cells. *PLoS Biol* **19**, e3001496 (2021).
83. Amasheh, S., Fromm, M. & Günzel, D. Claudins of intestine and nephron - a correlation of molecular tight junction structure and barrier function. *Acta Physiol (Oxf)* **201**, 133–140 (2011).
84. Lameris, A. L. *et al.* Expression profiling of claudins in the human gastrointestinal tract in health and during inflammatory bowel disease. *Scand J Gastroenterol* **48**, 58–69 (2013).
85. Hou, J. *et al.* Claudin-16 and claudin-19 interaction is required for their assembly into tight junctions and for renal reabsorption of magnesium. *Proc Natl Acad Sci U S A* **106**, 15350–15355 (2009).
86. Fordtran, J. S., Rector, F. C. & Carter, N. W. The mechanisms of sodium absorption in the human small intestine. *Journal of Clinical Investigation* **47**, 884 (1968).
87. Curry, J. N. & Yu, A. S. L. Magnesium Handling in the Kidney. *Adv Chronic Kidney Dis* **25**, 236 (2018).
88. Dimke, H., Hoenderop, J. G. J. & Bindels, R. J. M. Molecular basis of epithelial Ca2+ and Mg2+ transport: insights from the TRP channel family. *J Physiol* **589**, 1535 (2011).
89. Voets, T. *et al.* TRPM6 forms the Mg2+ influx channel involved in intestinal and renal Mg2+ absorption. *J Biol Chem* **279**, 19–25 (2004).
90. Schuchardt, J. P. & Hahn, A. Intestinal Absorption and Factors Influencing Bioavailability of Magnesium-An Update. *Curr Nutr Food Sci* **13**, 260 (2017).
91. de Baaij, J. H. F. Magnesium reabsorption in the kidney. *Am J Physiol Renal Physiol* **324**, F227–F244 (2023).
92. Ellison, D. H., Maeoka, Y. & McCormick, J. A. Molecular mechanisms of renal magnesium reabsorption. *Journal of the American Society of Nephrology* **32**, 2125–2136 (2021).
93. Kiuchi-Saishin, Y. *et al.* Differential expression patterns of claudins, tight junction membrane proteins, in mouse nephron segments. *J Am Soc Nephrol* **13**, 875–886 (2002).
94. Van Itallie, C. M. *et al.* Two splice variants of claudin-10 in the kidney create paracellular pores with different ion selectivities. *Am J Physiol Renal Physiol* **291**, (2006).
95. Wong, N. L. M., Dirks, J. H. & Quamme, G. A. Tubular reabsorptive capacity for magnesium in the dog kidney. *Am J Physiol* **244**, (1983).
96. Guglielmi, G. Almost half of cancer deaths are preventable. *Nature* (2022) doi:10.1038/D41586-022-02355-X.
97. Papadimitriou, N. *et al.* An umbrella review of the evidence associating diet and cancer risk at 11 anatomical sites. *Nature Communications 2021 12:1* **12**, 1–10 (2021).
98. Morze, J. *et al.* An updated systematic review and meta-analysis on adherence to mediterranean diet and risk of cancer. *Eur J Nutr* **60**, 1561–1586 (2021).

99. Isaksen, I. M. & Dankel, S. N. Ultra-processed food consumption and cancer risk: A systematic review and meta-analysis. *Clinical Nutrition* **42**, 919–928 (2023).
100. Bagheri, A., Naghshi, S., Sadeghi, O., Larijani, B. & Esmaillzadeh, A. Total, Dietary, and Supplemental Magnesium Intakes and Risk of All-Cause, Cardiovascular, and Cancer Mortality: A Systematic Review and Dose-Response Meta-Analysis of Prospective Cohort Studies. doi:10.1093/advances/nmab001.
101. Huang, W. Q. *et al.* Direct and indirect associations between dietary magnesium intake and breast cancer risk. *Scientific Reports 2019 9:1* **9**, 1–10 (2019).
102. Dana, N. *et al.* Magnesium intake and lung cancer risk: A systematic review and meta-analysis. *https://doi.org/10.1024/0300-9831/a000598* **91**, 539–546 (2019).
103. Zhong, G. C. *et al.* Magnesium intake and primary liver cancer incidence and mortality in the Prostate, Lung, Colorectal and Ovarian Cancer Screening Trial. *Int J Cancer* **147**, 1577–1586 (2020).
104. Wark, P. A., Lau, R., Norat, T. & Kampman, E. Magnesium intake and colorectal tumor risk: a case-control study and meta-analysis. *Am J Clin Nutr* **96**, 622–631 (2012).
105. Gupta, A. A., Shekatkar, M., Raj, A. T. & Kheur, S. Potential Role of Magnesium in Cancer Initiation and Progression. *Pathology and Oncology Research* **26**, 2001–2002 (2020).
106. Hartwig, A. Role of magnesium in genomic stability. *Mutation Research - Fundamental and Molecular Mechanisms of Mutagenesis* **475**, 113–121 (2001).
107. Kumar, G. *et al.* Magnesium improves cisplatin-mediated tumor killing while protecting against cisplatin-induced nephrotoxicity. *Am J Physiol Renal Physiol* **313**, F339–F350 (2017).
108. Nasulewicz, A. *et al.* Magnesium deficiency inhibits primary tumor growth but favors metastasis in mice. *Biochimica et Biophysica Acta (BBA) - Molecular Basis of Disease* **1739**, 26–32 (2004).
109. Nielsen, F. H. Magnesium deficiency and increased inflammation: current perspectives. *J Inflamm Res* **11**, 25 (2018).
110. Ashique, S. *et al.* A narrative review on the role of magnesium in immune regulation, inflammation, infectious diseases, and cancer. *J Health Popul Nutr* **42**, 1–14 (2023).
111. Workeneh, B. T., Uppal, N. N., Jhaveri, K. D. & Rondon-Berrios, H. Hypomagnesemia in the Cancer Patient. *Kidney360* **2**, 154 (2021).
112. Liamis, G., Hoorn, E. J., Florentin, M. & Milionis, H. An overview of diagnosis and management of drug-induced hypomagnesemia. *Pharmacol Res Perspect* **9**, (2021).
113. Vernon, H., Wehrle, C. J., Alia, V. S. K. & Kasi, A. Anatomy, Abdomen and Pelvis: Liver. *StatPearls* (2022).
114. Kalra, A., Yetiskul, E., Wehrle, C. J. & Tuma, F. Physiology, Liver. *StatPearls* (2023).
115. Jones, M. W., Small, K., Kashyap, S. & Deppen, J. G. Physiology, Gallbladder. *StatPearls* (2023).
116. Hundt, M., Wu, C. Y. & Young, M. Anatomy, Abdomen and Pelvis: Biliary Ducts. *StatPearls* (2023).
117. Tabibian, J. H., Masyuk, A. I., Masyuk, T. V., O'Hara, S. P. & LaRusso, N. F. Physiology of cholangiocytes. *Compr Physiol* **3**, 541–565 (2013).
118. Racanelli, V. & Rehermann, B. The liver as an immunological organ. *Hepatology* **43**, (2006).
119. Trefts, E., Gannon, M. & Wasserman, D. H. The liver. *Curr Biol* **27**, R1147 (2017).
120. Moeini, A., Haber, P. K. & Sia, D. Cell of origin in biliary tract cancers and clinical implications. *JHEP Rep* **3**, (2021).
121. Kitade, M., Kaji, K. & Yoshiji, H. Relationship between hepatic progenitor cell-mediated liver regeneration and non-parenchymal cells. *Hepatol Res* **46**, 1187–1193 (2016).
122. Friedman, J. R. & Kaestner, K. H. On the origin of the liver. *J Clin Invest* **121**, 4630 (2011).
123. Kalra, A., Yetiskul, E., Wehrle, C. J. & Tuma, F. Physiology, Liver. *StatPearls* (2023).
124. Trefts, E., Gannon, M. & Wasserman, D. H. The liver. *Curr Biol* **27**, R1147 (2017).
125. Vernon, H., Wehrle, C. J., Alia, V. S. K. & Kasi, A. Anatomy, Abdomen and Pelvis: Liver. *StatPearls* (2022).
126. Hundt, M., Basit, H. & John, S. Physiology, Bile Secretion. *StatPearls* (2022).
127. Banales, J. M. *et al.* Cholangiocyte pathobiology. *Nat Rev Gastroenterol Hepatol* **16**, 269 (2019).

128. Tabibian, J. H., Masyuk, A. I., Masyuk, T. V., O'Hara, S. P. & LaRusso, N. F. Physiology of cholangiocytes. *Compr Physiol* **3**, 541–565 (2013).
129. Devarbhavi, H. *et al.* Global burden of liver disease: 2023 update. *J Hepatol* **79**, 516–537 (2023).
130. Brindley, P. J. *et al.* Cholangiocarcinoma. *Nature Reviews Disease Primers 2021 7:1* **7**, 1–17 (2021).
131. Bragazzi, M. C. *et al.* New insights into cholangiocarcinoma: multiple stems and related cell lineages of origin. *Ann Gastroenterol* **31**, 42 (2018).
132. Cardinale, V., Paradiso, S. & Alvaro, D. Biliary stem cells in health and cholangiopathies and cholangiocarcinoma. *Curr Opin Gastroenterol* **40**, 92–98 (2024).
133. Banales, J. M. *et al.* Cholangiocarcinoma 2020: the next horizon in mechanisms and management. *Nat Rev Gastroenterol Hepatol* **17**, 557–588 (2020).
134. Clements, O., Eliahoo, J., Kim, J. U., Taylor-Robinson, S. D. & Khan, S. A. Risk factors for intrahepatic and extrahepatic cholangiocarcinoma: A systematic review and meta-analysis. *J Hepatol* **72**, 95–103 (2020).
135. Rizvi, S. & Gores, G. J. Pathogenesis, diagnosis, and management of cholangiocarcinoma. *Gastroenterology* **145**, 1215–1229 (2013).
136. Cardinale, V. Classifications and misclassification in cholangiocarcinoma. *Liver Int* **39**, 260–262 (2019).
137. Yamasaki, S. Intrahepatic cholangiocarcinoma: macroscopic type and stage classification. *J Hepatobiliary Pancreat Surg* **10**, 288–291 (2003).
138. Nagtegaal, I. D. *et al.* The 2019 WHO classification of tumours of the digestive system. *Histopathology* **76**, 182 (2020).
139. Alvaro, D. *et al.* EASL-ILCA Clinical Practice Guidelines on the management of intrahepatic cholangiocarcinoma. *J Hepatol* **79**, 181–208 (2023).
140. Labib, P. L., Goodchild, G. & Pereira, S. P. Molecular Pathogenesis of Cholangiocarcinoma. *BMC Cancer* **19**, 1–16 (2019).
141. Bertuccio, P. *et al.* Global trends in mortality from intrahepatic and extrahepatic cholangiocarcinoma. *J Hepatol* **71**, 104–114 (2019).
142. Vithayathil, M. & Khan, S. A. Current epidemiology of cholangiocarcinoma in Western countries. *J Hepatol* **77**, 1690–1698 (2022).
143. Antwi, S. O., Mousa, O. Y. & Patel, T. Racial, Ethnic, and Age Disparities in Incidence and Survival of Intrahepatic Cholangiocarcinoma in the United States; 1995-2014. *Ann Hepatol* **17**, 604–614 (2018).
144. Khosla, D. *et al.* Cholangiocarcinoma: Recent Advances in Molecular Pathobiology and Therapeutic Approaches. *Cancers (Basel)* **16**, 801 (2024).
145. Sripa, B. *et al.* Liver fluke induces cholangiocarcinoma. *PLoS Medicine* vol. 4 1148–1155 Preprint at https://doi.org/10.1371/journal.pmed.0040201 (2007).
146. Zheng, S. *et al.* Liver fluke infection and cholangiocarcinoma: a review. *Parasitol Res* **116**, 11–19 (2017).
147. Young, N. D. *et al.* The Opisthorchis viverrini genome provides insights into life in the bile duct. *Nat Commun* **5**, (2014).
148. Liau, M. Y. Q., Toh, E. Q. & Shelat, V. G. Opisthorchis viverrini-Current Understanding of the Neglected Hepatobiliary Parasite. *Pathogens* **12**, (2023).
149. Smout, M. J. *et al.* Infection with the carcinogenic human liver fluke, Opisthorchis viverrini. *Mol Biosyst* **7**, 1367–1375 (2011).
150. Gupta, A. & Dixon, E. Epidemiology and risk factors: intrahepatic cholangiocarcinoma. *Hepatobiliary Surg Nutr* **6**, 10104–10104 (2017).
151. Wang, Y., Yuan, Y. & Gu, D. Hepatitis B and C virus infections and the risk of biliary tract cancers: a meta-analysis of observational studies. *Infect Agent Cancer* **17**, 1–8 (2022).
152. Wongjarupong, N. *et al.* Non-alcoholic fatty liver disease as a risk factor for cholangiocarcinoma: a systematic review and meta-analysis. *BMC Gastroenterol* **17**, 149 (2017).
153. Boscoe, A. N., Rolland, C. & Kelley, R. K. Frequency and prognostic significance of isocitrate dehydrogenase 1 mutations in cholangiocarcinoma: a systematic literature review. *J Gastrointest Oncol* **10**, 751 (2019).

154. Li, J. *et al.* A Pancancer Analysis of the Expression Landscape and Clinical Relevance of Fibroblast Growth Factor Receptor 2 in Human Cancers. *Front Oncol* **11**, 644854 (2021).
155. Andersen, J. B. *et al.* Genomic and genetic characterization of cholangiocarcinoma identifies therapeutic targets for tyrosine kinase inhibitors. *Gastroenterology* **142**, (2012).
156. Yokoyama, M. *et al.* KRAS Mutation as a Potential Prognostic Biomarker of Biliary Tract Cancers. *Jpn Clin Med* **7**, 33 (2016).
157. Galdy, S. *et al.* HER2/HER3 pathway in biliary tract malignancies; systematic review and meta-analysis: a potential therapeutic target? *Cancer Metastasis Rev* **36**, 141–157 (2017).
158. Zhang, Y. *et al.* The genomic landscape of cholangiocarcinoma reveals the disruption of post-transcriptional modifiers. *Nat Commun* **13**, (2022).
159. Guo, C. *et al.* TP53 /KRAS Co-Mutations Create Divergent Prognosis Signatures in Intrahepatic Cholangiocarcinoma. *Front Genet* **13**, 844800 (2022).
160. Jiao, Y. *et al.* Exome sequencing identifies frequent inactivating mutations in BAP1, ARID1A and PBRM1 in intrahepatic cholangiocarcinomas. *Nat Genet* **45**, 1470–1473 (2013).
161. Shi, T., Morishita, A., Kobara, H. & Masaki, T. The Role of microRNAs in Cholangiocarcinoma. *Int J Mol Sci* **22**, 7627 (2021).
162. Zheng, B., Jeong, S., Zhu, Y., Chen, L. & Xia, Q. miRNA and lncRNA as biomarkers in cholangiocarcinoma(CCA). *Oncotarget* **8**, 100819 (2017).
163. Wang, L. J. *et al.* MiR-21 promotes intrahepatic cholangiocarcinoma proliferation and growth in vitro and in vivo by targeting PTPN14 and PTEN. *Oncotarget* **6**, 5932 (2015).
164. Goeppert, B. *et al.* Global alterations of DNA methylation in cholangiocarcinoma target the Wnt signaling pathway. *Hepatology* **59**, 544–554 (2014).
165. Merino-Azpitarte, M. *et al.* SOX17 Regulates Cholangiocyte Differentiation and Acts as a Tumor Suppressor in Cholangiocarcinoma. *J Hepatol* **67**, 72 (2017).
166. Yu, Y. *et al.* Epigenetic silencing of tumor suppressor gene CDKN1A by oncogenic long non-coding RNA SNHG1 in cholangiocarcinoma. *Cell Death Dis* **9**, (2018).
167. Meng, F., Wehbe-Janek, H., Henson, R., Smith, H. & Patel, T. Epigenetic regulation of microRNA-370 by interleukin-6 in malignant human cholangiocytes. *Oncogene* **27**, 378–386 (2008).
168. Isomoto, H. *et al.* Sustained IL-6/STAT-3 Signaling in Cholangiocarcinoma Cells due to SOCS-3 Epigenetic Silencing. *Gastroenterology* **132**, 384 (2007).
169. Jusakul, A. *et al.* Whole-Genome and Epigenomic Landscapes of Etiologically Distinct Subtypes of Cholangiocarcinoma. *Cancer Discov* **7**, 1116–1135 (2017).
170. Zhong, B., Liao, Q., Wang, X., Wang, X. & Zhang, J. The roles of epigenetic regulation in cholangiocarcinogenesis. *Biomedicine & Pharmacotherapy* **166**, 115290 (2023).
171. Zhang, J. *et al.* EZH2 Promotes Cholangiocarcinoma Development and Progression through Histone Methylation and microRNA-Mediated Down-Regulation of Tumor Suppressor Genes. *Am J Pathol* **192**, 1712–1724 (2022).
172. Fava, G. Molecular mechanisms of cholangiocarcinoma. *World J Gastrointest Pathophysiol* **1**, 12 (2010).
173. Fouassier, L. *et al.* Signalling networks in cholangiocarcinoma: Molecular pathogenesis, targeted therapies and drug resistance. *Liver International* **39**, 43–62 (2019).
174. Xin-Wei, Y. *et al.* STAT3 overexpression promotes metastasis in intrahepatic cholangiocarcinoma and correlates negatively with surgical outcome. *Oncotarget* **8**, 7710–7721 (2017).
175. Dokduang, H. *et al.* STATs profiling reveals predominantly-activated STAT3 in cholangiocarcinoma genesis and progression. *J Hepatobiliary Pancreat Sci* **21**, 767–776 (2014).
176. Zen, Y. *et al.* Intrahepatic cholangiocarcinoma escapes from growth inhibitory effect of transforming growth factor-beta1 by overexpression of cyclin D1. *Lab Invest* **85**, 572–581 (2005).

177. Araki, K. *et al.* E/N-cadherin switch mediates cancer progression via TGF-β-induced epithelial-to-mesenchymal transition in extrahepatic cholangiocarcinoma. *British Journal of Cancer 2011 105:12* **105**, 1885–1893 (2011).
178. Clapéron, A. *et al.* EGF/EGFR axis contributes to the progression of cholangiocarcinoma through the induction of an epithelial-mesenchymal transition. *J Hepatol* **61**, 325–332 (2014).
179. Chmiel, P., Gęca, K., Rawicz-Pruszyński, K., Polkowski, W. P. & Skórzewska, M. FGFR Inhibitors in Cholangiocarcinoma—A Novel Yet Primary Approach: Where Do We Stand Now and Where to Head Next in Targeting This Axis? *Cells* **11**, (2022).
180. Onori, P. *et al.* Secretin inhibits cholangiocarcinoma growth via dysregulation of the cAMP-dependent signaling mechanisms of secretin receptor. *Int J Cancer* **127**, 43–54 (2010).
181. Fabris, L. & Pol, J. Mast cells and histamine in cholangiocarcinoma: exploring overlooked avenues for enhanced patient management. *Gut* (2024) doi:10.1136/GUTJNL-2024-332288.
182. Scimeca, M. *et al.* Programmed Cell Death Pathways in Cholangiocarcinoma: Opportunities for Targeted Therapy. *Cancers (Basel)* **15**, (2023).
183. Lyons, A. M. & Boulter, L. NOTCH signalling - a core regulator of bile duct disease? *DMM Disease Models and Mechanisms* **16**, (2023).
184. Anichini, G., Carrassa, L., Stecca, B., Marra, F. & Raggi, C. The Role of the Hedgehog Pathway in Cholangiocarcinoma. *Cancers (Basel)* **13**, (2021).
185. Forner, A. *et al.* Clinical presentation, diagnosis and staging of cholangiocarcinoma. *Liver International* **39**, 98–107 (2019).
186. Rizvi, S., Khan, S. A., Hallemeier, C. L., Kelley, R. K. & Gores, G. J. Cholangiocarcinoma — evolving concepts and therapeutic strategies. *Nat Rev Clin Oncol* **15**, 95 (2018).
187. Tsung, C., Quinn, P. L. & Ejaz, A. Management of Intrahepatic Cholangiocarcinoma: A Narrative Review. *Cancers (Basel)* **16**, 739 (2024).
188. Huang, J., Bai, X., Qiu, Y. & He, X. Application of AI on cholangiocarcinoma. *Front Oncol* **14**, (2024).
189. Tsung, C., Quinn, P. L. & Ejaz, A. Management of Intrahepatic Cholangiocarcinoma: A Narrative Review. *Cancers (Basel)* **16**, 739 (2024).
190. Izquierdo-Sanchez, L. *et al.* Cholangiocarcinoma landscape in Europe: Diagnostic, prognostic and therapeutic insights from the ENSCCA Registry. *J Hepatol* **76**, 1109–1121 (2022).
191. Stenzinger, A. *et al.* Molecular profiling in cholangiocarcinoma: A practical guide to next-generation sequencing. *Cancer Treat Rev* **122**, 102649 (2024).
192. Lamarca, A. *et al.* Current standards and future perspectives in adjuvant treatment for biliary tract cancers. *Cancer Treat Rev* **84**, 101936 (2020).
193. Spolverato, G. *et al.* The Impact of Surgical Margin Status on Long-Term Outcome After Resection for Intrahepatic Cholangiocarcinoma. *Ann Surg Oncol* **22**, 4020–4028 (2015).
194. Nagino, M. *et al.* Evolution of surgical treatment for perihilar cholangiocarcinoma: a single-center 34-year review of 574 consecutive resections. *Ann Surg* **258**, 129–140 (2013).
195. DeOliveira, M. L. *et al.* Cholangiocarcinoma: thirty-one-year experience with 564 patients at a single institution. *Ann Surg* **245**, 755–762 (2007).
196. Primrose, J. N. *et al.* Capecitabine compared with observation in resected biliary tract cancer (BILCAP): a randomised, controlled, multicentre, phase 3 study. *Lancet Oncol* **20**, 663–673 (2019).
197. Bridgewater, J. *et al.* Long-Term Outcomes and Exploratory Analyses of the Randomized Phase III BILCAP Study. *Journal of Clinical Oncology* **40**, 2048–2057 (2022).
198. Stein, A. *et al.* Adjuvant chemotherapy with gemcitabine and cisplatin compared to observation after curative intent resection of cholangiocarcinoma and muscle invasive gallbladder carcinoma (ACTICCA-1 trial) - a randomized, multidisciplinary, multinational phase III trial. *BMC Cancer* **15**, (2015).
199. Chen, Y. *et al.* Original research: Clinical efficacy of adjuvant treatments for patients with resected biliary tract cancer: a systematic review and network meta-analysis. *BMJ Open* **12**, 51421 (2022).

200. Valle, J. *et al.* Cisplatin plus Gemcitabine versus Gemcitabine for Biliary Tract Cancer. *New England Journal of Medicine* **362**, 1273–1281 (2010).
201. Oh, D.-Y. *et al.* Durvalumab plus Gemcitabine and Cisplatin in Advanced Biliary Tract Cancer. *NEJM Evidence* **1**, (2022).
202. Kelley, R. K. *et al.* Pembrolizumab in combination with gemcitabine and cisplatin compared with gemcitabine and cisplatin alone for patients with advanced biliary tract cancer (KEYNOTE-966): a randomised, double-blind, placebo-controlled, phase 3 trial. *Lancet* **401**, 1853–1865 (2023).
203. Kim, S. T. *et al.* Capecitabine plus oxaliplatin versus gemcitabine plus oxaliplatin as first-line therapy for advanced biliary tract cancers: a multicenter, open-label, randomized, phase III, noninferiority trial. *Ann Oncol* **30**, 788–795 (2019).
204. Cho, J. Y. *et al.* Capecitabine combined with gemcitabine (CapGem) as first-line treatment in patients with advanced/metastatic biliary tract carcinoma. *Cancer* **104**, 2753–2758 (2005).
205. Sahai, V. *et al.* Nab-Paclitaxel and Gemcitabine as First-line Treatment of Advanced or Metastatic Cholangiocarcinoma: A Phase 2 Clinical Trial. *JAMA Oncol* **4**, 1707–1712 (2018).
206. Morizane, C. *et al.* Combination gemcitabine plus S-1 versus gemcitabine plus cisplatin for advanced/recurrent biliary tract cancer: the FUGA-BT (JCOG1113) randomized phase III clinical trial. *Ann Oncol* **30**, 1950–1958 (2019).
207. Gabriel, E. *et al.* Gemcitabine and capecitabine for advanced biliary cancer. *J Gastrointest Oncol* **8**, 728–736 (2017).
208. Chakravarty, D. *et al.* Somatic Genomic Testing in Patients With Metastatic or Advanced Cancer: ASCO Provisional Clinical Opinion. *J Clin Oncol* **40**, 1231–1258 (2022).
209. Li, Y. *et al.* Advances in targeted therapy of cholangiocarcinoma. *Ann Med* **56**, (2024).
210. Boilève, A. *et al.* Immunotherapy in Advanced Biliary Tract Cancers. *Cancers (Basel)* **13**, (2021).
211. Tong, X. *et al.* Targeting cell death pathways for cancer therapy: recent developments in necroptosis, pyroptosis, ferroptosis, and cuproptosis research. *Journal of Hematology & Oncology 2022 15:1* **15**, 1–32 (2022).
212. Chen, X., Kang, R., Kroemer, G. & Tang, D. Broadening horizons: the role of ferroptosis in cancer. *Nature Reviews Clinical Oncology 2021 18:5* **18**, 280–296 (2021).
213. Guo, J. *et al.* Ferroptosis: A Novel Anti-tumor Action for Cisplatin. *Cancer Res Treat* **50**, 445–460 (2018).
214. Su, L. *et al.* Isocitrate dehydrogenase 1 mutation in cholangiocarcinoma impairs tumor progression by sensitizing cells to ferroptosis. *Open Medicine (Poland)* **17**, 863–870 (2022).
215. Sun, X. *et al.* Activation of the p62-Keap1-NRF2 pathway protects against ferroptosis in hepatocellular carcinoma cells. *Hepatology* **63**, 173–184 (2016).
216. Wang, W. *et al.* CD8+ T cells regulate tumour ferroptosis during cancer immunotherapy. *Nature 2019 569:7755* **569**, 270–274 (2019).
217. Hanahan, D. & Weinberg, R. A. Leading Edge Review Hallmarks of Cancer: The Next Generation. doi:10.1016/j.cell.2011.02.013.
218. Liu, Y. *et al.* The diversified role of mitochondria in ferroptosis in cancer. *Cell Death & Disease 2023 14:8* **14**, 1–12 (2023).
219. Kroemer, G. *et al.* Classification of cell death: recommendations of the Nomenclature Committee on Cell Death 2009. *Cell Death Differ* **16**, 3 (2009).
220. Galluzzi, L. *et al.* Molecular mechanisms of cell death: recommendations of the Nomenclature Committee on Cell Death 2018. *Cell Death & Differentiation 2018 25:3* **25**, 486–541 (2018).
221. Tang, D., Kang, R., Berghe, T. Vanden, Vandenabeele, P. & Kroemer, G. The molecular machinery of regulated cell death. *Cell Research 2019 29:5* **29**, 347–364 (2019).
222. Fuchs, Y. & Steller, H. Programmed Cell Death in Animal Development and Disease. *Cell* **147**, 742 (2011).
223. Hajibabaie, F., Abedpoor, N. & Mohamadynejad, P. Types of Cell Death from a Molecular Perspective. *Biology (Basel)* **12**, 1426 (2023).

224. Yan, G., Elbadawi, M. & Efferth, T. Multiple cell death modalities and their key features (Review). *World Acad Sci J* **2**, 39–48 (2020).
225. Dixon, S. J. *et al.* Ferroptosis: an iron-dependent form of nonapoptotic cell death. *Cell* **149**, 1060–1072 (2012).
226. Li, J. *et al.* Ferroptosis: past, present and future. doi:10.1038/s41419-020-2298-2.
227. Yan, H. fa *et al.* Ferroptosis: mechanisms and links with diseases. *Signal Transduction and Targeted Therapy 2021 6:1* **6**, 1–16 (2021).
228. Stockwell, B. R. Ferroptosis turns 10: Emerging mechanisms, physiological functions, and therapeutic applications. *Cell* **185**, 2401–2421 (2022).
229. Chen, X., Yu, C., Kang, R. & Tang, D. Iron Metabolism in Ferroptosis. *Front Cell Dev Biol* **8**, 590226 (2020).
230. Gao, M. *et al.* Understanding the mechanistic regulation of ferroptosis in cancer: the gene matters. *J Genet Genomics* **49**, 913–926 (2022).
231. Liu, J. *et al.* NUPR1 is a critical repressor of ferroptosis. doi:10.1038/s41467-021-20904-2.
232. Huang, C. *et al.* NUPR1: A Critical Regulator of the Antioxidant System. *Cancers 2021, Vol. 13, Page 3670* **13**, 3670 (2021).
233. Chiang, S. K., Chen, S. E. & Chang, L. C. A Dual Role of Heme Oxygenase-1 in Cancer Cells. *Int J Mol Sci* **20**, (2018).
234. Emma, M. R. *et al.* NUPR1, a new target in liver cancer: implication in controlling cell growth, migration, invasion and sorafenib resistance. *Cell Death Dis* **7**, (2016).
235. Chen, C. Y. *et al.* Induction of nuclear protein-1 by thyroid hormone enhances platelet-derived growth factor A mediated angiogenesis in liver cancer. *Theranostics* **9**, 2361–2379 (2019).
236. Kim, K.-S. *et al.* Expression and roles of NUPR1 in cholangiocarcinoma cells. *Anat Cell Biol* **45**, 17 (2012).
237. Hou, B., Qin, L. & Huang, L. Liver cancer cells as the model for developing liver-targeted RNAi therapeutics. *Biochem Biophys Res Commun* **644**, 85–94 (2023).
238. Khan, A. A., Alanazi, A. M., Jabeen, M., Chauhan, A. & Ansari, M. A. Therapeutic potential of functionalized siRNA nanoparticles on regression of liver cancer in experimental mice. *Scientific Reports 2019 9:1* **9**, 1–16 (2019).
239. Debacker, A. J., Voutila, J., Catley, M., Blakey, D. & Habib, N. Delivery of Oligonucleotides to the Liver with GalNAc: From Research to Registered Therapeutic Drug. doi:10.1016/j.ymthe.2020.06.015.
240. Springer, A. D. & Dowdy, S. F. GalNAc-siRNA Conjugates: Leading the Way for Delivery of RNAi Therapeutics. *Nucleic Acid Ther* **28**, 109 (2018).
241. Padda, I. S., Mahtani, A. U. & Parmar, M. Small Interfering RNA (siRNA) Therapy. *StatPearls* (2023).
242. Cascella, M., Rajnik, M., Cuomo, A., Dulebohn, S. C. & Di Napoli, R. Features, Evaluation, and Treatment of Coronavirus (COVID-19). *StatPearls* (2023).
243. Zhou, P. *et al.* A pneumonia outbreak associated with a new coronavirus of probable bat origin. *Nature 2020 579:7798* **579**, 270–273 (2020).
244. Meyerowitz, E. A., Richterman, A., Gandhi, R. T. & Sax, P. E. Transmission of SARS-CoV-2: A Review of Viral, Host, and Environmental Factors. *Ann Intern Med* **174**, 69–79 (2021).
245. Msemburi, W. *et al.* The WHO estimates of excess mortality associated with the COVID-19 pandemic. *Nature 2022 613:7942* **613**, 130–137 (2022).
246. COVID-19 deaths | WHO COVID-19 dashboard. https://data.who.int/dashboards/covid19/deaths.
247. Edridge, A. W. D. *et al.* Seasonal coronavirus protective immunity is short-lasting. *Nature Medicine 2020 26:11* **26**, 1691–1693 (2020).
248. Park, S., Lee, Y., Michelow, I. C. & Choe, Y. J. Global Seasonality of Human Coronaviruses: A Systematic Review. *Open Forum Infect Dis* **7**, (2020).
249. Zhu, N. *et al.* A Novel Coronavirus from Patients with Pneumonia in China, 2019. *New England Journal of Medicine* **382**, 727–733 (2020).

250. Rambaut, A. *et al.* A dynamic nomenclature proposal for SARS-CoV-2 lineages to assist genomic epidemiology. *Nature Microbiology 2020 5:11* **5**, 1403–1407 (2020).
251. V'kovski, P., Kratzel, A., Steiner, S., Stalder, H. & Thiel, V. Coronavirus biology and replication: implications for SARS-CoV-2. *Nature Reviews Microbiology 2020 19:3* **19**, 155–170 (2020).
252. Gordon, D. E. *et al.* A SARS-CoV-2 protein interaction map reveals targets for drug repurposing. *Nature 2020 583:7816* **583**, 459–468 (2020).
253. Jamison, D. A. *et al.* A comprehensive SARS-CoV-2 and COVID-19 review, Part 1: Intracellular overdrive for SARS-CoV-2 infection. *European Journal of Human Genetics 2022 30:8* **30**, 889–898 (2022).
254. Jackson, C. B., Farzan, M., Chen, B. & Choe, H. Mechanisms of SARS-CoV-2 entry into cells. *Nature Reviews Molecular Cell Biology 2021 23:1* **23**, 3–20 (2021).
255. V'kovski, P., Kratzel, A., Steiner, S., Stalder, H. & Thiel, V. Coronavirus biology and replication: implications for SARS-CoV-2. *Nature Reviews Microbiology 2020 19:3* **19**, 155–170 (2020).
256. Hoffmann, M. *et al.* SARS-CoV-2 Cell Entry Depends on ACE2 and TMPRSS2 and Is Blocked by a Clinically Proven Protease Inhibitor. *Cell* **181**, 271-280.e8 (2020).
257. Fraser, B. J. *et al.* Structure and activity of human TMPRSS2 protease implicated in SARS-CoV-2 activation. *Nature Chemical Biology 2022 18:9* **18**, 963–971 (2022).
258. Cantuti-Castelvetri, L. *et al.* Neuropilin-1 facilitates SARS-CoV-2 cell entry and infectivity. *Science (1979)* **370**, (2020).
259. Zhang, W. *et al.* SARS-CoV-2 infection results in immune responses in the respiratory tract and peripheral blood that suggest mechanisms of disease severity. *Nature Communications 2022 13:1* **13**, 1–18 (2022).
260. Brodin, P. Immune determinants of COVID-19 disease presentation and severity. *Nature Medicine 2021 27:1* **27**, 28–33 (2021).
261. Fajgenbaum, D. C. & June, C. H. Cytokine Storm. *New England Journal of Medicine* **383**, 2255–2273 (2020).
262. Diamond, M. S. & Kanneganti, T. D. Innate immunity: the first line of defense against SARS-CoV-2. *Nat Immunol* **23**, 165–176 (2022).
263. Azagew, A. W. *et al.* Global prevalence of COVID-19-induced acute respiratory distress syndrome: systematic review and meta-analysis. *Syst Rev* **12**, 1–9 (2023).
264. Jamison, D. A. *et al.* A comprehensive SARS-CoV-2 and COVID-19 review, Part 1: Intracellular overdrive for SARS-CoV-2 infection. *European Journal of Human Genetics 2022 30:8* **30**, 889–898 (2022).
265. Stukalov, A. *et al.* Multilevel proteomics reveals host perturbations by SARS-CoV-2 and SARS-CoV. *Nature* **594**, 246–252 (2021).
266. Appelberg, S. *et al.* Dysregulation in Akt/mTOR/HIF-1 signaling identified by proteo-transcriptomics of SARS-CoV-2 infected cells. *Emerg Microbes Infect* **9**, 1748–1760 (2020).
267. Basile, M. S. *et al.* The PI3K/Akt/mTOR pathway: A potential pharmacological target in COVID-19. *Drug Discov Today* **27**, 848 (2022).
268. Bouhaddou, M. *et al.* The Global Phosphorylation Landscape of SARS-CoV-2 Infection. *Cell* **182**, 685-712.e19 (2020).
269. Forrester, S. J. *et al.* Angiotensin II Signal Transduction: An Update on Mechanisms of Physiology and Pathophysiology. *Physiol Rev* **98**, 1627 (2018).
270. Prato, M. *et al.* The Renin–Angiotensin System (RAS) in COVID-19 Disease: Where We Are 3 Years after the Beginning of the Pandemic. *Microorganisms* vol. 12 Preprint at https://doi.org/10.3390/microorganisms12030583 (2024).
271. Clinical Spectrum | COVID-19 Treatment Guidelines. https://www.covid19treatmentguidelines.nih.gov/overview/clinical-spectrum/.
272. Agrawal, U. *et al.* Severe COVID-19 outcomes after full vaccination of primary schedule and initial boosters: pooled analysis of national prospective cohort studies of 30 million individuals in England, Northern Ireland, Scotland, and Wales. *The Lancet* **400**, 1305–1320 (2022).

273. Taylor, C. A. *et al.* COVID-19-Associated Hospitalizations Among U.S. Adults Aged ≥65 Years - COVID-NET, 13 States, January-August 2023. *MMWR Morb Mortal Wkly Rep* **72**, 1089–1094 (2023).
274. Variation in the COVID-19 infection–fatality ratio by age, time, and geography during the pre-vaccine era: a systematic analysis. *The Lancet* **399**, 1469–1488 (2022).
275. Stokes, E. K. *et al.* Coronavirus Disease 2019 Case Surveillance - United States, January 22-May 30, 2020. *MMWR Morb Mortal Wkly Rep* **69**, 759–765 (2020).
276. Onder, G., Rezza, G. & Brusaferro, S. Case-Fatality Rate and Characteristics of Patients Dying in Relation to COVID-19 in Italy. *JAMA* **323**, 1775–1776 (2020).
277. Harrison, S. L., Fazio-Eynullayeva, E., Lane, D. A., Underhill, P. & Lip, G. Y. H. Comorbidities associated with mortality in 31,461 adults with COVID-19 in the United States: A federated electronic medical record analysis. *PLoS Med* **17**, (2020).
278. Cunningham, J. W. *et al.* Clinical Outcomes in Young US Adults Hospitalized With COVID-19. *JAMA Intern Med* **181**, 379–381 (2021).
279. Williamson, E. J. *et al.* OpenSAFELY: factors associated with COVID-19 death in 17 million patients. *Nature* **584**, 430 (2020).
280. Petrilli, C. M. *et al.* Factors associated with hospital admission and critical illness among 5279 people with coronavirus disease 2019 in New York City: prospective cohort study. *BMJ* **369**, (2020).
281. Marquez, N., Ward, J. A., Parish, K., Saloner, B. & Dolovich, S. COVID-19 Incidence and Mortality in Federal and State Prisons Compared With the US Population, April 5, 2020, to April 3, 2021. *JAMA* **326**, 1865–1867 (2021).
282. Zhou, F. *et al.* Clinical course and risk factors for mortality of adult inpatients with COVID-19 in Wuhan, China: a retrospective cohort study. *The Lancet* **395**, 1054–1062 (2020).
283. Ellinghaus, D. *et al.* Genomewide Association Study of Severe Covid-19 with Respiratory Failure. *N Engl J Med* **383**, 1522–1534 (2020).
284. Kousathanas, A. *et al.* Whole-genome sequencing reveals host factors underlying critical COVID-19. *Nature 2022 607:7917* **607**, 97–103 (2022).
285. Wu, Z. & McGoogan, J. M. Characteristics of and Important Lessons From the Coronavirus Disease 2019 (COVID-19) Outbreak in China: Summary of a Report of 72 314 Cases From the Chinese Center for Disease Control and Prevention. *JAMA* **323**, 1239–1242 (2020).
286. Dai, M. *et al.* Patients with Cancer Appear More Vulnerable to SARS-CoV-2: A Multicenter Study during the COVID-19 Outbreak. *Cancer Discov* **10**, 783 (2020).
287. Chow, N. *et al.* Preliminary Estimates of the Prevalence of Selected Underlying Health Conditions Among Patients with Coronavirus Disease 2019 - United States, February 12-March 28, 2020. *MMWR Morb Mortal Wkly Rep* **69**, 382–386 (2020).
288. Vitiello, A. *et al.* The impact of SARS-CoV-2 infection in patients with cystic fibrosis undergoing CFTR channel modulators treatment: a literature review. *Respir Res* **24**, 1–10 (2023).
289. Kuper, H. & Smythe, T. Are people with disabilities at higher risk of COVID-19-related mortality?: a systematic review and meta-analysis. *Public Health* **222**, 115–124 (2023).
290. Heidary, M. *et al.* COVID-19 in HIV-positive patients: A systematic review of case reports and case series. *J Clin Lab Anal* **36**, (2022).
291. Tartof, S. Y. *et al.* Obesity and Mortality Among Patients Diagnosed With COVID-19: Results From an Integrated Health Care Organization. *Ann Intern Med* **173**, 773–781 (2020).
292. Lighter, J. *et al.* Obesity in Patients Younger Than 60 Years Is a Risk Factor for COVID-19 Hospital Admission. *Clin Infect Dis* **71**, 896–897 (2020).
293. Sallis, R. *et al.* Physical inactivity is associated with a higher risk for severe COVID-19 outcomes: a study in 48 440 adult patients. *Br J Sports Med* **55**, 1099–1105 (2021).
294. Wastnedge, E. A. N. *et al.* Pregnancy and COVID-19. *Physiol Rev* **101**, 303–318 (2021).

295. Lowe, K. E., Zein, J., Hatipoğlu, U. & Attaway, A. Association of Smoking and Cumulative Pack-Year Exposure With COVID-19 Outcomes in the Cleveland Clinic COVID-19 Registry. *JAMA Intern Med* **181**, 709–711 (2021).
296. Michelon, I. *et al.* COVID-19 outcomes in patients with sickle cell disease and sickle cell trait compared with individuals without sickle cell disease or trait: a systematic review and meta-analysis. *EClinicalMedicine* **66**, (2023).
297. Nacif, L. S. *et al.* COVID-19 in solid organ transplantation patients: A systematic review. *Clinics* **75**, 1–11 (2020).
298. Busca, A. *et al.* Outcome of COVID-19 in allogeneic stem cell transplant recipients: Results from the EPICOVIDEHA registry. *Front Immunol* **14**, (2023).
299. Wang, Q. Q., Kaelber, D. C., Xu, R. & Volkow, N. D. COVID-19 risk and outcomes in patients with substance use disorders: analyses from electronic health records in the United States. *Mol Psychiatry* **26**, 30–39 (2021).
300. Migliori, G. B. *et al.* Tuberculosis and COVID-19 co-infection: description of the global cohort. *Eur Respir J* **59**, (2022).
301. Maia, R., Melo, L., Mendes, J. J. & Freitas, P. T. Corticosteroids in COVID-19: A double-edged sword – a retrospective study. *Med Intensiva* **46**, 229–231 (2022).
302. Krammer, F. SARS-CoV-2 vaccines in development. *Nature 2020 586:7830* **586**, 516–527 (2020).
303. Pan, L. *et al.* Prevention and control of coronavirus disease 2019 (COVID-19) in public places. *Environ Pollut* **292**, (2022).
304. Wu, Y. *et al.* Incubation Period of COVID-19 Caused by Unique SARS-CoV-2 Strains: A Systematic Review and Meta-analysis. *JAMA Netw Open* **5**, e2228008 (2022).
305. Menni, C. *et al.* Symptom prevalence, duration, and risk of hospital admission in individuals infected with SARS-CoV-2 during periods of omicron and delta variant dominance: a prospective observational study from the ZOE COVID Study. *Lancet* **399**, 1618–1624 (2022).
306. Fang, F. C., Naccache, S. N. & Greninger, A. L. The Laboratory Diagnosis of Coronavirus Disease 2019-Frequently Asked Questions. *Clin Infect Dis* **71**, 2996–3001 (2020).
307. Dinnes, J. *et al.* Rapid, point-of-care antigen and molecular-based tests for diagnosis of SARS-CoV-2 infection. *Cochrane Database Syst Rev* **3**, (2021).
308. Cheng, M. P. *et al.* Serodiagnostics for Severe Acute Respiratory Syndrome-Related Coronavirus 2 : A Narrative Review. *Ann Intern Med* **173**, 450–460 (2020).
309. Yuan, Y., Jiao, B., Qu, L., Yang, D. & Liu, R. The development of COVID-19 treatment. *Front Immunol* **14**, (2023).
310. Abebe, E. C. & Dejenie, T. A. Protective roles and protective mechanisms of neutralizing antibodies against SARS-CoV-2 infection and their potential clinical implications. *Front Immunol* **14**, (2023).
311. Ackermann, M. *et al.* Pulmonary Vascular Endothelialitis, Thrombosis, and Angiogenesis in Covid-19. *New England Journal of Medicine* **383**, 120–128 (2020).
312. Alhazzani, W. *et al.* Surviving Sepsis Campaign: guidelines on the management of critically ill adults with Coronavirus Disease 2019 (COVID-19). *Intensive Care Med* **46**, 854–887 (2020).
313. Gupta, A. *et al.* Extrapulmonary manifestations of COVID-19. *Nature Medicine 2020 26:7* **26**, 1017–1032 (2020).
314. Yadav, D. K. *et al.* Involvement of liver in COVID-19: systematic review and meta-analysis. *Gut* **70**, 807 (2021).
315. Sun, Y. *et al.* Characteristics and prognostic factors of disease severity in patients with COVID-19: The Beijing experience. *J Autoimmun* **112**, 102473 (2020).
316. Cai, Q. *et al.* COVID-19: Abnormal liver function tests. *J Hepatol* **73**, 566–574 (2020).
317. Chen, L. Y. *et al.* Liver damage at admission is an independent prognostic factor for COVID-19. *J Dig Dis* **21**, 512–518 (2020).

318. Wang, Y. *et al.* SARS-CoV-2 infection of the liver directly contributes to hepatic impairment in patients with COVID-19. *J Hepatol* **73**, 807–816 (2020).
319. Guan, W. *et al.* Clinical Characteristics of Coronavirus Disease 2019 in China. *N Engl J Med* **382**, 1708–1720 (2020).
320. Huang, C. *et al.* Clinical features of patients infected with 2019 novel coronavirus in Wuhan, China. *The Lancet* **395**, 497–506 (2020).
321. Chen, N. *et al.* Epidemiological and clinical characteristics of 99 cases of 2019 novel coronavirus pneumonia in Wuhan, China: a descriptive study. *The Lancet* **395**, 507–513 (2020).
322. Fan, Z. *et al.* Clinical Features of COVID-19-Related Liver Functional Abnormality. *Clin Gastroenterol Hepatol* **18**, 1561–1566 (2020).
323. Xu, L., Liu, J., Lu, M., Yang, D. & Zheng, X. Liver injury during highly pathogenic human coronavirus infections. *Liver International* **40**, 998–1004 (2020).
324. Lei, F. *et al.* Longitudinal Association Between Markers of Liver Injury and Mortality in COVID-19 in China. *Hepatology* **72**, 389–398 (2020).
325. Huang, H. *et al.* The association between markers of liver injury and clinical outcomes in patients with COVID-19 in Wuhan. *Aliment Pharmacol Ther* **52**, 1051–1059 (2020).
326. Hao, S. R. *et al.* Liver Enzyme Elevation in Coronavirus Disease 2019: A Multicenter, Retrospective, Cross-Sectional Study. *Am J Gastroenterol* **115**, 1075–1083 (2020).
327. Xu, Z. *et al.* Pathological findings of COVID-19 associated with acute respiratory distress syndrome. *Lancet Respir Med* **8**, 420–422 (2020).
328. Xiaohong, Y. *et al.* [A pathological report of three COVID-19 cases by minimal invasive autopsies]. *Zhonghua Bing Li Xue Za Zhi* **49**, 411–417 (2020).
329. Singh, S. & Khan, A. Clinical Characteristics and Outcomes of Coronavirus Disease 2019 Among Patients With Preexisting Liver Disease in the United States: A Multicenter Research Network Study. *Gastroenterology* **159**, 768-771.e3 (2020).
330. Moon, A. M. *et al.* High mortality rates for SARS-CoV-2 infection in patients with pre-existing chronic liver disease and cirrhosis: Preliminary results from an international registry. *J Hepatol* **73**, 705–708 (2020).
331. Ji, D. *et al.* Non-alcoholic fatty liver diseases in patients with COVID-19: A retrospective study. *J Hepatol* **73**, 451 (2020).
332. Kim, D. *et al.* Predictors of Outcomes of COVID-19 in Patients With Chronic Liver Disease: US Multi-center Study. *Clin Gastroenterol Hepatol* **19**, 1469-1479.e19 (2021).
333. Iavarone, M. *et al.* High rates of 30-day mortality in patients with cirrhosis and COVID-19. *J Hepatol* **73**, 1063–1071 (2020).
334. Marjot, T. *et al.* Outcomes following SARS-CoV-2 infection in patients with chronic liver disease: An international registry study. *J Hepatol* **74**, 567–577 (2021).
335. Ge, J. *et al.* Outcomes of SARS-CoV-2 Infection in Patients With Chronic Liver Disease and Cirrhosis: A National COVID Cohort Collaborative Study. *Gastroenterology* **161**, 1487-1501.e5 (2021).
336. Bajaj, J. S. *et al.* Comparison of mortality risk in patients with cirrhosis and COVID-19 compared with patients with cirrhosis alone and COVID-19 alone: multicentre matched cohort. *Gut* **70**, 531–536 (2021).
337. Ioannou, G. N. *et al.* Cirrhosis and Severe Acute Respiratory Syndrome Coronavirus 2 Infection in US Veterans: Risk of Infection, Hospitalization, Ventilation, and Mortality. *Hepatology* **74**, 322 (2021).
338. Marjot, T. *et al.* Outcomes following SARS-CoV-2 infection in patients with chronic liver disease: An international registry study. *J Hepatol* **74**, 567–577 (2021).
339. Ai, J. *et al.* Safety and Immunogenicity of SARS-CoV-2 Vaccines in Patients With Chronic Liver Diseases (CHESS-NMCID 2101): A Multicenter Study. *Clinical Gastroenterology and Hepatology* **20**, 1516 (2022).
340. Chai, X. *et al.* Specific ACE2 Expression in Cholangiocytes May Cause Liver Damage After 2019-nCoV Infection. *bioRxiv* (2020) doi:10.1101/2020.02.03.931766.

341. Hamming, I. *et al.* Tissue distribution of ACE2 protein, the functional receptor for SARS coronavirus. A first step in understanding SARS pathogenesis. *J Pathol* **203**, 631–637 (2004).
342. Benedicto, A., García-Kamiruaga, I. & Arteta, B. Neuropilin-1: A feasible link between liver pathologies and COVID-19. *World J Gastroenterol* **27**, 3516 (2021).
343. Fiel, M. I. *et al.* Findings of Hepatic Severe Acute Respiratory Syndrome Coronavirus-2 Infection. *Cell Mol Gastroenterol Hepatol* **11**, 763–770 (2021).
344. Melquist, S. *et al.* COVID-19 presenting as fulminant hepatic failure: A case report. *Medicine* **99**, E22818 (2020).
345. Kubes, P. & Jenne, C. Immune Responses in the Liver. *Annu Rev Immunol* **36**, 247–277 (2018).
346. Sprague, A. H. & Khalil, R. A. Inflammatory cytokines in vascular dysfunction and vascular disease. *Biochem Pharmacol* **78**, 539–552 (2009).
347. Hiltebrand, L. B. *et al.* Dynamic study of the distribution of microcirculatory blood flow in multiple splanchnic organs in septic shock. *Crit Care Med* **28**, 3233–3241 (2000).
348. Mittal, M., Siddiqui, M. R., Tran, K., Reddy, S. P. & Malik, A. B. Reactive Oxygen Species in Inflammation and Tissue Injury. *Antioxid Redox Signal* **20**, 1126 (2014).
349. Wang, K., Gheblawi, M. & Oudit, G. Y. Angiotensin Converting Enzyme 2. *Circulation* **142**, 426–428 (2020).
350. Benigni, A., Cassis, P. & Remuzzi, G. Angiotensin II revisited: new roles in inflammation, immunology and aging. *EMBO Mol Med* **2**, 247–257 (2010).
351. Anirvan, P. *et al.* Cytokine-induced liver injury in coronavirus disease-2019 (COVID-19): untangling the knots. *Eur J Gastroenterol Hepatol* **33**, E42–E49 (2021).
352. Q, L. *et al.* Gross examination report of a COVID-19 death autopsy. *Fa Yi Xue Za Zhi* **36**, 21–23 (2020).
353. Pott-Junior, H. *et al.* Elevations in Liver Transaminases in COVID-19: (How) Are They Related? *Front Med (Lausanne)* **8**, 705247 (2021).
354. Huang, H. *et al.* Prevalence and Characteristics of Hypoxic Hepatitis in COVID-19 Patients in the Intensive Care Unit: A First Retrospective Study. *Front Med (Lausanne)* **7**, 607206 (2020).
355. Henrion, J. Hypoxic hepatitis. *Liver International* **32**, 1039–1052 (2012).
356. Tazarghi, A. *et al.* Liver injury in COVID-19: an insight into pathobiology and roles of risk factors. *Virol J* **21**, 1–13 (2024).
357. Li, X. *et al.* Drug-induced liver injury in COVID-19 treatment: Incidence, mechanisms and clinical management. *Front Pharmacol* **13**, 1019487 (2022).
358. Kumar-M, P. *et al.* Coronavirus disease (COVID-19) and the liver: a comprehensive systematic review and meta-analysis. *Hepatol Int* **14**, 711–722 (2020).
359. Andrade, R. J. *et al.* Drug-induced liver injury. *Nat Rev Dis Primers* **5**, (2019).
360. Younossi, Z. M. *et al.* Clinical profiles and mortality rates are similar for metabolic dysfunction-associated steatotic liver disease and non-alcoholic fatty liver disease. *J Hepatol* **80**, 694–701 (2024).
361. Chan, K. E. *et al.* Global Prevalence and Clinical Characteristics of Metabolic-associated Fatty Liver Disease: A Meta-Analysis and Systematic Review of 10 739 607 Individuals. *J Clin Endocrinol Metab* **107**, 2691–2700 (2022).
362. Pinyol, R. *et al.* Molecular characterisation of hepatocellular carcinoma in patients with non-alcoholic steatohepatitis. *J Hepatol* **75**, 865–878 (2021).
363. Bertot, L. C. & Adams, L. A. The Natural Course of Non-Alcoholic Fatty Liver Disease. *Int J Mol Sci* **17**, (2016).
364. Arab, J. P., Arrese, M. & Trauner, M. Recent Insights into the Pathogenesis of Nonalcoholic Fatty Liver Disease. *Annu Rev Pathol* **13**, 321–350 (2018).
365. Eslam, M. *et al.* A new definition for metabolic dysfunction-associated fatty liver disease: An international expert consensus statement. *J Hepatol* **73**, 202–209 (2020).
366. Buzzetti, E., Pinzani, M. & Tsochatzis, E. A. The multiple-hit pathogenesis of non-alcoholic fatty liver disease (NAFLD). *Metabolism* **65**, 1038–1048 (2016).

367. Yang, K. & Song, M. New Insights into the Pathogenesis of Metabolic-Associated Fatty Liver Disease (MAFLD): Gut–Liver–Heart Crosstalk. *Nutrients 2023, Vol. 15, Page 3970* **15**, 3970 (2023).
368. Fernández, T., Viñuela, M., Vidal, C. & Barrera, F. Lifestyle changes in patients with non-alcoholic fatty liver disease: A systematic review and meta-analysis. *PLoS One* **17**, (2022).
369. Sangro, P., de la Torre Aláez, M., Sangro, B. & D'Avola, D. Metabolic dysfunction–associated fatty liver disease (MAFLD): an update of the recent advances in pharmacological treatment. *J Physiol Biochem* **79**, 869 (2023).
370. Harrison, S. A. *et al.* A Phase 3, Randomized, Controlled Trial of Resmetirom in NASH with Liver Fibrosis. *N Engl J Med* **390**, 497–509 (2024).
371. Huang, Y. *et al.* Effect of metformin on nonalcoholic fatty liver based on meta-analysis and network pharmacology. *Medicine (United States)* **101**, E31437 (2022).
372. Said, A. & Akhter, A. Meta-Analysis of Randomized Controlled Trials of Pharmacologic Agents in Non-alcoholic Steatohepatitis. *Ann Hepatol* **16**, 538–547 (2017).
373. Bugianesi, E. *et al.* A randomized controlled trial of metformin versus vitamin E or prescriptive diet in nonalcoholic fatty liver disease. *Am J Gastroenterol* **100**, 1082–1090 (2005).
374. Zhang, Y., Wang, H. & Xiao, H. Metformin Actions on the Liver: Protection Mechanisms Emerging in Hepatocytes and Immune Cells against NASH-Related HCC. *Int J Mol Sci* **22**, (2021).
375. Ganesh, A. & Randall, M. D. Does metformin affect outcomes in COVID-19 patients with new or pre-existing diabetes mellitus? A systematic review and meta-analysis. *Br J Clin Pharmacol* **88**, 2642 (2022).
376. Bramante, C. T. *et al.* Outpatient treatment of COVID-19 and incidence of post-COVID-19 condition over 10 months (COVID-OUT): a multicentre, randomised, quadruple-blind, parallel-group, phase 3 trial. *Lancet Infect Dis* **23**, 1119–1129 (2023).
377. Montal, R. *et al.* Molecular classification and therapeutic targets in extrahepatic cholangiocarcinoma. *J Hepatol* **73**, 315–327 (2020).
378. Chaisaingmongkol, J. *et al.* Common Molecular Subtypes Among Asian Hepatocellular Carcinoma and Cholangiocarcinoma. *Cancer Cell* **32**, 57-70.e3 (2017).
379. Job, S. *et al.* Identification of Four Immune Subtypes Characterized by Distinct Composition and Functions of Tumor Microenvironment in Intrahepatic Cholangiocarcinoma. *Hepatology* **72**, 965–981 (2020).
380. Ahn, K. S. *et al.* Prognostic subclass of intrahepatic cholangiocarcinoma by integrative molecular-clinical analysis and potential targeted approach. *Hepatol Int* **13**, 490–500 (2019).
381. Andersen, J. B. *et al.* Genomic and genetic characterization of cholangiocarcinoma identifies therapeutic targets for tyrosine kinase inhibitors. *Gastroenterology* **142**, (2012).
382. Li, L. *et al.* Differential requirement for de novo lipogenesis in cholangiocarcinoma and hepatocellular carcinoma of mice and humans. *Hepatology* **63**, 1900–1913 (2016).
383. Kleiner, D. E. *et al.* Design and validation of a histological scoring system for nonalcoholic fatty liver disease. *Hepatology* **41**, 1313–1321 (2005).
384. Tolosa, L. *et al.* Human Upcyte Hepatocytes: Characterization of the Hepatic Phenotype and Evaluation for Acute and Long-Term Hepatotoxicity Routine Testing. *Toxicol Sci* **152**, 214–229 (2016).
385. Crawford, K. H. D. *et al.* Protocol and Reagents for Pseudotyping Lentiviral Particles with SARS-CoV-2 Spike Protein for Neutralization Assays. *Viruses* **12**, (2020).
386. Chen, X. & Calvisi, D. F. REVIEW Hydrodynamic Transfection for Generation of Novel Mouse Models for Liver Cancer Research. *Am J Pathol* **184**, 912–923 (2014).
387. Vadolas, J. *et al.* SLN124, a GalNac-siRNA targeting transmembrane serine protease 6, in combination with deferiprone therapy reduces ineffective erythropoiesis and hepatic iron-overload in a mouse model of β-thalassaemia. *Br J Haematol* **194**, 200–210 (2021).
388. Casar, B. *et al.* Blocking of CDCP1 cleavage in vivo prevents Akt-dependent survival and inhibits metastatic colonization via PARP1-mediated apoptosis of cancer cells. *Oncogene* **31**, 3924 (2012).

389. Merlos Rodrigo, M. A. *et al.* Extending the Applicability of In Ovo and Ex Ovo Chicken Chorioallantoic Membrane Assays to Study Cytostatic Activity in Neuroblastoma Cells. *Front Oncol* **11**, (2021).
390. Crespo, P. & Casar, B. The Chick Embryo Chorioallantoic Membrane as an in vivo Model to Study Metastasis. *Bio Protoc* **6**, (2016).
391. Zijlstra, A. *et al.* A Quantitative Analysis of Rate-limiting Steps in the Metastatic Cascade Using Human-specific Real-Time Polymerase Chain Reaction 1. *Cancer Res* **62**, 7083–7092 (2002).
392. Prieto-Fernández, E. *et al.* Hypoxia reduces cell attachment of SARS-CoV-2 spike protein by modulating the expression of ACE2, neuropilin-1, syndecan-1 and cellular heparan sulfate. *Emerg Microbes Infect* **10**, 1065–1076 (2021).
393. Hughes, C. S. *et al.* Single-pot, solid-phase-enhanced sample preparation for proteomics experiments. *Nature Protocols 2018 14:1* **14**, 68–85 (2018).
394. Meier, F. *et al.* Parallel accumulation-serial fragmentation (PASEF): Multiplying sequencing speed and sensitivity by synchronized scans in a trapped ion mobility device. *J Proteome Res* **14**, 5378–5387 (2015).
395. Tyanova, S. *et al.* The Perseus computational platform for comprehensive analysis of (prote)omics data. *Nature Methods 2016 13:9* **13**, 731–740 (2016).
396. Fernández-Tussy, P. *et al.* Anti-miR-518d-5p overcomes liver tumor cell death resistance through mitochondrial activity. *Cell Death & Disease 2021 12:6* **12**, 1–16 (2021).
397. Dieterle, F., Ross, A., Schlotterbeck, G. & Senn, H. Probabilistic Quotient Normalization as Robust Method to Account for Dilution of Complex Biological Mixtures. Application in 1H NMR Metabonomics. *Anal Chem* **78**, 4281–4290 (2006).
398. Veselkov, K. A. *et al.* Optimized preprocessing of ultra-performance liquid chromatography/mass spectrometry urinary metabolic profiles for improved information recovery. *Anal Chem* **83**, 5864–5872 (2011).
399. Fan, B. *et al.* Cholangiocarcinomas can originate from hepatocytes in mice. *J Clin Invest* **122**, 2911–2915 (2012).
400. Wang, J. *et al.* Loss of Fbxw7 synergizes with activated Akt signaling to promote c-Myc dependent cholangiocarcinogenesis. *J Hepatol* **71**, 742–752 (2019).
401. Zhang, S. *et al.* Pan-mTOR inhibitor MLN0128 is effective against intrahepatic cholangiocarcinoma in mice. *J Hepatol* **67**, 1194–1203 (2017).
402. Izquierdo-Sanchez, L. *et al.* Cholangiocarcinoma landscape in Europe: Diagnostic, prognostic and therapeutic insights from the ENSCCA Registry. *J Hepatol* **76**, 1109–1121 (2022).
403. Serra-Camprubí, Q. *et al.* Human Metastatic Cholangiocarcinoma Patient-Derived Xenografts and Tumoroids for Preclinical Drug Evaluation. *Clin Cancer Res* **29**, 432–445 (2023).
404. Fan, B. *et al.* Cholangiocarcinomas can originate from hepatocytes in mice. **122**, (2012).
405. Wang, J. *et al.* Loss of Fbxw7 synergizes with activated AKT signaling to promote c-Myc dependent cholangiocarcinogenesis. *J Hepatol* **71**, 742 (2019).
406. Zhang, S. *et al.* Pan-mTOR inhibitor MLN0128 is effective against intrahepatic cholangiocarcinoma induced in mice by AKT and Yap co-expression. *J Hepatol* **67**, 1194 (2017).
407. Biquard, L., Valla, D. & Rautou, P. E. No evidence for an increased liver uptake of SARS-CoV-2 in metabolic-associated fatty liver disease. *J Hepatol* **73**, 717 (2020).
408. Hoffmann, M. *et al.* SARS-CoV-2 Cell Entry Depends on ACE2 and TMPRSS2 and Is Blocked by a Clinically Proven Protease Inhibitor. *Cell* **181**, 271-280.e8 (2020).
409. Ji, D. *et al.* Non-alcoholic fatty liver diseases in patients with COVID-19: A retrospective study. *J Hepatol* **73**, 451 (2020).
410. Zhou, Y. J. *et al.* Younger patients with MAFLD are at increased risk of severe COVID-19 illness: A multicenter preliminary analysis. *J Hepatol* **73**, 719 (2020).
411. Zhou, Y. J. *et al.* Metabolic-associated fatty liver disease is associated with severity of COVID-19. *Liver Int* **40**, 2160–2163 (2020).

412. Zhu, L. *et al.* Association of Blood Glucose Control and Outcomes in Patients with COVID-19 and Pre-existing Type 2 Diabetes. *Cell Metab* **31**, 1068-1077.e3 (2020).
413. Mauvais-Jarvis, F., Clegg, D. J. & Hevener, A. L. The Role of Estrogens in Control of Energy Balance and Glucose Homeostasis. *Endocr Rev* **34**, 309 (2013).
414. Harcourt, J. *et al.* Severe Acute Respiratory Syndrome Coronavirus 2 from Patient with Coronavirus Disease, United States. *Emerg Infect Dis* **26**, 1266 (2020).
415. Jia, H., Yue, X. & Lazartigues, E. ACE2 mouse models: a toolbox for cardiovascular and pulmonary research. *Nature Communications 2020 11:1* **11**, 1–11 (2020).
416. Benedicto, A., García-Kamiruaga, I. & Arteta, B. Neuropilin-1: A feasible link between liver pathologies and COVID-19. *World J Gastroenterol* **27**, 3516–3528 (2021).
417. Stukalov, A. *et al.* Multilevel proteomics reveals host perturbations by SARS-CoV-2 and SARS-CoV. *Nature 2021 594:7862* **594**, 246–252 (2021).
418. Taneri, P. E. *et al.* Anemia and iron metabolism in COVID-19: a systematic review and meta-analysis. *Eur J Epidemiol* **35**, 763–773 (2020).
419. Sonnweber, T. *et al.* Persisting alterations of iron homeostasis in COVID-19 are associated with non-resolving lung pathologies and poor patients' performance: a prospective observational cohort study. *Respir Res* **21**, (2020).
420. Maio, N. *et al.* Fe-S cofactors in the SARS-CoV-2 RNA-dependent RNA polymerase are potential antiviral targets. *Science* **373**, 236–241 (2021).
421. Wenzhong, L. & Hualan, L. COVID-19: captures iron and generates reactive oxygen species to damage the human immune system. *Autoimmunity* **54**, 213–224 (2021).
422. Del Nonno, F. *et al.* Hepatic Failure in COVID-19: Is Iron Overload the Dangerous Trigger? *Cells* **10**, (2021).
423. Walter, P. B. *et al.* Iron deficiency and iron excess damage mitochondria and mitochondrial DNA in rats. *Proc Natl Acad Sci U S A* **99**, 2264–2269 (2002).
424. Galaris, D., Barbouti, A. & Pantopoulos, K. Iron homeostasis and oxidative stress: An intimate relationship. *Biochim Biophys Acta Mol Cell Res* **1866**, (2019).
425. Cao, X., Song, L. N. & Yang, J. K. ACE2 and energy metabolism: the connection between COVID-19 and chronic metabolic disorders. *Clin Sci (Lond)* **135**, 535–554 (2021).
426. Song, L. N. *et al.* Angiotensin-(1-7), the product of ACE2 ameliorates NAFLD by acting through its receptor Mas to regulate hepatic mitochondrial function and glycolipid metabolism. *FASEB J* **34**, 16291–16306 (2020).
427. Shi, T. T. *et al.* Angiotensin-converting enzyme 2 regulates mitochondrial function in pancreatic β-cells. *Biochem Biophys Res Commun* **495**, 860–866 (2018).
428. Focusing on mitochondrial form and function. *Nature Cell Biology 2018 20:7* **20**, 735–735 (2018).
429. Ott, M., Gogvadze, V., Orrenius, S. & Zhivotovsky, B. Mitochondria, oxidative stress and cell death. *Apoptosis* **12**, 913–922 (2007).
430. Robson Augusto Souza Santos, X. *et al.* The ACE2/Angiotensin-(1-7)/MAS Axis of the Renin-Angiotensin System: Focus on Angiotensin-(1-7). *Physiol Rev* **98**, 505–553 (2018).
431. Trougakos, I. P. *et al.* Insights to SARS-CoV-2 life cycle, pathophysiology, and rationalized treatments that target COVID-19 clinical complications. *J Biomed Sci* **28**, (2021).
432. Stefan, N., Birkenfeld, A. L. & Schulze, M. B. Global pandemics interconnected — obesity, impaired metabolic health and COVID-19. *Nature Reviews Endocrinology 2021 17:3* **17**, 135–149 (2021).
433. Fondevila, M. F. *et al.* Obese patients with NASH have increased hepatic expression of SARS-CoV-2 critical entry points. *J Hepatol* **74**, 469 (2021).
434. Simón, J. *et al.* Magnesium accumulation upon cyclin M4 silencing activates microsomal triglyceride transfer protein improving NASH. *J Hepatol* **75**, 34–45 (2021).
435. Cao, S. *et al.* Neuropilin-1 promotes cirrhosis of the rodent and human liver by enhancing PDGF/TGF-beta signaling in hepatic stellate cells. *J Clin Invest* **120**, 2379–2394 (2010).

436. Trautwein, C. Neuropilin and Liver Fibrosis : Hitting Three Birds with One Stone ? (2011).
437. LI, Y., LIU, L., WANG, B., WANG, J. & CHEN, D. Metformin in non-alcoholic fatty liver disease: A systematic review and meta-analysis. *Biomed Rep* **1**, 57–64 (2013).
438. Rena, G., Hardie, D. G. & Pearson, E. R. The mechanisms of action of metformin. *Diabetologia* **60**, 1577 (2017).
439. Pernicova, I. & Korbonits, M. Metformin--mode of action and clinical implications for diabetes and cancer. *Nat Rev Endocrinol* **10**, 143–156 (2014).
440. Yang, W., Sun, X., Zhang, J. & Zhang, K. The effect of metformin on mortality and severity in COVID-19 patients with diabetes mellitus. *Diabetes Res Clin Pract* **178**, (2021).
441. Varghese, E., Samuel, S. M., Liskova, A., Kubatka, P. & Büsselberg, D. Diabetes and coronavirus (SARS-CoV-2): Molecular mechanism of Metformin intervention and the scientific basis of drug repurposing. *PLoS Pathog* **17**, (2021).
442. Borém, L. M. A., Neto, J. F. R., Brandi, I. V., Lelis, D. F. & Santos, S. H. S. The role of the angiotensin II type I receptor blocker telmisartan in the treatment of non-alcoholic fatty liver disease: a brief review. *Hypertens Res* **41**, 394–405 (2018).
443. Zhong, G. C. *et al.* Magnesium intake and primary liver cancer incidence and mortality in the Prostate, Lung, Colorectal and Ovarian Cancer Screening Trial. *Int J Cancer* **147**, 1577–1586 (2020).
444. Nasulewicz, A. *et al.* Magnesium deficiency inhibits primary tumor growth but favors metastasis in mice. doi:10.1016/j.bbadis.2004.08.003.
445. Mazur, A. *et al.* Magnesium and the inflammatory response: Potential physiopathological implications. *Arch Biochem Biophys* **458**, 48–56 (2007).
446. Aoyagi, K., Takeshige, K., Sumimoto, H., Nunoi, H. & Minakami, S. Role of Mg2+ in activation of nadph oxidase of human neutrophils: Evidence that Mg2+ acts through G-protein. *Biochem Biophys Res Commun* **186**, 391–397 (1992).
447. Chen, H.-C., Su, L.-T., González-Pagán, O., Overton, J. D. & Runnels, L. W. A Key Role for Mg 2+ in TRPM7's Control of ROS Levels During Cell Stress. doi:10.1042/BJ20120248.
448. Liu, J. *et al.* NUPR1 is a critical repressor of ferroptosis. *Nat Commun* **12**, (2021).
449. Gao, L. *et al.* Inhibition of mir-10a-5p suppresses cholangiocarcinoma cell growth through downregulation of AKT pathway. *Onco Targets Ther* 11–6981 (2018) doi:10.2147/OTT.S182225.
450. Cai, J. *et al.* Fatostatin induces ferroptosis through inhibition of the AKT/mTORC1/GPX4 signaling pathway in glioblastoma. *Cell Death Dis* **14**, (2023).
451. Yi, J., Zhu, J., Wu, J., Thompson, C. B. & Jiang, X. Oncogenic activation of PI3K-AKT-mTOR signaling suppresses ferroptosis via SREBP-mediated lipogenesis. doi:10.1073/pnas.2017152117/-/DCSupplemental.
452. Cahuzac, K. M. *et al.* AKT activation because of PTEN loss upregulates xCT via GSK3β/NRF2, leading to inhibition of ferroptosis in PTEN-mutant tumor cells. *Cell Rep* **42**, (2023).
453. Yi, J., Zhu, J., Wu, J., Thompson, C. B. & Jiang, X. Oncogenic activation of PI3K-AKT-mTOR signaling suppresses ferroptosis via SREBP-mediated lipogenesis. doi:10.1073/pnas.2017152117/-/DCSupplemental.
454. Hu, Z. *et al.* miR-21-5p Inhibits Ferroptosis in Hepatocellular Carcinoma Cells by Regulating the AKT/mTOR Signaling Pathway through MELK. (2023) doi:10.1155/2023/8929525.
455. Liu, Y. *et al.* Protein Kinase B (PKB/AKT) Protects IDH-Mutated Glioma from Ferroptosis via Nrf2. *Clinical Cancer Research* **29**, 1305–1316 (2023).
456. Rizzo, A., Ricci, A. D. & Brandi, G. IDH inhibitors in advanced cholangiocarcinoma: Another arrow in the quiver? *Cancer Treatment and Research Communications* vol. 27 Preprint at https://doi.org/10.1016/j.ctarc.2021.100356 (2021).
457. Alvaro, D. *et al.* EASL-ILCA Clinical Practice Guidelines on the management of intrahepatic cholangiocarcinoma. *J Hepatol* **79**, 181–208 (2023).
458. Izquierdo-Sanchez, L. *et al.* Cholangiocarcinoma landscape in Europe: Diagnostic, prognostic and therapeutic insights from the ENSCCA Registry. (2022) doi:10.1016/j.jhep.2021.12.010.

459. Zhang, C., Liu, X., Jin, S., Chen, Y. & Guo, R. Ferroptosis in cancer therapy: a novel approach to reversing drug resistance. *Molecular Cancer* vol. 21 Preprint at https://doi.org/10.1186/s12943-022-01530-y (2022).
460. Okon, I. S. & Zou, M.-H. Mitochondrial ROS and cancer drug resistance: Implications for therapy. *Pharmacol Res* **100**, 170–174 (2015).
461. Nie, Z. *et al.* Ferroptosis and Tumor Drug Resistance: Current Status and Major Challenges. *Frontiers in Pharmacology* vol. 13 Preprint at https://doi.org/10.3389/fphar.2022.879317 (2022).
462. Kongpetch, S., Kukongviriyapan, V., Prawan, A., Senggunprai, L. & Kukongviriyapan, U. Crucial Role of Heme Oxygenase-1 on the Sensitivity of Cholangiocarcinoma Cells to Chemotherapeutic Agents. *PLoS One* **7**, 34994 (2012).
463. Batlle, E. & Clevers, H. Cancer stem cells revisited. *Nature Medicine 2017 23:10* **23**, 1124–1134 (2017).
464. Cosialls, E. *et al.* Ferroptosis: Cancer Stem Cells Rely on Iron until 'to Die for' It. (2021) doi:10.3390/cells10112981.
465. Raggi, C. *et al.* Dysregulation of Iron Metabolism in Cholangiocarcinoma Stem-like Cells. doi:10.1038/s41598-017-17804-1.
466. Shiozawa, Y., Nie, B., Pienta, K. J., Morgan, T. M. & Taichman, R. S. Cancer stem cells and their role in metastasis. *Pharmacology and Therapeutics* vol. 138 285–293 Preprint at https://doi.org/10.1016/j.pharmthera.2013.01.014 (2013).
467. Zhu, Z. *et al.* FBXO31 sensitizes cancer stem cells-like cells to cisplatin by promoting ferroptosis and facilitating proteasomal degradation of GPX4 in cholangiocarcinoma. *Liver International* **42**, 2871–2888 (2022).
468. Mani, S. A. *et al.* The Epithelial-Mesenchymal Transition Generates Cells with Properties of Stem Cells. *Cell* **133**, 704–715 (2008).
469. Metastatic cancer stem cells: from the concept to therapeutics.
470. Yuan, X. *et al.* SOX9 expression decreases survival of patients with intrahepatic cholangiocarcinoma by conferring chemoresistance. *Br J Cancer* 119 (2018) doi:10.1038/s41416-018-0338-9.
471. Viswanathan, V. S. *et al.* Dependency of a therapy-resistant state of cancer cells on a lipid peroxidase pathway. *Nature* **547**, 453–457 (2017).
472. Tsoi, J. *et al.* Multi-stage differentiation defines melanoma subtypes with differential vulnerability to drug-induced iron-dependent oxidative stress. *Cancer Cell* **33**, 890 (2018).
473. Hangauer, M. J. *et al.* Drug-tolerant persister cancer cells are vulnerable to GPX4 inhibition. *Nature Publishing Group* (2017) doi:10.1038/nature24297.
474. Feng, L. *et al.* SLC7A11 regulated by NRF2 modulates esophageal squamous cell carcinoma radiosensitivity by inhibiting ferroptosis. *J Transl Med* **19**, 367 (2021).
475. He, Q. *et al.* IL-1β-Induced Elevation of Solute Carrier Family 7 Member 11 Promotes Hepatocellular Carcinoma Metastasis Through Up-regulating Programmed Death Ligand 1 and Colony-Stimulating Factor 1. *Hepatology* **74**, 3174–3193 (2021).
476. Nagpal, A. *et al.* Neoadjuvant neratinib promotes ferroptosis and inhibits brain metastasis in a novel syngeneic model of spontaneous HER2+ve breast cancer metastasis. *Breast Cancer Res* **21**, (2019).
477. Guan, D. *et al.* The DpdtbA induced EMT inhibition in gastric cancer cell lines was through ferritinophagy-mediated activation of p53 and PHD2/hif-1α pathway. *J Inorg Biochem* **218**, 111413 (2021).
478. Oliveira, T. *et al.* HDAC inhibition induces EMT and alterations in cellular iron homeostasis to augment ferroptosis sensitivity in SW13 cells. *Redox Biol* **47**, (2021).
479. Lu, J., Tan, M. & Cai, Q. The Warburg effect in tumor progression: Mitochondrial oxidative metabolism as an anti-metastasis mechanism. *Cancer Lett* **356**, 156–164 (2015).
480. Hsu, P. P. & Sabatini, D. M. Cancer cell metabolism: Warburg and beyond. *Cell* vol. 134 703–707 Preprint at https://doi.org/10.1016/j.cell.2008.08.021 (2008).
481. Alvaro, D. *et al.* Role of Glucose Metabolism Reprogramming in the Pathogenesis of Cholangiocarcinoma. *Frontiers in Medicine | www.frontiersin.org* **1**, 113 (2020).

482. Zhang, C. *et al.* Tumour-associated mutant p53 drives the Warburg effect. *Nat Commun* (2013) doi:10.1038/ncomms3935.
483. Raggi, C. *et al.* Mitochondrial oxidative metabolism contributes to a cancer stem cell phenotype in cholangiocarcinoma. *J Hepatol* **74**, 1373–1385 (2021).
484. Saengboonmee, C., Seubwai, W., Pairojkul, C. & Wongkham, S. High glucose enhances progression of cholangiocarcinoma cells via STAT3 activation OPEN. (2015) doi:10.1038/srep18995.
485. Zheng, J. & Conrad, M. The Metabolic Underpinnings of Ferroptosis. doi:10.1016/j.cmet.2020.10.011.
486. Lu, S., Wu, L., Yang, L., Yang, L. & Wang, J. The diversified role of mitochondria in ferroptosis in cancer. doi:10.1038/s41419-023-06045-y.
487. Suzuki, S. *et al.* GLS2 Is a Tumor Suppressor and a Regulator of Ferroptosis in Hepatocellular Carcinoma. *Cancer Res* **82**, 3209–3222 (2022).
488. Su, L. *et al.* Isocitrate dehydrogenase 1 mutation in cholangiocarcinoma impairs tumor progression by sensitizing cells to ferroptosis. (2022) doi:10.1515/med-2022-0477.
489. Kim, J., Kim, J. & Bae, J.-S. ROS homeostasis and metabolism: a critical liaison for cancer therapy. *Exp Mol Med* **48**, 269 (2016).
490. Perillo, B. *et al.* ROS in cancer therapy: the bright side of the moon. *Experimental and Molecular Medicine* vol. 52 192–203 Preprint at https://doi.org/10.1038/s12276-020-0384-2 (2020).
491. Yang, M., Li, M., Lyu, Z. & Yang, Z. Implication of Ferroptosis in Cholangiocarcinoma: A Potential Future Target? (2023) doi:10.2147/CMAR.S406150.
492. Search for: GalNAc siRNA | Card Results | ClinicalTrials.gov. https://clinicaltrials.gov/search?intr=GalNAc%20siRNA.
493. Springer, A. D. & Dowdy, S. F. Reviews GalNAc-siRNA Conjugates: Leading the Way for Delivery of RNAi Therapeutics. doi:10.1089/nat.2018.0736.
494. Shaib, Y. H., El-Serag, H. B., Davila, J. A., Morgan, R. & Mcglynn, K. A. Risk factors of intrahepatic cholangiocarcinoma in the United States: A case-control study. *Gastroenterology* **128**, 620–626 (2005).
495. Yu, T. H. *et al.* Viral hepatitis is associated with intrahepatic cholangiocarcinoma with cholangiolar differentiation and N-cadherin expression. *Modern Pathology 2011 24:6* **24**, 810–819 (2011).
496. Sempoux, C. *et al.* Intrahepatic cholangiocarcinoma: New insights in Pathology. *Semin Liver Dis* **31**, 49–60 (2011).
497. Fujimoto, A. *et al.* Whole-genome mutational landscape of liver cancers displaying biliary phenotype reveals hepatitis impact and molecular diversity. *Nature Communications 2015 6:1* **6**, 1–8 (2015).
498. Sekiya, S. & Suzuki, A. Brief report Intrahepatic cholangiocarcinoma can arise from Notch-mediated conversion of hepatocytes. *J Clin Invest* **122**, (2012).
499. Saito, Y. *et al.* Induction of differentiation of intrahepatic cholangiocarcinoma cells to functional hepatocytes using an organoid culture system OPEN. *Scientific RepoRts* | **8**, 2821 (2018).
500. Hegyi, P. J. *et al.* Metabolic Associated Fatty Liver Disease Is Associated With an Increased Risk of Severe COVID-19: A Systematic Review With Meta-Analysis. *Front Med (Lausanne)* **8**, (2021).
501. Letko, M., Marzi, A. & Munster, V. Functional assessment of cell entry and receptor usage for SARS-CoV-2 and other lineage B betacoronaviruses. *Nat Microbiol* **5**, 562–569 (2020).
502. Chu, H. *et al.* Multicenter Analysis of Liver Injury Patterns and Mortality in COVID-19. *Front Med (Lausanne)* **7**, 584342 (2020).
503. Harcourt, J. *et al.* Isolation and characterization of SARS-CoV-2 from the first US COVID-19 patient. *bioRxiv* (2020) doi:10.1101/2020.03.02.972935.
504. Yang, L. *et al.* A Human Pluripotent Stem Cell-based Platform to Study SARS-CoV-2 Tropism and Model Virus Infection in Human Cells and Organoids. *Cell Stem Cell* **27**, 125-136.e7 (2020).
505. McCarron, S. *et al.* Functional Characterization of Organoids Derived From Irreversibly Damaged Liver of Patients With NASH. *Hepatology* **74**, 1825–1844 (2021).

506. Zhao, B. *et al.* Recapitulation of SARS-CoV-2 infection and cholangiocyte damage with human liver ductal organoids. *Protein Cell* **11**, 771–775 (2020).
507. Saleh, J., Peyssonnaux, C., Singh, K. K. & Edeas, M. Mitochondria and microbiota dysfunction in COVID-19 pathogenesis. *Mitochondrion* **54**, 1 (2020).
508. Icard, P. *et al.* The key role of Warburg effect in SARS-CoV-2 replication and associated inflammatory response. *Biochimie* **180**, 169–177 (2021).
509. Yaneske, E., Zampieri, G., Bertoldi, L., Benvenuto, G. & Angione, C. Genome-scale metabolic modelling of SARS-CoV-2 in cancer cells reveals an increased shift to glycolytic energy production. *FEBS Lett* **595**, 2350–2365 (2021).
510. Bharadwaj, S., Singh, M., Kirtipal, N. & Kang, S. G. SARS-CoV-2 and Glutamine: SARS-CoV-2 Triggered Pathogenesis via Metabolic Reprograming of Glutamine in Host Cells. *Front Mol Biosci* **7**, (2021).
511. Simon, J. *et al.* Targeting Hepatic Glutaminase 1 Ameliorates Non-alcoholic Steatohepatitis by Restoring Very-Low-Density Lipoprotein Triglyceride Assembly. *Cell Metab* **31**, 605-622.e10 (2020).
512. Meijnikman, A. S., Bruin, S., Groen, A. K., Nieuwdorp, M. & Herrema, H. Increased expression of key SARS-CoV-2 entry points in multiple tissues in individuals with NAFLD. *J Hepatol* **74**, 748–749 (2021).
513. Wang, Y. *et al.* Metformin Improves Mitochondrial Respiratory Activity through Activation of AMPK. *Cell Rep* **29**, 1511-1523.e5 (2019).
514. Han, Y. *et al.* Post-translational regulation of lipogenesis via AMPK-dependent phosphorylation of insulin-induced gene. *Nat Commun* **10**, (2019).
515. Song, L. *et al.* LKB1 obliterates Snail stability and inhibits pancreatic cancer metastasis in response to metformin treatment. *Cancer Sci* **109**, 1382–1392 (2018).
516. Vakifahmetoglu-Norberg, H., Ouchida, A. T. & Norberg, E. The role of mitochondria in metabolism and cell death. *Biochem Biophys Res Commun* **482**, 426–431 (2017).
517. Icard, P. *et al.* How the Warburg effect supports aggressiveness and drug resistance of cancer cells? *Drug Resist Updat* **38**, 1–11 (2018).
518. Li, Z. & Cui, J. Targeting the lactic acid metabolic pathway for antitumor therapy. *Mol Ther Oncolytics* **31**, 100740 (2023).
519. Sumbria, D., Berber, E., Mathayan, M. & Rouse, B. T. Virus Infections and Host Metabolism—Can We Manage the Interactions? *Front Immunol* **11**, 594963 (2021).
520. Sies, H. & Jones, D. P. Reactive oxygen species (ROS) as pleiotropic physiological signalling agents. *Nature Reviews Molecular Cell Biology 2020 21:7* **21**, 363–383 (2020).
521. Perillo, B. *et al.* ROS in cancer therapy: the bright side of the moon. *Experimental & Molecular Medicine 2020 52:2* **52**, 192–203 (2020).
522. Gain, C., Song, S., Angtuaco, T., Satta, S. & Kelesidis, T. The role of oxidative stress in the pathogenesis of infections with coronaviruses. *Front Microbiol* **13**, 1111930 (2023).
523. Zhang, S. *et al.* Double-edge sword roles of iron in driving energy production versus instigating ferroptosis. *Cell Death & Disease 2021 13:1* **13**, 1–13 (2022).
524. González-Recio, I. *et al.* Restoring cellular magnesium balance through Cyclin M4 protects against acetaminophen-induced liver damage. *Nat Commun* **13**, (2022).
525. Ali, F. E. M., Abd El-Aziz, M. K., Ali, M. M., Ghogar, O. M. & Bakr, A. G. COVID-19 and hepatic injury: cellular and molecular mechanisms in diverse liver cells. *World J Gastroenterol* **29**, 425 (2023).

Appendix

Publications during the PhD

1. **Mercado-Gómez M.**, Goikoetxea-Usandizaga N., J.C. Kerbert A., Uraga Gracianteparaluceta L., Serrano-Maciá M., Lachiondo-Ortega S., Rodriguez-Agudo R., Gil-Pitarch C., Simón J., González-Recio I., F Fondevila M., Santamarina-Ojeda P., F. Fraga M., Nogueiras R., de las Heras J., Jalan R., Martínez-Chantar M.L.**, Delgado T.C.** (2024). The lipopolysaccharide-TLR4 axis regulates hepatic glutaminase 1 expression promoting liver ammonia build-up as steatotic liver disease progresses to steatohepatitis. Metabolism. **These authors jointly supervised this work: Martínez-Chantar M.L. and Delgado T.C.
2. Rodríguez-Agudo, R., González-Recio, I., Serrano-Maciá, M., Bravo, M., Petrov, P., Blaya, D., Herranz, J. M., **Mercado-Gómez, M.**, Rejano-Gordillo, C. M., Lachiondo-Ortega, S., Gil-Pitarch, C., Azkargorta, M., Van Liempd, S. M., Martinez-Cruz, L. A., Simão, A. L., Elortza, F., Martín, C., Nevzorova, Y. A., Cubero, F. J., Delgado T.C., Argemi J.M., Bataller R., Schoonjans K., Banales J.M., Castro R.E., Sancho-Bru P., Avila M.A., Julve J., Jover R., Mabe J., Simon J., Goikoetxea-Usandizaga N.**, Martínez-Chantar M. L. **(2023). Anti-miR-873-5p improves alcohol-related liver disease by enhancing hepatic deacetylation via SIRT1. JHEP Reports: Innovation in Hepatology, 6(1). https://doi.org/10.1016/J.JHEPR.2023.100918. **These authors jointly supervised this work: Goikoetxea-Usandizaga N., Martínez-Chantar M.L.
3. Sauve, F., Nampoothiri, S., Clarke, S. A., Fernandois, D., Ferreira Coêlho, C. F., Dewisme, J., Mills, E. G., Ternier, G., Cotellessa, L., Iglesias-Garcia, C., Mueller-Fielitz, H., Lebouvier, T., Perbet, R., Florent, V., Baroncini, M., Sharif, A., Ereño-Orbea, J., **Mercado-Gómez, M.**, Palazon, A., Mattot V., Pasquier F., Catteau-Jonard S., Martínez-Chantar M. L. , Hrabovszky E., Jourdain M., Deplanque D., Morelli A., Guarnieri G., Strome L., Robil C., Trottein F., Nogueiras R., Schwaninger M., Pigny P., Poissy J., Chachlaki K., Maurage C-A., Giacobini P., Dhillo W., Rasika., Prevot, V. (2023). Long-COVID cognitive impairments and reproductive hormone deficits in men may stem from GnRH neuronal death. EBioMedicine, 96. https://doi.org/10.1016/J.EBIOM.2023.104784
4. González-Recio, I., Simón, J., Goikoetxea-Usandizaga, N., Serrano-Maciá, M., **Mercado-Gómez, M.**, Rodríguez-Agudo, R., Lachiondo-Ortega, S., Gil-Pitarch, C., Fernández-Rodríguez, C., Castellana, D., Latasa, M. U., Abecia, L., Anguita, J., Delgado, T. C., Iruzubieta, P., Crespo, J., Hardy, S., Petrov, P. D., Jover, R., Avila M. A., Martín C., Schaeper U., Tremblay M. L., Dear J. W., Masson S., McCain M. V., Reeves H. L., Andrade R. J., Lucena M. I., Buccella D., Martínez-Cruz L. A., Martínez-Chantar, M. L. (2022). Restoring cellular magnesium balance through Cyclin M4 protects against acetaminophen-induced liver damage. Nature Communications, 13(1). https://doi.org/10.1038/S41467-022-34262-0
5. **Mercado-Gómez, M**.*, Prieto-Fernández, E.*, Goikoetxea-Usandizaga, N., Vila-Vecilla, L., Azkargorta, M., Bravo, M., Serrano-Maciá, M., Egia-Mendikute, L., Rodríguez-Agudo, R., Lachiondo-Ortega, S., Lee, S. Y., Eguileor Giné, A., Gil-Pitarch, C., González-Recio, I., Simón, J., Petrov, P., Jover, R., Martínez-Cruz, L. A., Ereño-Orbea, J., Delgado T. C., Elortza F., Jiménez-Barbero J., Nogueiras R., Prevot V., Palazon A.**, Martínez-Chantar, M. L.** (2022). The spike of SARS-CoV-2 promotes metabolic rewiring in hepatocytes. Communications Biology, 5(1). https://doi.org/10.1038/S42003-022-03789-9. *These authors contributed equally: Mercado-

Gómez M., Prieto-Fernández E. **These authors jointly supervised this work: Martínez-Chantar M.L., Palazon A.

6. Rodríguez-Agudo, R.*, Goikoetxea-Usandizaga, N.*, Serrano-Maciá, M., Fernández-Tussy, P., Fernández-Ramos, D., Lachiondo-Ortega, S., González-Recio, I., Gil-Pitarch, C., **Mercado-Gómez, M.**, Morán, L., Bizkarguenaga, M., Lopitz-Otsoa, F., Petrov, P., Bravo, M., Van Liempd, S. M., Falcon-Perez, J. M., Zabala-Letona, A., Carracedo, A., Castell, J. V. Jover R., Martínez-Cruz L. A., Delgado T. C., Cubero F. J., Lucena M. I., Andrade R. J., Mabe J., Simón J.**, Martínez-Chantar, M. L.** (2022). Methionine Cycle Rewiring by Targeting miR-873-5p Modulates Ammonia Metabolism to Protect the Liver from Acetaminophen. Antioxidants (Basel, Switzerland), 11(5). https://doi.org/10.3390/ANTIOX11050897. *These authors contributed equally: Rodríguez-Agudo, R., Goikoetxea-Usandizaga, N. **These authors jointly supervised this work: Simón J., Martínez-Chantar, M. L.
7. da Silva Lima, N., Fondevila, M. F., Nóvoa, E., Buqué, X., **Mercado-Gómez, M.**, Gallet, S., González-Rellan, M. J., Fernandez, U., Loyens, A., Garcia-Vence, M., Chantada-Vazquez, M. del P., Bravo, S. B., Marañon, P., Senra, A., Escudero, A., Leiva, M., Guallar, D., Fidalgo, M., Gomes, P., Claret M., Sabio G., Varela-Rey M., Delgado T. C., Montero-Vallejo R., Ampuero J., López M., Diéguez C., Herrero L., Serra D., Chwaninger M., Prevot V., Gallego-Duran R., Romero-Gomez M., Iruzubieta P., Crespo J., Martinez-Chantar M. L., Garcia-Monzon C., Gonzalez-Rodriguez A., Aspichueta P., Nogueiras, R. (2022). Inhibition of ATG3 ameliorates liver steatosis by increasing mitochondrial function. Journal of Hepatology, 76(1), 11–24. https://doi.org/10.1016/J.JHEP.2021.09.008
8. Goikoetxea-Usandizaga, N., Serrano-Maciá, M., Delgado, T. C., Simón, J., Fernández Ramos, D., Barriales, D., Cornide, M. E., Jiménez, M., Pérez-Redondo, M., Lachiondo-Ortega, S., Rodríguez-Agudo, R., Bizkarguenaga, M., Zalamea, J. D., Pasco, S. T., Caballero-Díaz, D., Alfano, B., Bravo, M., González-Recio, I., **Mercado-Gómez, M**., Gil-Pitarch C., Mabe J., Gracia-Sancho J., Abecia L., Lorenzo O., Martín-Sanz P., Abrescia N. G. A., Sabio G., Rincón M., Anguita J., Miñambres E., Martín C., Berenguer M., Fabregat I., Casado M., Peralta C., Varela-Rey M., Martínez-Chantar, M. L. (2022). Mitochondrial bioenergetics boost macrophage activation, promoting liver regeneration in metabolically compromised animals. Hepatology, 75(3), 550–566. https://doi.org/10.1002/HEP.32149
9. Serrano-Maciá, M., Simón, J., González-Rellan, M. J., Azkargorta, M., Goikoetxea-Usandizaga, N., Lopitz-Otsoa, F., De Urturi, D. S., Rodríguez-Agudo, R., Lachiondo-Ortega, S., **Mercado-Gómez, M.**, Gutiérrez de Juan, V., Bizkarguenaga, M., Fernández-Ramos, D., Buque, X., Baselli, G. A., Valenti, L. V. C., Iruzubieta, P., Crespo, J., Villa, E., Banales J. M., Avila M. A., Marin J. J. G., Aspichueta P., Sutherland J., Barrio R., Mayor U., Elortza F., Xirodimas D. P., Nogueiras R., Delgado T. C., Martínez-Chantar, M. L. (2021). Neddylation inhibition ameliorates steatosis in NAFLD by boosting hepatic fatty acid oxidation via the DEPTOR-mTOR axis. Molecular Metabolism, 53. https://doi.org/10.1016/J.MOLMET.2021.101275
10. Simón, J., Goikoetxea-Usandizaga, N., Serrano-Maciá, M., Fernández-Ramos, D., Sáenz de Urturi, D., Gruskos, J. J., Fernández-Tussy, P., Lachiondo-Ortega, S., González-Recio, I., Rodríguez-Agudo, R., Gutiérrez-de-Juan, V., Rodríguez-Iruretagoyena, B., Varela-Rey, M., Gimenez-Mascarell, P., **Mercado-Gómez, M.**, Gómez-Santos, B., Fernandez-Rodriguez, C., Lopitz-Otsoa, F.,

Bizkarguenaga, M., Dames S., Schaeper U., Martin F., Sabio G., Iruzubieta P., Crespo J., Aspichueta P., Chu K. H-Y., Bucella D., Mastín C., Delgado T. C., Martínez-Cruz L. A., Martínez-Chantar, M. L. (2021). Magnesium accumulation upon cyclin M4 silencing activates microsomal triglyceride transfer protein improving NASH. Journal of Hepatology, 75(1), 34–45. https://doi.org/10.1016/J.JHEP.2021.01.043

11. **Mercado-Gómez, M.**, Lopitz-Otsoa, F., Azkargorta, M., Serrano-Maciá, M., Lachiondo-Ortega, S., Goikoetxea-Usandizaga, N., Rodríguez-Agudo, R., Fernández-Ramos, D., Bizkarguenaga, M., Gutiérrez-De Juan, V., Lectez, B., Aloria, K., Arizmendi, J. M., Simon, J., Alonso, C., Lozano, J. J., Avila, M. A., Banales, J. M., Marin, J. J. G., Beraza N., Mato J. M., Elortza F., Barrio R., Sutherland J. D., Mayor U., Martínez-Chantar, M. L., Delgado, T. C. (2020). Multi-Omics Integration Highlights the Role of Ubiquitination in CCl_4-Induced Liver Fibrosis. International Journal of Molecular Sciences, 21(23), 1–19. https://doi.org/10.3390/IJMS21239043
12. Fondevila, M. F.*, **Mercado-Gómez, M.***, Rodríguez, A.*, Gonzalez-Rellan, M. J.*, Iruzubieta, P., Valentí, V., Escalada, J., Schwaninger, M., Prevot, V., Dieguez, C., Crespo, J., Frühbeck, G., Martinez-Chantar, M. L.**, Nogueiras, R.** (2021). Obese patients with NASH have increased hepatic expression of SARS-CoV-2 critical entry points. Journal of Hepatology, 74(2), 469–471. https://doi.org/10.1016/J.JHEP.2020.09.027. *These authors contributed equally: Fondevila, M. F., **Mercado-Gómez, M.**, Rodríguez, A., Gonzalez-Rellan, M. J. ** These authors jointly supervised this work: Martinez-Chantar, M. L., Nogueiras, R.
13. Lachiondo-Ortega, S., **Mercado-Gómez, M.**, Serrano-Maciá, M., Lopitz-Otsoa, F., Salas-Villalobos, T. B., Varela-Rey, M., Delgado, T. C., Martínez-Chantar, M. L. (2019). Ubiquitin-Like Post-Translational Modifications (Ubl-PTMs): Small Peptides with Huge Impact in Liver Fibrosis. Cells, 8(12). https://doi.org/10.3390/CELLS8121575